Growth and applications of wafer-scale hexagonal boron nitride

Dipankar Chugh

A thesis submitted for the degree of

Doctor of Philosophy

Of

The Australian National University

Department of Electronic Materials Engineering
Research School of Physics
College of Physical and Mathematical Sciences

© Copyright Dipankar Chugh 2020
All Rights Reserved

Certificate

This thesis, to the best of my knowledge and belief, does not contain any results previously published by another person or submitted for a degree or diploma at any university except where due references is made in the text.

Dipankar Chugh

January 2020

Acknowledgements

The opportunity to pursue my doctoral studies at the Department of Electronic Materials Engineering at ANU is and shall always remain a matter of great privilege for me. I am grateful to a number of people who have guided and assisted me during the course of my program.

Firstly, I sincerely thank my principal supervisor, Prof. Hoe Tan, for accepting me as one of his students, and giving me the opportunity to work on an exciting research project. Thank you for constant your support and guidance, which made my Ph.D. an enjoyable learning experience. I am very grateful to Prof. Jagadish for providing valuable and constructive advice. He has always inspired and motivated me through words of encouragement and his own achievements.

I want to thank A/Prof. Jennifer Wong-Leung for her supervision and guidance, especially for taking the time to discuss experimental data, scientific literature and helping me with TEM imaging. The TEM images that are included in this work were only made possible due to her expertise.

I thank Dr. Mykhaylo Lysevych for training me on the MOVPE equipment and sharing his knowledge on epitaxial growth processes. His expertise on the MOVPE machine and process proved to be very valuable.

I express my gratitude and appreciation towards the academic staff at the EME department, in particular to Prof. Rob Elliman for fruitful discussions and allowing me to attend his lectures on condensed matter physics. I thank Dr. Christian Notthoff for sharing his expertise, training and valuable advice on spectrometry. I also thank Dr. Larrisa Huston and Prof. Jodie Bradby for training and access to the Raman spectrometer.

I gratefully acknowledge the training and assistance I received from Dr. Fan Wang, Dr. Sudha Mokkapati and Dr. Ziyuan Li with respect to photoluminescence spectroscopy. I am also very grateful to A/Prof. Marcus Doherty, Dr. Michael Barson and Dr. Tobias Vogl for many insightful discussions and for sharing their knowledge on quantum emitters with me. I sincerely thank Prof. Vince Craig for training and open access to the AFM instruments in his lab.

The ANFF team provided excellent support for which I am extremely grateful. I want to acknowledge and thank Dr. Fouad Karouta, Dr. Li Li, Dr. Kaushal Vohra, Dr. Mark Lockrey (now at UTS, NSW), Dr. Olivier Lee Cheong Lem and Ms. Sue Berkeley, for their constant help and support in the undertaking my research work. During my program, I have learned many new fabrication techniques and processes, which was made possible through the training I received from them.

I am deeply grateful to our collaborators, Prof. Igor Aharonovich and his team (in particular Noah Mendelson) at the University of Technology Sydney, and Prof. Anushree Roy at Indian Institute of Technology (Kharagpur) for their interests in our work on hBN. It was a great experience working and learning from with these excellent scientists.

I would like to thank the technical staff at EME - Mr. Chris Kafer, Mr. Tom Ratcliff, Mr. Dane Kelly and Mr. Joshua Carr. I also thank Ms. Julie Arnold, Ms. Liudmila Mangos, Ms. Karen Nulty and Ms. Liz Micallef for their tireless work as department and school administrators and helping HDR students.

I have been very fortunate to share this journey with my fellow group members (past and present). To all my friends in EME- Inseok, Rowena, Roccio (from NLP), Naiyin, Bijun, Zahra, Reddy, Joshua, Vidur, Sonachand, Nikita, Aswani, Fanlu, Wei – thank you all for your friendship that I value dearly. There has never been a dull moment at work, with morning and afternoon tea, drinks and evenings spent together in Canberra. By being a part of EME, I have made new lifelong friends and memorable experiences that I shall cherish forever.

It is with the deepest sense of gratitude, I thank my parents, for teaching me the things that really matter in life. I am blessed to have a sister who shares and gets all of my idiosyncrasies, like no one else. I thank my wife, for her love, support and companionship throughout this program, and providing me the strength to persevere and work hard towards achieving my goal. I thank my extended family members and friends in India, US and Australia, for their unwavering support and encouragement. My work has often kept me away from you all, whilst I have been selfishly busy with pursuing my goals. I thank you all for your understanding.

Abstract

Hexagonal boron nitride (hBN) is a two-dimensional (2D) material that has attracted considerable attention in recent years. As a layered material and a wide bandgap semiconductor, hBN has been used in different applications, ranging from deep UV emitters to gate dielectric in field effect devices based on 2D materials. In another application, hBN has been used as a substrate for growing conventional III-V semiconductors, via van der Waals epitaxy, for the development of flexible optoelectronic devices. More recently, single photon emission (SPE) from defects in hBN have generated new interests in this material for quantum computing related applications.

Many of the applications, as described above, rely on facile exfoliation of atomically thin layers of hBN from commercially available bulk crystals. The lateral dimensions of these exfoliated flakes is typically restricted to only a few tens of μm or less, which severely limits scale-up and large-area applications of hBN. Therefore, this thesis explores wafer-scale growth of hBN, using metal organic vapour phase epitaxy (MOVPE). As a deposition technique, MOVPE is a scalable process and offers accurate control over a number of growth parameters, such as temperature, precursor flow rate, deposition pressure, which can be individually varied to optimize the growth conditions.

In this study, hBN was deposited as continuous thin films over commercially available 2” sapphire substrates. Triethylboron (TEB) and ammonia were used as B and N growth precursors, respectively. The thickness of the films was varied by changing the growth time. Due to severe parasitic reactions between the precursors, hBN growth rates were extremely low. To overcome this, a flow-modulation scheme for precursor injection was adopted. A comprehensive characterization of the deposited films was undertaken using different experimental techniques. hBN films deposited on sapphire had a wrinkled surface morphology, which was studied using atomic force microscopy. Nanometer-sized debris like particles were also found on the surface of hBN films. Using transmission electron microscopy (TEM), these debris was identified as randomly oriented 3D hBN particles, which are formed due to parasitic gas-phase reactions between growth precursors. Cross-sectional TEM was

used to evaluate the stacking of the induvial hBN crystal planes. The (0002) basal planes of hBN were oriented parallel with respect to each other and also the c-plane of the sapphire substrate. Interestingly, the hBN basal planes were observed to bend and conform to the shape of wrinkles, whilst maintaining their layered atomic arrangement. Raman spectroscopy provided a quick and nondestructive method for confirming hBN deposition and also analyzing residual strain in the deposited films. MOVPE-hBN films were found to be under compressive strain, indicated by a blue shift in its E_{2g} peak position, measured using Raman spectroscopy. The composition of hBN was further evaluated using X-ray photoelectron spectroscopy, which revealed a strong dependence of carbon incorporation on TEB flux and overall growth rate of the films.

The optical properties of MOVPE-hBN were studied using photo/cathodo-luminescence spectroscopies and benchmarked against commercially available single crystal hBN. Due to high carbon incorporation, no bandedge luminescence was recorded from MOVPE-hBN. Instead, the emission spectra of MOVPE-hBN was dominated by impurity related sub-bandgap UV luminescence between 300-350 nm, and at visible wavelengths between 570-750 nm (rPL). A strong dependence of TEB flux and carbon incorporation on the rPL intensity was also observed. Single photon emission (SPE) from MOVPE-grown hBN films are reported for the first time. SPEs were only observed in hBN grown with the lowest configurable TEB flux (i.e. 10 μmol/min). These films have the lowest achievable carbon doping and negligible rPL. Interestingly, the emission spectrum of a typical SPE closely matched the shape of rPL. Although the exact nature of defect responsible for SPE in hBN is unknown, results reported herein, point towards an underlying role of carbon in both cases. Furthermore, many of the SPEs found in MOVPE-hBN were photo-stable, displayed a characteristic phonon-side band and had a narrow spectral distribution of the emission wavelength. Emitter lifetime was measured to be of the order of few nanoseconds, which is consistent with recent reports on emitters found in commercially available hBN samples.

hBN films grown on sapphire were transferred onto different substrates. It was found that films thicker than 20 nm spontaneously self-delaminated in a water bath, while for thinner films, a wet-chemical transfer process was specifically designed. Using these methods, few-layer thick hBN films were also transferred onto substrates containing silver and gold nanoparticles (NPs). Being atomically thin and flexible,

hBN was able to effectively wrap around Ag nanoparticles to form an impermeable barrier, which was found to be effective in preventing oxidation of Ag NPs even at elevated temperatures. Consequently, the plasmonic activity of the hBN covered Ag NPs remained preserved and was demonstrated through surface enhanced Raman spectroscopy. This study showcases the application of large-area hBN films for protecting nanostructured metallic surfaces.

In a different application, wafer-scale hBN films on sapphire were used as substrates for the growth of AlN, using MOVPE. Amongst III-nitrides, AlN is the principal candidate for the development of solid-state deep-UV devices. In this thesis, AlN was grown on hBN (and on sapphire for comparison) under different conditions to study the effect of growth parameters on the surface morphology and crystallinity of AlN films. A detailed structural and morphological analysis of AlN films has been undertaken. Using a standard two-step process, involving a low-temperature nucleation layer, AlN growth on hBN resulted in polycrystalline film with a rough morphology. This could be attributed to random nucleation due to low mobility of Al atoms on hBN. Hence a modified, multi-step high temperature growth process was utilized for obtaining planar AlN films, with improved crystallinity. AlN films grown on hBN were easily delaminated from the sapphire wafers and showed a relaxation in compressive strain, which was studied using Raman spectroscopy.

Overall, this work provides valuable insights into wafer-scale growth of hBN using MOVPE. The crystallinity, morphology and luminescent properties of MOVPE-hBN films were studied in detail and found to be critically affected by the choice of growth parameters. The study also showcases the versatility of large-area hBN films. Different applications of the MOVPE-hBN films, ranging from passivation of Ag NPs, to SPEs and van der Waals epitaxy of AlN films were demonstrated.

List of publications

Journal Papers (only on research work related to hBN)

1. D. Chugh, J. Wong-Leung, L. Li, M. Lysevych, H.H. Tan, and C. Jagadish, Flow modulation epitaxy of hexagonal boron nitride. *2D Materials*, 2018. 5(4): p. 045018.
2. D. Chugh, C. Jagadish, and H. Tan, Large-Area Hexagonal Boron Nitride for Surface Enhanced Raman Spectroscopy. *Advanced Materials Technologies*, 2019. 4(8): p. 1900220.
3. D. Chugh, S. Adhikari, J. Wong-Leung, M. Lysevych, C. Jagadish, and H.H. Tan, Improving the Morphology and Crystal Quality of AlN Grown on Two-Dimensional hBN. *Crystal Growth & Design*, 2020. **20**(3): p. 1811-1819.
4. Bera, K., D. Chugh, A. Patra, H.H. Tan, C. Jagadish, and A. Roy, Strain distribution in wrinkled hBN films. *Solid State Communications*, 2020. **310**: p. 113847.
5. N. Mendelson, D. Chugh, J. R. Reimers, T. S. Cheng, A. Gottscholl, H. Long, C. J. Mellor, A. Zettl, V. Dyakonov, P. H. Beton, S. V. Novikov, C. Jagadish, H. H. Tan, M. J. Ford, M. Toth, C. Bradac and I. Aharonovich, Identifying Carbon as the Source of Visible Single Photon Emission from Hexagonal Boron Nitride. *https://arxiv.org/abs/2003.00949 (under review)*.

Conference papers

1. D. Chugh, J. Wong-Leung, L. Li, M. Lysevych, H.H. Tan, and C. Jagadish, MOVPE grown hexagonal boron nitride for SERS application. *13th International Conference on Nitride Semiconductors*, 2019 (ICNS-13), Seattle, USA.
2. D. Chugh, J. Wong-Leung, L. Li, M. Lysevych, H.H. Tan, and C. Jagadish, Large area hexagonal boron nitride coating for SERS application with silver nanoparticles. *Compound Semiconductor Week 2019* (CSW'19), Nara, Japan.

3. D. Chugh, J. Wong-Leung, L. Li, M. Lysevych, H.H. Tan, and C. Jagadish, Wafer-scale growth of hexagonal boron nitride on sapphire substrates using metal organic vapour phase epitaxy. *2018 Conference On Optoelectronic And Microelectronic Materials And Devices* (COMMAD), Perth, Australia.
4. D. Chugh, J. Wong-Leung, L. Li, M. Lysevych, H.H. Tan, and C. Jagadish, Wafer-scale growth of hexagonal boron nitride on sapphire substrates using metal organic vapour phase epitaxy. *The 19th International Conference on Metalorganic Vapor Phase Epitaxy* (ICMOVPE-XIX), Nara, Japan.
5. D. Chugh, J. Wong-Leung, L. Li, M. Lysevych, H.H. Tan, and C. Jagadish, Wafer-scale epitaxial growth of hexagonal boron nitride on sapphire substrates. *International Conference on Nanoscience and Nanotechnology (ICONN'18)*, Wollongong, Australia.

Abbreviations and acronyms

AFM	Atomic force microscopy
ANU	Australian National University
BNNS	Boron nitride nanosheet
CCD	Charge-coupled device
CCS	Closed coupled showerhead
CFG	Continuous flow growth
CL	Cathodoluminescence
CTE	Coefficient of thermal expansion
CVD	Chemical vapour deposition
CW	Continuous wave
DI	De-ionized
EDS	Energy dispersive X-ray spectroscopy
EM	Electromagnetic
FET	Field effect transistor
FFT	Fast Fourier transform
FIB	Focused ion beam
FLG	Few layer graphene
FM	Flow modulation
FME	Flow modulation epitaxy
FWHM	Full width at half maximum
GI	Grazing incidence
aBN	Amorphous boron nitride

hBN	hexagonal boron nitride
*t*hBN	Turbostratic hBN
t-hBN	Thin hBN
HBT	Hanbury-Brown-Twiss
HEMT	High electron mobility transistor
HR	High resolution
HT	High temperature
IQE	Internal quantum efficiency
LED	Light emitting diode
LO/TO	Longitudinal optical/Transverse optical
LT	Low temperature
MBE	Molecular beam epitaxy
MO	Metal-organic
MOVPE	Metal-organic vapour phase epitaxy
MQW	Multi-quantum well
NBE	Near band edge
NL	Nucleation layer
NP(s)	Nanoparticle(s)
OBG	Optical band gap
PL	Photoluminescence
PMMA	Polymethyl methacrylate
PMT	Photo-multiplier tube
PSB	Phonon side band
PVA	Polyvinyl alcohol

QE	Quantum emitter
R6G	Rhodamine 6G
SADP	Selective area diffraction pattern
sccm	Standard cubic centimeter per minute
SE	Secondary electrons
SEM	Scanning electron microscopy
SERS	Surface enhanced Raman spectroscopy
SHINERS	Shell isolated nanoparticle enhanced Raman spectroscopy
SIMS	Secondary ion mass spectroscopy
SLM	Standard liter per minute
SPE	Single photon emitter (or emission)
STEM	Scanning tunneling electron microscopy
TCSPC	Time correlated single photon counting
TEB	Triethylboron
TEM	Transmission electron microscopy
t-hBN	Thin hBN
TMA	Trimethylaluminium
UV	Ultra violet
XPS	X-ray photoelectron spectroscopy
XRC	X-ray rocking curve
XRD	X-ray diffraction
ZPL	Zero phonon line

Common symbols

Symbol	Description
λ	wavelength
ω	Incidence angle of X-ray with respect to sample
θ	Half of the diffraction angle (degree)
τ	Lifetime of charge carrier (nanosecond)
T_G	Growth temperature during MOVPE (degree Celsius)
η	Refractive index
d_{hkl}	Distance between lattice planes with Miller indices hkl
hkl	Miller indices of a lattice plane
$\Delta\omega$	Raman shift in wavenumber (cm^{-1})
α	Absorption coefficient
h	Planck's constant
v	Frequency of photon
E_b	Binding energy
Φ	Work function
R_q	Surface roughness (root mean square)
I_x	Intensity of the XPS peaks
S_x	Sensitivity factor for atoms in XPS
g^2	Second order autocorrelation function

Table of Contents

Certificate .... **i**

Acknowledgements .... **ii**

Abstract .... **iv**

List of publications .... **vii**

Abbreviations and acronyms .... **ix**

Common symbols .... **xii**

Table of Contents .... **xiii**

Chapter 1. Introduction **1**

1.1 Introduction 1

1.2 Two-dimensional materials 2

1.3 Thesis Synopsis 7

Chapter 2. Literature Review **9**

2.1 Introduction 9

2.2 Crystal structure and basic properties 9

2.3 Applications 13
- 2.3.1 Lubricant and high temperature composites 13
- 2.3.2 Electronics 15
- 2.3.3 Heteroepitaxy 16
- 2.3.4 Surface passivation 17
- 2.3.5 Optical applications 17

2.4 Synthesis 20
- 2.4.1 Bulk crystal growth from melt 21
- 2.4.2 Chemical vapour deposition 23
- 2.4.3 Metal organic vapor phase epitaxy 25

2.5 Summary 28

Chapter 3. Experimental Methods **30**

3.1 Introduction 30

3.2 CVD and MOVPE 30

3.3 X-Ray Diffraction 35

3.4 Atomic force microscopy 36

3.5 Raman Spectroscopy 37

3.6 Ultraviolet-visible (UV-Vis) absorption spectroscopy 39

3.7 X-ray photoelectron spectroscopy 40

3.8 Photoluminescence spectroscopy 40

3.9 Scanning electron microscopy and cathodoluminescence 42

3.10 Transmission electron microscopy 44

Chapter 4. MOVPE growth and characterization of hBN ... 45

4.1 Introduction ... 45

4.2 MOVPE process overview ... 45

4.3 Continuous flow growth ... 48

4.4 Flow Modulation Epitaxy ... 53

4.5 Effect of TEB flux ... 57

4.6 Effect of Ammonia flux ... 61

4.7 Effect of Growth Temperature ... 63

4.8 Spontaneous delamination of hBN films ... 64

4.9 Plan view TEM of debris ... 68

4.10 Summary ... 70

Chapter 5. Optical properties and single photon emitters in MOVPE-grown hBN ... 71

5.1 Introduction ... 71

5.2 Photo/Cathodo-luminescence studies on hBN: Literature review ... 71
- 5.2.1 Excitonic/NBE recombination (5.76 and 5.86 eV) ... 71
- 5.2.2 Luminescence from bound/ trapped excitons (5.2 – 5.7 eV) ... 73
- 5.2.3 Defect and impurity related sub-bandgap UV luminescence (3.0 - 4.5 eV) ... 75
- 5.2.4 Quantized visible emissions ... 76

5.3 Photo/Cathodoluminescence studies on MOVPE-grown hBN ... 78

5.4 Effect of TEB flux on sub-bandgap luminescence in MOVPE grown hBN films ... 80

5.5 Single photon emitters in MOVPE-grown hBN films ... 84

5.6 Summary ... 89

Chapter 6. MOVPE-grown hBN for SERS applications ... 90

6.1 Introduction ... 90

6.2 Surface enhanced Raman spectroscopy: a brief overview ... 90

6.3 Fabrication of hBN-SERS substrates ... 93

6.4 SERS measurements results ... 96
- 6.4.1 SERS performance of hBN covered Au and Ag NPs ... 96
- 6.4.2 hBN for preventing oxidation of Ag NPs ... 98

6.5 Droplet-based SERS chip ... 103

6.6 Summary ... 105

Chapter 7. Epitaxial growth and characterization of AlN on hBN ... 106

7.1 Introduction ... 106

7.2 III-nitride growth on hBN: Literature review ... 106

7.3 MOVPE deposition of AlN on hBN (and sapphire) ... 109
- 7.3.1 Two-step AlN growth ... 110
- 7.3.2 One-step AlN growth ... 111
- 7.3.3 Multi-step AlN growth ... 118

7.4 Delamination/Peeling-off AlN films ... 121

7.5 Effect of hBN thickness on AlN growth 123
7.6 Summary 124
Chapter 8. Conclusions and future work 126
8.1 Outcomes 126
8.2 Recommendations for future work 129
8.2.1 Improving the quality of hBN films 129
8.2.2 Alloying of hBN 130
8.2.3 Doping 130
8.2.4 Flexible optoelectronic devices 131
8.2.5 Quantum emitters 131
References 133

Chapter 1. Introduction

1.1 Introduction

Over the years, the world has witnessed many technological revolutions which have played an important role in shaping our lives. The discovery, invention and application of new materials have always been at the heart of new technological advancements. Every time a new material is discovered or becomes available, new technologies can be developed that improve the quality of human life and through this, drive societal changes. In fact, some of the archaeological time periods, spanning hundred to thousands of years, such as the Stone Age (2.5 M - 3000 B.C.E.), Bronze Age (3,000 to 1,200 B.C.E.) or Iron Age (~ 1,300 to 500 B.C.E) have indeed been named after a material. This nomenclature underscores the importance of these materials to new developments during the early days of human civilization. Initially, technological and scientific advances, were limited by materials such as wood, stone, soil, animal bones/skin, which were naturally available to humans. As civilizations progressed, new materials were discovered and even created such as metallic alloys, glass/quartz, ceramics, polymers etc. This story of materials, intertwined with human progress has continued through the centuries, since the Neolithic time periods.

Starting in the middle of the 20th Century, the world has witnessed another technological revolution, which has been unfolding over the last 70 years. It has been brought about through the use of a very special class of materials called semiconductors. The name 'semiconductor' is derived from and is indicative of the electrical conductivity of these materials, which is in between that of a metal and an insulator. However, it is the ability to modulate the electrical conductivity of these materials, either through application of electric fields or by introduction of foreign impurities as dopants, which proved to be of great technological importance. It enabled new electronic functions, such as switching, amplification etc. and laid the foundations of digital electronics. Hence, starting with the development of a simple diode, to (field-effect) transistors, integrated circuits (ICs) and eventually digital electronic devices, including computers, mobile phones etc., the technological developments (and the resulting societal changes) have been rapid, disruptive and unprecedented. Silicon,

which is an elemental semiconductor, has been fundamental to all these developments and today, is unquestionably the cornerstone of the multi-billion dollar semiconductor industry [1].

In addition to silicon, another family of semiconductor materials have been developed, which consist of two elements. These are binary-octet type compounds of the form $A^{N}B^{8-N}$ (with 8 electrons in the outer most shell). Most prominent amongst these are the III-V materials, such as GaAs, InP and GaN, which are composed of one element from column III and another from column V of the periodic table. Similarly, II-VI type compound semiconductor materials like ZnO, CdS and ZnSe and IV-IV materials like SiC are also well-known.

Compound semiconductor materials have many unique attributes. For example, most III-V materials have a direct bandgap, which makes these materials extremely efficient at absorbing and emitting photons. Hence, they are widely used for optoelectronic applications such as LEDs, laser diodes, photodetectors and photovoltaics. It is therefore not surprising that today, solar cells and laser diodes, with record efficiencies are made using III-V materials like InP and GaAs. Similarly, the energy efficient white-light LEDs, used as downlights in households, offices, street lighting and billboards, has indeed been made possible through the III-nitride material system [2]. It is predicted that in U.S. alone, the total electricity consumption for lighting (~ 18 % of total electricity consumed) can be reduced by a third, through large scale adoption of energy efficient white-light LEDs [3]. This not only translates into dollar savings of several billions annually but also helps to reduce the carbon emissions associated with energy production. In addition to this, compound semiconductor materials have high charge carrier mobility, are hard and robust materials which makes them suitable for high electron mobility transistors and power electronic applications. Overall these materials are of great technological and socio-economic importance.

1.2 Two-dimensional materials

The quest for new materials is forever ongoing. Silicon, which has been remained the most favoured material for electronic applications over the last fifty years is reaching its limitations, as predicted by Moore's Law [4]. On the other hand, the performance of III-Vs is still to reach its pinnacle, yet research into exploring new

materials for the next generation of electronic and optoelectronic devices is already underway. These new devices are envisioned to not only be more energy efficient, with superior performance than its predecessors, but also light weight and even stretchable or flexible [5-7]. This paradigm shift in electronic devices from rigid to flexible/conformal can be realized through the advent of a new class of materials, known as 2D materials, which first came to attention with the discovery of graphene in 2004 [8].

2D materials, also referred as layered materials are composed of single to multiple layers of atoms, with lateral dimensions varying from a few microns to mm. Atoms within the layer are covalently bonded, whilst individual, single-atom thick layers are stacked on top of each other and held together by van der Waals forces. A few examples of commonly used 2D materials are illustrated in Figure 1-1.

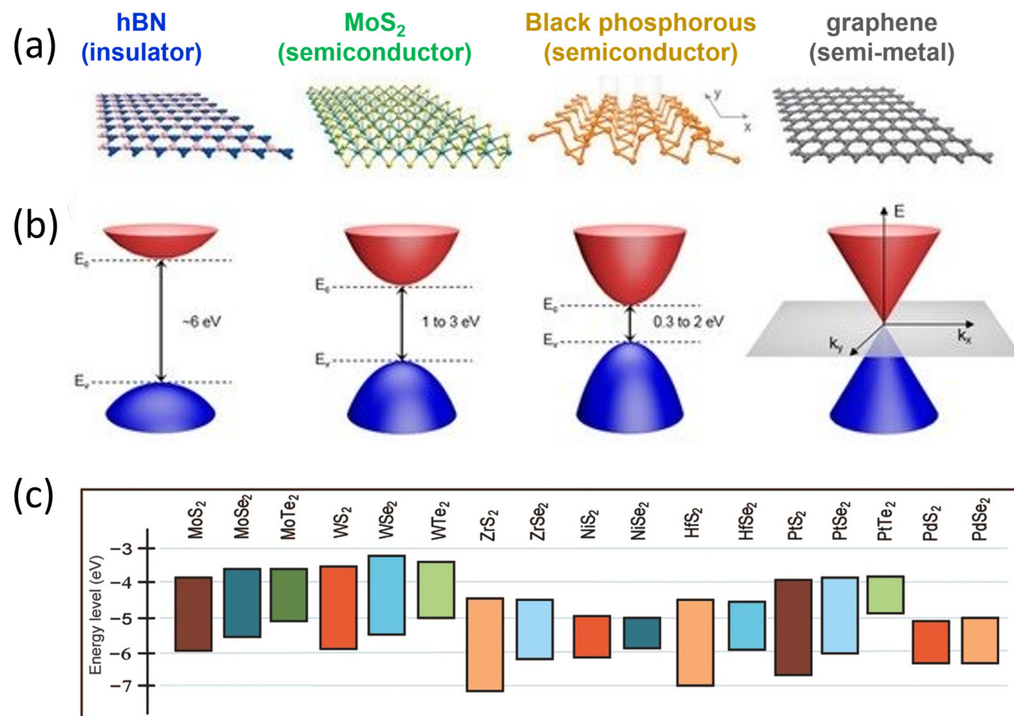

Figure 1-1 (a-b) Crystal structure and band energy diagram of a few commonly known 2D materials, namely hBN, MoS_2, WSe_2 and graphene. (c) Energy spectrum of some additional 2D materials [9, 10].

It is interesting to note that for a very long time, except for theoretical predictions, the practical existence of 2D materials was questionable. It was suggested

that in such low dimensional crystals, thermal vibrations of atoms at room temperature will cause atomic displacements, of the order of interatomic distances, which will make the material highly unstable [11]. In fact, many 3D materials like steel, silicon etc. indeed become unstable and disintegrate when thinned down to a few atomic layers. Therefore, in order for these 2D materials to exist, the in-plane bonding between atoms has to be strong enough to overcome fluctuations caused by atomic vibrations. This is indeed the case and it should not be surprising that materials like graphene and hBN are amongst the strongest known materials [12-14].

Within the last decade, starting with the discovery of graphene, the repertoire of 2D materials both in type and functionality has increased rapidly. Based on a recent report, nearly 700 2D materials are expected to be stable, many of which are yet to be synthesised [15]. Some of the commonly utilized 2D materials are listed in Table 1-1.

Table 1-1 A library of 2D materials [16]. Monolayers stable under ambient are shaded in blue; those only stable in inert atmosphere are shaded in pink. Grey shading indicates 3D compounds which have been successfully exfoliated to monolayers. 'Others' indicate newly found 2D materials of nitrides, carbides etc.

Graphene family	Graphene	hBN 'white graphene'	BCN	Fluorographene	Graphene oxide
2D chalcogenides	MoS_2, WS_2, $MoSe_2$, WSe_2	Semiconducting dichalcogenides: $MoTe_2$, WTe_2, ZrS_2, $ZrSe_2$ and so on	Metallic dichalcogenides: $NbSe_2$, NbS_2, TaS_2, TiS_2, $NiSe_2$ and so on	Layered semiconductors: GaSe, GaTe, InSe, Bi_2Se_3 and so on	
2D oxides	Micas, BSCCO	MoO_3, WO_3	Perovskite-type: $LaNb_2O_7$, $(Ca,Sr)_2Nb_3O_{10}$, $Bi_4Ti_3O_{12}$, $Ca_2Ta_2TiO_{10}$ and so on	Hydroxides: $Ni(OH)_2$, $Eu(OH)_2$ and so on	
	Layered Cu oxides	TiO_2, MnO_2, V_2O_5, TaO_3, RuO_2 and so on		Others	

In addition to being physically strong, 2D materials have many unusual properties. Owing to their unique layered crystal structure, charge carriers (i.e. electrons and holes) and phonons are effectively confined within the individual layers, resulting in exceptionally high charge carrier mobility [8, 17, 18] and very high thermal conductivity [19]. Similarly, due to reduced dielectric screening, electron-hole pair (excitons) interactions in 2D material are relatively strong (compared to conventional 3D materials), giving rise to novel optical properties [20-22]. Furthermore, due to weak inter-layer forces, mono- to few-layers of 2D materials can

be readily exfoliated from bulk crystals using small mechanical forces and transferred onto desired substrates, as illustrated in Figure 1-2 [23, 24]. Using this simple approach, atomically thin layers of different 2D materials can also be stacked on top of each other to form hetero-structure devices, as illustrated in Figure 1-3, such as field-effect transistors, solar cells, LEDs and optical detectors, [8, 16, 25-29]. Hence, based on their novel properties described above, the practical application of these atomically thin 2D materials has been established and bench-marked against conventional devices.

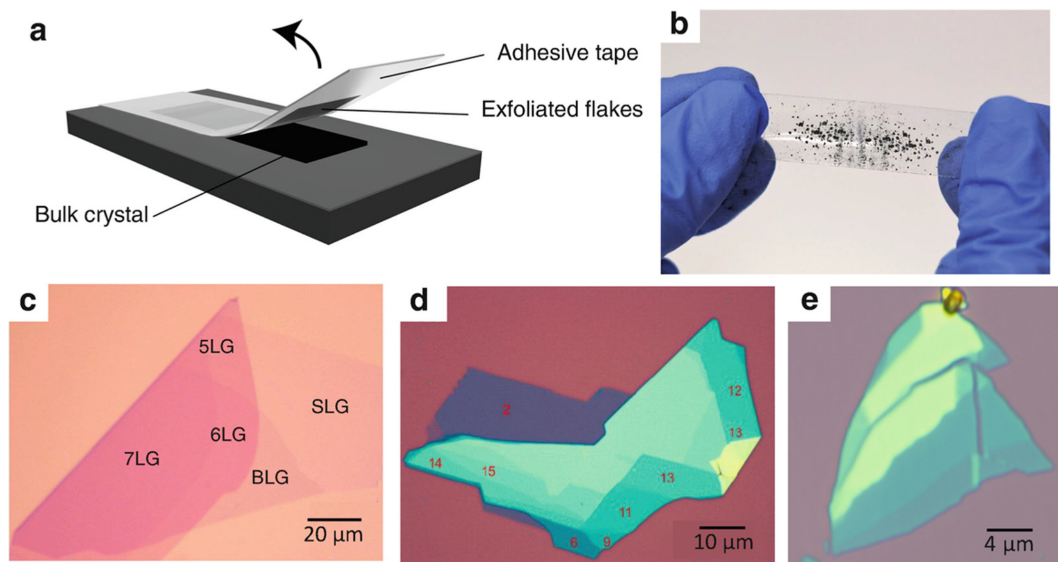

Figure 1-2 (a) Schematic illustration of mechanical exfoliation of 2D material, (b) a piece of tape with crystal of 2D material, (c-e) optical micrographs of mono to few layers of graphene, MoS_2 and hBN exfoliated on a SiO_2/Si substrate, respectively [30, 31].

In the absence of wafer-sized bulk 2D crystals, device fabrication relies on thin layers of 2D materials obtained from micron-sized bulk crystals through mechanical exfoliation, as described above. This approach provides quick, cheap and easy access to high quality single crystal layers, which are proving to be valuable for performing fundamental studies and proof-of-concept type applications. However, scale-up and large area application of 2D materials is severely restricted. To overcome this limitation, the epitaxial growth of 2D materials, on suitable substrates has gained significant attention. The work presented in this thesis, falls within this realm and explores wafer-scale growth of a 2D material – hexagonal boron nitride (hBN), using

metal organic vapour phase epitaxy (MOVPE). Within the family of 2D materials, hBN occupies a unique position. Owing to its large bandgap and an atomically smooth surface, free of dangling bonds, hBN has been accepted as a universal substrate and an insulating gate dielectric for various devices based on 2D materials [17]. Due to its high thermal and chemical stability, atomically thin layers of hBN have also been used to protect other 2D materials and metallic surfaces against oxidation or hydroxylation [32-35]. Furthermore, hBN has also attracted considerable attention as an optically active material, with luminescence varying from deep UV to visible wavelengths, including non-classical emission from defects [36-38]. For these reasons, wafer-scale growth (and applications) of hBN is pursued in this study. A brief overview of the thesis is given below.

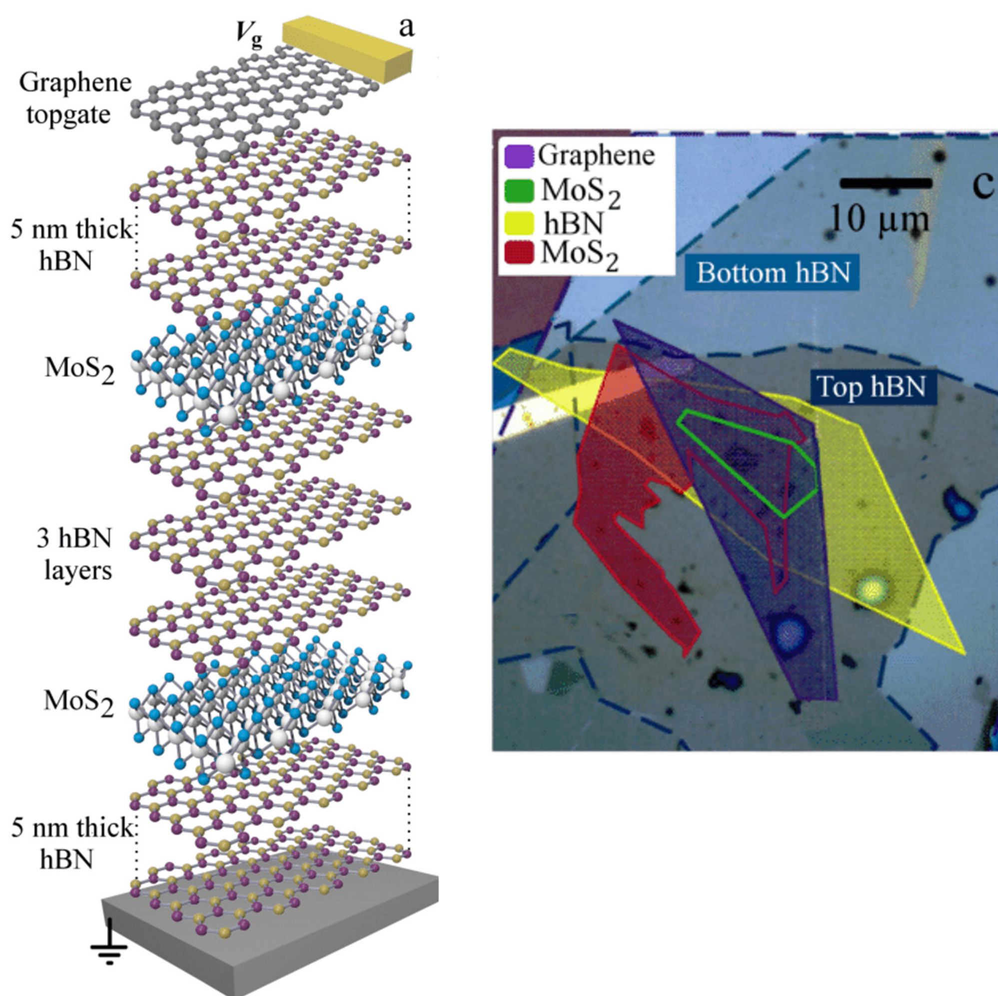

Figure 1-3 (a) a schematic illustration of a stack of 2D materials consisting of hBN, graphene and MoS_2 that forms a quantum-well heterostructure device and (b) a false coloured optical micrograph of the actual device shown in (a) [39].

1.3 Thesis Synopsis

Following this introduction, Chapter 2 provides an overview of boron nitride compounds, its structure, properties, applications and synthesis of hBN using different techniques. Chapter 3 provides the theoretical background behind the experimental techniques used in this study, for the growth and characterization of hBN.

Wafer-scale growth of hBN on sapphire using MOVPE is systematically investigated and key findings are presented in Chapter 4. hBN growth is compared under different conditions. The study highlights many challenges which are unique to hBN growth, such as severe parasitic reactions, high levels of impurity incorporation and the requirement of high growth temperatures. In addition to this, MOVPE-grown hBN were characterized using various techniques, such as atomic force microscopy (AFM), transmission electron microscopy (TEM), X-ray photoelectron spectroscopy (XPS), Raman and UV-vis absorbance spectroscopy, which are detailed in Chapter 4.

The luminescence properties of MOVPE-hBN, studied using Photo/Cathodo-luminescence spectroscopy are presented in Chapter 5. The emission properties of MOVPE-hBN films were benchmarked against commercially available single crystal hBN. The influence of carbon, which is incorporated as an impurity (unintentionally), on the luminescence properties of MOVPE-hBN was also investigated. Furthermore, a number of single photon emitters (SPEs) were also found in selected MOVPE grown hBN films. Key results obtained from characterization of SPEs in hBN using photoluminescence spectroscopy have been included in Chapter 5.

In Chapter 6, the application of MOVPE-hBN films for surface enhanced Raman spectroscopy (SERS) is presented. In this study, hBN films were used to protect silver nanoparticles (NPs) from oxidation and preserve their plasmonic functionality, which was demonstrated through SERS. Being atomically thin and flexible, hBN was able to effectively wrap around Ag NPs to form an impermeable barrier that prevented oxygen from attacking them, even when samples were heated in air at 400ºC.

The growth of III-Vs on 2D materials like hBN has attracted attention in recent years for the development of flexible optoelectronic devices. The unique crystal structure of 2D materials, wherein, individual layers are held together by weak van der Waals forces (as opposed to strong covalent bonds) form a shear plane. This offers a convenient method to detach heterostructure devices from substrates post epitaxy. In

Chapter 7, epitaxial growth of AlN on hBN/sapphire substrates was investigated, which could serve as templates for the development of flexible deep-UV optoelectronic devices. AlN films grown on MOVPE-hBN could be successfully detached from sapphire substrates due to hBN.

Finally, some conclusions and suggestions for future work are outlined in Chapter 8.

The principal achievements of this research are:

i. Optimized MOVPE process for wafer-scale growth of hexagonal boron nitride. The study has also highlighted several challenges associated with the growth of hBN, including severe parasitic reactions between precursors, resulting in extremely low growth rates.

ii. Developed methods for the transfer of cm-sized hBN films from sapphire to other substrates. The applicability of the transfer methods was further demonstrated through the passivation of Ag nanoparticles for surface enhanced Raman spectroscopy.

iii. Single photon emissions from MOVPE-grown hBN are reported for the first time. Carbon was identified as a major impurity, which is incorporated in hBN through the use of TEB as boron precursor. The effect of carbon on the luminescent properties of hBN, including SPE have also been studied.

iv. The thesis also explored the application of wafer-scale thin films of hBN as templates for epitaxial growth of AlN. A multi-step MOVPE growth process was optimised for depositing AlN films on hBN, which could further aid in the development of flexible deep-UV optoelectronic devices.

Chapter 2. Literature Review

2.1 Introduction

Boron nitride (BN) is not a new material. Its origin can indeed be traced back to the mid-19th century when it was first synthesized by W. H. Balmain by reacting boric acid with potassium cyanide [40]. After almost a century since its first synthesis, BN (powders) were synthesized in industrial quantities and since then, have been primarily used as a lubricant and refractory material. Only recently, during the last decade, its resurgence as a semiconductor material has catalyzed new interest in it. Atomically thin layers of crystalline hexagonal boron nitride (hBN) can be obtained easily and applied for various applications. Being a wide bandgap semiconductor, which is also optically active and with exceptional thermal and chemical stability, in many aspects, hBN is certainly more interesting than its more illustrious counterpart – graphene. This chapter reviews existing literature and discusses some of the fundamental properties of hBN. It is divided into three main sections: First, the crystal structure and properties of hBN, some of which are unique owing to its two-dimensional structure, are discussed. This is followed by a discussion of prominent applications of hBN and lastly, we review different methods to synthesize hBN, ranging from solution-based synthesis of single crystal hBN to large-area thin films grown using vapour deposition methods.

2.2 Crystal structure and basic properties

Boron, carbon and nitrogen are neighbouring atoms in the periodic table. Allotropes of carbon such as diamond (cubic form of carbon), graphite or graphene (single atomic layer) are well known. Lonsdaleite, another rare and lesser known allotrope, is made of carbon atoms arranged in wurtzite structure (known as 'hexagonal diamond' and is harder than cubic diamond) [41-43]. Analogous to this, boron and nitrogen together are able to structurally mimic the many different allotropes of carbon. For example, cubic boron nitride – a material as hard as diamond, is used for making machining tools. Wurtzite boron nitride, is a rare and metastable form of BN [42, 44], however, it is the two dimensional (2D) hexagonal boron nitride (or hBN)

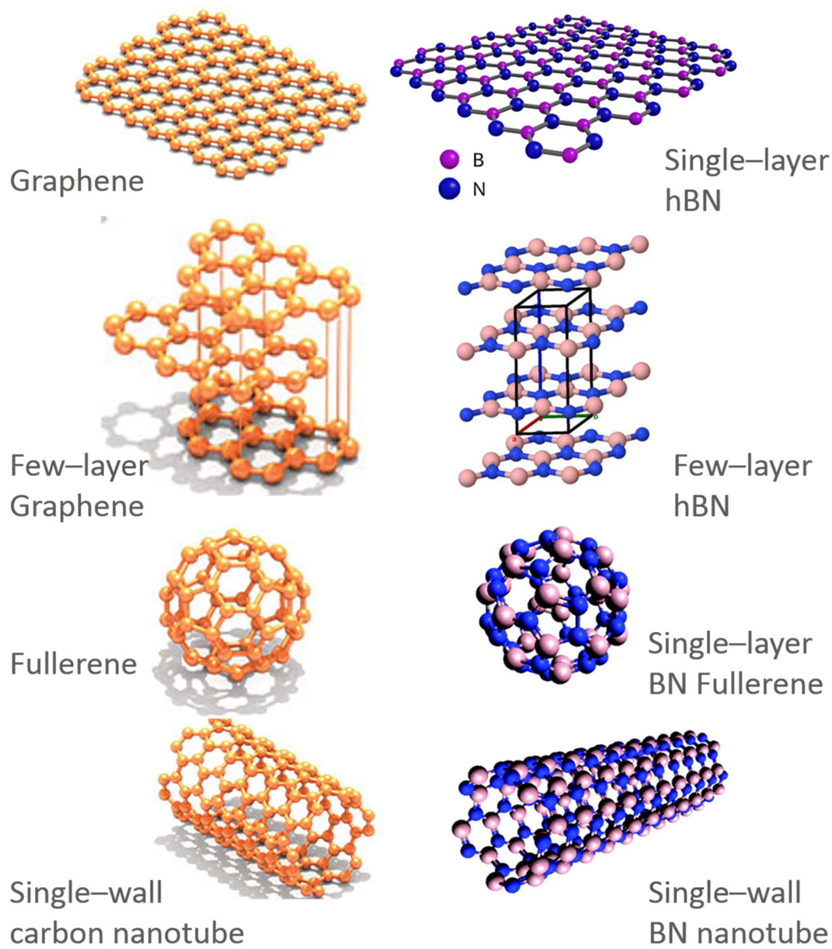

Figure 2-1 Structural polymorphs of sp^2 hybridized carbon and boron nitride [45].

with a layered structure similar to graphene that is of interest in context of the present study. Amorphous forms of carbon (e.g. coal) and BN are also known.

The crystal structure of hBN is similar to that of graphene, with a layered 2D material, as shown in Figure 2-1. Each individual layer comprises of alternating sp^2 hybridized boron and nitrogen atoms arranged in a hexagonal honeycomb-like lattice. hBN's crystal symmetry is commonly represented by space group $P6_3/mmc$, wherein basal planes are aligned along the c-direction (perpendicular to basal planes) in such a way so that B atoms are directly on top of the N atoms and vice versa, as shown in Figure 2-2 [46]. Every atom forms three σ bonds with its neighboring atoms and has a bond length of 1.44 Å (compared to 1.42 Å for C-C bond in graphene) [47-49]. Individual layers are held together by weak van der Waals forces and the distance

between them is 3.34 Å. In real hBN samples, space groups other than $P6_3/mmc$ have also been identified [49]. Furthermore, a partially and completely disordered phase of hBN also exists. Turbostratic BN (t-BN), which is a partially disordered phase, consists of randomly stacked (hexagonal, sp^2 bonded) basal planes, while amorphous BN lacks any structural ordering at the atomic level [50]. Due to stacking disorder, interlayer spacing in tBN is larger than hBN and this parameter is commonly used to distinguish between the two phases, using XRD [51]. Lastly, in addition to the planar, two-dimensional form of hBN, sp^2 hybridized BN can also exist in other forms such as nanotubes and fullerenes, as shown in Figure 2-1.

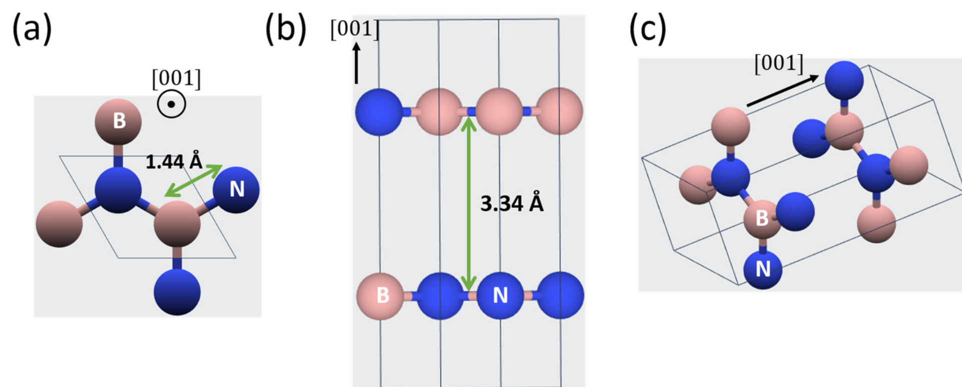

Figure 2-2(a-c) Differently oriented hBN unit cells with space group $P6_3/mmc$. Direction of [001] axis is indicated in each figure.

Owing to the structural similarity between graphite (or graphene for single layer) and hBN (with small lattice mismatch of nearly 1.7% between the two), several properties of hBN are comparable to that of graphite. The unique 2D structure and associated variation in bond strength, i.e. strong in-plane bonds and weak out of plane van der Waals bonds, gives rise to huge anisotropy in many material properties. For instance, due to weak van der Waals bonding between atomic planes, it is possible to isolate single to few layers of graphene with relative ease (using scotch tape). At the same time, with strong in-plane covalent bonding between carbon atoms, graphene has been proven to be the strongest known material, with a Young's modulus of 1.0 GPa and a breaking strength of 130 GPa [13, 52]. hBN is not far behind in this regard. Single to few layers of hBN can be obtained using mechanical exfoliation and has a Young's modulus of 0.86 – 1.16 TPa, with a breaking strength of 70 GPa [14].

Similarly, the in-plane (a-direction) coefficient of thermal expansion (CTE) for hBN is negative at -2.9 x 10^{-6} K^{-1}, while it is positive and ten times higher at 4.05 x 10^{-5} K^{-1} along the out-of-plane or c-direction [46, 53, 54]. The same is true for graphene [55-58]. In a recent study, the anisotropic nature of thermal conductivity (in-plane - κ_α and through-plane κ_z) in single crystal hBN was determined experimentally and reported for the first time. In-plane thermal conductivity was measured to be 420 $Wm^{-1}K^{-1}$ and is ten times higher than through plane thermal conductivity value of 4.8 $Wm^{-1}K^{-1}$ [59]. Furthermore, κ_α for hBN is found to be layer dependent, with values ranging from 750 to 290 $Wm^{-1}K^{-1}$ [60, 61]

Despite these similarities, it is the difference in their electrical properties that distinguishes the two materials and gives them their own unique identity. Graphene is a zero-bandgap semiconductor (or semi-metal) with excellent in-plane electrical conductivity [62-64]. In 2004, Geim and co-workers at the University of Manchester (U.K.) isolated mono- to few-layer graphene (FLG) by mechanical exfoliation from highly oriented pyrolytic graphite and transferred them on to oxide coated silicon (SiO_2/Si) substrates. They demonstrated strong ambipolar field effect behavior in FLG [8]. It was this study which brought graphene to the forefront of worldwide attention and fueled an explosion of interest in this material[1]. On the other hand, hBN is an insulator, with a band gap of ~ 6 eV [44, 49], which puts graphene and hBN at opposite ends of electrical conductivity spectrum, one as a 2D conductor and the other as insulator, respectively. To understand this, we once again refer to the crystal structure of graphene and hBN.

As illustrated in Figure 2-3(a), in graphene, sp^2 hybridized carbon atoms are arranged in a honeycomb lattice. Each carbon atom with four valence electrons, forms three σ bonds with its neighboring carbon atoms, while the π-bonds are oriented out-of-plane. Since all carbon atoms are identical, the σ-bond is truly covalent (equal sharing of electrons), while the π-bond electrons are delocalized (not adhere to any single carbon atom) and free to move, providing graphene with extraordinary electrical conduction (one free electron per carbon atom). However, in case of hBN, the electro-

---

[1] Andre Geim and Konstatin Novoselov were jointly awarded the 2010 Nobel Prize in Physics for their research work "*for groundbreaking experiments regarding the two-dimensional material graphene*"

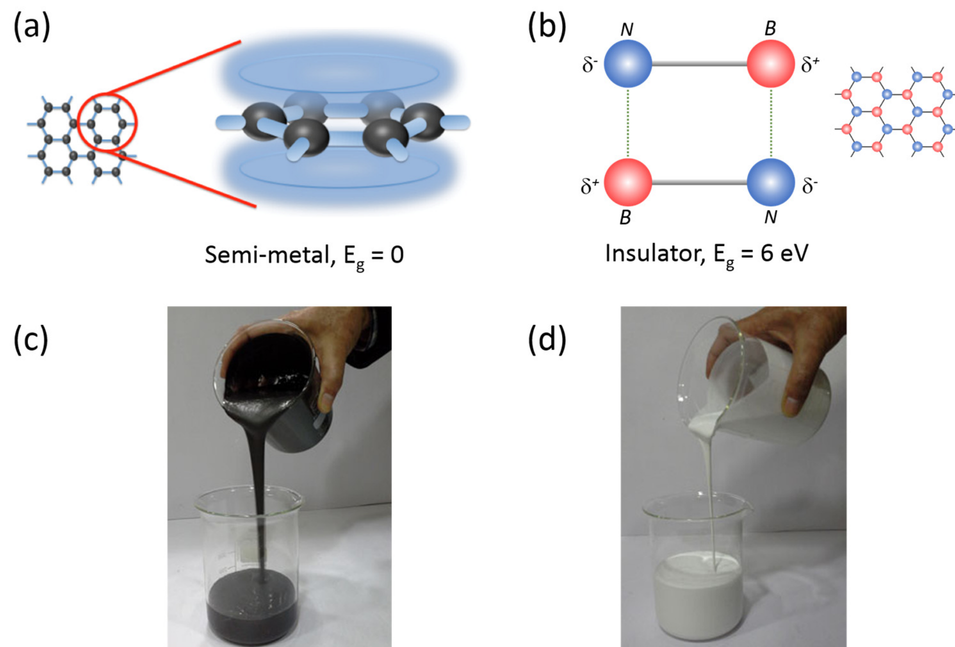

Figure 2-3 (a) Honeycomb lattice of graphene and delocalized electron cloud giving it excellent electrical conduction properties, (b) partially ionic honeycomb lattice of hBN which makes it an insulator, (c) graphitic carbon suspension appears black due to a zero bandgap and (d) BN suspension appears white due to its large bandgap [65].

negativity difference between boron and nitrogen atoms imparts the covalent bonds (between the B and N) with a slight ionic character. The ionic honeycomb lattice, with partial charges on boron (δ^+) and nitrogen (δ^-), restricts free movement of the π-electrons, which manifests itself into an electronic bandgap.

Application of hBN as a gate dielectric is discussed in section 2.3.2. The apparent bandgap difference between the two materials is also responsible for their different light absorption properties. Graphite, with a zero-bandgap appears black, while hBN with a bandgap of 6 eV, is unable to absorb any visible radiation and appears transparent or white (in case of powders). hBN is therefore often referred to a 'white graphite' (Figure 2-3(d)).

2.3 Applications

2.3.1 Lubricant and high temperature composites

Nano-crystalline, powder form of hBN are commercially available and can be produced in industrial scale quantities [66, 67]. hBN powders have been used in a wide

range of technological applications. van der Waals bonding between the layers results in a slippery nature and both graphite and hBN (powder) have been used as solid and wet lubricants [68, 69]. However hBN's ability to withstand high temperatures and oxidizing atmosphere makes it better suited for lubrication, especially in harsh environments and outperforms graphite [70, 71]. These properties also make hBN a valuable refractory material. Crucibles, rods, bars, sheets etc., made from hBN can withstand temperatures up to 1600 ºC (in inert atmosphere) [72-74]. Due to its chemical inertness and colourless or white appearance, hBN powders are widely used in the cosmetic industry and skin care products [75-77]. For many of these applications, hBN powders maybe used as it is or as a component of resins, suspensions etc. Amongst insulating materials, hBN has the highest thermal conductivity and is often blended with polymers and elastomers to improve their mechanical strength and thermal conductivity [78, 79]. Figure 2-4(a-c), shows examples of commercially available hBN and products. SEM image of hBN particles (from Graphene Supermarket) shown in Figure 2-4(d) reveals the shape and size of individual crystallites, which appear to be flakes (1-5 atomic layer thick) with lateral dimensions of few hundred nanometres.

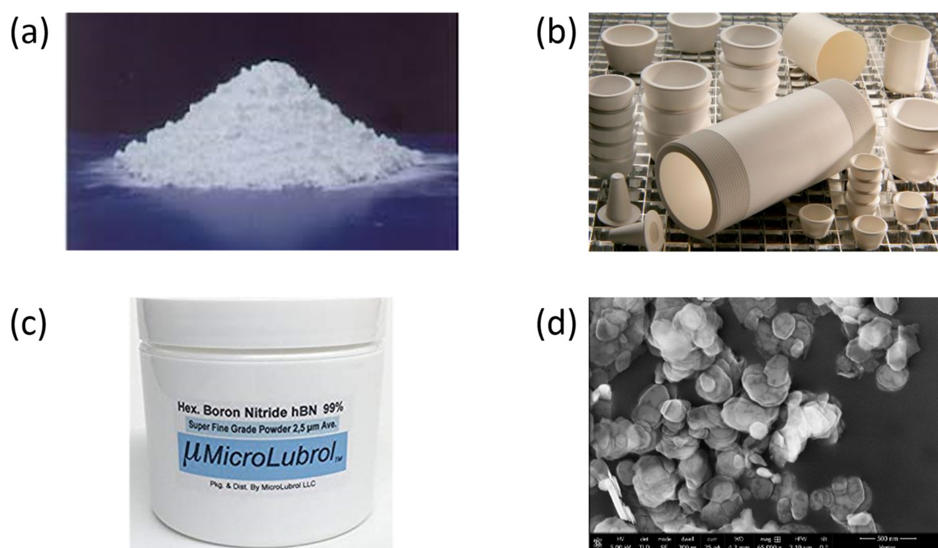

Figure 2-4 (a) Photograph of commercially available BN powders, (b) crucibles, tubes made from BN can withstand very high temperatures, (c) commercially available suspension of BN powder and (d) SEM image of boron nitride nanosheets [76].

2.3.2 Electronics

For over a decade, graphene has been heralded as a wondrous material. Electronic properties of FLG were showcased by Geim and co-workers in 2004 and room temperature charge carrier motilities of 10,000 – 15,000 $cm^2V^{-1}s^{-1}$ were reported for FLG exfoliated on to SiO_2/Si substrates[2] [8]. However these values were far below the theoretically predicted value of 250,000 $cm^2V^{-1}s^{-1}$ [62, 64]. Reduced carrier mobility observed in FLG was due to scattering of charge carriers by surface charge states (e.g. dangling bonds present at surface of 3D materials), defects and impurities present on the underlying SiO_2 substrate. By removing the substrate, charge carrier mobilities in suspended graphene were measured to be over 200, 000 $cm^2V^{-1}s^{-1}$ [18, 80, 81].

As a 2D material, the surface of hBN is also devoid of charge states and dangling bonds, thus making insulating, single crystal hBN with large bandgap as an excellent substrate for graphene based field effect devices. Hence for graphene layers exfoliated on hBN, shown in Figure 2-5(a), charge carrier mobility ~ 100,000 $cm^2V^{-1}s^{-1}$ could be achieved [17]. Dielectric properties, chemical inertness and high thermal conductivity of hBN has established it as a substrate and gate dielectric in electronic devices based on 2D materials (Figure 2-5(b)) [16, 25, 82-86].

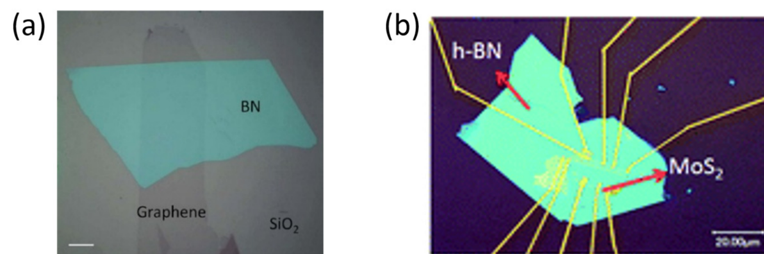

Figure 2-5 (a) Graphene layer exfoliated on hBN and (b) 2D device made from MoS_2 with hBN underneath it as a substrate [87, 88].

In the absence of wafer-scale substrates, for such applications, hBN flakes are typically obtained from bulk crystals utilizing techniques already developed for

---

[2] For comparison, room temperature electron and hole mobility for silicon is nearly 1,400 and 450 $cm^2V^{-1}s^{-1}$ respectively. Similarly, for gallium arsenide, a III-V compound semiconductor material, popularly used for making HEMTs has an electron mobility of 8500 $cm^2V^{-1}s^{-1}$.

graphene exfoliation. However, lateral dimensions of hBN (and graphene) flakes obtained using such methods are typically restricted to tens of microns, which is a limitation in the scaling-up of such devices. Hence, there is a great push towards realizing large-area growth of high quality 2D materials utilizing CVD methods, which will be discussed in the following sections.

2.3.3 Heteroepitaxy

hBN has been utilized as an effective release layer for conventional III-Nitride LED heterostructures grown on sapphire substrates [89-92]. Rather than growing III-Nitrides directly on sapphire substrate, a thin layer of hBN is sandwiched between the two, as shown schematically in Figure 2-6(a). The unique 2D crystal structure of hBN,

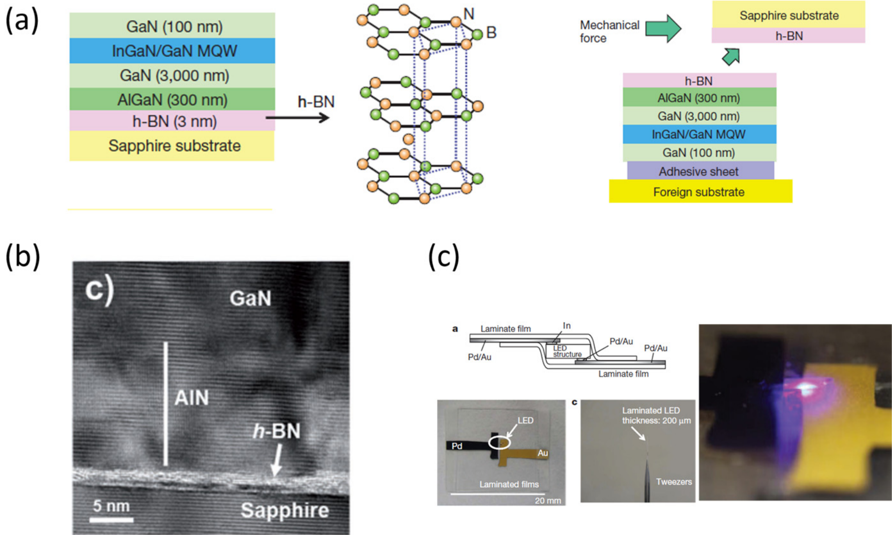

Figure 2-6 (a) Schematic illustration of hBN as a sacrificial release layer for mechanical exfoliation of a MQW LED device from the sapphire substrate, (b) cross-section HR-TEM of hBN layer showing a thin hBN layer sandwiched between sapphire and AlN and (c) a MQW LED detached from sapphire substrate and laminated between polymer sheets to form a flexible device [89].

wherein individual layers, held together by weak van der Waals forces (as opposed to strong covalent bonds) form a shear plane and facilitate detachment of LEDs structures from substrates post epitaxy. Figure 2-6(b) show a cross-sectional TEM image of the substrate-hBN-AlN interface. A 3 nm–thick layer of hBN can be clearly identified. This furthermore opens up new avenues such as, forming electrical contacts without any need for conventional etching and transferring devices grown on sapphire onto

flexible substrates (Figure 2-6(c)) or even metal plates to improve heat dissipation [93-99]. Thin hBN layers as intermediates may be used to facilitate epitaxial growth of conventional III-Vs on cheaper silicon substrates [100, 101]. Furthermore, nitride films grown on silicon substrates suffer from severe cracking due to thermal tensile stress during cool down from growth temperatures. hBN buffer layers can be applied to alleviate tensile stress due CTE mismatch between film and substrate and, overcome film cracking. In Chapter 7, we report on the growth of high quality AlN layers on hBN grown by MOVPE as templates for deep UV LEDs.

2.3.4 Surface passivation

The honeycomb lattice of graphene and hBN is impermeable to all atoms and molecules, including hydrogen, under ambient conditions [102-105]. Carefully perforated, atomically thin layers of these materials are being developed as membranes for selective transport of molecules, which can be applied in gas purification, desalination etc. [106-108]. However, unlike graphene, which oxidizes in air at temperatures above 250°C, hBN is chemically inert and thermally stable at high temperatures even in oxidative environments, which makes it a valuable material for surface passivation. hBN coatings have been shown to protect metals (copper, steel, nickel) not only against oxidation at high temperatures, but also against chemical corrosion and biofouling [33, 34, 70, 71, 109-112]. In addition to passivating planar thin metal surfaces, the flexibility of atomically thin films of hBN allows it to conform to 3D features like metal nanoparticles etc., extending its utility to the field of plasmonics [35, 113-116]. One such example is surface enhanced Raman spectroscopy (SERS). In the present study, atomically thin layers of hBN grown using MOVPE were utilized for protecting silver nanoparticles against oxidation and preserve its SERS activity [117]. These results are detailed in Chapter 6.

2.3.5 Optical applications

hBN is an unusual member of the III-Nitride semiconductor family. Its 2D structure sets it apart from other nitride materials namely AlN, GaN and InN, all of which have a wurtzite crystal structure. More importantly, these materials have a direct bandgap and have revolutionized the field of solid-state lighting, with the development

of GaN based blue LEDs which facilitated energy efficient white light LED sources[3]. In the past, experimental attempts to determine the band structure of hBN using spectroscopic methods have yielded varying results, with bandgap values ranging between 4 – 7 eV that has been attributed to differences in material purity [118-123]. Only in 2004, Watanabe et al. managed to synthesize high-purity hBN crystals and observed strong emission and even lasing at room temperature at 215 nm, as shown in Figure 2-7(a) [37]. This seminal report, suggested a direct bandgap nature and put forward hBN as a new material suitable for developing deep UV devices [124, 125]. Contrary to this, first-principle calculations have always predicted hBN to have an indirect bandgap [48, 49, 126-128]. Only recently, it has been experimentally

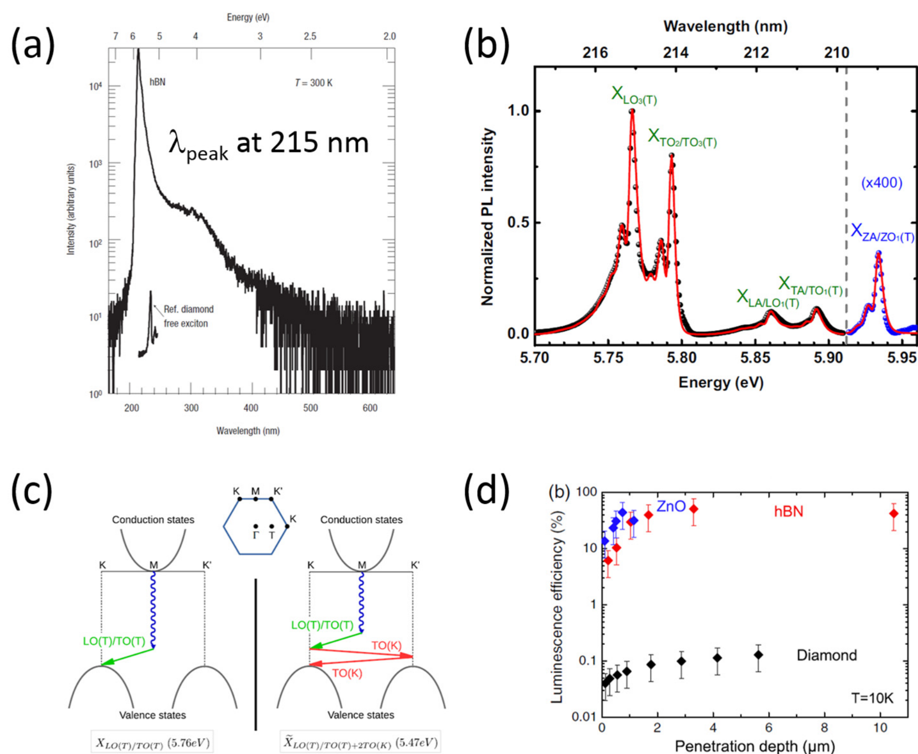

Figure 2-7 (a) Room temperature CL spectrum of single crystal hBN reported in [37], (b) PL spectra of single crystal hBN taken at 10 K [129], (c) schematic representation of phonon assisted electronic transition from conduction to valence band as reported in [130] and (d) a comparison of luminescence efficiency of hBN, ZnO and diamond as reported in [131].

[3] In 2014, three prominent Japanese scientists, Isamu Akasaki, Hiroshi Amano and Shuji Nakamura were jointly awarded Nobel Prize in Physics *"for the invention of efficient blue light-emitting diodes which has enabled bright and energy-saving white light sources."*

established that hBN has an indirect bandgap and the strong deep UV emission at 5.75 eV (or 215 nm) from hBN are indeed phonon (LO/TO) assisted transitions [132]. It is thus a remarkable property and at the same time fascinating that while being indirect bandgap material, hBN can give rise to strong NBE luminescence, which in some cases is comparable or even stronger than that of direct bandgap materials [129-131, 133, 134]. The phonon assisted transitions from hBN are shown in Figure 2-7(b-c) along with a comparison of luminescence efficiency (measured using cathodoluminescence) between hBN, ZnO (direct bandgap) and diamond as shown in Figure 2-7(d).

In addition to this, sub-bandgap emission from isolated point defects in hBN, shown in Figure 2-8, has been reported as single photon sources. This has generated new interest in the use of hBN for quantum computing [36, 135-139]. Unlike other 2D materials like transition metal dichalcogenides, which show quantum emission at cryogenic temperatures [140-144], hBN single photon emitters have been shown to be not only bright and stable at room temperatures, but can survive harsh environmental conditions, which is extremely useful for practical applications [136, 145]. Single photon emitters were also observed in hBN layers grown using MOVPE in this study and are discussed along with other optical spectroscopic measurements in Chapter 5.

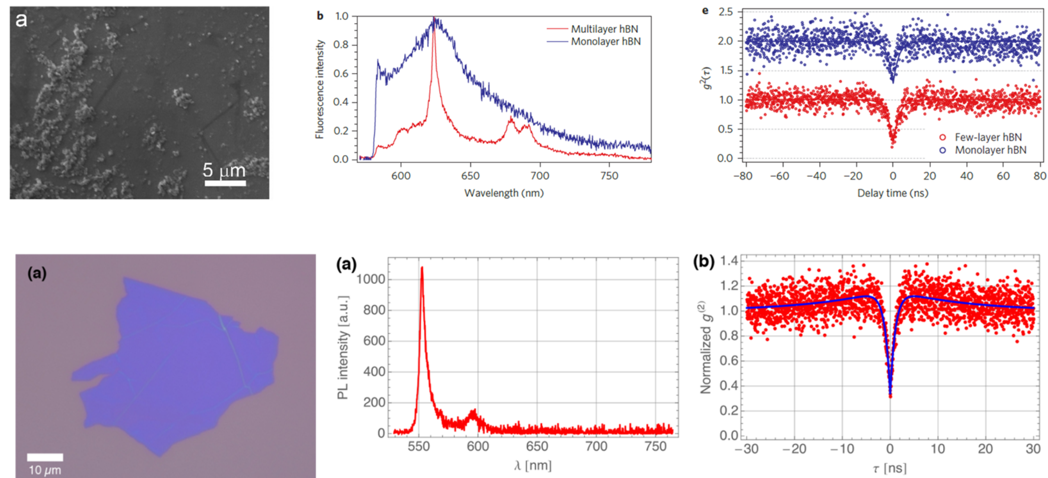

Figure 2-8 Top-row (left to right): SEM image of BNNS, sub-bandgap PL spectra from SPEs in BNNS hBN, anti-bunching curve to validate that the emission from emitter is quantized [36]. Bottom-row (left to right): optical microscope image of a mechanically exfoliated hBN flake from bulk crystal, PL spectra from an isolated defect in the hBN flake and its corresponding anti-bunching measurement to prove it as SPE [138].

2.4 Synthesis

Unlike graphite, which was first discovered off the coast of England in the 16th century[4], BN is not a naturally occurring substance but a synthetic compound. Over the years, several methods have been reported for synthesizing BN. Large-scale chemical synthesis of BN (powders) has been discussed briefly. However, for semiconductor, optoelectronic and van der Waals epitaxial growth applications described above, high purity and single crystal hBN is required.

Figure 2-9 summarizes three different types of BN which are commercially available. These are: (1) BN nano-sheets (BNNS) available as a dry powder or a suspension shown in Figure 2-9(a) (SEM image of BNNS is also shown in Figure 2-4(d)), (2) mm-sized single crystal hBN (Figure 2-9(b)) from which, single to few layer hBN with lateral sizes of tens of microns can be mechanically exfoliated, as shown in Figure 2-9(c) and (3) large-area hBN deposited as thin films (on copper foil

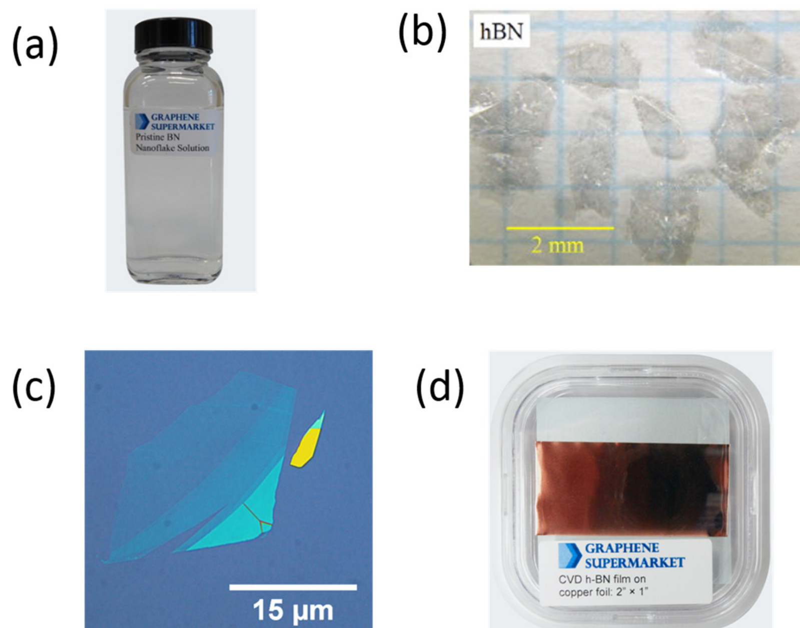

Figure 2-9 (a) Commercially available suspension of BNNS, (b) photograph of single crystal bulk hBN synthesized using high temperature melt technique, (c) mechanically exfoliated flakes of hBN and (d) commercially available CVD grown few-layer hBN on copper foils.

[4] Cumbria in North England

as shown in Figure 2-9(d)) using CVD methods. Each of the hBN type is individually suited for different applications. In the following section we review the different methods used for synthesizing single crystal BN, with emphasis on CVD and MOVPE growth methods.

2.4.1 Bulk crystal growth from melt

In the semiconductor industry, the growth of large, single crystal wafers of silicon and other compound semiconductors materials like GaAs, InP using the Czochralski process is well known [146, 147]. In this method, the material of interest is melted under a controlled atmosphere (in a non-reacting container) and a seed crystal (of the same material) is immersed in the melt. The seed crystal is then slowly pulled from the melt and during this step, by controlling the melt temperature, the molten material is made to crystallize on the seed crystal to form a large single-crystal ingot of the material. Wafers of desired size and shape can be diced from the ingot and subsequently polished.

Due to extremely high melting temperature of boron nitride (> 2950 ºC), the crystal growth from a melt using the Czochralski process is challenging. Alternatively, solvent growth techniques are employed for obtaining single crystal hBN. In this method, commercially available hBN powders (used as source material) are dissolved in a metal solvent (also known as flux) to form a saturated solution at high temperature (1500 – 1750 ºC) [37, 148]. By slowly cooling the saturated solution, hBN crystal can be precipitated. The solidified flux/solvent is subsequently dissolved using suitable chemicals to obtain hBN crystals. Using this method, high purity single crystal hBN has been obtained, however the lateral size of the crystals is typically tens of μm wide (tens-hundred μm thick), as shown in Figure 2-9(c). A few different metal solvents, such as Ba-BN, Mg-BN, Ni-Mo, Ni-Cr and Fe-Cr have been found suitable for obtaining single crystal hBN using solvent growth technique [148-155]. Watanabe et al., have discussed the attributes of metal flux/solvents desired for solvent based process specifically in the context of hBN growth [156].

Bulk crystal growth studies reported so far have also played an important role in highlighting the challenging nature of hBN synthesis in terms of material purity. As mentioned above, strong UV emission and lasing at 215 nm was demonstrated from bulk hBN crystals [37]. However, NBE luminescence is highly sensitive to impurity

atoms, specifically carbon and oxygen, which are easily incorporated in hBN during synthesis and give rise to sub-bandgap luminescence at 300-350 nm. Taniguchi et al., demonstrated that the level of impurity atoms in hBN has to be below $10^{18}/cm^3$ (or below 1 ppm, estimated using SIMS) to observe strong NBE [149]. Otherwise sub-bandgap luminescence dominates over NBE, as shown in Figure 2-10 [149].

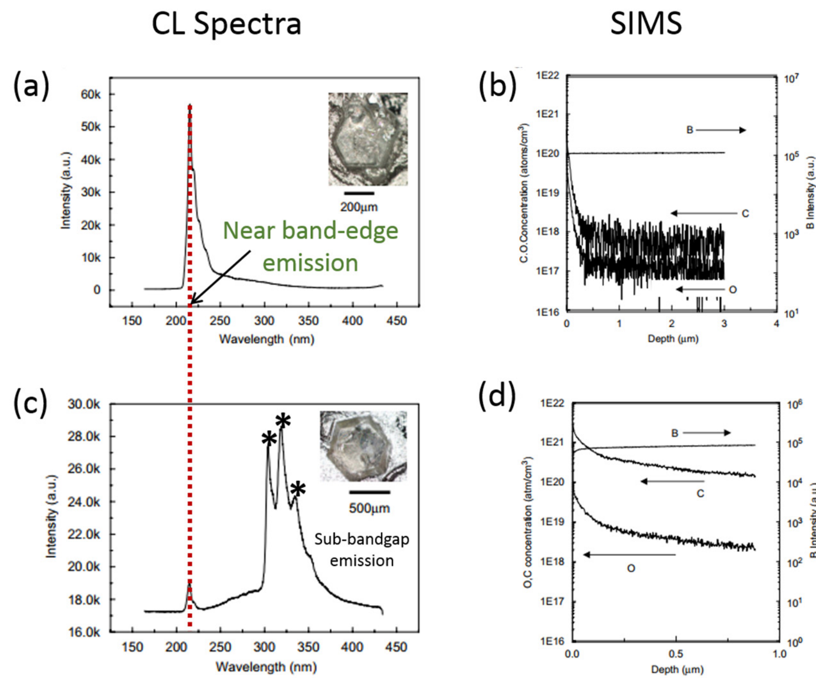

Figure 2-10 (a) PL spectra from high purity bulk hBN crystals, (b) SIMS data of pure hBN crystals showing oxygen and carbon impurity levels below 10^{18} atoms/cm^3, (c) PL spectra from an impure bulk hBN crystal and (d) corresponding SIMS data with oxygen and carbon levels above 10^{18} and 10^{19} atoms/cm^3 respectively [149].

In a related study, Schue et al., compare the CL spectra collected from different commercially available hBN samples (Figure 2-11), and show that NBE (and impurity luminescence) can vary drastically from sample to sample, which can be attributed to differences in material purity [157]. In spite of these challenges, single crystal hBN obtained using the solvent growth techniques is the highest quality (and purity) hBN available today. From these µm to mm sized crystals, mono to few-layers of hBN are mechanically exfoliated routinely, which are free of defects and grain boundaries, atomically smooth and well-suited for many applications described above. However,

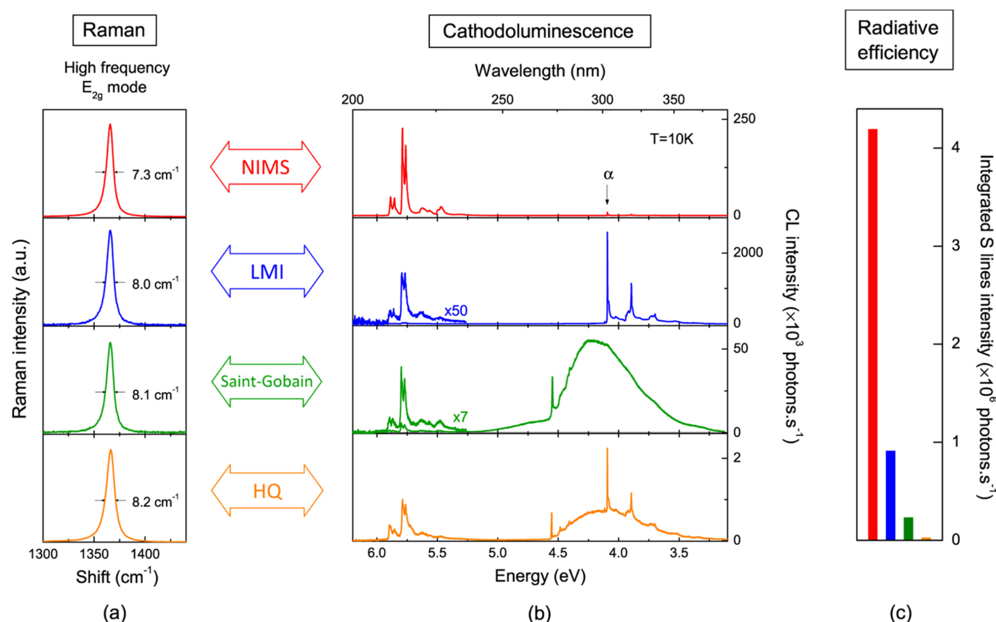

Figure 2-11 CL spectra of different commercially available bulk hBN crystals [157].

the small lateral size of the bulk crystals (typically μm to mm) limits large area application and scalability. So far, scaling-up of solvent based methods to obtain wafer-scale (few inches) single crystal hBN has not been demonstrated. Under these circumstances, epitaxial growth methods such as CVD and MOVPE are being explored for deposition of wafer-scale, thin films of hBN on a range of substrates, which is also at heart of research study undertaken in this thesis.

2.4.2 Chemical vapour deposition

Since graphene's debut as a semiconductor in 2004, CVD based growth processes have been actively pursued for large-area preparation of mono- to few-layer graphene for various applications [158-162]. In more recent years, CVD techniques have been extended for the deposition of 2D materials in general [163-167]. Numerous studies on CVD growth of hBN, over large areas, typically on transition and noble metals such as Ni [168-171], Cu [172-174], Pt [175, 176], Pd [177, 178], Ag [179], Au [180], Fe[181-183], Rh [184], Ru [175, 185], Rh [184] as substrates have also been reported [186]. Of these, growth on Ni(111) and Cu(111) deserves a special mention, as both are lattice matched to hBN and are relatively low-cost materials. In addition to this, a wide range of different growth precursors have also been used. For ease of use, single molecule precursors containing both B and N, such as ammonia borane (BNH_6),

borazine ($B_3H_6N_3$) are preferred over combination of precursors such as diborane (B_2H_6) and ammonia (NH_3).

CVD process typically involves substrates (commercially available thin metal foils) which are heated to desired temperatures (900 – 1100 °C) in a tube furnace. Vapours of the precursors are passed over heated substrates in a controlled atmosphere for a desired amount of time, which results in hBN deposition. hBN growth proceeds through an initial nucleation. The nuclei grow laterally and coalesce to form a smooth continuous film. Kim et al. were the first ones to show formation of triangular shaped hBN grains (on Cu) with N-terminated edges [173]. Grain coalescence often results in the formation of grain boundaries and defects, which are detrimental for device applications. Currently, a large body of work is dedicated towards reducing nucleation density whilst increasing lateral growth of hBN grains [181, 187-189]. hBN films with single crystal domains as large as few hundred of microns have been achieved [182, 189-191].

Furthermore, transition and noble metals, like Ni, Pd, etc. have high binding energy (with hBN) and result in strong chemisorption of hBN [192]. Lattice matching and high binding energy give rise to a catalytic effect, which plays a critical role in deposition of high quality hBN at relatively low temperatures (compared to MOVPE, discussed below). The catalytic activity of metal substrates limits hBN growth to a monolayer and once the metal surface is covered with hBN, further growth is terminated. hBN growth is thus self-limiting, especially under low pressure growth condition [193-195].

While monolayer hBN is useful for some applications like growth template and passivation membranes, it is not useful as a gate dielectric, since tunnelling currents through it are high. Thus, growth of multi-layer hBN is being actively pursued which is more suitable for device applications. By increasing process pressure, multi-layer hBN on Cu and Ni can be deposited (atmospheric pressure CVD). However, overall quality of the layers is relatively poor [194]. Furthermore, while Ni and Cu foils predominantly result in the deposition of monolayer hBN, Kim et al., have demonstrated the use of Fe foils for depositing multi-layer hBN films [183]. This transition from self-limiting growth to deposition of thick hBN layers is attributed to a higher solubility of B and N in Fe. Similarly, Uchida et al. have used Ni-Fe alloys to further improve the crystallinity of hBN films grown on pure Fe foils [196].

Overall, CVD deposition of hBN is a catalytic, thermal growth process. It has emerged as a promising and leading process for the deposition of large area, high quality mono- to few-layer hBN films. Whilst, catalytic activity from the metal substrates can facilitate lowering of the deposition temperatures, hBN films grown on metal substrates cannot be applied usefully and need to be transferred to dielectric substrates. Chemical and other transfer processes invariably induce defects and contaminants. Direct growth of hBN on insulating substrates such as sapphire is desirable and is explored in the following section.

2.4.3 Metal organic vapor phase epitaxy

MOVPE is a matured technology and the preferred process for wafer-scale epitaxial growth of compound semiconductor materials like GaAs, InP and their alloys, which are used in the fabrication of LEDs, laser diodes, photodetectors etc. The deposition is generally carried out on lattice matched bulk substrates. However, in the absence of bulk substrates for certain materials like GaN, other substrates such as silicon, silicon carbide and sapphire have been used [197-199]. The research work presented in this thesis investigates the deposition of hBN thin films using MOVPE on sapphire substrates. A general discussion on epitaxial growth process and its fundamentals is presented in Chapter 3, followed by a detailed experimental investigation on hBN growth in Chapter 4. Since hBN is a relatively new semiconductor material with many interesting properties and applications, over the last few years, there has been a growing interest to understand its deposition using MOVPE. Due to the unavailability of bulk substrates, hBN growth is largely undertaken on lattice mismatched substrates like sapphire and in some instances on silicon carbide and silicon [200-204]. Sapphire is used more commonly due to its low cost and ability to withstand high growth temperatures.

For hBN growth, the metal-organic (MO) boron precursor of choice is triethylboron (TEB, $(C_2H_5)_3B$) which is pyrophoric material and requires safe handling. More importantly, TEB is a carbon rich precursor, which leads to unintentional carbon incorporation in the hBN film during growth and will be discussed in later chapters. It is worthwhile to mention that although trimethylboron (TMB, $(CH_3)_3B$), another MO, has lower amount of carbon per boron atom, it is highly volatile compound (due to its high vapour pressure), and not readily available as a boron precursor. Boron trichloride (BCl_3), another potential boron precursor, is not

favoured for use in MOVPE reactors due to its highly toxic chlorine-based chemistry, which can etch several reactor components. Due to these constraints, only a very few and limited number of reports are available in literature on the use of TMB and BCl_3 as boron precursor for hBN growth [205]. Similarly, ammonia is the favoured nitrogen precursor, as it has a high degree of thermal dissociation at growth temperatures compared to N_2. Hydrogen is commonly used as a carrier gas.

One of the first studies on hBN growth (on sapphire, using TEB and ammonia) was reported by Nakamura, wherein growth temperature was varied from 900 - 1200 °C. Here, a change in its c-lattice parameter (measured using XRD) with growth temperature was observed [206]. By extrapolating the experimental data, a process temperature as high as 1500 °C was predicted for hBN growth on sapphire. Such a high growth temperature cannot be achieved in many commercially available MOVPE systems and remains one of the major challenges for obtaining high quality hBN to date. The majority of studies reported on hBN growth are at lower temperatures [200, 207-209]. Based on the appearance of the hBN deposited under different TEB and NH_3 flow rates, Nakamura's study also alluded to the requirement of high V/III ratio for hBN growth. In 2006, Kobayashi et al. reported on the deposition of hBN on silicon carbide [210]. Their study highlighted another important critical issue, which is the strong parasitic reaction between TEB and NH_3, resulting in very low hBN growth rates [200, 201]. To overcome parasitic reactions between precursors, the authors adopted flow modulation epitaxy (FME), wherein, the precursors are introduced in the reactor as short alternating pulses as opposed to introducing them simultaneously. Historically, FME has been utilized for the growth of conventional III-V materials (GaAs, GaN, AlN etc.) using MOVPE [211-215]. FME is particularly effective in the epitaxial growth of compounds, wherein adatom mobility is low (e.g. aluminium) and either due to reactor's limitation or thermal stability of III-V compound, growth temperatures cannot be increased. By pulsing the flow of growth precursors, adatoms with low surface mobility get additional time to migrate and get incorporated at the correct lattice sites. This helps in reducing dislocations and improves the crystallinity of the deposited material. This technique is also known as migration enhanced MOVPE (ME-MOVPE) [216-218]. For hBN growth, FME proved to be effective in reducing parasitic reactions and has been widely adopted for hBN growth using MOVPE since then [208, 219].

In 2011, Dahal et al. reported epitaxial growth of hBN on sapphire using a two-step method, which involves a thin, low-temperature (LT) nucleation layer deposited at 800 ºC and a thicker layer (using FME) at 1350 ºC [200]. Using this method, a 1 μm thick hBN layer was grown on sapphire. Characteristics of the LT-hBN layer and its utility have not been reported. More importantly, they also demonstrated p-type doping of hBN using Mg as dopant and measured its electrical properties using Hall effect [200]. Based on their study, the acceptor activation energy (E_A) for p-hBN was measured to be 31 meV [200]. This is of significance, because within the III-Nitride family, with an increase in bandgap energy, the acceptor activation energy increases from 170 meV for GaN to 500 meV for AlN. Due to high acceptor activation energy, p-AlN layers have very low hole concentration and are insulating, which is a major bottleneck for developing deep UV LEDs with high external quantum efficiency [199, 220]. However, hBN, with a bandgap as large as AlN, has the lowest measured E_A within the III-Nitride family and therefore, p-hBN layers with high hole concentration can be considered a viable replacement for p-AlN for device applications. In another related study, Majety et al. grew p-hBN on top of n-AlGaN layer and demonstrated diode like behaviour of the p-n junction formed between the two [221].

While several studies in the past have shown that higher temperatures are generally preferred for hBN growth [206, 222, 223], hBN growth at lower temperatures have also been explored. Paduano et al. and Snure et al. studied growth of hBN at lower temperatures between 1000 – 1100 ºC under continuous flow conditions and report that hBN deposition on sapphire can be self-limiting [224]. In their study, thickness of hBN layer (estimated using Raman spectroscopy and x-ray reflectometry) deposited at relatively lower temperature and high V/III ratio remains unchanged at 3-5 layers with an increase in growth time from 5 – 60 mins. However, growth at low V/III ratios (< 900, by increasing TEB flux) results in the deposition of amorphous BN (aBN), which is not self-limiting. In a similar study, Kim et al. used FME for hBN growth at low temperatures [225]. Although it is not known whether hBN growth was self-limiting under these circumstances, overall growth rates were very low. Such studies suggest that hBN nucleation takes place readily on the sapphire substrate, but once the sapphire surface is covered with few layers of hBN, nucleation and further growth, now on a 2D material, devoid of dangling bonds, is restricted.

To overcome the regime of self-limiting growth, growth temperature can be increased (to 1300 ºC) which provides extra thermal energy to help overcome energy barrier and facilitate nucleation and further growth [208, 209]. Even at such temperatures, hBN growth rate (controlled by TEB flux), has to be restricted to few tens of nm/hour. High growth rates often result in the deposition of disordered BN (tBN or aBN).

There are limited number of reports on hBN growth at temperatures in excess of 1300-1350 ºC, as such high temperatures cannot be achieved in commercially available MOVPE reactors and require customized modifications. For example, most MOVPE reactors are equipped with a graphite susceptor with a SiC protective coating, which can be etched at high temperatures in hydrogen-rich environments, typical of hBN growth conditions. Chubarov et al. and Rice et al. have used specialized tantalum carbide coated graphite susceptor to grow hBN at 1500 ºC [222, 223, 226]. A more serious concern arises due to the thermal stability of the sapphire substrate, which is known to get etched under hydrogen environments at high temperatures [227]. Degradation of the substrate surface, can results in a rough surface morphology and delamination of hBN layers, which may not be suitable for practical applications.

2.5 Summary

Based on the review of various studies on hBN growth using MOVPE reported over the last few years, challenges associated with hBN growth can be summarized as follows:

1. It appears that the boron adatom mobility on substrate surface is low which severely effects the crystallinity of grown hBN films. Low adatom mobility also results in the deposition of tBN or even aBN, especially when the overall growth rate is high, as adatoms do not get sufficient time to get incorporated at correct lattice site. To overcome this, the adatom mobility and quality of hBN films can be improved either by increasing growth temperature or decreasing the overall growth rate by controlling the TEB flux [208].

2. Parasitic reactions between TEB and NH_3 are severe resulting in very low growth rates. FME is an attractive approach towards reducing parasitic reactions and overcoming low adatom mobility.
3. Impurity incorporation in hBN can significantly quench NBE. Using carbon-rich, metal organic sources such as TEB indeed makes it more difficult to reduce unintentional carbon incorporation in hBN films. This is discussed in more detail in Chapter 4.

Chapter 3. Experimental Methods

3.1 Introduction

This chapter describes the operation and principles of key experimental techniques used in the growth and characterization hBN and AlN layers reported in this thesis. hBN and AlN layers were grown using MOVPE on sapphire and hBN-sapphire templates, respectively. A wide range of characterization techniques were employed to investigate different aspects of the grown material, such as surface morphology, crystallinity, elemental and material composition etc., to develop a holistic view of the quality of hBN and AlN layers.

This chapter is arranged as follows: first, the fundamental principles of MOVPE are presented. This is followed by a description and discussion of characterisation techniques, which are diffraction (XRD), atomic force microscopy (AFM), Raman spectroscopy, UV-visible absorption spectroscopy, X-ray photoelectron spectroscopy (XPS), photoluminescence (PL) spectroscopy, scanning electron microscopy (SEM) and transmission electron microscopy (TEM), used in this study.

3.2 CVD and MOVPE

CVD is a well-established technique employed for depositing thin films of different materials on to a desired substrate. This is achieved primarily through chemical reaction between precursor molecules in the vapour phase (containing atoms which constitute the material being deposited) over a heated substrate, to deposit the material layer by layer, atom by atom. CVD is used for depositing a wide variety of materials ranging from metals, polymers, amorphous oxides and even single crystal films of semiconductor materials.

Over the years, many variants of CVD have been developed as specialized techniques for depositing a particular sub-class of materials. MOVPE is one such variant of CVD, which utilizes metal organics (e.g. trimethylgallium or TMGa, trimethylaluminium or TMAl, triethylboron or TEB,) and hydrides (e.g. arsine, phosphine, ammonia) as precursors for depositing single crystal films (often of

compound semiconductor materials like gallium arsenide, indium phosphide, gallium nitride etc.) over a substrate that is also crystalline. The term 'epitaxy' refers to a specific case of thin film deposition, where the growing crystalline film has a well-defined crystallographic relationship with the underlying substrate. Detailed discussion on various aspects of the MOVPE growth process can be found in [228]. Today, MOVPE stands as a matured technology and has become a major production process used in the manufacture of commercial electronic (e.g. high-electron mobility transistors – HEMTs, field effect transistors – FETs) and photonic devices (e.g. light emitting diodes, laser diodes, photodetectors and solar cells etc.). Figure 3-1(a-b) shows a picture of AIXTRON's 3x2 CCS type MOVPE system at ANU which was utilized for undertaking this research.

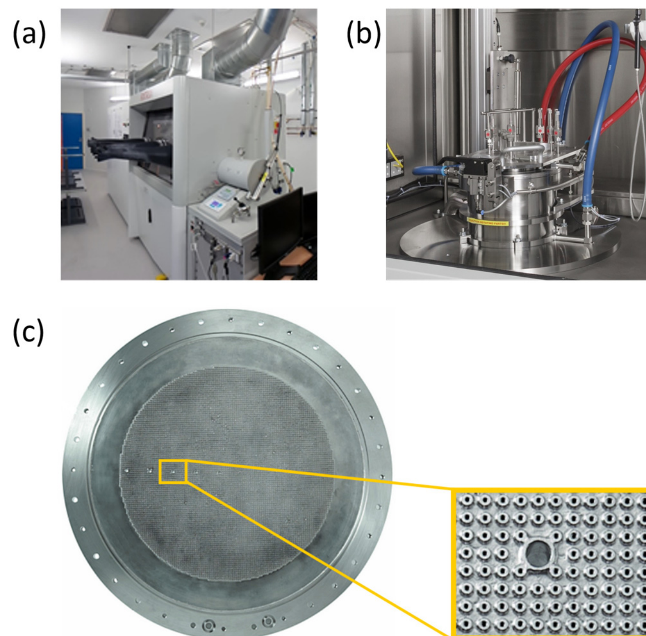

Figure 3-1 (a) AIXTRON 3x2" CCS-type MOVPE reactor at ANU, (b) reactor chamber inside the glove box and (c) close coupled showerhead (CCS) © AIXTRON.

MOVPE is a complex process involving a series of vapour-phase and surface reactions along with many different physio-chemical processes, which are illustrated in Figure 3-2 and briefly described as follows:

1. Transport of the reagents in to the reactor by means of a carrier gas.
2. Diffusion of the molecules towards the substrate.

3. Adsorption on the substrate surface.
4. Pyrolysis of precursors and migration of the atoms to lattice sites on the growing film.
5. Desorption of species (by-products chemical reaction and precursor pyrolysis).
6. Diffusion of gaseous by-products.
7. Exhaust of by-products out of the reactor.

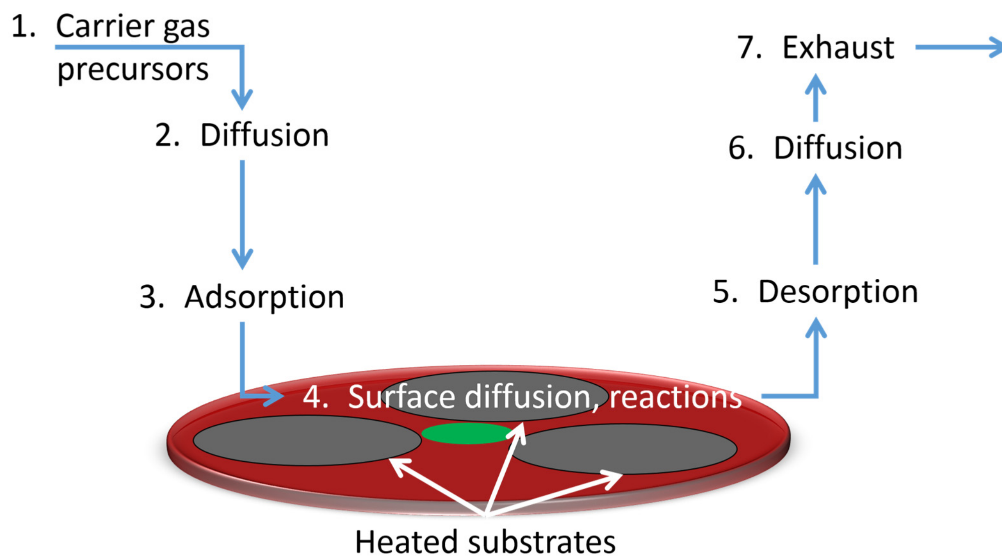

Figure 3-2 Schematic illustration of the physio/chemical processes during CVD/ MOVPE processes.

The process is carried out inside a specially designed reaction chamber, also known as the 'reactor'. Metal-organic (MO) precursors are either in liquid or solid form, however since most of them are pyrophoric, they are stored in special (steel) containers known as 'bubblers'. A carrier gas (hydrogen or nitrogen) is bubbled through the 'bubbler' and MO vapours are delivered to the reactor through an elaborate gas delivery system. Hydride precursors such as ammonia are already in gas phase and are delivered as such. The purity of all precursors and carrier gas used in the process is extremely high (> 99.99995%), which is essential for minimizing impurities incorporated in the growing film. It is well known that impurity atoms can severely hamper the performance of electronic and photonic devices [229]. In addition to this,

parasitic reactions between MO and hydride precursors can be severe. Therefore, to minimize it, the two are delivered separately and not mixed until inside the reactor.

Modern-day MOVPE reactors are equipped with 'closed couple showerhead' (CCS) type system to facilitate uniform delivery of precursors over the substrates. A photograph of vertical flow CCS is shown in Figure 3-1(c). The substrates are placed onto a graphite susceptor (often coated with silicon carbide) and heated to a desired temperature using either inductive heating or resistive heating. Substrate temperature, also known as growth temperature (T_G) is an important process parameter, which provides the much needed thermal energy to overcome the activation energy (E_A) of any chemical reaction and thus, needs to be carefully optimized. The two major considerations when selecting growth temperature are: (1) T_G should be high enough to ensure high degree of precursor pyrolysis to generate reaction species and adatoms, which form the growing film and, (2) T_G should be low enough to prevent decomposition of growing film and desorption of atoms from the solid surface. Hence, the growth rate of the film is a function of T_G and can be summarised into three regimes, as shown in Figure 3-3. At low temperatures, growth rate is determined by the kinetics of the chemical reactions. In this regime, due to low thermal energy, pyrolysis of the precursors is incomplete and growth rate tends to increase with temperature. In the second regime, T_G is high enough to dissociate precursors and growth rate is independent of temperature but limited by the mass flow rate of the precursors. Furthermore, by providing extra thermal energy (or increasing T_G further),

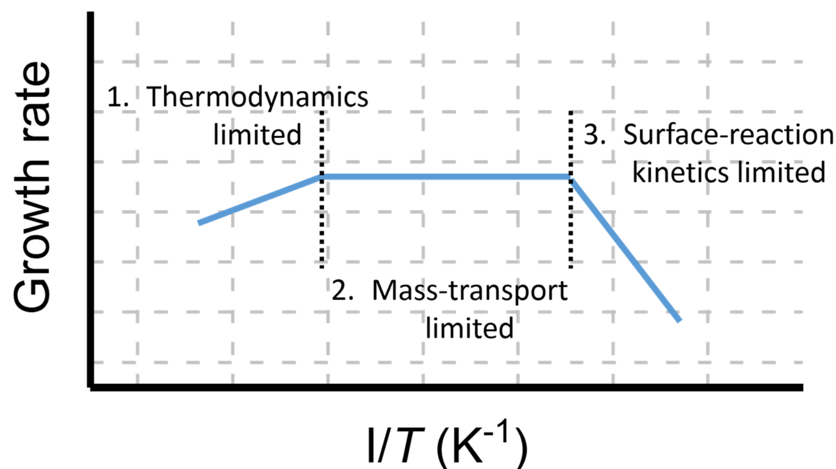

Figure 3-3 Graph showing dependence of growth rate on temperature.

surface mobility of adatoms can be enhanced. This allows them to migrate to its correct epitaxial location, which overall may help in improving the crystallinity of the film. Finally, in the third regime, which is thermodynamically limited, high temperatures lead to decomposition of the growing film through desorption of atoms from the growing surface of the film and essentially manifests as a growth rate, which decreases with increasing temperature. Other process parameters such as, reactor pressure, carrier gas flow rates etc. may also affect the properties of the film. During the MOVPE process, the effluents and reaction by products are constantly pumped out of the reactor.

In this thesis, hBN and AlN layers were deposited on single crystal sapphire substrates using an AIXTRON CCS-type MOVPE reactor. The reactor is equipped with Laytec's EpiTT module for real-time in-situ measurement of surface temperature during the growth process, as illustrated in Figure 3-4. The EpiTT module also provides a measure of film thickness based on interferometry using a 405 nm laser

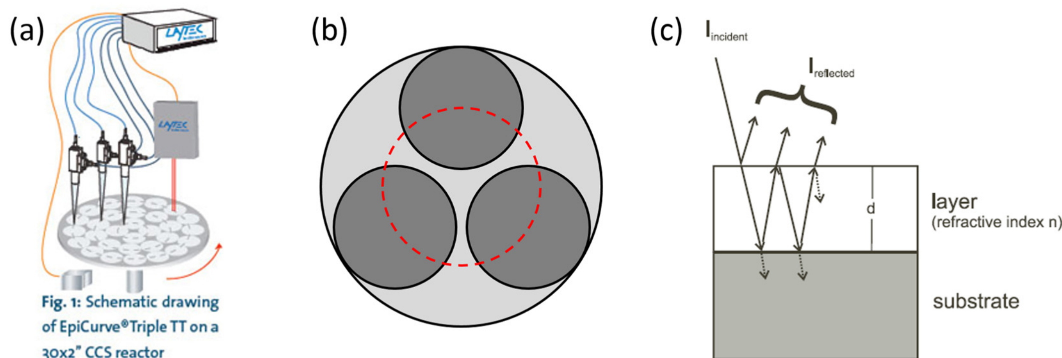

Figure 3-4 (a) Schematic illustration of Laytec's EpiTT module, (b) schematic illustration of wafers on the susceptor (as viewed from top). The dotted redline is representative of the arc traced by the EpiTT's laser spot where temperature and reflectance measurements are made in situ during growth and (c) schematic illustration showing incident and reflected beams for measuring films thickness via interferometry technique.

beam. Interference between reflected laser beam from the surface of growing film and film-substrate interface results in modulation of the light intensity, which is measured by a detector. The period of intensity oscillation provides a measure of film thickness as per equation 3.1

$$one\ complete\ oscillation = \frac{\lambda}{2\eta} \qquad (3.1)$$

where, λ is the wavelength of laser (405 nm) and η is the refractive index of the films (@ λ).

3.3 X-Ray Diffraction

In the field of material science, knowledge of atomic arrangement within a solid is critical for understanding many of the material properties (e.g. thermal and electrical conductivity, optical transparency, magnetism etc.) and the associated anisotropy (directional dependence of material properties along different lattice directions). XRD is one of the primary methods used for finding out how atoms are arranged in a solid material and determining its crystal structure [230, 231]. It is based on the principle that X-ray wavelengths are of the same scale as the spacing between atoms (~ 1 Å) and hence, atoms within a solid can scatter X-rays. Periodic arrangement of atoms within a crystal thus give rise to constructive interference of scattered X-rays (coherent scattering), resulting in a diffraction pattern, which was first demonstrated in 1912 by Max von Laue (Nobel Prize 1914).

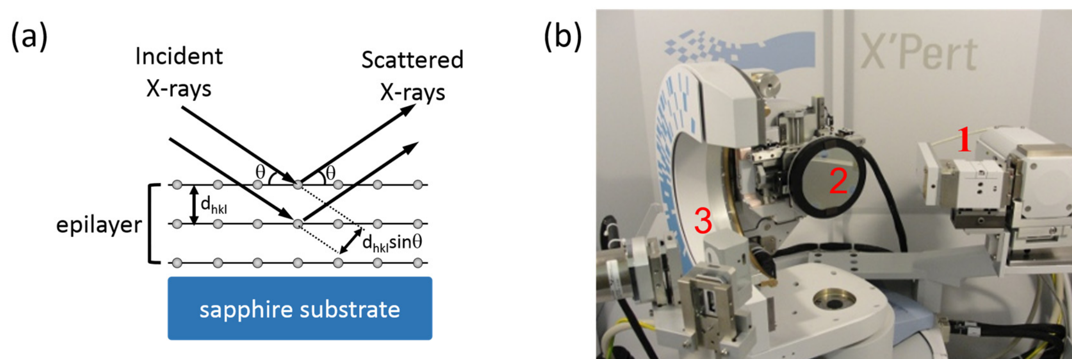

Figure 3-5 (a) Schematic illustration of Bragg's law and (b) photograph of the PANalytical high resolution X-ray diffractometer. Labels (1), (2) and (3) represent the three essential components of the instrument namely, X-ray source, goniometer and detector, respectively.

An X-ray diffraction pattern thus serves as a fingerprint for a given crystalline solid material. The condition of coherent scattering can be simplified and expressed

mathematically using equation 3.2, known as Bragg's Law, which is also illustrated in Figure 3-5(a),

$$n\lambda = 2d_{hkl} \sin\theta \qquad (3.2)$$

where, n is the order of diffraction (usually n = 1), λ is X-ray wavelength, d_{hkl} is the spacing between crystal planes with Miller indices h, k and l, and θ is the angle the X-ray beam makes with the crystal planes and is half the X-ray scattering angle 2θ.

For epitaxially grown thin films using MOVPE, XRD serves as a non-contact, non-destructive technique for analysing material composition, phase information, strain state and defect density of the epilayers. A detailed discussion on this technique can be found in [232]. Figure 3-5(b), shows an image of the PANalytical MRD high-resolution X-ray diffractometer used in the present study to analyse the hBN and AlN films. The image also highlights three main components of the instrument namely: (1) a copper (Cu) based X-ray source, which is filtered using a monochromator for only Cu K_{a1} wavelength; (2) a high precision goniometer that holds the sample and has six axes of motion (ω, ψ, ϕ, x, y and z) and (3) detector for measuring scattered X-rays. Two scan types, namely ω–2θ scan and ω–scan, were employed for analysing the crystalline properties of the hBN and AlN epilayers.

3.4 Atomic force microscopy

Atomic force microscopy is a valuable tool for studying the surface topography of thin films with nm resolution. It also provides a quantitative measure of a range of parameters such as surface roughness, surface potentials etc. A typical AFM apparatus consists of an extremely sharp probe mounted on a cantilever beam which is scanned over a sample mounted on a piezoelectric stage. The tip can be in full contact or held at a proximity to the scanned surface, which are known as contact and non-contact mode of measurements, respectively. A combination of the two can also be employed, which is known a tapping mode AFM. As the tip scans over the sample (in a rastering fashion), any deflection in its motion due to superficial features (up/down or sideways) is measured by a laser beam reflected off the tip, which is measured by a photodetector, as shown schematically in Figure 3-6, reproduced from [233]. In this way, deflection

in the AFM cantilever is recorded and subsequently used for generating a surface topography map of the sample.

The surface topography of sapphire, hBN and AlN films were studied routinely using tapping mode AFM (MultiMode 8 AFM, Bruker). Surface roughness values were obtained using Nanocope Analysis software. Thickness of hBN films were also measured using AFM, as detailed in Chapter 4.

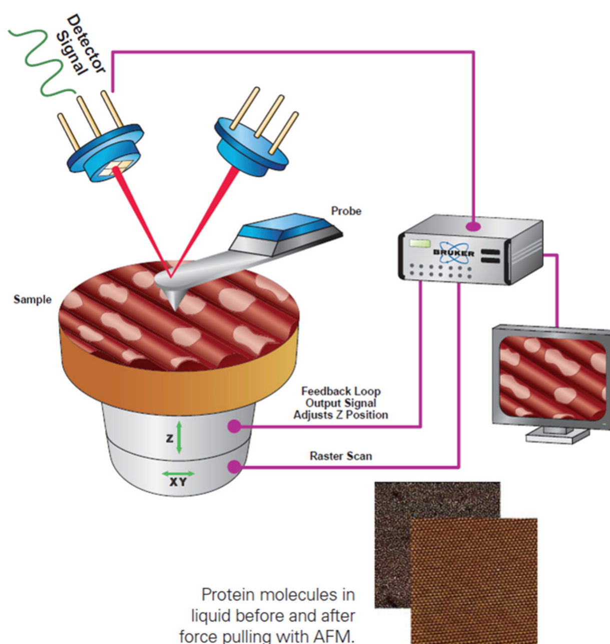

Figure 3-6 Schematic illustration of the measurement principle of AFM. Reproduced from [233]. © Bruker

3.5 Raman Spectroscopy

Raman spectroscopy is a well-established analytical technique, widely applied in the fields of chemistry, biology, material science and more. It is a non-contact and non-destructive technique based on measuring inelastically scattered photons from a material. The shift in the frequency of incidents photons due to atomic and molecular vibrations serves as a fingerprint for identifying different materials, thus making it a valuable diagnostic technique.

Figure 3-7, schematically illustrates the inelastic scattering process. Photons, typically from a laser source in the UV-visible-near infrared spectrum are incident on a sample. Most of the light is scattered as is, without loss of energy, which is known as Rayleigh scattering. However, some photons undergo inelastic scattering upon interacting with the sample and lose energy, which is equal to vibrational energy of the molecules within the material. In crystalline materials, vibrational energy is quantized and represented by phonons. The energy lost during inelastic scattering is

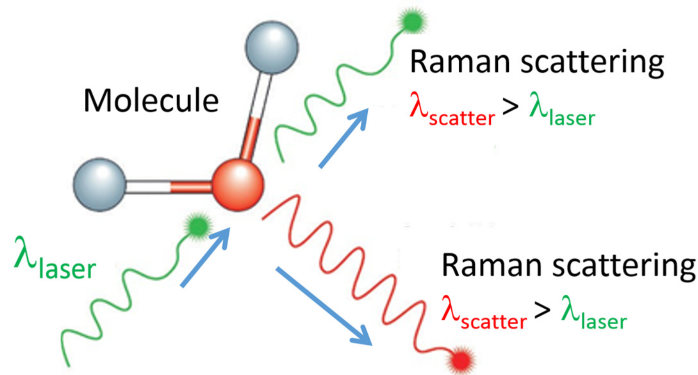

Figure 3-7 Schematic illustration of the principle of Raman scattering [234].

equal to phonon energy and causes a shift in the frequency of the incoming photons, which is measured by a spectrometer. Raman shifts are typically measured in terms of wavenumbers, as described by equation 3.3,

$$\Delta\omega = \left(\frac{1}{\lambda_0} - \frac{1}{\lambda}\right) \qquad (3.3)$$

where, $\Delta\omega$ (cm^{-1}) is the change in wavenumber, λ_o and λ (nm) are wavelengths of the incident and inelastically scattered photon, respectively.

In the present study, Raman spectra of hBN films were measured using a Horiba's Jobin Yvon spectrometer. A 532 nm laser was used as the excitation source, while scattered photons were measured using a liquid nitrogen cooled CCD. Raman spectroscopy provided a fast and easy method for confirming the deposition of hBN films on the sapphire substrates. Raman peaks were also fitted with Lorentzian functions for determining spectral parameter (such as position and FWHM) which can provide information on the crystalline quality and residual strain in the films. Generally, compressive and tensile stress result in blue and red shift of the Raman

peak, respectively, while residual strain in the film can be computed using Gruenissen's parameter for the material [235-237].

3.6 Ultraviolet-visible (UV-Vis) absorption spectroscopy

UV-Vis absorption spectroscopy measurements were performed to estimate the bandgap energy of the hBN layers. For semiconductors, the band gap energy *(E_g)* is related to the spectral dependence of absorption coefficient α (Unit: m^{-1}) using the Tauc's relation [238, 239], given as:

$$\alpha h\nu = (h\nu - E_g)^m \qquad (3.4)$$

where, h is Planck's constant and ν is frequency of light, while m is 0.5 for direct bandgap materials (or direct transitions). With the help of Tauc's plot of $(\alpha h\nu)^2$ vs $h\nu$, E_g can be estimated by extrapolating the linear part of the curve and determining its intersection with the abscissa. For this, α needs to be measured experimentally, which is done by collecting the optical transmission spectra for the sample. Equations 3.5 and 3.6 provide the necessary relation between the two quantities as,

$$\alpha = -\frac{\ln(T)}{l} \qquad (3.5)$$

and

$$T(\lambda) = \frac{I(\lambda)}{I_o(\lambda)} \qquad (3.6)$$

where, l is the film thickness, $I_o(\lambda)$ and $I(\lambda)$ are the intensities of incident and transmitted light, respectively.

In this study, transmission spectra of the hBN samples were collected using a commercial UV-Vis spectrometer (Cary 5000 UV-Vis, Agilent), from which absorbance was measured using equations 3.5 and 3.6. The system utilizes a combination of two light sources (Deuterium UV lamp and mercury lamp), covering a spectral range from 170 to 3300 nm. The spectrometer is equipped with a silicon detector to measure the transmitted light. A bare sapphire wafer was used as a blank for subtracting any absorption by the substrate itself.

3.7 X-ray photoelectron spectroscopy

XPS is a surface sensitive characterization technique primarily used to quantitatively determine the elemental composition and the nature of chemical bonding between atoms in a given material. The working principle of the technique is based on Einstein's photoelectric effect. The sample under investigation is illuminated by high-energy monochromatic X-ray photons (Al K_α @ 1486.68 eV) under vacuum conditions, which excites the inner shell electrons of the atoms and ejects them from the surface. By measuring the kinetic energy (E_k) of the ejected electrons and obtaining the work function of the instrument (Φ), the binding energy of the electron (E_b, which is characteristic of the different atoms and its environment) can be computed using equation 3.7,

$$E_b = h\nu - (E_k + \Delta \mathrm{E}) - \Phi \qquad (3.7)$$

where, h is Planck's constant and v is frequency of incident X-ray photon and ΔE is the chemical shift in binding energy due to bonding with other elements. Experimentally, a spectrum of ejected photoelectron energy is obtained, with intensity peaks at specific energy values. By comparing these values with established databases, the elemental composition and nature of chemical bonding within the material can be obtained.

In the present study, hBN films were deposited using TEB as the growth precursor, which is most likely the source of carbon atoms that get incorporated in the growing film. XPS was therefore utilized to determine the nature and extent of carbon impurities present in the hBN films. XPS measurements presented in Chapter 4 were performed using ESCALAB250Xi (Thermo Scientific U.K.) at the Surface Analysis Laboratory, University of New South Wales, Australia.

3.8 Photoluminescence spectroscopy

Steady state PL spectroscopy is the study of light emitted from a sample (luminescence), due to an external stimuli (incident light), as a function of wavelength [240, 241]. It is a non-contact, non-destructive, fast and convenient technique commonly employed in the characterization of semiconductor materials. In direct bandgap semiconductors (e.g. GaAg, GaN, InP etc.), a photon is emitted upon

electron-hole pair recombination (described below), which is known as radiative recombination, a property that is central to the operation of LEDs and laser diodes. In indirect semiconductors, radiative recombination is only possible via phonon-assisted transition (for momentum conservation), which is a less probable process and typically results in little to no light emission. PL spectroscopy is thus used to estimate semiconductor bandgaps, study impurities and optically active defects in semiconductors.

Figure 3-8(a) shows a typical PL setup. It consists of three essential components, which are (1) excitation source (typically a laser) along with mirror and lenses to focus light on to the sample, (2) a sample stage (with X-Y-Z motion control) with cryostat (optional) for low temperature measurements and (3) a spectrometer coupled to a photodetector (such as a charged couple device – CCD or a photomultiplier tube – PMT) for measuring the intensity of emitted light as a function of wavelength. A microscope may also be used for focusing the laser on to the sample (especially in case of sample with micron sized features).

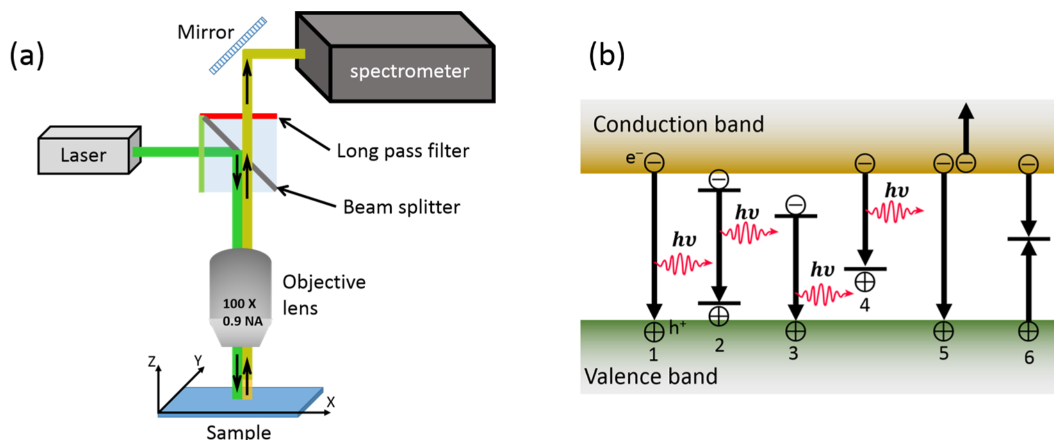

Figure 3-8 (a) Schematic illustration of a PL setup and (b) different carrier recombination processes which take place in a semiconductor. (1) – (4) are radiative recombination processes, while (5) and (6) are nonradiative recombination processes.

Photons, typically from a laser source, with energy greater than the bandgap of semiconductor are illuminated on the sample, which excites electrons from valence to conduction band. As a result, a non-equilibrium concentration of charge carriers

(electrons in conduction band and holes in valence band) is created within the volume of illumination. The photo-excited carriers (electron-hole pairs) diffuse through the material and recombine through a number of different radiative and non-radiative recombination processes, to return the excited carriers to their ground state, as illustrated in Figure 3-8(b). These could be: - (1) band-to-band or direct recombination, (2) exciton recombination, (3) donor-to-band recombination, (4) Acceptor-to-band recombination, (5) Auger recombination and (6) recombination via deep levels. Detailed discussion on these can be found in [241, 242]. Luminescence from the sample (due to radiative recombination) is collected and directed into a spectrometer and measured by the detector.

In the present study, sub-bandgap luminescence from MOVPE grown hBN was measured using a custom built PL spectrometer (similar to that shown in Figure 3-8(a)). The hBN samples were excited either with 266 nm Q-switched Nd:YAG pulsed laser (Ultra 100, Quantel) or 532 nm CW laser, while the emission was measured using a spectrometer (SP-2750, Princeton Instruments) coupled with a photomultiplier tube (PMT, R10699) (Hamamatsu, Japan).

3.9 Scanning electron microscopy and cathodoluminescence

SEM is a powerful technique for visualizing submicron features, which are otherwise invisible or unresolvable in optical microscopes [243]. In SEM, a beam of electrons (instead of visible light) is directed on to a sample to generate a highly magnified image. The resolution of a benchtop light microscope is typically of the order of 200 nm, which is determined by the wavelength of light. However, in an SEM, the de Broglie wavelength of electrons is sub-nanometer, because of which, a resolution of 10 nm (and magnification up to 300, 000 times) can be easily achieved. In addition to this, electron-matter interactions in an SEM generate many other electromagnetic radiations, which are useful for material characterization, as described below.

An SEM typically consists of three components namely: (1) an electron gun to generate a beam of electrons, (2) a set of electromagnetic lenses to shape the electron beam and (3) a sample chamber at the base, kept under vacuum by a pump. The electron beam is raster-scanned on the sample, which interacts with the sample to

generate a number of signals, as summarised schematically in Figure 3-9(b). Of these, secondary electrons and backscattered electrons are commonly used for imaging. Secondary electrons (SE) are generated as a result of inelastic collision between incoming electrons and outer shell electrons of the atoms comprising the sample, resulting in expulsion of the latter from their atomic orbitals. SE typically have low energy (< 50 eV) and are mostly reabsorbed within the sample. Only those SE that are close to surface are able to escape and contribute to imaging. More importantly, SE

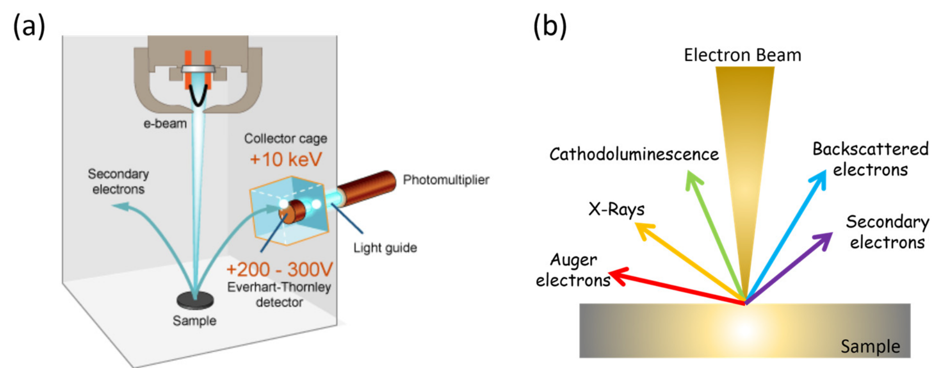

Figure 3-9 (a) Schematic illustration of an SEM and (b) different types of signals generated in the SEM due to interaction of electron beam with the sample.

signal intensity is dependent on surface topography, i.e. edges and ridges emit more SE than a flat surface and appear brighter. Hence, SE provides great details about sample's topography and are extremely useful for imaging.

During inelastic collisions, if the vacancy due to the creation of a secondary electron, as described above, is filled by an electron through transition from a higher level orbital (within the atom), an X-ray photon characteristic of transition energy is produced. These X-ray emissions are unique for different elements and thus can be used for determining the elemental composition of the material. This technique is also known as energy dispersive X-ray spectroscopy (EDS).

In case of semiconductors, the incident electron beam also generates electron-hole pairs, which is similar to e-h pair generation using a laser light in PL spectroscopy. The light emitted due to radiative recombination is analysed using a spectrometer coupled to the SEM. This technique is known as Cathodoluminescence (CL) [244]. In CL, energy of the incident electrons is typically of the order of few keV and is much

higher than the photon energy of commercially available visible and UV lasers used in PL spectroscopy. This makes CL, a very useful technique, especially for studying luminescence from large bandgap semiconductors like hBN or AlN. In addition to this, CL can be combined with nanometer resolution of an SEM that can facilitate luminescence measurements selectively from micron to submicron feature such as nanowires, quantum dot structure etc. Overall, SEM and CL has proven to be a very powerful technique in the field of material science.

3.10 Transmission electron microscopy

TEM is a technique which can achieve atomic resolution and is widely used for analysing crystallinity and microstructure of materials. In TEM, electron energy is of the order of 100 to 1000 keV (higher than that used in SEM), with de Broglie wavelength in the range of a few picometer. Samples analysed in TEM have to be very thin (typically < 100 nm) for them to allow the electron beam to transmit through it. Thus, in some ways TEM is analogous to optical microscopy performed in transmission mode when an optically transparent sample is used.

High resolution TEM of the hBN films was carried out at the Centre for Advanced Microscopy, ANU. A JEOL 2100F instrument operated at 200 keV was used for imaging. Electron transparent lamellae were prepared using focused ion beam milling (using FEI's Helios 600 NanoLab) for cross-sectional TEM. For plan-view TEM, hBN films were transferred on to copper TEM grids using water-assisted delamination.

Chapter 4. MOVPE growth and characterization of hBN

4.1 Introduction

With any new material, a large part of the initial research is dedicated towards its synthesis or growth. Such studies are aimed at investigating the influence of various process parameters on material quality and at the same time, optimize, streamline and even scale-up deposition techniques to reliably obtain the material for various applications. Since hBN is a relatively new semiconductor material, different techniques for the growth and synthesis of single crystal hBN are being examined, some of which have been reviewed in Chapter 2. Wafer-scale deposition methods are of particular interest, as large-area hBN is needed for scale-up of various intended applications. Therefore, a comprehensive study of MOVPE growth of hBN on sapphire wafers has been an important objective and milestone of the research presented in this thesis. In this chapter, results from experimental study on the MOVPE growth of hBN on sapphire substrates is presented.

4.2 MOVPE process overview

A general description of the MOVPE growth process has been presented in Chapter 3 and is illustrated schematically in Figure 4-1(a). hBN layers were deposited on commercially available 2” sapphire wafers (300 μm thick) with (0001) orientation and a ±0.2^{o} offcut towards m-plane (Cryscore). Films were deposited using a closed couple showerhead type MOVPE reactor from AIXTRON. The reactor is equipped with an interferometer and pyrometer (EpiTT, Laytec) for in-situ monitoring of film thickness and surface temperature during growth. The interferometer signal also provides an estimate of the surface roughness of the growing film. Sapphire substrates are placed on the SiC coated graphite susceptor and heated under hydrogen flow and reduced pressure. Prior to hBN deposition, substrates are pre-treated by annealing in hydrogen, followed by ammonia for nitridation [245-247]. hBN growth is initiated by introducing TEB and ammonia into the reactor through the dual plenum showerhead

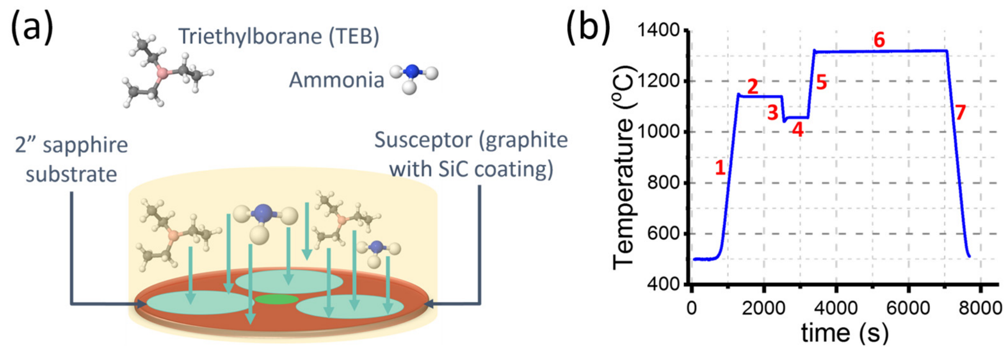

Figure 4-1 (a) Schematic illustration of the MOVPE process and (b) an example of temperature profile during different growth steps in a typical process cycle.

to minimize pre-mixing and cross-reactions between the two. Figure 4-1(b) shows the temperature profile during various steps involved in a typical growth cycle and are described as follows:

1. Substrates were heated to pre-growth annealing temperature of 1150 ºC under a hydrogen flow, which is the preferred carrier gas during hBN growth. H_2 helps in removing ethyl groups from TEB and thus minimizes carbon incorporation as an impurity in the hBN film.

2. At 1150 ºC, sapphire wafers were annealed in hydrogen for 20 minutes. During annealing the reactor pressure was 200 mbar and the total hydrogen flow was set to 10 SLM. Thermal annealing removed polishing marks from sapphire, resulting in a very smooth surface. Figure 4-2(b) shows the surface topography of an annealed sapphire substrate. Atomic terraces, present due to offcut are clearly visible. Such a surface is ideal for hBN deposition.

3. Next, the temperature was decreased to 1050 ºC.

4. At this stage, ammonia was introduced in the reactor for nitridation. This results in the formation of thin (~ 1 nm) AlN layer on sapphire [245]. Although nitridation is not essential for hBN deposition, some studies have suggested that it can be beneficial [226, 248, 249]. During hBN growth, very high V/III ratios are typically used. Under such circumstances, random, unintentional nitridation of the substrate is unavoidable, which may lead to a rough surface morphology. Hence, controlled nitridation is performed, which is better suited for hBN deposition. During this step, the ammonia flow was set to 2 SLM, while maintaining the total gas flow at

10 SLM. The total nitridation time was 5 minutes.

5. After nitridation, the ammonia flow was stopped and the sample was heated to hBN growth temperature under a hydrogen flow. The maximum growth temperature achievable in the MOVPE reactor is 1330 ºC, which was used for the majority of hBN depositions undertaken during the course of this research work. During temperature ramp-up, the reactor pressure was further reduced to between 85-100 mbar. By reducing process pressure, the residence time of precursors within the growth chamber decreases, which helps in minimizing parasitic reactions. Total carrier gas flow was also increased to 18 SLM (unless stated otherwise) to reduce debris accumulation on growing surface and is discussed later.
6. Once the growth temperature is reached, TEB and ammonia are introduced in the reactor without any further delay. Precursors were either introduced simultaneously into the reactor for continuous flow growth (CFG) or as short alternating pulses, as in flow modulation epitaxy (FME). At growth temperatures, TEB undergoes pyrolysis at the substrate surface to form BH_3 by removal of the ethyl groups. NH_3 and BH_3 further decompose and react to form hBN film on the substrate. Ammonia decomposition also provides hydrogen radicals, which along with the H_2 carrier gas, remove the carbon species from the reactor. Growth time was varied to study change in film thickness with time.
7. Finally, to stop growth, precursor flow is terminated, and samples are cooled down to ambient under hydrogen flow.

Overall, MOVPE is a complex process which requires precise control over various steps such as samples heating, actuation of MFCs, pressure control etc. A process recipe is prepared using a graphic user interface supplied with the instrument. The entire growth process and various steps of process recipe are executed in a sequential fashion by an automated control system. The hBN growth study involved optimization of multitude of growth parameters, which are listed in Table 4-1. In the following sections, key experimental findings from a comprehensive hBN growth and characterization study are presented. The influence of various growth parameters is

studied systematically and different characterization techniques are employed to develop a holistic view of the challenges associated with hBN growth.

Table 4-1 A list of MOVPE process parameters which are optimized for hBN growth.

	Growth parameter	Range	Impact on hBN growth
1	Temperature	< 1350 °C	Provides thermal energy for precursor dissociation; adatom mobility and crystallinity of the hBN films.
2	Pressure	50–200 mbar	Low pressure reduces gas phase parasitic reactions between precursor molecules.
3	TEB Flux	10–100 µmol/min	Source of Boron atoms; shows a direct control over hBN growth rate and carbon incorporation in hBN film.
4	NH_3 Flux	100 – 5000 sccm	Source of Nitrogen atoms; does not influence hBN growth rate; provides hydrogen radicals for carbon removal; required for nitridation of sapphire.
5	Carrier gas (H_2)	2 – 20 SLM	Provides hydrogen radicals for removal of carbon based impurities from the hBN film.
6	Pulse Duration (TEB)	1 – 5 s	TEB flux duration has a similar effect as TEB flux. Longer pulse duration increases hBN growth rates.
7	Pulse Duration (NH_3)	1 – 5 s	Changes the net ammonia flux and V/III ratio.

4.3 Continuous flow growth

Even though the severity of parasitic reaction between TEB and ammonia is well-known and emphasized in previous sections, CFG has been utilized in the past for depositing hBN over different substrates. For example, Li et al. used CFG for the deposition of high quality hBN layers on sapphire using a CCS type MOVPE reactor. hBN layers with thickness up to 60 nm were deposited at a growth rate of 15 nm/hr [209]. In a different study, Chubarov et al. reported that crystallinity of hBN deposited using CFG at temperatures lower than 1500 ºC is poor and is mostly turbostratic [222, 250]. Some studies have indicated that hBN growth on sapphire can also be self-limiting, especially with a large V/III ratio. However, hBN deposition temperatures used in those studies were relatively low [207, 224]. Hence, the varying nature of

results reported so far provided a strong reason to investigate hBN growth under CFG mode.

hBN growth was performed using the process outlined in steps 1-7 described in Section 4.2. After a few trial runs, TEB and NH_3 flow rates were selected as 60 μmol/min and 67 mmol/min (V/III ~ 1100), respectively. Substrate temperature (at the surface) was set to 1330 °C and total gas flow rate was kept at 18 SLM. Growth time was varied from 5 minutes to 1, 4 and 8 hours to observe changes in film thickness and surface morphology with time. Post growth, samples were analyzed using a combination of characterization techniques such as Raman spectroscopy, AFM and TEM.

Figure 4-2(a) shows the Raman spectra of the four samples, collected using a 532 nm laser (laser power incident on sample was 3 mW/cm^2). The peak at 1370 cm^{-1} corresponds to the E_{2g} vibrational mode of sp^2 bonded boron nitride, thus confirming hBN deposition [251-254]. Raman spectrum of a blank sapphire substrate is also included for reference and the peak from substrate is observed at 750 cm^{-1} [255]. As

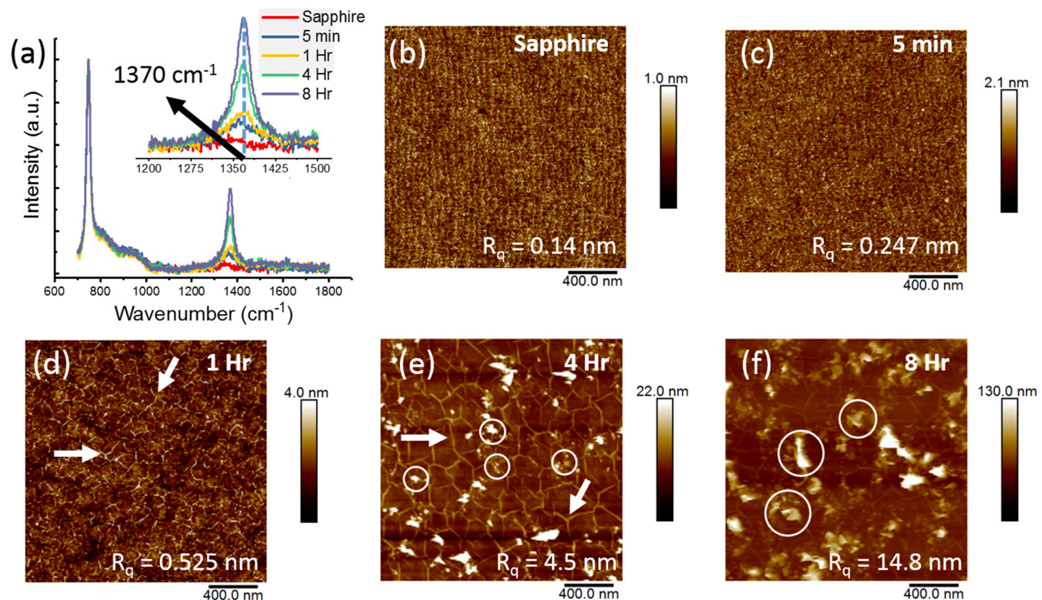

Figure 4-2 (a) Raman spectra of CFG hBN for different time periods. Spectrum of blank sapphire is also included for reference, (b) surface topography (measured using AFM) of sapphire after hydrogen annealing and (c-f) surface topography of hBN films deposited under continuous flow conditions. Wrinkles in hBN films are indicated with white arrows in (d) and (e), while debris due to parasitic reactions are indicated by white circles in (e) and (f).

the deposition time increased from 5 minutes to 8 hours, the E_{2g} band intensity from hBN also increases, which indicates deposition of thicker films. Hence, we can conclude that the hBN growth is not self-limiting. Furthermore, compared to experimentally measured E_{2g} values for bulk hBN (~1366 cm^{-1}), the Raman peaks for MOVPE-grown hBN layers have shifted to higher frequencies. In general, tensile and compressive strain in the material cause red and blue shifts in Raman peak, respectively. The magnitude of shift in phonon frequency can be calculated using the Gruneisen parameters for the material [235, 256]. This suggests that MOVPE grown hBN is under compressive stress, which is consistent with previous studies [174, 209].

The surface morphology of the hBN films was studied using AFM, which is shown in Figure 4-2 (c-f). Growth times are as indicated on the figures. Prior to hBN growth, an atomically smooth sapphire surface (with atomic terraces) is obtained after hydrogen annealing, as shown in Figure 4-2 (b). This surface is optimum for epitaxial growth. After a growth period of 5 minutes, the surface still looks pristine and only a very small increase in the E_{2g} band intensity can be observed in its Raman spectrum. It is possible that after such a short growth duration, hBN only partially covers sapphire surface and does not exist as a continuous film. This is consistent with the lack of a wrinkles (indicated by white arrows), which are observed in AFM scans for thicker films deposited for 1, 4 and 8 hours. The surface roughness of hBN films also increases with deposition time, estimated as R_q (root mean square roughness). Apparently, due to very high surface roughness, wrinkles are not visible in Figure 4-2 (f), where the hBN layer is deposited for 8 hours. The wrinkled surface morphology can be attributed to compressive stress in the hBN films and is discussed in more details later. More importantly, the transition from a smooth to wrinkled morphology is indicative of a continuous film and increase in film thickness and is consistent with the increase in E_{2g} peak intensities shown in Figure 4-2(a).

Using cross-sectional TEM, the film thicknesses for 1 and 4 hour growths were measured to be 1-1.5 nm (3-5 layers) and 5 nm (±0.5 nm), respectively, as shown in Figure 4-3(a-b). The thickness of the hBN film grown for 8 hours was measured using AFM and found to be13.5 nm (±0.5 nm), as shown in Figure 4.3(c-d). Based on these measurements, hBN growth rate was estimated to be nearly 1-1.5 nm/hour. This is extremely low compared to growth rate of wurtzite III-nitride materials that are typically three orders of magnitude higher. Figure 4-2(e) and 4-2(f) also highlight

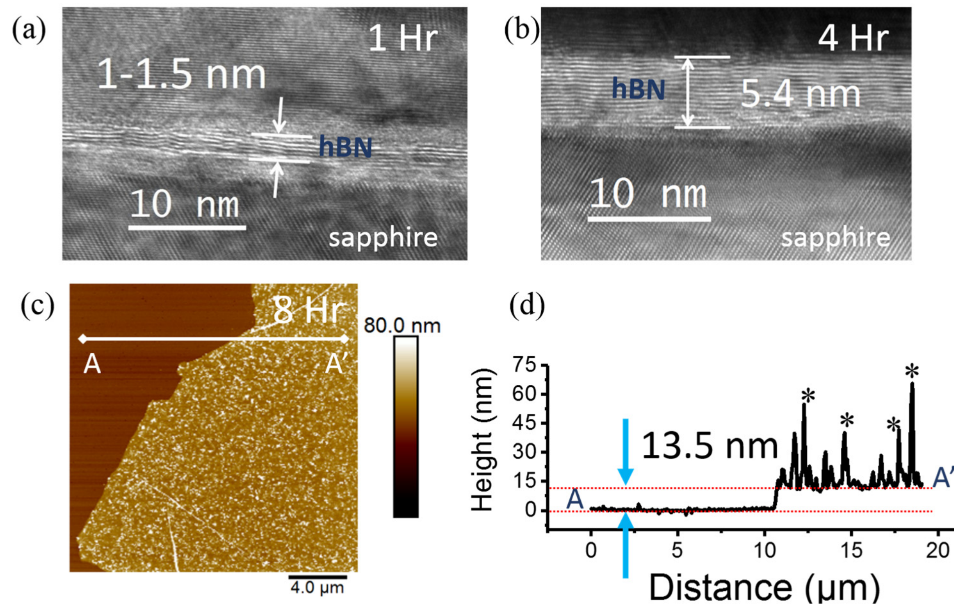

Figure 4-3 (a) Cross-sectional TEM of CFG hBN grown for 1 and 4 hours respectively, (c) AFM of CFG hBN grown for 8 hours and (d) AFM line scan showing height profile of line AA' in (c). Note that the spikes marked with '*' (d) are debris which are deposited on the film during growth.

particle like features encircled in white, which are referred to as debris. These debris are suspected to form as a result of gas phase reactions between precursors and accumulate on the surface of the growing hBN film with time, resulting in rough surface morphology. Using plan-view TEM analysis, detailed in section 4.9, these debris (on similar hBN films) were identified as randomly oriented hBN particles.

Cross-sectional TEM of hBN grown for 4 hours using continuous flow conditions, with layer thickness of ~ 5 nm is shown in Figure 4-4 (a). For lamella preparation using FIB, the sapphire wafer flat (oriented along the (11-20), also known as the a-plane) was utilized for alignment and the lamella was prepared parallel to wafer flat. Consequently, during TEM imaging, the zone axis of sapphire was pre-determined to be [-2110]. Individual hBN layers, oriented parallel to the basal plane of the sapphire substrate can be clearly identified. Fast Fourier transform (FFT) of selected areas (red boxes) for sapphire and hBN were obtained using DigitalMicrograph software and are presented in Figure 4-4 (b) and 4-4(c) respectively. The diffraction spots have been indexed. Based on the available FFT patterns, the zone axis of hBN is identified as [1-100], which is parallel to zone axis

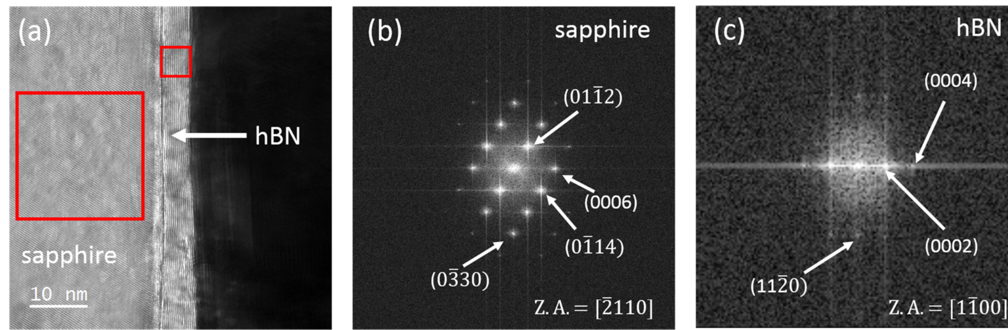

Figure 4-4 (a) High magnification cross-sectional TEM of 5 nm hBN grown under continuous flow conditions for 4 hours, (b-c) FFT of sapphire and hBN indicated by the red boxes in (a) respectively.

the [-2110] of sapphire. Thus the epitaxial relation between hBN and sapphire is [0001]hBN||[0001]sapphire and [1-100]hBN||[-2110]sapphire. Therefore, the hBN lattice has a 30° in plane rotation with respect to sapphire, which is consistent with previous reports [219, 257, 258]. This preferred orientation reduces lattice mismatch between hBN and sapphire and is consistent with that observed in case of other III-nitrides, e.g. GaN and AlN grown on sapphire.

Under CFG, changing TEB and ammonia (and thus V/III ratio) flux invariably yielded similar results. For example, by decreasing TEB flux (increasing V/III ratio), hBN growth rate dropped significantly and resulted in nearly no growth, whilst increasing TEB flux (lowering V/III ratio) led to deposition of hBN films with a very rough morphology, similar to that seen in Figure 4-2 (f). These observations and results are consistent with the issue of gas phase reactions between precursors.

Overall, this experimental study provides a valuable insight into the nature of hBN growth using CFG conditions. In addition to the issue of low growth rates, other aspects of hBN growth using CFG have also been presented. For instance, the changes in hBN's surface morphology with growth time was studied using AFM. The structural characteristics of debris was obtained using plan-view TEM and is discussed in the following sections. It is reasonable to believe that a large amount of debris on the surface of hBN layers (during growth) can obstruct the formation of a continuous hBN film over a large area and the rough surface limits further application of such films.

4.4 Flow Modulation Epitaxy

To overcome the issue of slow growth rates and rough surface profiles of hBN films obtained under CFG conditions, flow modulation (FM) scheme for precursors was investigated next. Under FM scheme, the precursors (TEB and ammonia) were introduced into the reactor as short alternating pulses. At no instance in time, were both precursors introduced into the chamber simultaneously. Each loop consisted of a short 1 second pulse of TEB, after which the TEB flow is terminated and followed by a 3 second pulse of ammonia (without any delay), as illustrated in Figure 4-5(a). The number of loops was changed to get hBN films of desired thickness.

FM scheme proved to be effective and suitable for depositing better quality hBN films, described as follows. Figure 4-5(b) shows a photograph of a whole 2” sapphire wafer with a 20 nm-thick hBN layer deposited using FM scheme for 8 hours (or 7200 loops). For convenience, this hBN is also referred to as ‘FM-hBN’. A TEB flux of 10

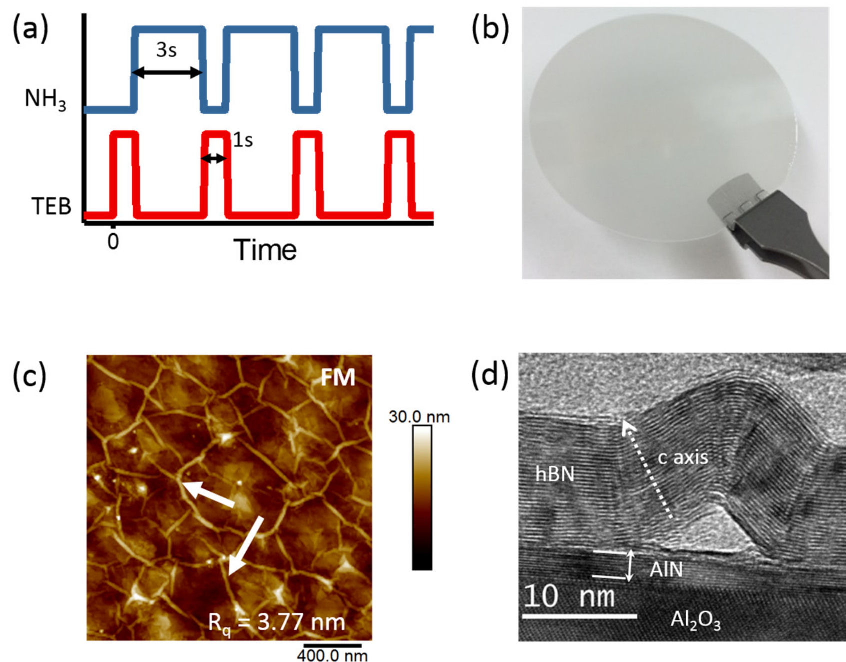

Figure 4-5 (a) Precursor flow sequence used in the flow modulation scheme. TEB and ammonia flow rates were 10 sccm and 1500 sccm respectively, (b) optical micrograph of a whole 2” sapphire substrate with a 20 nm FM-hBN, (c) surface topography of 20 nm-thick hBN films deposited using FM scheme for 8 hours. A few wrinkles in the hBN film have been marked by white arrows and (d) cross sectional HR-TEM of hBN deposited on sapphire (Al_2O_3) substrate. Sample for HR-TEM was grown separately. The dotted arrow in white indicates the direction of the c-axis in the wrinkled part of the hBN layer.

μmol/min was used during growth, which is a sixth of the TEB flux used for CFG. The ammonia and carrier gas flow rates were kept at 67 μmol/min (V/III ~ 6600) and 18 SLM, respectively, which are same as used in CFG. The surface topography of the FM- hBN film, measured using AFM is shown in Figure 4-5(c). In contrast to hBN grown under continuous flow conditions (Figure 4-2(f)), the surface of FM-hBN film is devoid of debris. hBN growth rate also doubled, in spite of using a lower TEB flux. Both of these attributes, a debris-free surface and higher growth rates are attributed to reduced gas phase reactions.

The hBN film also exhibits a wrinkled morphology that is characteristic of 2D material growth. Similar wrinkles have also been reported in case of CVD growth of other 2D materials including hBN on metallic and dielectric substrates [161, 173, 259-262]. Wrinkles in the hBN most likely form during sample cooling (from 1330 ºC to room temperature). Due to a mismatch in the thermal expansion coefficient between the sapphire substrate and hBN (α_{hBN} = -2.9 × 10^{-6} K^{-1} [53] and $\alpha_{sapphire}$ = 7× 10^{-6} K^{-1} [supplier data sheet]), the film experiences a compressive stress during cool down. During this time, a lack of covalent bonding between the film and substrate results in local delamination and wrinkling of the hBN films. Furthermore, in spite of eliminating debris, the surface roughness (R_q) of FM-hBN film is still large, compared to the specular III-nitride films deposited using MOVPE. Though this large roughness is predominantly due to formation of wrinkles, roughness of the underlying sapphire substrate can also contribute to R_q, as detailed further in section 4.8. Figure 4-5(d), shows a high resolution cross-sectional TEM image of a wrinkle in the hBN film, grown using FME[5]. It can be seen that the orientation of the individual hBN basal planes is maintained throughout the wrinkle and remains parallel with respect to each other. A void can also be seen between the film and the substrate (below the apex of the wrinkle), which confirms localized delamination of hBN, in the wrinkled region of the film. Furthermore, a thin layer (~ 1 nm) of aluminium nitride can be seen sandwiched between the hBN layer and sapphire substrate, due to nitridation of the sapphire substrate [246, 247], performed prior to hBN growth.

---

[5] Cross-sectional TEM lamella were prepared by focused ion beam (FIB) milling using FEI's Helios 600 NanoLab. Samples for TEM were grown separately after optimizing the growth conditions. It was found that capping hBN layers with AlN (grown in situ) helped to protect the hBN layers from FIB damage and overall sample preparation.

The Raman spectrum of FM-hBN is shown in Figure 4-6(a). The experimentally measured Raman peak is fitted to Lorentz functions and FWHM was estimated to be 25 cm^{-1} for FM-hBN films (and 29.6 cm^{-1} for hBN grown under continuous flow for 8 hours), which is comparable to CVD and MBE grown hBN films [172, 201, 207, 209, 223, 258, 263]. However, these values are considerably higher compared to single crystal hBN, which has a much smaller FWHM, typically in the range of 7-9 cm^{-1}. The relatively large FWHM values for MOVPE grown hBN may be attributed to small grain size and relatively poorer crystal quality [157]. Additionally, compressive strain in the film can also contribute to an increase in FWHM. Although wrinkles formed in the hBN films can release some of the compressive stress, complete stress relaxation (due to wrinkling) in the continuous hBN film over the entire 2” wafer cannot be expected. Mohiuddin et al. have reported a similar phenomenon in graphene, where externally applied tensile strain on single layer graphene caused broadening of the G

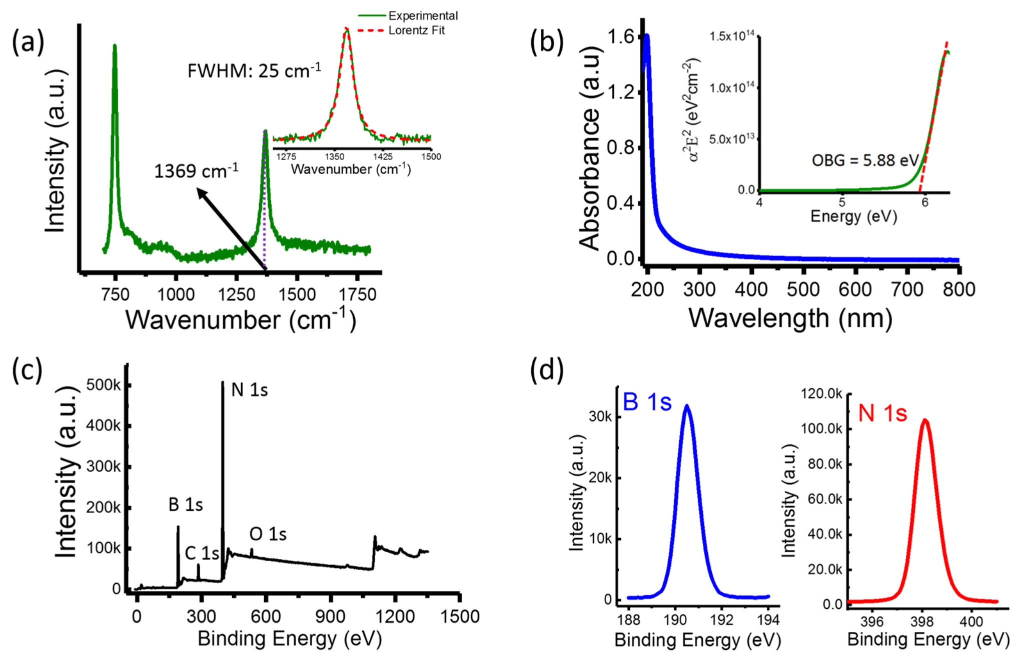

Figure 4-6 (a) Raman spectrum of FM-hBN on sapphire. The inset shows experimental data fitted to a Lorentz function for estimating peak characteristics, (b) UV-Vis absorbance spectra for 20 nm-thick FM-hBN. The inset shows the Tauc’s plot for estimating optical bandgap (OBG) and (c-d) XP spectra showing various elements identified along with high-resolution spectra pertaining to boron and nitrogen 1s photoelectrons, respectively.

band (due to E_{2g} phonon mode at 1590 cm^{-1}) which, eventually split in to two peaks [235]. Similar phenomena has been observed in other 2D materials, including hBN [256, 264].

The optical band-gap for the FM-hBN film was estimated with the help of UV-Vis absorption spectroscopy as shown in Figure 4-6(b). The inset shows the Tauc's plot from where a band gap value of 5.88 eV was estimated from the extrapolation of the linear regime of the curve. The estimated band gap of the FM- hBN film is smaller than the band gap of bulk hBN (6 eV). Recently, bulk hBN has been shown to have an indirect bandgap, with phonon assisted emissions reported at 5.86 and 5.75 eV and exciton binding energy of 130 meV [265]. Therefore, bandgap value obtained for FM-hBN is most likely due to exciton transitions within the film. XPS analysis of FM-hBN was carried out to determine the elemental composition and nature of chemical bonding in the grown film. A survey spectrum was first obtained, with different peaks indexed, as shown in Figure 4-6(c). High resolution XPS scans show symmetric peaks of the B 1s and N 1s photoelectrons at 190.59 and 398.2 eV respectively, as shown in Figure 4-6(d). These two peaks correspond to sp^2 hybridized B and N atoms. After adjusting for the sensitivity factors (obtained by using a commercially available bulk hBN crystal as reference), the B/N ratio was determined to be 1.025.

Figure 4-7 shows a plan view TEM image of FM-hBN (transferred on to a Cu TEM grid) along with its SADP pattern. hBN films appears to be nanocrystalline with

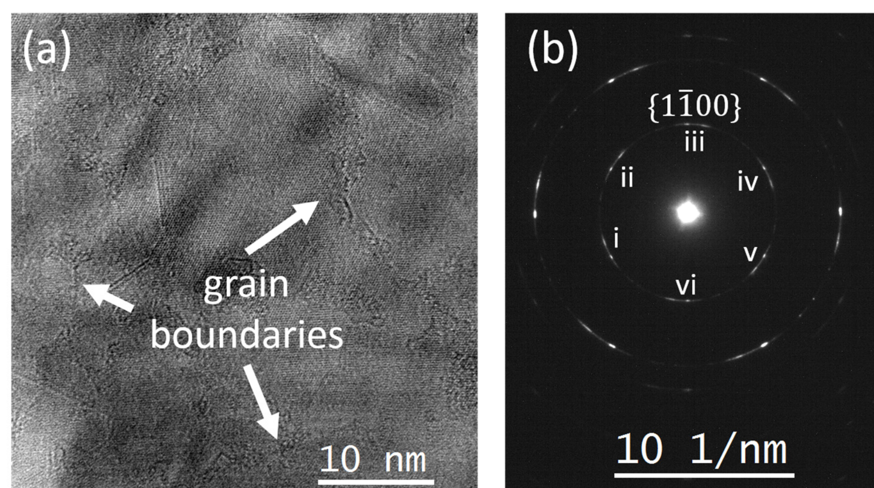

Figure 4-7 (a) High magnification, plan view TEM of FM-hBN. White arrows are pointing to grain boundaries, (b) SADP pattern of hBN layer, showing six diffused spots marked (i)-(vi), representative of hexagonal symmetry of the hBN lattice.

grain size of the order of only a few tens of nanometers. The six bright diffraction spots marked in Figure 4-7(b) correspond to $(1\bar{1}00)$ planes and represent the six-fold hexagonal symmetry of the BN lattice. The diffractions spots have an arc shape, which is due to in-plane rotation of hBN grains with respect to underlying layers and alludes to a partially turbostratic nature of the hBN films.

Furthermore, it is to be noted that the random in-plane orientation of hBN nano-crystallites presented above is not consistent with the well-defined epitaxial relation between hBN and sapphire lattices, as presented previously in Figure 4-4. Based on the results obtained in the present thesis and similar studies reported so far, it appears that the extent of in-plane disordering (or rotation) of lattice planes may be dependent on the thickness of the hBN film. As the thickness of hBN increases, the in-plane misalignment of hBN nano-crystallites also increases. For thinner hBN films, due to stronger interfacial forces present at hBN-sapphire interface (because of dangling bonds present on the surface of sapphire), the first few atomic layers of hBN may have a well-defined lattice relation with the underlying substrate. However, as the thickness of hBN film increases, the epitaxial orientation of the new hBN grains being added on top of existing hBN layers, is now influenced by weaker van der Waals forces. This may result in an increased degree of misalignment. The cross-sectional TEM and diffraction pattern analysis presented in relation to Figure 4-4, pertain to a thinner hBN film (thickness ~ 5 nm). On the other hand, the in-plane TEM images shown in Figure 4-7, where randomly oriented hBN grains have been observed, correspond to a much thicker hBN film (20 nm). Plan-view TEM images of thinner hBN films could not be obtained, due to challenges in sample preparation. Further investigation will be undertaken in the future to fully understand the relation between hBN thickness and in-plane rotation of lattice planes.

4.5 Effect of TEB flux

The effect of TEB flux on hBN growth rate and film quality were studied. Using the FM scheme depicted in Figure 4-5(a), four hBN films were grown on sapphire, with TEB flux of 10, 20, 30 and 60 μmol/min. The ammonia and carrier gas flow rates were kept constant at 45 mmol/min and 12 SLM respectively. This corresponds to a variation in V/III ratio from 735 (for TEB = 60 μmol/min) to 4400 (for TEB = 10

μmol/min). Note that a slightly smaller carrier gas flow rates have been used here. This increased the growth rate of hBN and thus reduced the overall deposition time.

AFM scans shown in Figure 4-8(a-c) for the 3 hBN films highlight a wrinkled surface topography, which is consistent with hBN growth. A few debris, encircled in white in Figure 4-8(a-c), are also seen on the hBN. It is important to note that through FME, parasitic reactions between precursors is minimized, but not eliminated completely. Hence, a few debris were still deposited on the surface of hBN films shown in Figure 4-8(a-c). However, compared to hBN deposited using CFG, their overall density is much less. Debris density could be reduced even further by using higher flow rate of the carrier gas (H_2), which was effective in flushing out debris from the reactor during hBN growth. Reasons for using a smaller carrier gas flow rates have been described above. Detailed structural characterization of the debris using electron microscopy is presented in Section 4.8. In a recent study, Yang et al. have observed similar debris like features (termed as 'islands') on hBN films deposited on sapphire using TEB and ammonia, and its density was found to be a function of ammonia flux [219]. Similarly, Paduano et al. have reported that BN deposited at low V/III ratio (=450) consists of 3D nuclei of hBN and rough surface morphology [207, 224]. In the present study, the morphology of hBN grown using 60 μmol/min of TEB is different (from the remaining samples), as shown in Figure 4-8(d). No wrinkles are observed in this case. It is likely that with the use of high TEB flux of 60 μmol/min, parasitic reactions in the chamber increase significantly and the surface gets covered by a large

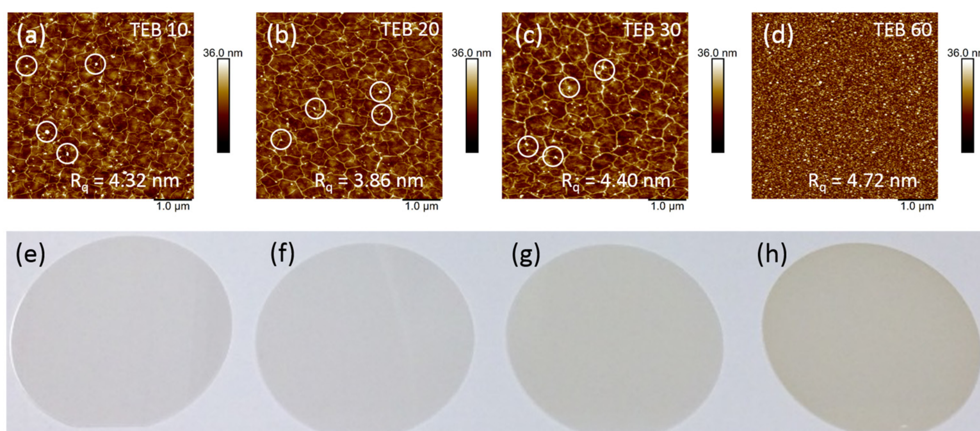

Figure 4-8(a-d) Surface topography of hBN films deposited using TEB flow rates as indicated on the image (unit is μmol/min) and (e-h) Complete 2" sapphire substrates with hBN films deposited using TEB flux of 10, 20, 30 and 60 μmol/min, respectively.

amount of debris that is reflected in the morphology of the hBN film. hBN films were also transferred on to SiO_2/Si substrates and the film thickness was measured using AFM (not shown here). The growth rate changed from 7 to 160 nm/hr as the TEB flux was increased from 10 to 60 μmol/min.

Figure 4-8(e-h), shows optical images of complete 2” sapphire wafers with hBN films deposited using TEB flux of 10, 20, 30 and 60 μmol/min respectively. Films deposited with higher TEB flux have a more yellowish appearance suggesting impurity incorporation. XPS analysis was done on the four samples to determine impurities and the nature of chemical bonding in the hBN films. Prior to collecting the XPS data, a gentle cleaning and etching of the hBN films was performed using an Ar beam. This removes adventitious surface impurities and hence, obtain measurements from the bulk region of the hBN film. From the XPS survey spectra (an example of which is also shown in Figure 4-6(c) for TEB = 10 μmol/min), carbon was identified as the main impurity and originates from the use of a metal organic precursor TEB as the boron source. The high resolution carbon spectra for the four samples can be seen in Figure 4-9(a-d). Upon deconvolution of the carbon spectra using Gaussian functions, two main peaks pertaining to B–C bond (boron carbide) at 283.02 eV and C–C bond at 284.8 eV were identified in all four samples [266-268]. The intensity of graphitic carbon peak remains nearly constant across all samples (see C–C peak in Figure 4-9(a-d)) and may be due to ambient environment. However, the intensity of B–C peak (and C–N peak) increases and becomes more prominent with an increase in the TEB flow rate. The relative concentration of boron carbide (calculated as percentage) was estimated using equation 4.1,

$$C_x = \frac{I_x/S_x}{\Sigma I_x/S_x} \times 100 \tag{4.1}$$

where, I_x is the integrated peak intensity obtained experimentally and S_x is the atomic sensitivity factor, available from the database supplied with the instrument. The overall growth rate of hBN films and the total percentage of boron-carbide in hBN are both directly proportional to TEB flux, as shown in Figure 4-9(e). This indicates that carbon incorporation in the hBN films has a direct correlation to the growth rate. Therefore, incorporation of less carbon in hBN necessitates the use of low TEB flux, which also leads to slow growth rates. Increased boron carbide formation can be explained as follows. In FM growth, during each TEB pulse (when ammonia flow is switched-off),

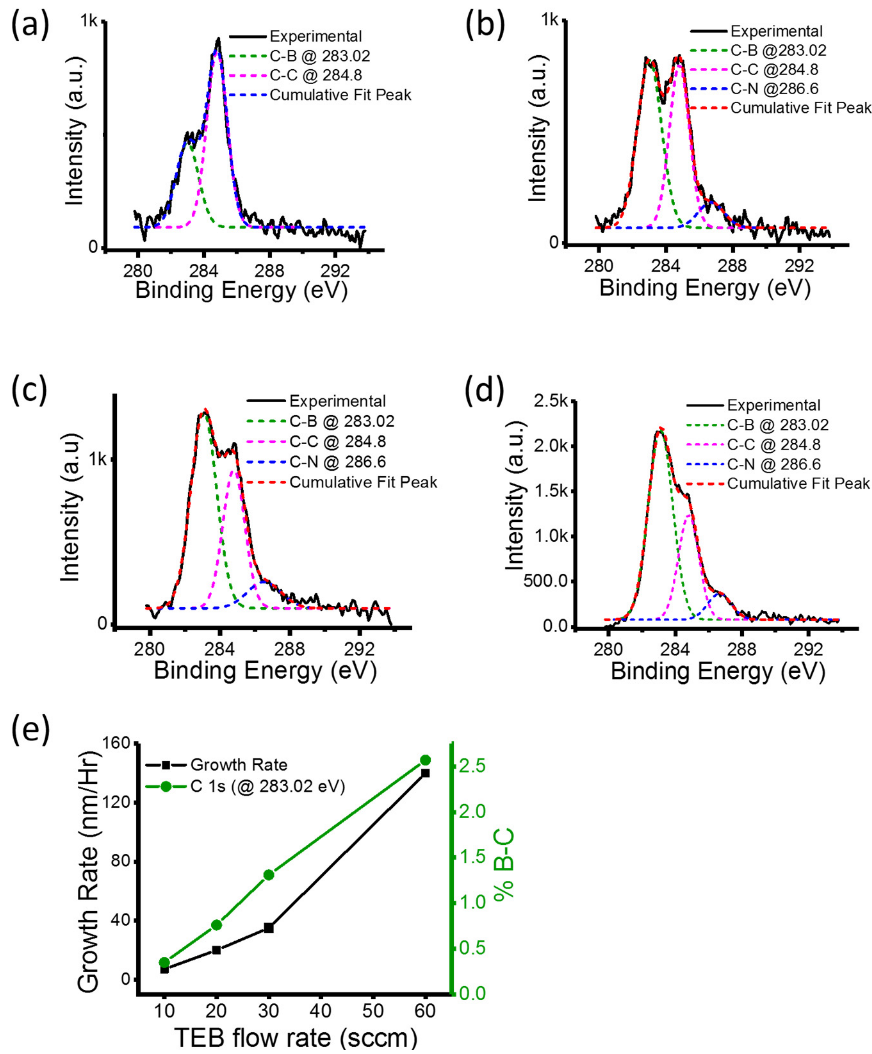

Figure 4-9 (a-d) C 1s spectra collected from hBN film deposited using TEB flux of 10, 20, 30 and 60 µmol/min, respectively. All spectra were collected after argon etching to remove adventitious carbon from the film's surface and (e) growth rate and percentage of boron carbide incorporated in hBN films as a function of TEB flow rate.

it is likely that a greater fraction of TEB 'self-reacts' and gets converted into boron carbide without combining with ammonia to form hBN. As the TEB flux increases, the percentage of B-C formation also increases. Incorporation of boron carbide can disrupt the long range ordering of hBN basal planes and reduce the crystalline quality of the deposited films. In addition to the yellowish appearance, sub-bandgap luminescence from the hBN films was also recorded. While the PL measurements are discussed in Chapter 5, due to sub-bandgap luminescence, the Raman spectrum of these hBN films could not be obtained, as the E_{2g} peak was completely swamped by

fluorescence from the samples. Other laser wavelengths such as 325 and 633 nm were also tried for obtaining the Raman spectra, but to no avail.

4.6 Effect of Ammonia flux

In this section, the effect of ammonia flux on hBN growth is presented. For this, a separate set of 5 hBN samples were prepared using FME, with NH_3 flux of 4.5 mmol/min (100 sccm), 22.3 mmol/min (500 sccm), 45 mmol/min (1000 sccm), 85 mmol/min (2000 sccm) and 134 mmol/min (3000 sccm), respectively. TEB flux was kept constant at 10 µmol/min, to minimize the amount of carbon incorporated in hBN. Total carrier gas flow rate was 12 SLM and growth time was set to 7 hours (or 6300 loops). For computing the average growth rate, thickness of the hBN films were measured using methods described in section 4.8.

Figure 4-10(a) shows the growth rate of hBN as a function of ammonia flow. It can be seen that the hBN growth rate decreases from 13 to 4 nm/hr as the NH_3 flow rate increases from 100 to 3000 sccm. Hence, only a marginal change in the hBN growth rate is observed (< 3 times), which is not proportional to the change in ammonia flow rates (30 times). This suggests that in the present scenario, the growth rate of hBN has a weak dependence on the amount of group V precursor and is largely limited by the group III precursor. Figure 4-10(b) and 4-10(c) show the AFM surface profiles of hBN grown using NH_3 flow rates of 3000 and 100 sccm, respectively. The surface of hBN film grown using 3000 sccm of ammonia has a much higher density of debris, as compared to sample grown using only 100 sccm of ammonia. The debris density is

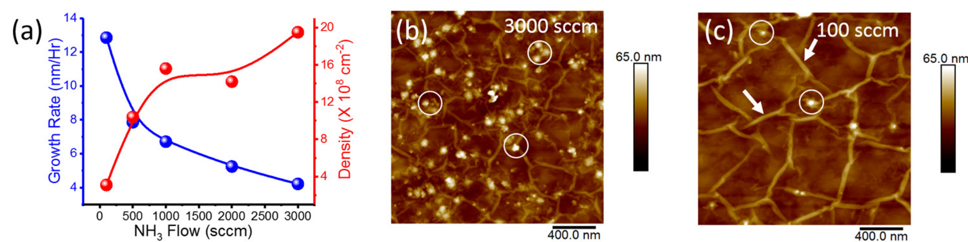

Figure 4-10 (a) hBN growth rate and particle density as a function of ammonia flow rate and (b-c) AFM images of hBN film deposited using ammonia flow of 3000 and 100 sccm. Note: the debris density reduces by an order of magnitude on reducing NH_3 flow to 100 sccm. Wrinkles are still visible for both films and indicated by white arrow in (c).

also shown as a function of ammonia flow rate for all 5 samples in Figure 4-10(a). To summarize the two results shown in Figure 4-10(a), it can be said that as the ammonia flow rate increases, the growth rate of hBN decreases, whilst the debris density increases. Both, these results point towards increased parasitic reactions with the use of larger ammonia flux.

The Raman spectra of the set of five hBN films are shown in Figure 4-11(a), along with the spectrum of bare sapphire for reference. For comparison, individual Raman spectrum were first normalized with respect to the sapphire substrate peak. The E_{2g} peak pertaining to hBN is clearly visible for most of the samples. However, a gradual increase in background fluorescence from these sample can be seen as the ammonia flux decreases. For hBN sample grown with ammonia flux of 100 sccm, the background luminescence is strong enough to completely swamp the E_{2g} band of hBN. In the previous section, it was shown that the increase in background fluorescence is most likely caused by incorporation of carbon in the hBN films. Therefore, XPS analysis of the 5 samples grown using different ammonia flux were performed. These analyses are similar to that presented in the previous section, hence a detailed description of the same is not presented here. XPS results confirm carbon incorporation in hBN films as B-C (with a C 1s peak at 283.02 eV).

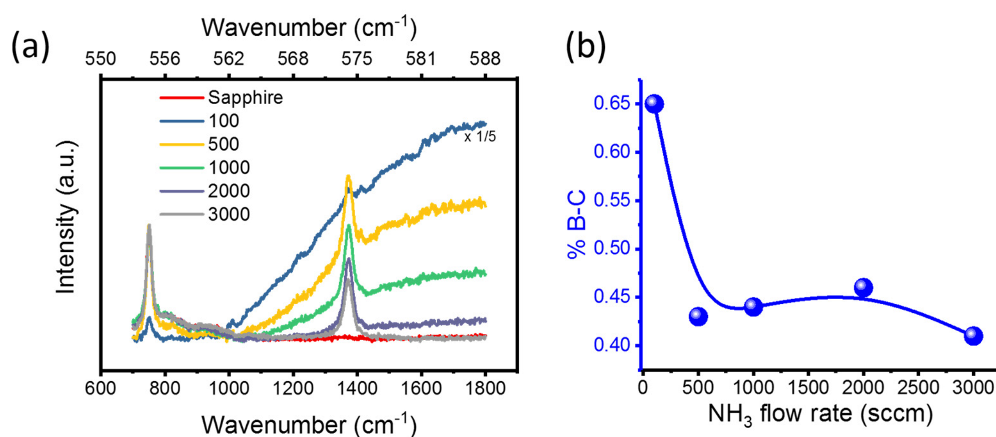

Figure 4-11 (a) Raman spectra of hBN films growth with different ammonia flux and (b) percentage of boron carbide in hBN films, measured using XPS, as a function of ammonia flow rate.

Furthermore, Figure 4-11(b) shows the total percentage of B-C in hBN as a function of ammonia flow rate. Amongst the five samples, the B-C concentration was

highest for the hBN sample grown with ammonia flow of 100 sccm, which can be explained as follows. During hBN growth, ammonia dissociation provides hydrogen radicals (in addition to nitrogen atoms) which along with H_2 as carrier gas, remove the ethyl groups from TEB precursor. Hence, with a decrease in ammonia flux, it is likely that a higher amount of carbon gets incorporated in the growing film.

Based on these results, it is clear that along with other growth parameters, a careful optimization of ammonia flow rates is also needed for hBN growth. Excessive ammonia flow rates indeed enhanced parasitic reactions. This not only decreased the overall growth rate, but also increased the amount of debris that get deposited on the surface of the growing film. On the other hand, if ammonia flow is less than the optimum, then a higher amount of carbon gets incorporated in hBN.

4.7 Effect of Growth Temperature

The growth temperature is an important parameter in MOVPE and influences many different physio-chemical processes during growth such as precursor dissociation, adatom mobility etc., as discussed in previously. Excessively high temperatures can also result in etching and degradation of both the substrate and deposited material. An initial study by Nakamura predicted process temperatures close to 1500 ºC for deposition of hBN using MOVPE [206]. Previous studies have indicated that high growth temperatures are favourable for hBN deposition and help improve its crystallinity [222, 223]. For hBN deposition using MBE, a process closely related to MOVPE, substrate temperature up to 1800 ºC have also been employed [258, 269]. Due to reactor limitations, the maximum achievable substrate surface temperature during the MOVPE process in this study is 1350 ºC. Though most of the hBN growth was undertaken at 1330 ºC using FME, we also investigated hBN growth at lower temperatures. Figure 4-12 (a-c) shows the surface morphology (measured using AFM) of hBN films deposited at 1150, 1250 and 1330 ºC. All other growth parameters were kept the same across the three samples, with TEB and ammonia flux at 10 μmol/min and 67 mmol/min respectively. Only the sample grown at 1330 ºC appears to have a film-like morphology with wrinkles, indicative of hBN basal planes oriented parallel to c-plane of the substrate. On the other hand, hBN deposited at lower temperatures have a very rough surface, with randomly oriented hBN particles. One possible reason

for the rough surface morphology is that at lower growth temperatures, boron adatoms have low surface mobility. This limits the surface migration of adatoms, thus resulting in random nucleation and growth. Due to rough surface morphologies, the study of hBN films grown at lower temperatures was not pursued any further. Raman spectra of the three sample, as shown in Figure 4-12(d), confirms hBN deposition. The FWHM (obtained by fitting a Lorentzian to experimental curves) decreases from 32 to 29 and 24 cm^{-1}, with increase in growth temperatures for the three samples, indicating improvement in crystallinity.

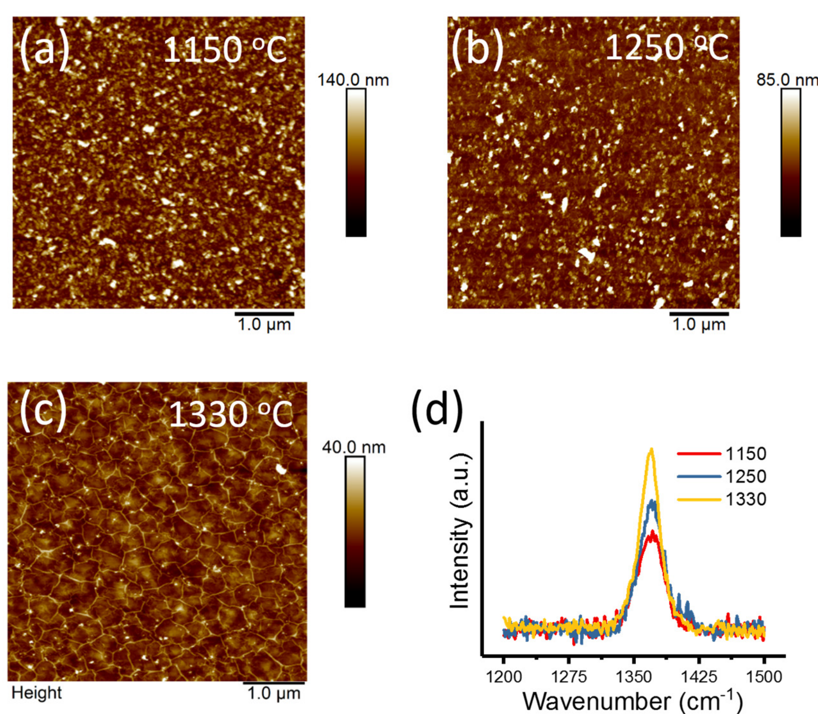

Figure 4-12 (a-c) AFM scans and (d) Raman spectra of hBN films grown at different temperatures.

4.8 Spontaneous delamination of hBN films

Adhesion between hBN films and the underlying sapphire substrate is poor due to the lack of covalent bonding between the two. Consequently, we observed that hBN films (> 15 nm thick), when brought in contact with de-ionized (DI) water (or any other aqueous solution), spontaneously delaminated from sapphire. For this, an hBN coated sapphire wafer was randomly diced into smaller fragments using a diamond tipped scribe and a small piece (~ 10 mm) was dipped into a DI water bath for a few

minutes. While the sample was immersed in the water bath, hBN delamination initiated at the edges and gradually spreads inwards. Within a few minutes the entire layer was delaminated but remained loosely attached to the substrate. At this stage, by carefully bringing the sapphire to the surface of the water bath, the film completely detached from the substrate and floated on the water surface. The hBN layer was then carefully transferred onto a piece of silicon substrate with 90 nm-thick oxide layer for maximum optical contrast [252]. An optical micrograph of the transferred hBN layer is shown in Figure 4-13(a). Some large scale wrinkles (indicated with black arrows) can also be seen in the optical micrograph of transferred hBN. These 'lamination' wrinkles form during the transfer process on account of poor wettability of silicon oxide surface by de-ionized water and are different to growth wrinkles formed during cooling, after growth. hBN films up to few millimetres wide (see Figure 4-13(b)) could be transferred easily without using any polymer support layers like PMMA, PVA etc. that are commonly used in the transfer of CVD grown 2D materials [270-272]. AFM was performed at the edge of the transferred hBN and thickness of the film was measured to be 40 nm, as shown in Figure 4-13(c-d). Raman spectrum from the underlying sapphire substrate, after hBN delamination was obtained, as shown in Figure 4-13(e). The negligible intensity of the E_{2g} band from this substrate, compared to intensity from the as-grown sample (hBN on sapphire) confirms nearly complete hBN delamination during the transfer process. Surface topography of the sapphire substrate post hBN delamination was also measured using AFM, as shown in Figure 4-13(f). A high density of pits can be observed on the surface of sapphire. These pits in the substrate are attributed to hydrogen etching at elevated temperatures [209, 227]. Figure 4-13(g) shows the height profile obtained using AFM line scan along a pit marked with a green line in Figure 4-13(f). Based on these AFM measurements, it is reasonable to assume that the surface roughness of the underlying sapphire substrate, prior to hBN deposition is relatively high. Due to considerably low hBN growth rates (5.0 nm/hr), the sapphire substrate gets unintentionally exposed to large ammonia and hydrogen flow rates at high temperatures, leading to excessive nitridation and etching of the sapphire and results in a rough surface.

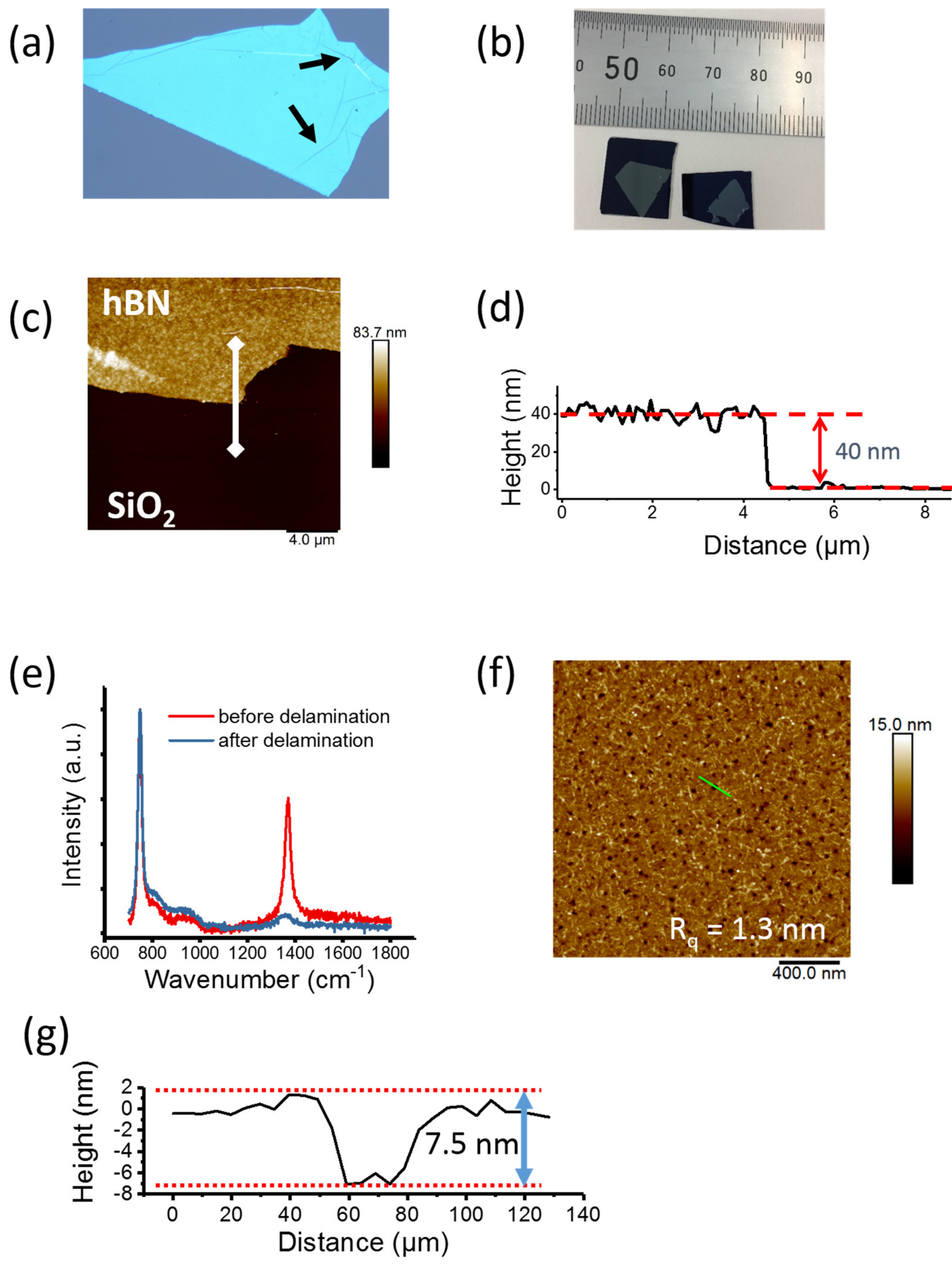

Figure 4-13 (a) Delaminated hBN film, shown in light blue colour, which has been transferred onto a SiO_2 coated silicon wafer. 'Lamination' wrinkles are marked with black arrows, (b) centimetre-sized hBN films (40 nm thick in the image) transferred on to SiO_2/Si substrates, (c) AFM of a transferred hBN near a step edge, (d) AFM line-scan along the white line shown in (c) for determining the thickness of the transferred hBN layer, (e) a comparison of Raman spectra of hBN coated sapphire before and after delamination of hBN films. Note that the E_{2g} band intensity from sapphire post delamination is negligible, (f) AFM of sapphire after hBN film has been removed from it and (g) AFM line-scan showing along the green line in (f) showing the height profile along a pit in the substrate.

The AFM scan of the transferred hBN onto SiO_2 is shown in Figure 4-14(a). Interestingly, wrinkles seen in as-grown hBN films, cannot be observed in the AFM of the transferred films. They seem to have flattened out during the de-lamination process, which is illustrated schematically in Figure 4-14(b). On a related note, even after flattening of wrinkles, the overall surface roughness of the transferred hBN layer is high. This roughness can be attributed to and originates from the roughness of as-grown hBN on sapphire, as discussed above. Furthermore, the flattening of the wrinkles is not surprising, since during delamination the hBN film is no longer physically adhered to the sapphire substrate and is free to attain a minimum energy and strain free morphology. The absence of wrinkles in transferred hBN films would therefore suggest a release of compressive stress post delamination. This is indeed the case and is further corroborated through Raman spectroscopy measurements on delaminated hBN layers, as shown in Figure 4-14(c). Here, both, a red shift in the Raman peak position and reduced FWHM value (22.6 cm^{-1}) compared to the as-grown FM-hBN on sapphire (24.8 cm^{-1}), suggests a relaxation in compressive strain. However, even after delamination, the Raman peak position is still slightly blue shifted

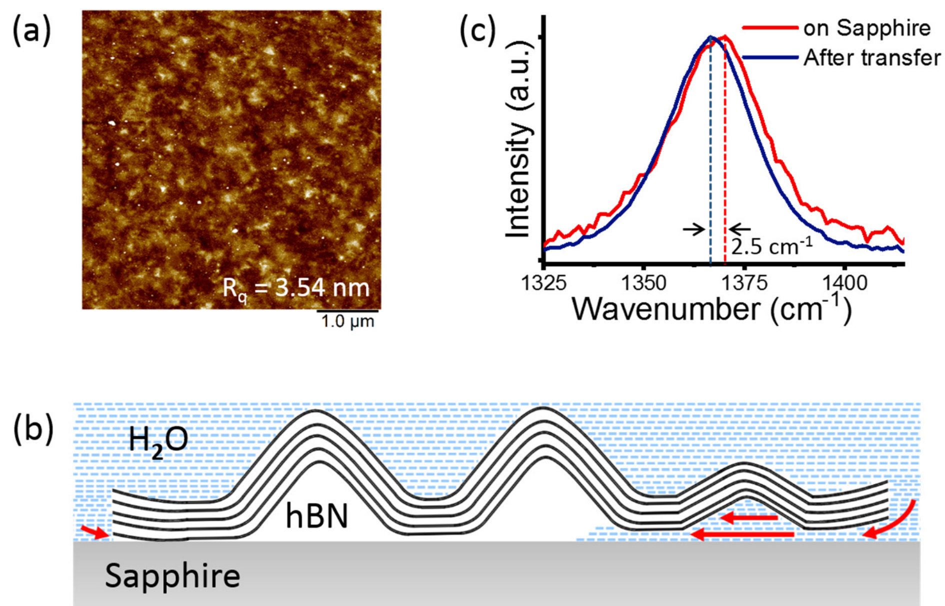

Figure 4-14 (a) Surface topography of the transferred hBN layer (note that the wrinkles are gone), (b) comparison of the Raman spectra between as-grown hBN layer on sapphire and after transfer on to silicon SiO_2/Si substrate and, (c) a schematic diagram illustrating the spontaneous delamination of hBN layer from sapphire substrate upon immersion in water.

compared to completely relaxed bulk hBN (1366 cm^{-1}). Hence, some strain still remains in the transferred hBN film.

A few reasons behind self-delamination of hBN films are also discussed briefly here. The process of self-delamination is likely to be caused by differential wetting between the hBN layer and sapphire substrate. hBN is known to be hydrophobic [183, 273], while sapphire is hydrophilic, which results in preferential wetting of sapphire over hBN. Delamination in low surface tension, organic solvents like ethanol, iso-propyl alcohol and acetone was also observed, but the process was much slower, as such solvents wet both hBN and sapphire equally. The spontaneity of hBN delamination from sapphire also depends on the thickness of the films. Self-delamination of hBN films thinner than 15 nm was not observed even after immersing them in a water bath for several days. Therefore, thinner hBN films (1.5 – 10 nm) were transferred using a PMMA based process detailed in Chapter 6

4.9 Plan view TEM of debris

Taking advantage of the water-assisted spontaneous delamination, we transferred FM-hBN films with debris (encircled in white in Figure 4-8(a-c)) onto a copper TEM grid as shown in Figure 4-15(a). This helped in preparing samples for further evaluation of the structure and orientation of debris using electron microscopy. Plan view TEM images shown in Figure 4-15 (b-f) reveal that the debris have a layered structure similar to hBN, Therefore, these debris are indeed 3D hBN particles, some of which seem to be oriented perpendicular to planar film. Several debris were imaged and it was consistently found that the debris comprised of randomly oriented hBN layers. High resolution imaging helps visualize individual planes in the debris and spacing between them was measured to be 0.325 nm, which is close to d_{0002} for bulk hBN. It is likely that these debris may acts as nuclei for further hBN growth in random directions.

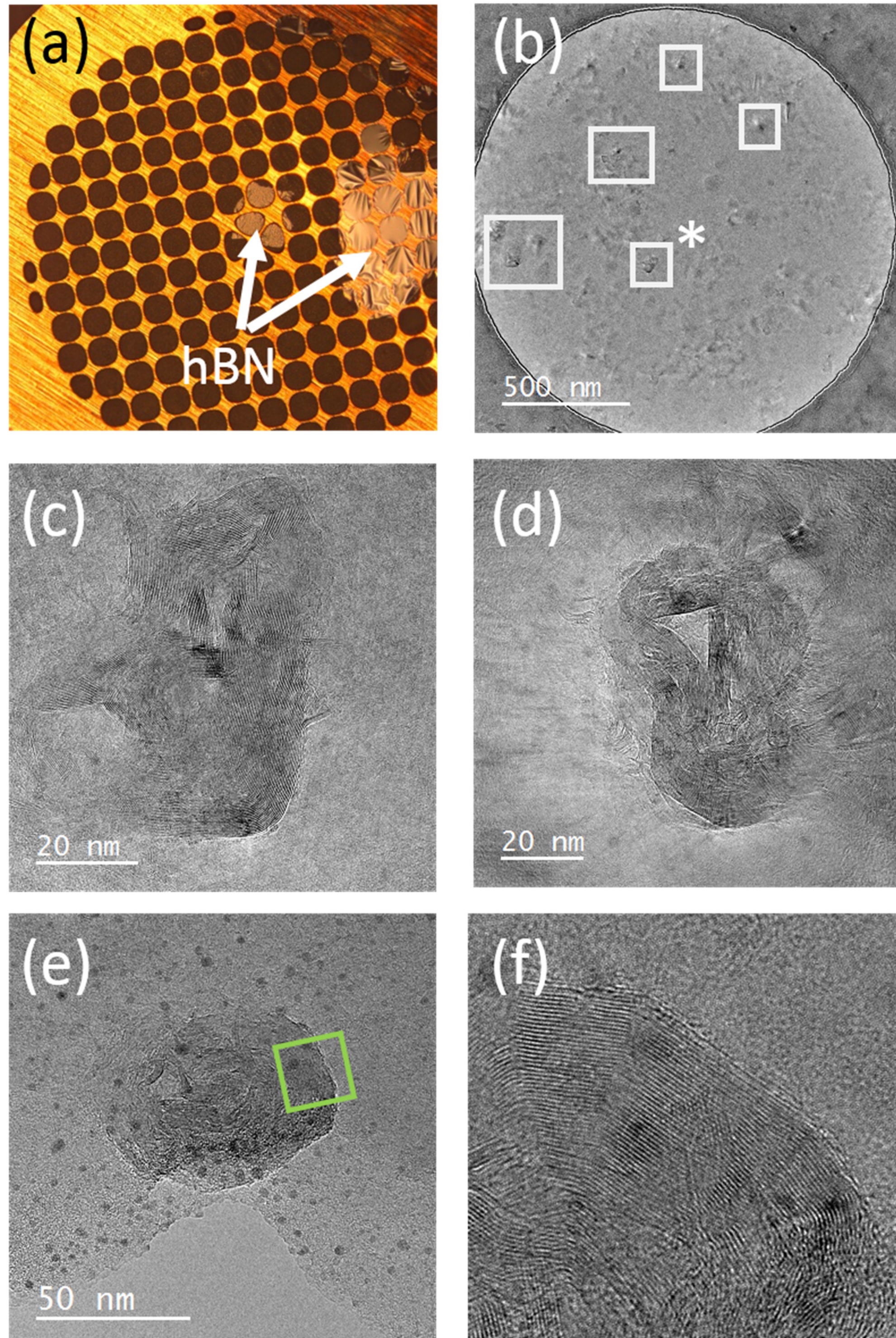

Figure 4-15 (a) MOVPE grown hBN film, indicated by white arrows, transferred onto a copper TEM grid, (b) low-magnification plan view TEM of hBN film. Note: debris are highlighted by the white boxes, (c-e) high magnification plan view TEM of different debris and (f) an enlarged view of the region highlighted by the green box in (e).

4.10 Summary

1. Growth of hexagonal boron nitride films on sapphire substrates using MOVPE under both CFG and FME was studied. Parasitic reactions between ammonia and TEB could significantly be reduced by adopting the FM scheme, which also improved the surface morphology of the hBN films.
2. The surface topography of as-grown hBN films was obtained using AFM. hBN films were wrinkled, which is attributed to thermal compressive strain resulting from a mismatch in CTE between the film and the substrate.
3. High resolution TEM was used to confirm the layer orientation and stacking of hBN basal planes with respect to c-pane of the sapphire substrate. Localized delamination of hBN film was also observed in the wrinkled region of the film.
4. Using XPS, carbon was identified as the dominant impurity in the hBN film. The carbon concentration increased with higher TEB flow and therefore was governed by the overall growth rate of the hBN film. Hence, hBN films deposited at slow growth rates (~2-3 nm/hr) were found to be of the best quality.
5. The water-assisted self-delamination of hBN films was observed on account of poor adhesion between hBN and sapphire. This assisted in polymer-free transfer of hBN layers on to different substrates.
6. Plan view TEM analysis reveal that debris are indeed hBN particles formed due to gas phase reaction between precursors. The debris density was successfully minimized by using FM growth mode and low TEB flux simultaneously. Debris density was also found to be directly dependent on ammonia flow rates.

Chapter 5. Optical properties and single photon emitters in MOVPE-grown hBN

5.1 Introduction

hBN is a highly luminescent material and its optical properties have been the subject of numerous studies in the past. At the same time, experimental findings vary and lack general consensus [118-122]. A prominent challenge has been the difficulty in synthesizing high purity crystals, which is all the more important, given that impurity incorporation in hBN can dramatically alter its optical properties, as established in later studies [37, 148]. Some of these aspects have already been discussed in Chapter 2.

Overall, the emission spectrum of hBN is highly complex on account of strong electron–phonon interactions. Emissions from hBN extends from near band-edge (NBE) at 215 nm to sub-bandgap luminescence from mid-UV (300 nm) to visible wavelengths. Recently, it has been established that hBN has an indirect bandgap of 5.955 eV [132]. In spite of this, its ability to emit light, with luminescent efficiencies (~ IQE of 50 %) comparable to direct bandgap materials makes it an unusual and unique material [131, 157].

In this chapter, optical spectroscopic studies, performed on FM-hBN grown using MOVPE are presented. However, we first review some of the recently reported studies on the luminescence properties of hBN. This will help lay the foundation and provide the necessary framework for the discussion and understanding of the optical properties of FM-hBN, including single photon emissions.

5.2 Photo/Cathodo-luminescence studies on hBN: Literature review

5.2.1 Excitonic/NBE recombination (5.76 and 5.86 eV)

The emission spectra of high-purity bulk hBN is dominated by strong excitonic emission at 5.76 eV [124, 131, 134, 274, 275], which was first reported by Watanabe and co-workers in 2004 [37]. Excitons in hBN were initially described as Wannier-Mott type [37, 276] and later as Frenkel type [277], with large exciton binding energies

of the order of 500-700 meV, estimated using ab initio calculations [278, 279]. In general, dielectric screening of charge carriers in 2D materials is reduced (compared to conventional semiconductor materials with high dielectric constant) due to the layered arrangement of atoms. This results in excitons that are stable at room temperature and govern the optical response of these materials, including that of hBN [20, 21].

However, excitons in hBN are of indirect nature, as demonstrated by Cassabosis et al. and the strong luminescence observed from hBN is indeed due to phonon-assisted recombination of electron-hole (e–h) pairs [129, 132]. Low temperature PL measurements, as shown in Figure 5.1(a) for bulk hBN crystals, reveals the finer details of its NBE emission spectrum. It comprises of 4 distinct peaks at 5.89, 5.86, 5.79 and 5.76 eV, collectively known as the ‘S-series’ [134, 275, 277]. Each of the observed peaks in Figure 5-1(a) is a phonon side band of the primary indirect exciton. The e–h recombination is accompanied by emission of optical and acoustic phonons to fulfil momentum conservation, as summarized in Table 5.1 [132, 133]. Due to more favourable interaction between electrons and the optical phonons (LO/TO), the intensity of S_3 and S_4 lines is higher. Furthermore, at room temperature, due to thermal broadening of emission peaks, a combined $S_{3,4}$ emission line at 5.76 eV (215 nm) is usually observed and considered as representative of free-excitonic emission from hBN.

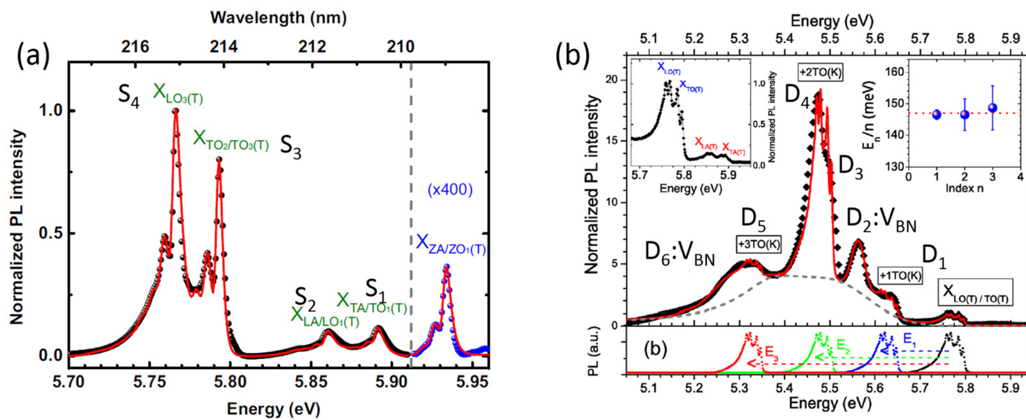

Figure 5-1 (a-b) PL spectra of bulk hBN obtained at 10K, showing the S- and D-series of excitonic emissions, respectively [129, 130].

Still, the strong luminescence observed in hBN (with internal quantum efficiency of 50 %) is inconsistent with the indirect nature of its bandgap. In a recent study, Vuong et al. have shown that this unusual phenomenon in hBN is attributed to strong exciton-phonon coupling [133]. As a result, phonon assisted recombination is much more favorable as compared to other indirect bandgap materials like silicon or diamond. The exciton lifetime in hBN, measured experimentally, is of the order of sub-nanoseconds, which is similar to direct bandgap materials [124, 280, 281]. Consequently, recombination assisted by phonons is fast enough to evade nonradiative relaxation pathways. Furthermore, with the help of CL mapping, it has also been shown that S-series lines are only observable from regions of hBN that are free of lattice/crystal defects such as stacking faults and impurities [124, 134, 282, 283]. Exciton recombination in hBN also shows a dependence on the number of layers [284]. Only recently, in 2019, it was reported that monolayer hBN has a direct bandgap [285]. This cross-over from indirect bandgap for bulk hBN to a direct bandgap for monolayer hBN has also been previously reported in case of other 2D materials [286-289].

Table 5-1 List of NBE emission lines from bulk hBN and associated phonon that take part in e–h recombination [129, 130].

Energy (eV)	Label	Phonon type
5.93		ZA/ZO (z-axis)
5.89	S_1	transverse acoustic (TA)
5.86	S_2	longitudinal acoustic (LA)
5379	S_3	transverse optic (TO)
5.76	S_4	longitudinal optic (LO)
5.62	D_1	$S_{3,4}$ + 1TO
5.56	D_2	V_{BN}
5.47	$D_{3,4}$	$S_{3,4}$ + 2TO
5.32	D_5	$S_{3,4}$ + 3TO
5.27	D_6	V_{BN}

5.2.2 Luminescence from bound/ trapped excitons (5.2 – 5.7 eV)

Luminescence from hBN extends beyond the recombination of free excitons (or the S-series) described above, to lower values between 5.2 – 5.65 eV. Once again, a

set of discrete emission peaks are observed, known as the D-series, as shown in Figure 5.1(b) [130]. The most prominent (in terms of luminescence intensity) amongst which is the D_4 line at 5.46 eV (or 227 nm). Furthermore, initial studies attributed the D-series emission to excitons trapped at stacking faults [124, 134, 275, 277].

As a 2D material, individual layers in hBN are stacked in *AA'* order, as discussed in Chapter 2. Since the layers are held together by weak van der Waals forces, they can glide over each other and the *AA'* lattice ordering can be easily disrupted. This introduces stacking faults in hBN. In a previous study, Watanabe et al. observed that by applying a relatively small mechanical force on high-purity bulk crystals (e.g. by pinching hBN crystals between the tip of the fingers) to deform it, the luminescence spectrum of hBN can be changed significantly [283]. In the deformed crystal, the excitonic luminescence at 215 nm was quenched and replaced by emission at 227 nm. Interestingly, this effect was reversible and with the help of thermal annealing, the excitonic emission at 215 nm could be retrieved.

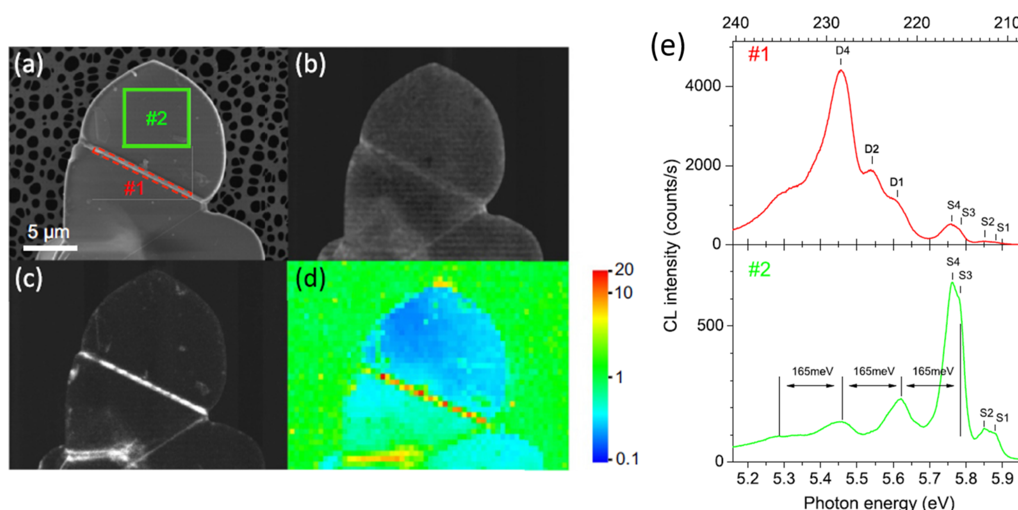

Figure 5-2 (a) SEM image of an hBN crystallite. Region '#1' is a grain boundary and '#2' is defect-free. (b-c) monochromatic CL images of area shown in (a) recorded at 5.76 (S_4) and 5.46 eV (D_4) respectively. (d) Map of D/S intensity ratio. (e) CL spectra of hBN crystallite recorded from region '#1' and '#2' as marked in (a) [134].

In addition to this, with the help of CL mapping studies on different hBN samples types (BNNS or exfoliated flakes), the spatial distribution of D– and S–series emissions was studied [134, 157, 275, 282]. It was observed that the emission

pertaining to free-excitons (S-lines) was homogeneous over the entire sample. On the other hand, emission from D-series was localized to only certain regions on the sample associated with defects, such as grain boundaries or folds, which are visible at sub-micrometer scale, as shown in Figure 5.2. The CL spectra of regions '#1' (a grain boundary) and '#2' (defect-free), as marked in Figure 5.2(a), is dominated by D and S lines, respectively. In another study, Bourrellier et al. obtained hyperspectral maps of BNNS by coupling CL to a STEM. This provides direct visualization and correlation between the distribution of D and S lines to structural defects [290, 291]. Overall, a strong spatial anti-correlation between the S and D emission was observed (i.e. the S-emission is absent where D-lines are present and vice versa), which further indicates that the latter may be attributed to excitons bound at lattice defects in hBN.

As per the latest reports, the D-Series emission is again suggested to be phonon assisted recombination of bound exciton. Two important differences, are to be noted when compared with the S-series. First, unlike the S-series, multiple phonons are involved in the recombination process that gives rise to the D lines [130]. These are summarized in Table 5.1. Secondly, structural defects in hBN generate real electronic states within the bandgap. Hence, in comparison to S-series, where virtual electronic states are involved, the D-lines are associated with real electronic states within the bandgap [130]. These real electronic states are introduced by stacking faults and provide a more efficient carrier relaxation pathway. The presence of stacking faults, thus quenches S series emission, which explains the spatial anti-correlation between D-and S-series luminescence. In fact, the S_4/D_4 intensity ratio may also be used as a measure of material quality.

5.2.3 Defect and impurity related sub-bandgap UV luminescence (3.0 - 4.5 eV)

Sub-bandgap UV luminescence from hBN is composed of two parts: (1) a broad emission band between 3.0 – 4.5 eV and (2) a well-structured band consisting of four equidistant peaks (of varying intensities) at 4.09, 3.91, 3.73 and 3.54 eV ($\Delta E = 175$ meV), which appear to be superimposed on the broad emission [157, 274, 292]. The peak at 4.09 eV is considered as the zero-phonon line (ZPL), whilst the remaining peaks are its phonon side bands (PSBs). Although the exact source of these emissions is not completely known, based on previous studies they are generally attributed to intrinsic and extrinsic defects, such as vacancies and impurities [149].

For instance, with the help of photoluminescence excitation spectroscopy, Museur et al. have shown that the broad emission band appears only when excitation energy is above 5.0 eV and has a multi-exponential decay [292]. When the excitation energy is below 5.0 eV, the spectra comprises of only the four peaks, as described above. Furthermore, by irradiating hBN samples with an electron beam having an energy over 60 keV, the intensity of broad luminescence could be increased, as compared to pristine samples [139]. At such values, electron beam is energetic enough to knock-off atoms from hBN's lattice and create point defects and vacancies. Hence, the broad luminescence is generally believed to be recombination at donor-acceptor sites formed due to atomic vacancies and related defects.

On the other hand, the structured UV emission from hBN (Figure 2.10) is due to presence of impurities, specifically C and O, which may be incorporated during synthesis. Based on bulk crystal growth studies, it has been experimentally shown that NBE luminescence is highly sensitive to impurities. The level of impurity atoms in hBN should be below $10^{18}/cm^3$ (or below 1 ppm, estimated using SIMS) to observe emissions from free-excitons at NBE, or it will be nearly quenched and sub-bandgap UV luminescence dominates, as discussed previously in Chapter 2, [149].

5.2.4 Quantized visible emissions

Defect-luminescence from hBN even extends to the visible range of the EM spectrum. However, in this case, the emissions are non-classical or quantized. Isolated defects in hBN are optically active and behave as single photon emitters (SPEs), which were reported for the first time in 2016 [36, 136]. Since then, research in this material has expanded rapidly, generating new interest in the use of hBN for quantum computing [38, 144, 293, 294]. Figure 5.3 shows PL spectra of a typical SPEs found in hBN. Characteristic features include a ZPL close to 580 nm and phonon side band due to Stokes shift. The emitters can be excited by a 532 nm CW laser and with the help of Hanbury-Brown-Twiss (HBT) interferometry, time-correlated single photon counting (TCSPC) measurements are performed to validate whether the emissions are quantized.

SPEs in hBN have many desirable attributes. They are not only bright and stable at room temperature, but can survive harsh environmental conditions, which is extremely useful for practical applications [136, 145]. So far, SPE have been

successfully observed in different hBN types, such as BNNS, exfoliated flakes from bulk crystals and epitaxially grown thin films [36, 136, 294-297]. Similarly, various processing techniques have been employed to create or stabilize the single photon emissions such as (but not limited to) thermal annealing, chemical etching, plasma etching, ion or electron irradiation etc. [135-138, 298]. However, in spite of numerous studies, the exact nature of defect giving rise to quantum emission is not completely known [38, 299]. This creates a bottle-neck in its application, as there are no deterministic methods for creating emitters in hBN. So far, SPEs are believed to originate from crystalline defects in hBN, configuring a two-state system within its bandgap with a ground and excited state [299].

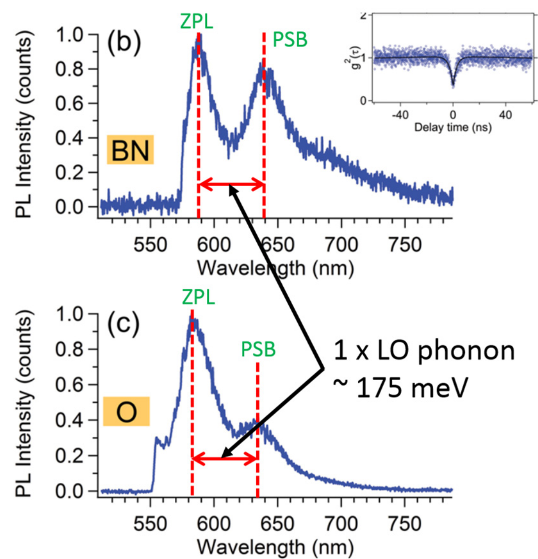

Figure 5-3 Representative PL spectra of quantum emitters in hBN [136].

In summary, understanding the optical properties of hBN has been a work of active research for more than a decade. Several recently published studies have shed light and helped uncover some unusual phenomena in hBN, including the origins of exciton recombination in hBN. Nevertheless, many aspects of its optical properties still remain to be fully understood and continue to remain under active investigation.

5.3 Photo/Cathodoluminescence studies on MOVPE-grown hBN

The luminescence properties of hBN films grown on sapphire using MOVPE were studied using CL and PL spectroscopy. The near band-edge luminescence was measured using CL, while sub-bandgap luminescence was measured using both CL and PL spectroscopies. Due to the insulating nature of the sapphire substrate, as-grown hBN was transferred on to SiO_2/Si substrates to avoid charging by electron beam during CL measurements. This also helps eliminate the relatively strong luminescence around 330 nm from sapphire due to oxygen vacancies [300, 301], which overlaps with the impurity based luminescence from hBN. The CL spectrum from single crystal bulk hBN (Graphene Supermarket, UK) was also measured and used as reference.

Figure 5.4(a) shows the CL spectrum of bulk hBN sample obtained at 77K. At room temperature, CL signal intensity from bulk hBN is much weaker, while at low temperature, luminescence is weak but measurable. Two broad emission bands can be observed: one is close to band edge at 215 nm and another at 340 nm, attributed to impurity related emission. The relatively low intensity ratio of NBE to the impurity related emission suggests that these bulk hBN crystals are not as pure as the hBN reported in [37]. The same is true for similar commercially available hBN samples, where NBE emissions are quite weak [157].

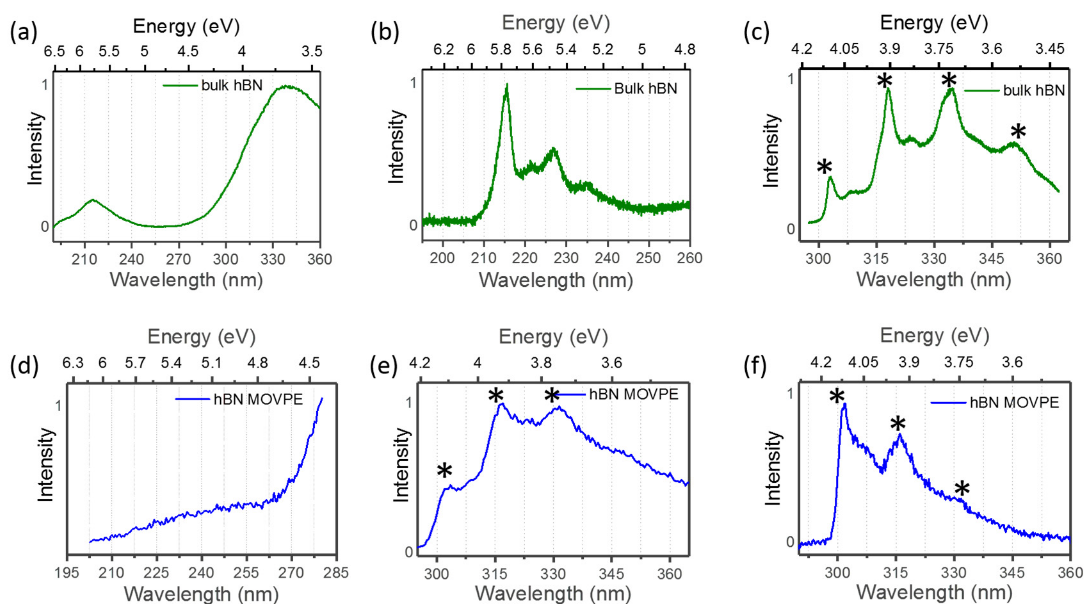

Figure 5-4 CL spectra of (a-c) bulk hBN and (d-e) MOVPE-hBN obtained at 77K. (f) PL spectra of MOVPE-hBN obtained using a 266 nm laser at 10K.

In order to resolve the spectral features, a higher resolution CL spectrum of the two bands were obtained separately. Figure 5.4(b) shows the NBE CL spectrum, where the two peaks at 215 and 227 nm can be identified as the S_4 and D_4 lines pertaining to excitonic emission from hBN, as described in sections 5.2.1 and 5.2.2. The impurity related spectrum of hBN is shown in Figure 5.4(c). It is comprised of a structured emission band composed of one ZPL and three PSBs peaks. The four peaks are marked with '*' and appear to be superposed on top of a broad band, as described in section 5.2.3. Overall, these measurements are consistent with previously reported impurity related emission from hBN [149, 274, 292].

Given that excitonic emission from hBN is highly sensitive to impurities, only MOVPE-grown hBN samples, having the minimum amount of carbon were chosen for CL measurements. Based on XPS studies presented in Chapter 4, carbon doping in hBN films grown using a TEB flux of 10 μmol/min was found to be the lowest achievable in this study. Its CL spectrum, obtained at 77K, is shown in Figure 5.4(d). No measurable excitonic luminescence could be observed from the sample. This is not surprising because the carbon content in MOVPE-hBN is still much higher than that in bulk hBN used as a reference sample. Furthermore, the PL intensity increases sharply for wavelengths above 270 nm. This is due to impurity related UV luminescence from hBN, shown separately in Figure 5.4(e). Here, the spectrum consists of three individual peaks at 302, 317 and 332 nm. The first peak is the ZPL, while the remaining two are PSBs. A fourth PSB, seen in the case of bulk hBN, is not observed for MOVPE-hBN, perhaps due to lower intensity. Furthermore, the 3 distinct peaks shown in Figure 5-4(e), appear to be superposed on top of a broad band. Overall, the impurity related CL spectrum from MOVPE-hBN is similar to that obtained for bulk hBN.

UV luminescence from impurities in MOVPE-hBN was also recorded using PL spectroscopy. A 266nm Q-switch pulsed laser (Quantel) was used as the excitation source, while the emission was measured using a photomultiplier tube coupled to a spectrometer. A liquid helium cryostat was used to cool down the sample to 9 K to reduce thermal broadening of the emission peaks. The low temperature PL spectrum is shown in Figure 5.4(f). Once again, a set of three peaks of varying intensities can be identified, which have been marked by '*'. On comparison with the CL spectrum of the same sample shown in Figure 5-4(e), it appears that the broad band is absent from

the PL spectrum obtained using the 266 nm laser. The appearance of this broad band is conditional and is visible only when the sample is excited with energy higher than 5 eV [292]. Therefore, due to lower energy of the UV photons, compared to energy of electrons incident on the sample during CL, the broad band is absent for the PL spectrum of MOVPE-hBN.

The absence of any observable excitonic emission from MOVPE-hBN can be attributed to the use of the metal-organic TEB as boron source, which results in unintentional carbon doping in the hBN films. Even for samples, where the carbon impurity was the lowest achievable, excitonic emission could not be measured and only sub-bandgap UV luminescence was observed. Excitonic emissions from epitaxially grown hBN on sapphire have been reported in the past. However, in these studies, hBN growth temperatures were as high as 1500 ºC or even higher. For example, Chubarov et al. have shown that growth at such temperatures (~ 1500 °C) helps in improving crystallinity and reducing the concentration of impurity atoms (carbon and oxygen) in hBN (also grown on sapphire using TEB), which has a direct impact on its PL properties [222, 250]. NBE emissions have also been reported for hBN grown using molecular beam epitaxy (MBE), wherein growth temperatures were close to 1700 ºC [269]. Reports on hBN growth at such high temperatures are rare as it cannot be achieved in most commercial MOVPE reactors (or MBE and CVD systems) without making expensive and customized modifications. Likewise, in the present study, hBN growth temperatures higher than 1330 ºC were not obtainable due to the engineering limitation of the MOVPE system.

5.4 Effect of TEB flux on sub-bandgap luminescence in MOVPE grown hBN films

Based on the studies detailed in Chapter 4, a direct relationship between TEB flux, growth rate and amount of carbon incorporated in hBN was established. It was also observed that hBN films grown using a larger TEB flux also have a yellowish appearance, indicating significant changes to their optical properties. Hence, the effect of TEB flux on the luminescence properties of hBN films was investigated further. For this, 40 nm thick hBN films grown using TEB flux of 10, 20 and 30 μmol/min were transferred on to SiO_2/Si substrates, using water-assisted self-delamination procedures

described in Chapter 4. CL spectroscopy failed to detect any measureable NBE emission from these samples. Therefore, the following study focuses on the sub-bandgap luminescence from hBN using different excitation energies.

First, the impurity related UV luminescence for the three samples was measured using a 266 nm pulsed laser, as described above. All measurements were made at room temperature. PL spectra of the three samples are shown in Figure 5.5(a). The overall shape of each individual spectrum is asymmetric, which extends from 290 – 370 nm. Upon close observation, three individual peaks can be identified at 302, 317 and 332 nm, which have been labelled in Figure 5.5(a). Together, these peaks represent the well-known impurity-related structured UV emission from hBN. At room temperature, the PL spectrum of MOVPE-hBN appears as a broad asymmetric band. However, PL and CL measurements at cryogenic temperatures for the hBN grown using 10 μmol/min have already been discussed (Figure 5.4(f)), wherein the ZPL and PSBs are well-separated and clearly distinguishable. Note that in Figure 5.5(a), the asymmetric shape of the spectrum can be explained by variation in the relative intensities of ZPL and PSB. In the present context, the intensity of PSB is higher than that of the ZPL.

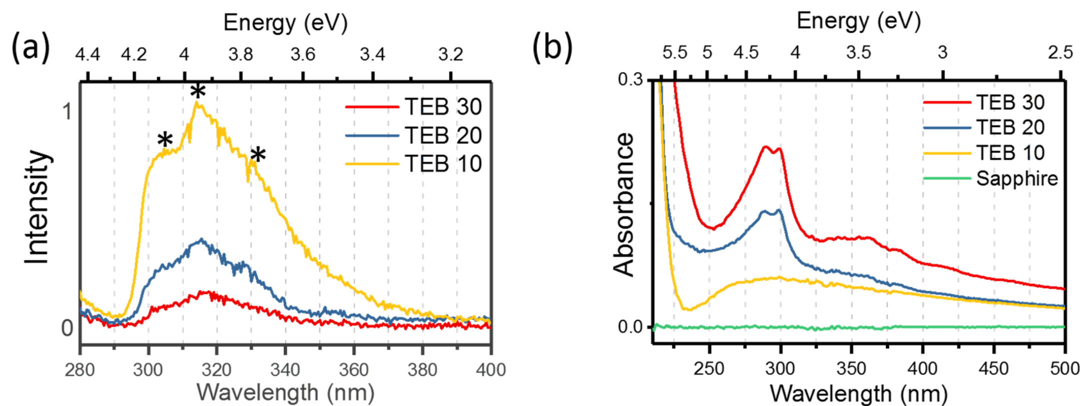

Figure 5-5 (a) Room temperature PL spectra and (b) UV-vis absorbance spectra of MOVPE hBN grown using different TEB flux. The '*' indicates the peaks at 302, 317 and 332 nm which representative of the structured UV emissions from hBN.

More importantly and contrary to expectation, the UV PL intensity from hBN samples decreases with an increase in TEB flux. In other words, while hBN film with a higher carbon content was expected to give stronger impurity related UV luminescence, in

the present case, experimental results show the opposite trend. The PL measurements were repeated several times and the results were consistently the same.

Furthermore, the absorption properties of as-grown hBN films on sapphire substrates were also measured by UV-vis absorbance spectroscopy. The absorption spectra of the hBN samples are shown in Figure 5.5(b). A bare sapphire substrate was used as a blank in these measurements. For all three hBN samples, a sharp increase in absorbance for wavelengths below 225 nm is observed. This is attributed to absorption near the band edge and consistent with the large bandgap of hBN. In addition to this, a strong absorbance peak at around 300 nm can also be observed for all samples. This is associated with same impurity related states within the bandgap that also give rise to UV emissions, as discussed above. In this instance, the absorbance increases with TEB flux and is consistent with increasing levels of carbon impurity in the films. Thus, based on the PL (with a 266 nm laser) and UV-vis absorption spectroscopy, we can infer that although hBN films grown with higher TEB flux are able to absorb more UV light (due to a higher carbon incorporation), there is a concurrent decrease in impurity related UV emissions. The underlying reasons for the observed decrease in UV luminescence are not known yet. It is possible that carbon doping in hBN may result in additional deep-level, defect states that offer alternate carrier relaxation pathways, thus quenching the UV luminescence. To investigate this further, additional PL measurements were performed and discussed as follows.

The emission properties of MOVPE grown hBN were measured using a 532 nm CW laser. Figure 5.6(a) shows the PL spectra of hBN samples grown using different TEB flux. Samples grown using TEB flux of 20 and 30 μmol/min show strong luminescence, extending from 550 to 750 nm, with a peak at 590 nm. A large part of the spectrum overlaps with red to near-infrared wavelengths. Hence, for convenience only, it will be referred as red PL (or rPL) from hBN. On the other hand, the PL intensity from hBN grown using 10 μmol/min of TEB is weak and nearly the same as that from a bare substrate, included as reference, in Figure 5.6(a). Thus, a direct dependence of rPL intensity on TEB flux and carbon incorporation is evident. Furthermore, the shape of the individual spectrum suggests that it is comprised of multiple peaks. Low temperature PL spectrum of hBN sample grown using TEB flux of 20 μmol/min was also obtained, as show in Figure 5.6(b). Due to reduction in PL peak width, the multiple peaks become more discernible. The experimentally obtained

PL spectrum could be easily fitted using three Gaussian functions centred at 2.10, 1.97 and 1.84 eV with an average spacing of 0.13 eV.

It is worth mentioning here that based on available literature on PL studies of different hBN samples (available commercially or otherwise), rPL has not been observed/reported so far (to the best of our knowledge). The rPL from hBN has characteristics which are similar to yellow/defect luminescence from GaN and ZnO. Both do not show any appreciable change in either intensity or spectral broadness, when cooled to cryogenic temperatures. In GaN, the origins of yellow luminescence are not exactly known but generally attributed to defects and impurities [302]. At this stage, one can only speculate on the role of carbon, in creating additional multiple states within the bandgap, giving rise to the observed luminescence. This may or may not be related to quenching of impurity related UV luminescence in same samples, observed under excitation by the 266 nm laser, as seen in Figure 5.5(a). Interestingly, a majority of single photon emitters found in hBN, especially those grown using MBE, CVD or MOVPE (as observed in the present study) have peak emission wavelengths (or the ZPL) between 580-600 nm [296]. The spectrum of an SPE also has one or even

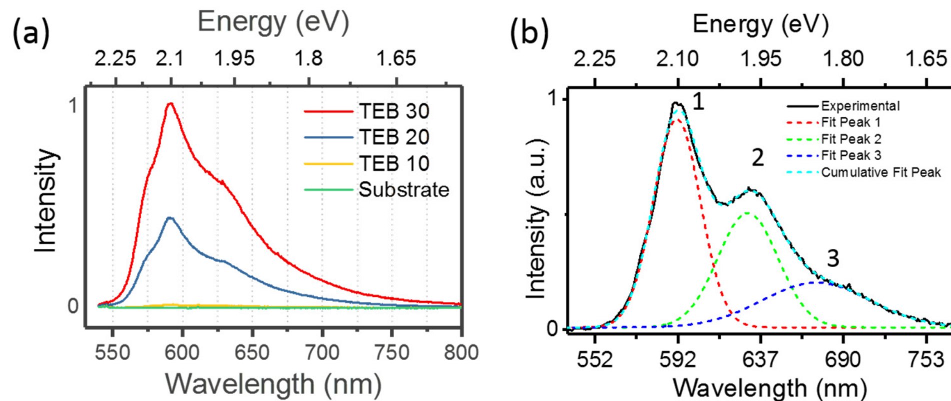

Figure 5-6 (a) Room temperature PL spectra of MOVPE hBN grown using different TEB flux. A 532 nm laser was used for excitation. (b) PL spectrum of hBN grown using 20 µmol/min of TEB flux, obtained at 10K. The spectrum if fitted using 3 Gaussian functions.

two PSB(s) at longer wavelength, thus extending the overall luminescence to NIR wavelengths, as shown in Figure 5.3. It is noteworthy that the shape of PL spectrum of these single emitters bears a close resemblance to rPL from MOVPE-grown hBN

(with TEB = 20 and 30 μmol/min), obtained using 532 nm laser. At present, it is not known whether there is any commonality between defects responsible for single photon emissions in hBN and that giving rise to rPL in MOVPE-hBN. The width and shape of rPL band can be due to emissions from an ensemble of defects. Other than this, B_xC_yN form a wide range of fluorescent compounds, with luminescence spanning from near UV to NIR wavelengths based on material composition [303-306]. Formation of B_xC_yN clusters during MOVPE growth is also possible, which may be responsible for observed luminescence. The origins of rPL from hBN need further investigation.

5.5 Single photon emitters in MOVPE-grown hBN films

So far, single photon emitters have been found in different types of hBN samples, such as BNNS, exfoliated flakes from bulk crystals and CVD grown hBN films on transition metal substrates. Quantum emitters (QE) in MOVPE grown hBN have not been reported thus far. In the previous section, rPL from MOVPE-grown hBN (TEB 20 and 30 μmol/min) was discussed. Three distinct attributes of rPL from these two samples came to light. These are (1) it is relatively strong, (2) is homogeneous and ubiquitous over the entire sample and (3) closely matches the spectrum of a typical SPE in hBN. However, these two samples are not appropriate for investigating the presence of SPE in MOVPE-hBN for two reasons. First, the high background fluorescence will either partly or completely swamp any luminescence from a single emitter, if at all present. Secondly, due to a high background fluorescence, the necessary condition of anti-bunching (i.e. $g^2_{(\tau=0)} < 0.5$) will never be satisfied. On the other hand, hBN grown using TEB flux of 10 μmol/min does not show any noticeable rPL, which makes it ideal for investigating SPEs, described below.

A 40 nm-thick MOVPE-hBN, grown using 10 μmol/min of TEB was transferred on to SiO_2/Si substrates. These films self-delaminated in a DI water bath, as described in section 4.8. Hence, the transfer of hBN films was achieved without using any photo-resist or chemicals, which is advantageous, as these chemicals are sources of contamination and auto-fluorescence [64]. An optical image of a transferred samples is shown in Figure 5.7(a). The samples were not annealed, as reported previously in some studies [40].

PL measurements were carried out at room temperature using a scanning confocal microscope with a 532 nm laser (CW). The laser beam was focused on the sample through a high numerical aperture objective lens (100X, NA 0.9) and raster scanned using a X-Y piezo mirror. PL from the sample was collected using the same objective and directed to a CCD coupled to a spectrometer. Alternatively, for single photon emissions, the PL was directed on to two fiber coupled avalanche photodiodes (APDs, Excelitas Technologies). The electronic output from APDs was analyzed by a TCSPC module (PicoHarp 300, PicoQuant) for anti-bunching measurements. A schematic of the HBT experimental setup is shown in Figure 5.8(a).

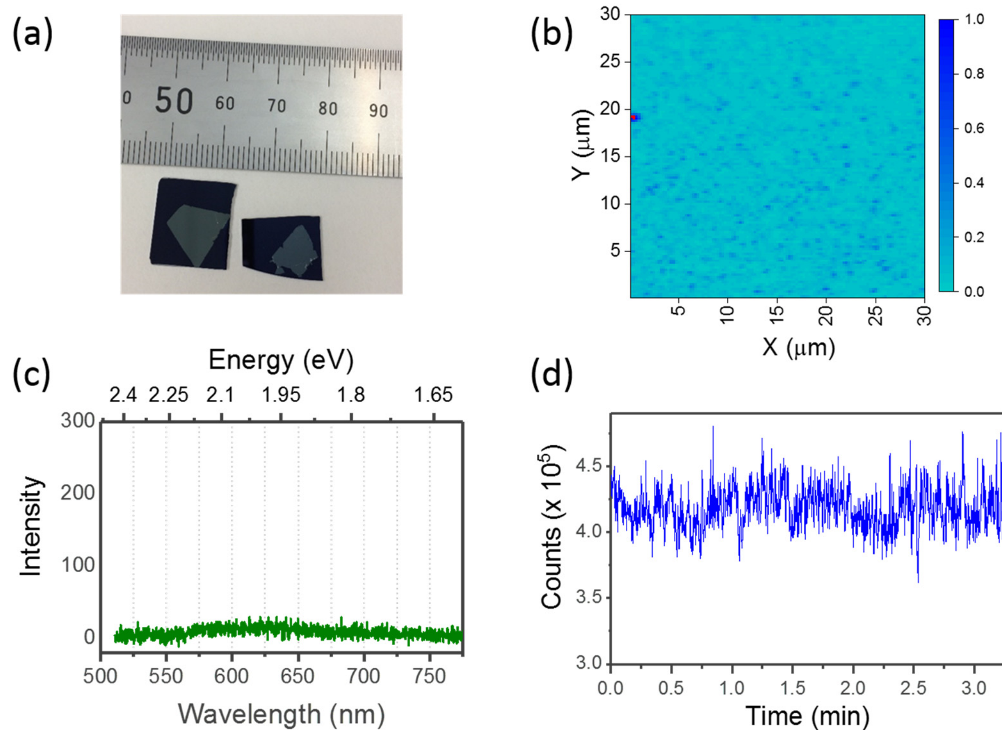

Figure 5-7 (a) An optical image of a 40 nm thick hBN transferred onto a SiO_2/Si substrate, (b) PL intensity map for a 30×30 μm hBN area on sample shown in (a), (c) representative PL spectrum obtained at an arbitrary point which is not an emitter and (d) single photon count rate as a function of time, showing photo-stability of an SPE.

Figure 5.7(b) shows a PL intensity map (false colour) obtained through confocal mapping of an arbitrarily chosen 30×30 μm area on the 40 nm thick hBN sample. A step size of 0.25 μm was used during mapping and PL spectrum was recorded at each point. The PL at any arbitrarily chosen point consists of a featureless spectrum and

representative of background luminescence, as shown in Figure 5.7(c). At some randomly interspersed points, luminescence with a well-defined spectrum is observed. A total of 26 such points were obtained within the scanned area. Representative PL spectra of 4 such luminescent points are shown in Figure 5.9(a-d). The spectral characteristics includes a sharp peak at 590 nm (± 10 nm) and a secondary peak, red-shifted by 0.17 eV that is LO phonon energy of hBN [251]. Hence the primary and secondary peaks are ZPL and PSB of the emitter, respectively. In some instances, the intensity of the PSB is stronger than ZPL, as shown in Figure 5.9(c).

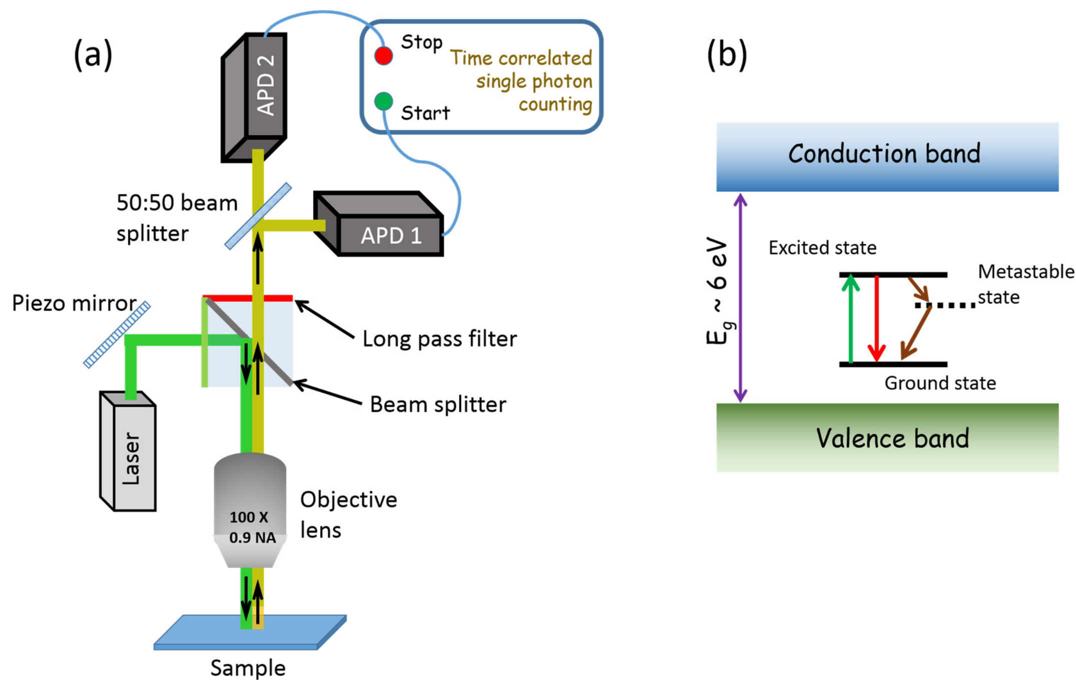

Figure 5-8 (a) Schematic representation of scanning confocal PL setup used for photon anti-bunching measurements and (b) schematic representation of a three-level system for modelling SPE in hBN.

The non-classical nature of these emissions was determined by recording the second order auto-correlation function, $g^2(t)$. The $g^2(t)$ graphs are shown alongside the spectral graphs for the 4 emitters in Figure 5.9. The dip at zero time delay (t = 0) is below 0.5 for all 4 emitters, which is necessary condition for the emitter to be considered as an SPE. Of the 26 emitters, only 7 were SPE. For remaining emitters, the dip at zero time delay for the g^2 function was found to be above 0.5 and thus, they were not classified as SPEs. The emission at these points displayed bunching characteristics and were referred as ensembles [296]. Possible reasons for bunching

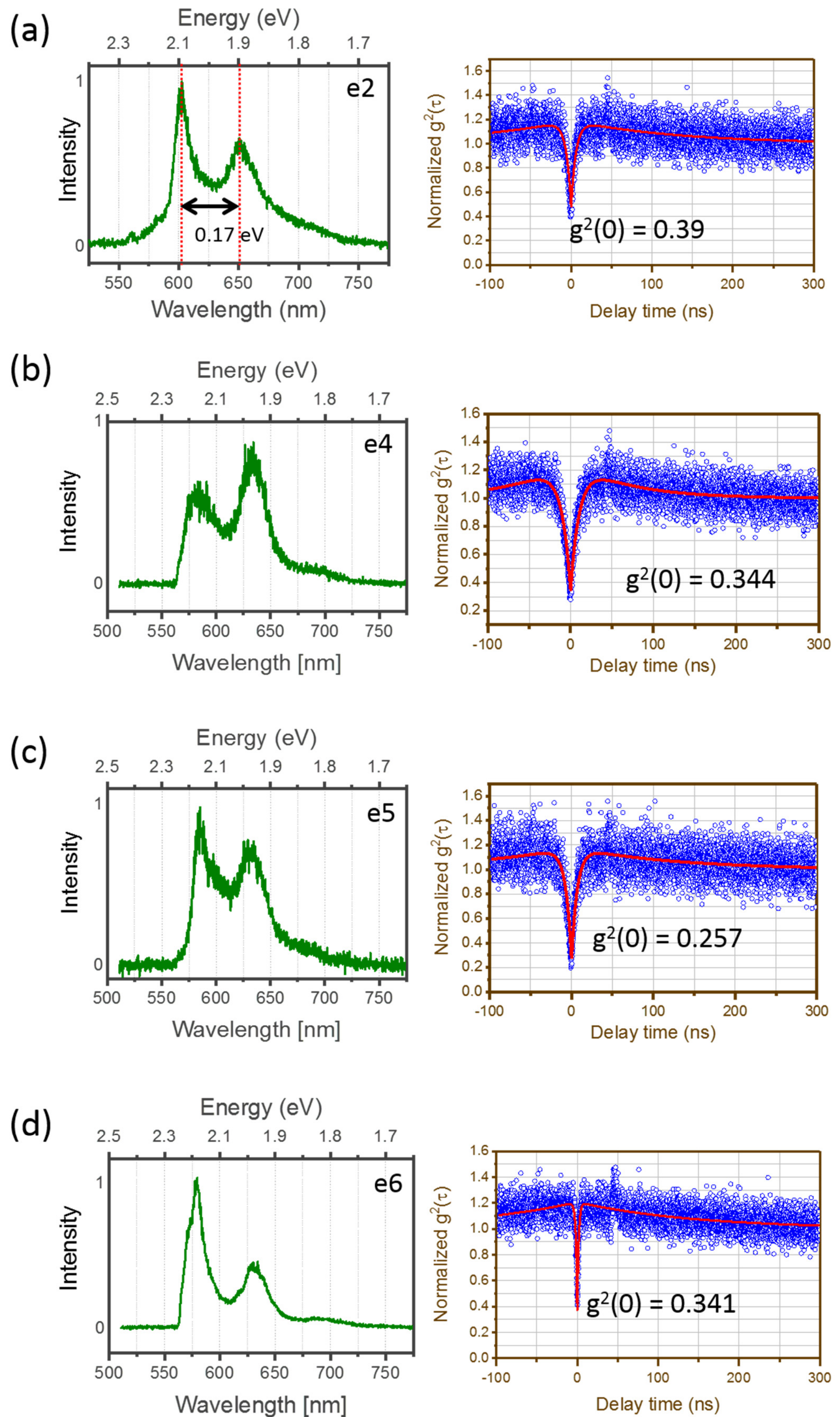

Figure 5-9 (a-d) Representative PL spectra and corresponding $g^2(t)$ curves of 4 quantum emitters in MOVPE-hBN.

behavior could be higher background fluorescence from the hBN or simultaneous excitation of multiple emitters (as ensembles) due to close spatial proximity. Furthermore, in previous studies, quantum emitters in hBN have been described using a three-level system consisting of a ground, excited and a metastable state, as illustrated schematically in Figure 5-8(b) [36, 136, 293]. Using the same approach, the experimentally obtained $g^2(t)$ curves were fitted using the equation 5.1 given below,

$$g^{(2)}(t) = 1 - Ae^{-\left|\frac{t}{\tau_1}\right|} + Be^{-\left|\frac{t}{\tau_2}\right|} \quad (5.1)$$

where, τ_1 and τ_2 are the life times of the excited and metastable states, while A and B are antibunching and bunching coefficients, respectively. The fitting parameters A, B, τ_1 and τ_2 for a total of 7 emitters (including 4 shown in Figure 5.9) have been summarized in Table 5.2 . Emitter lifetimes, τ_1, were in the range of a few nanoseconds and found to be in good agreement with previously reported values [138, 293]. The g^2 at zero time delay was computed using the fitting parameters and equation 5.1. These have been indicated on each of the curves shown in Figure 5.9. Photo-stability of the SPE in hBN was checked in the time range of a few minutes. Figure 5.7(d) shows the photon count rate as a function of time, which suggests that the emitter is stable. Some emitters also displayed photo-bleaching, where their photon count rates completely dropped to zero/background after a few seconds of illumination. These are excluded from the set of 26 emitters described above.

Table 5-2 List of fitting parameters pertaining to equation 5.1, obtained for the 7 emitters found in MOVPE-hBN.

Emitter No.	A	B	τ_1 (ns)	τ_2 (ns)
e1	0.787 (±0.018)	0.18 (0.003)	2.2 (0.077)	120.7 (3.37)
e2	0.806 (0.028)	0.202 (0.003)	2.038 (0.102)	178.8 (5.41)
e3	0.72 (0.014)	0.193 (0.005)	5.94 (0.204)	131.62 (4.722)
e4	0.931 (0.015)	0.275 (0.014)	10.685 (0.304)	67.1 (3.12)
e5	0.925 (0.016)	0.182 (0.006)	6.98 (0.21)	125.51 (5.82)
e6	0.867 (0.025)	0.208 (0.003)	1.634 (0.066)	143.86 (3.37)
e7	0.859 (0.016)	0.274 (0.003)	2.62 (0.074)	113.10 (1.93)

One of the highly desirable characteristics of an ideal single photon source is precise control over its emission wavelength. For all of the 26 emitters identified (including ensembles), the ZPL wavelength was found to be between 575-595 nm, which is consistent with CVD grown hBN. Some variation in ZPL may be caused by compressive strain in hBN film grown by MOVPE/CVD methods [208, 307]. On the other hand, spectral distribution of ZPL in commercially available hBN (bulk and BNNS) is much larger and spans from 500 to 850 nm [136]. A narrow distribution and control over ZPL wavelengths suggest that defects responsible for SPEs can be engineered with a greater degree of control in epitaxially grown hBN (including MOVPE), than in bulk crystals or BNNS. This provides the former with a much required attribute, especially for technological applications.

5.6 Summary

The optical properties of MOVPE grown hBN have been presented. Due to carbon incorporation, excitonic emission from the grown samples could not be observed. Instead, samples give rise to strong impurity related luminescence that show a significant dependence on TEB flux. PL at visible wavelengths was also observed from the MOVPE-grown hBN, which has not been reported previously. The rPL intensity shows a clear dependence on TEB flux. It points towards the role of carbon incorporation in creating additional multiple states within the bandgap, which may give rise to the observed luminescence. Single photon emissions were studied and reported for the first time in MOVPE-grown hBN films. QE were only studied in hBN grown with TEB flux of 10 sccm (the minimum achievable value), as it showed negligible rPL, unlike samples grown with higher TEB. It was found that hBN samples host a high density of stable QEs, with narrow spectral distribution of emission lines. Although several aspects of QE in hBN remain to be investigated, this preliminary study can help to uncover new applications of MOVPE-hBN.

Chapter 6. MOVPE-grown hBN for SERS applications

6.1 Introduction

hBN is a wide bandgap semiconductor which has high thermal and chemical stability. A single atomic layer of hBN is able to withstand temperatures as high as 850 °C in a reactive atmosphere, unlike many other 2D materials, including graphene [34, 71, 308]. The thermal stability of bulk hBN and BNNS is even higher, as discussed in Chapter 2. In this chapter, the application of atomically thin layers of hBN for passivating gold and silver nanoparticles (NPs) was investigated and its potential use is demonstrated through surface enhanced Raman spectroscopy (SERS). Silver NPs readily oxidize in air, resulting in a significant decrease in its SERS activity. To prevent this, wafer-scale hBN is grown using MOVPE and centimeter-sized hBN layers are transferred on to silver NPs. hBN acts as an impermeable barrier and protects silver NPs from oxidation, even at elevated temperatures, which helps retain its SERS activity. Thermal stability of hBN coated Ag NPs is studied in detail. The chapter is organized as follows: first a brief introduction of SERS is presented. This is followed by sample preparation methods, employed for transferring hBN layers on to silver and gold NPs. Finally, experimental results and comparison of SERS activity of hBN covered and bare nanoparticles is presented along with some useful discussions. The experimental results presented in this chapter have also been reported in [117].

6.2 Surface enhanced Raman spectroscopy: a brief overview

A brief introduction to Raman spectroscopy has already been presented in Chapter 3. Compared to Rayleigh scattering, Raman signals are typically much weaker, which limits its application outside of laboratory environments. However, with the use of nanostructured metallic surfaces, Raman signals can be amplified by several orders of magnitude, which led to the emergence of SERS [309]. In SERS, metallic nanoparticles, through plasmonic effects cause enhancement of the local electromagnetic (EM) fields, (between gaps of neighbouring metallic surfaces) also

known as ‘hot-spots’, which consequently amplifies the Raman signals [310, 311]. Hence, over the years, SERS has emerged as a powerful and ultra-sensitive diagnostic technique even capable of single molecule detection [312, 313].

Gold and silver are the two most commonly used metals for SERS applications, in terms of ease of fabrication and enhancement effect obtained with commercially available visible laser sources. Between the two, silver gives a higher enhancement effect due to lower interband losses [314]. However, Ag easily oxidizes in air resulting in the loss of SERS activity [315-319]. Despite large enhancement factors, a number of issues arise with use of metal nanoparticles for SERS. These include, charge transfer between metal and adsorbed molecules, metal catalysed reactions, adsorption induced vibrations that are non-characteristic of the molecule, photocarbonization and adsorption of carbonaceous species, which lead to non-reproducible and undesired peaks [320]. Li et al demonstrated that these challenges could be overcome by encapsulating the metal nanoparticles with a thin layer of silica or alumina shell and

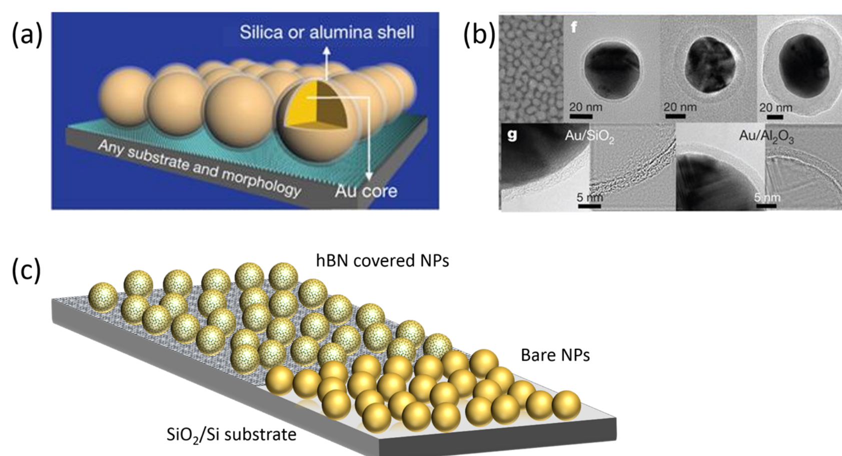

Figure 6-1 (a) Schematic illustration of a SHINERS substrate with Au NPs covered with a silica shell, (b) TEM image of SHINERS substrate reproduced from [321]. (c) Schematic illustration of hBN covered nanoparticles used in this study.

thus prevent any direct contact between metal and molecule (also known as SHINERS – Shell isolated nanoparticle enhanced Raman spectroscopy) [321], illustrated schematically in Figure 6-1(a). While passivation of metallic nanoparticles results in cleaner and reliable Raman signals, a certain minimum thickness (> 5 nm) of shell is often needed to form pinhole-free coating. As the EM field intensity (‘hot spots’)

decrease exponentially with the distance from nanoparticle surface, passivation with dielectric materials comes at a cost of reduced enhancement.

As discussed in Chapter 2, atomically thin layers of two-dimensional (2D) materials, such as graphene and hexagonal boron nitride (hBN) have been used for passivating metallic nanoparticles for SERS applications [35, 114, 115, 322, 323]. Mono- to few layers of graphene and hBN were shown to be highly effective in wrapping around metal nanoparticles and thereby preserving EM 'hot spots'. Unlike graphene, which oxidizes in air at temperatures above 250 ºC, atomically thin hBN (nano) sheets have been shown to be stable at high temperatures, even in oxidative environments [70]. Recent studies have shown that hBN coatings can protect metals (copper, steel, nickel) not only against oxidation at high temperatures, but also against chemical corrosion and biofouling [33, 34, 70, 111, 324]. In contrast to hBN, graphene can in fact accelerate metal oxidation through galvanic corrosion [325, 326]. Furthermore, in the context of SERS, the semi-metallic nature of graphene can dissipate EM fields, resulting in reduced sensitivity and enhancement. In comparison, hBN is a wide bandgap semiconductor, electrically insulating and thus more effective in retaining EM hot spots. Hence, because of the above attributes, hBN is overall, better suited than graphene for passivation of metal nanoparticles and SERS applications. As a relatively new semiconductor material, hBN has gained importance only in recent years and in the context of SERS, only few studies have explored hBN for passivating silver and gold nanoparticles. For this, hBN is primarily obtained through mechanically exfoliating thin layers from bulk crystals, often restricted to small sizes (few hundred µm or less), which is well suited for demonstrating proof-of-concept and not scalable nor practical in real applications. A couple of studies have also used CVD grown layers [115, 322].

In this study, MOVPE grown large area hBN is utilized for passivating silver and gold nanoparticles and its application for SERS is assessed. A schematic of hBN covered SERS substrate is shown in Figure 6-1(b). Ag NPs, which yield the highest sensitivity for SERS, are prone to rapid oxidation in ambient and hence not preferred over gold NPs. It is demonstrated in this chapter that oxidation of Ag NPs can be prevented by hBN coating, and its SERS activity can be retained even after annealing at 400 ºC in air. Long term stability of Ag NPs, through extended annealing in air is also explored. In section 6.5, the application of large area hBN is showcased through

a droplet-based SERS platform, wherein Ag NPs are patterned into an array of circular spots and protected with a single continuous sheet of hBN. The SERS platforms will be ideal for droplet based analysis as detailed in the following sections.

6.3 Fabrication of hBN-SERS substrates

In Chapter 4 (section 4.8), water assisted self-delamination of hBN layers from sapphire substrates is described. Using this technique, as-grown hBN films, with thickness greater than 20 nm could be readily transferred on to desired substrates. However, for SERS application, thin hBN layers are required that do not self-

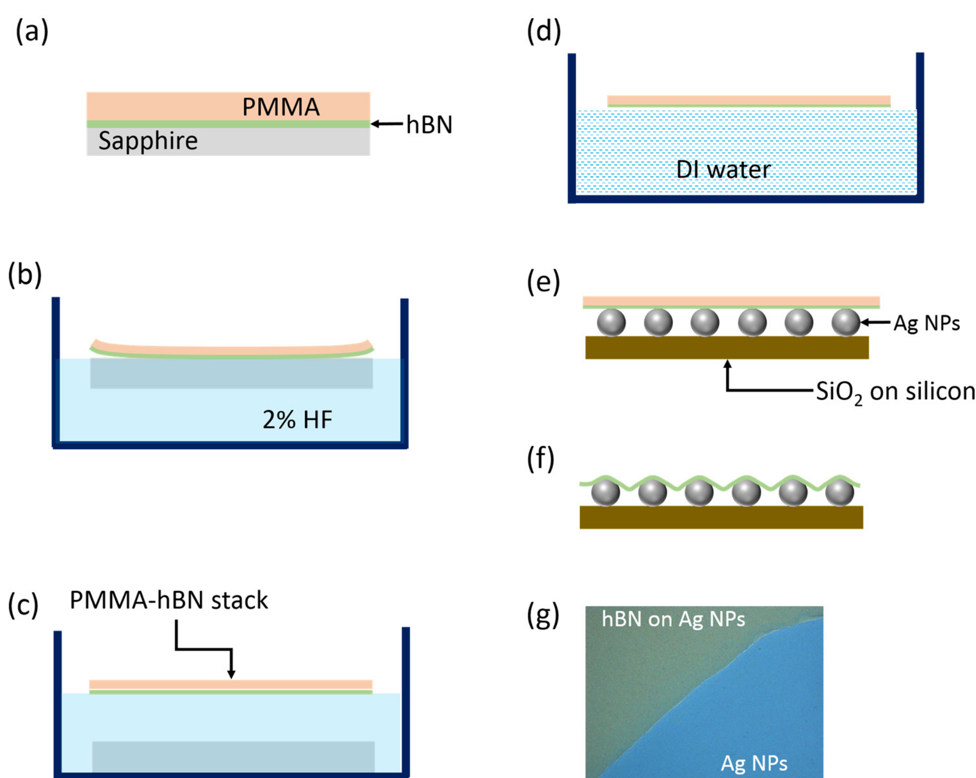

Figure 6-2 (a-f) Schematic illustration of hBN transfer process using chemical etching method and (g) optical microscope image of hBN-AgSERS substrate, showing hBN covered and uncovered regions, as indicated on the image.

delaminate in a water bath. Transfer of thin hBN films was achieved using a chemical etching process, adapted from the methods developed for transferring CVD grown 2D materials on transition metal substrates [160]. The transfer process used in the present

study is schematically illustrated in Figure 6-2. PMMA (450K A4, MicroChem) was spin coated on centimetre sized hBN coated sapphire pieces and baked on a hot plate. The PMMA coated pieces were then floated on a bath of 2% hydrofluoric acid (HF). Within a few minutes, the PMMA-hBN film was separated from the sapphire (due to under-etching of the sapphire by HF) and floated on surface of the acid bath. The PMMA-hBN stack was washed in de-ionized water bath (three times, to completely remove HF) before being transferred onto a desired substrate.

For characterization, the PMMA-hBN stack was transferred onto a plain SiO_2/Si substrate. PMMA was removed through thermal decomposition, achieved by annealing samples in air at 500 °C for two hours [327]. Successful transfer of hBN was confirmed with help of Raman spectroscopy and the thickness was determined by tapping mode AFM. Figure 6-3(a-c) shows optical microscope images of hBN films with different thickness transferred on to SiO_2/Si substrates along with AFM images and linescans performed for measuring thickness. The Raman spectra of hBN films are also shown in Figure 6-3(d). The integrated intensity of the E_{2g} band (at 1369 cm^{-1}) shows a linear dependence on hBN film thickness (Figure 6-3(e)), which can be used for thickness calibration. Figure 6-3(f) shows a picture of the hBN film (1.5 nm) transferred on to a patterned substrate, further highlighting the versatility of the transfer process.

For preparation of SERS substrates, 5 nm of Ag or Au was evaporated onto SiO_2/Si substrate. For droplet based SERS chip (discussed in section 6.5), the metal layers were deposited through a shadow mask, to obtain a patterned layer. As-deposited metal layers comprised of discrete NPs rather than a continuous film and were plasmonically active without any need for further treatment. Next, with the help of chemical etching process, PMMA-hBN stack was transferred onto Ag and Au coated substrates. For the SERS study, the hBN film thickness used was limited to 3-5 layers, obtained by adjusting the growth time to 1 hour under CFG conditions [208]. Lastly, PMMA was removed by acetone. The effect of annealing temperature was studied, wherein after removing PMMA by acetone, samples were annealed in air at different temperatures in a quartz tube furnace.

The surface of the hBN coated SERS substrate was imaged using SEM, as shown in Figure 6-4(a). A continuous (pinhole-free) hBN layer can be clearly identified which blankets the underlying Ag NPs (in the left half of the image). A few lamination

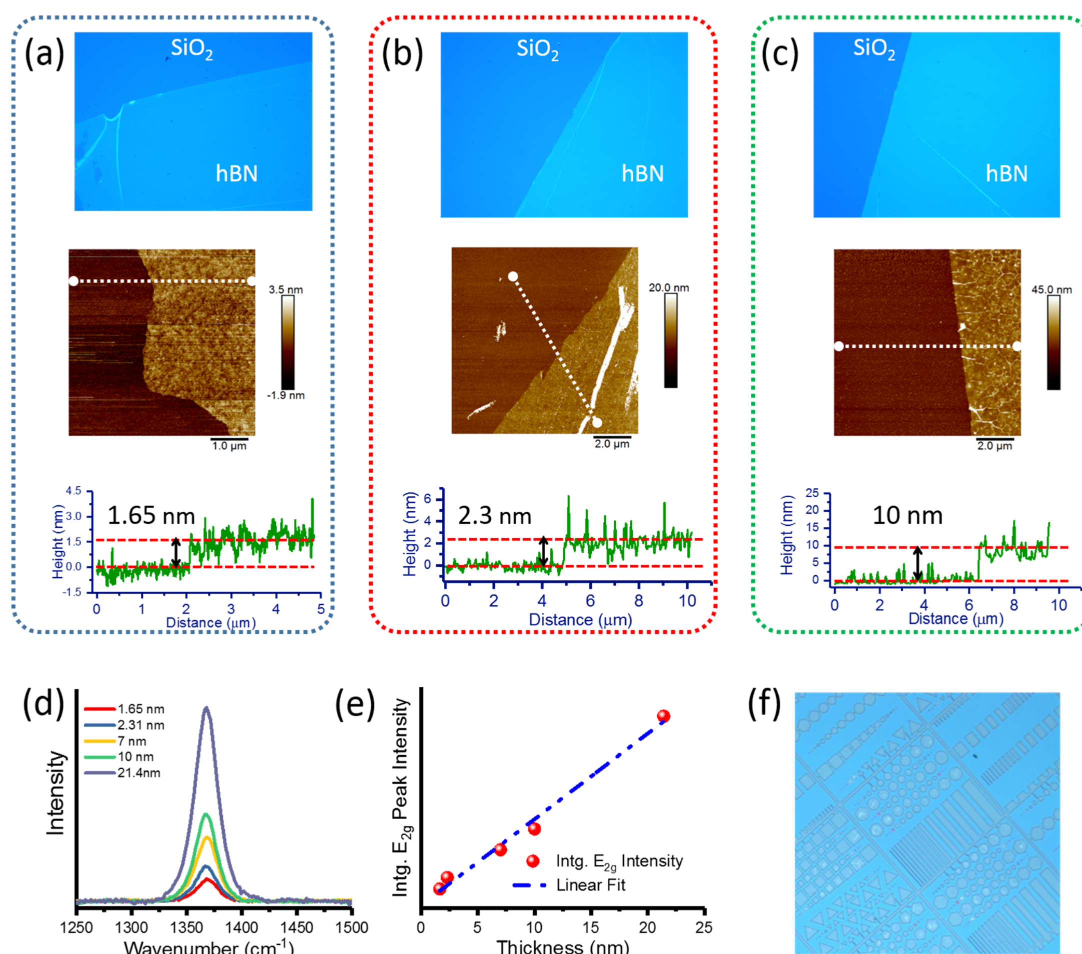

Figure 6-3 (a-c) Characterization of hBN films transferred on to SiO2/Si substrate for three film thicknesses. It includes an optical microscope image of the sample along with AFM image and linescan for measuring film thickness. (d) Raman spectra of hBN films, (e) graph showing dependence of E_{2g} peak intensity on hBN films thickness (transferred on to SiO_2/Si substrates) and (f) hBN films transferred on to a patterned substrate.

wrinkles can also be seen, known to form as a result of the transfer process. The morphology and distribution of Ag NPs, under hBN and non-hBN covered regions, as observed in Figure 6-4(a) are nearly same. This confirms that the wet chemical transfer process did not result in any noticeable change or re-distribution of Ag NPs. The average diameter of the Ag NPs is 21.7 nm, while average gap between the NPs is 10 nm, which is comparable to values in previously reported studies [114, 115].

The surface morphology of the SERS substrate was also measured using AFM, as shown in Figure 6-4(b). Individual Ag NPs can be clearly identified in the non-hBN region, while the hBN layer over Ag NPs is observed to be wrinkled. The flexibility of atomically thin hBN allows it to conform to underlying Ag NPs, which is essential

for preserving EM 'hot-spots' and critical for SERS effect. AFM line scan shown in Figure 6-4(b) reveals height variations along the dashed line (in white) and the extent of contouring as hBN enfolds the Ag NPs.

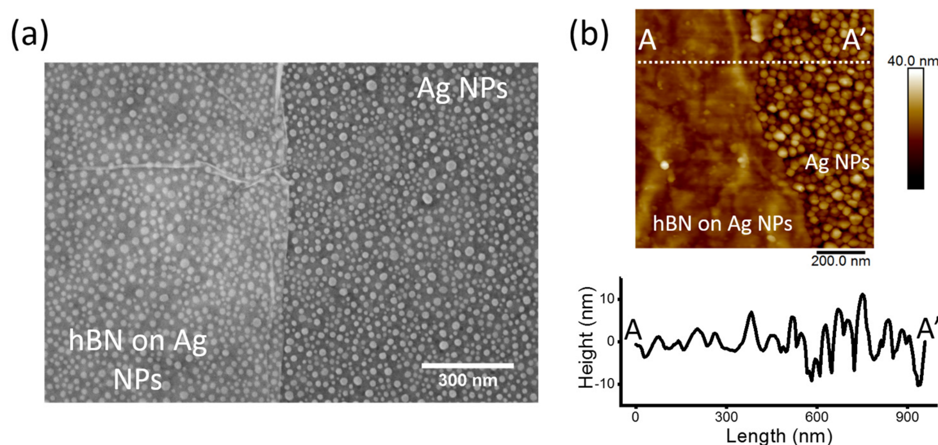

Figure 6-4 (a) SEM of hBN-AgSERS substrate showing hBN covered and uncovered regions, as marked on the image and (b) AFM image and line scan showing height profile along line AA'.

6.4 SERS measurements results

The SERS performance was evaluated using Rhodamine 6G (R6G) from Sigma Aldrich as a model molecule. The hBN coated SERS substrates were immersed in a solution of R6G prepared in DI water for 1 hour. Concentration of R6G solution was varied from 10^{-3} to 10^{-9} M. After soaking, samples were rinsed thoroughly with DI water. Raman spectra were collected using Horiba's JOBIN VYON spectrometer using a 532 nm laser and its intensity incident on the sample was set to 50 μW cm^{-2}. Baseline corrections on collected spectra were performed for subtracting background fluorescence from hBN and Ag NPs using LabSpec software supplied with the spectrometer.

6.4.1 SERS performance of hBN covered Au and Ag NPs

It is well-known that the surface plasmon resonance for Ag NPs lies in the near ultraviolet range due to which it yields the highest sensitivity in SERS with commonly used visible wavelength lasers. However, Ag is prone to rapid oxidation in ambient

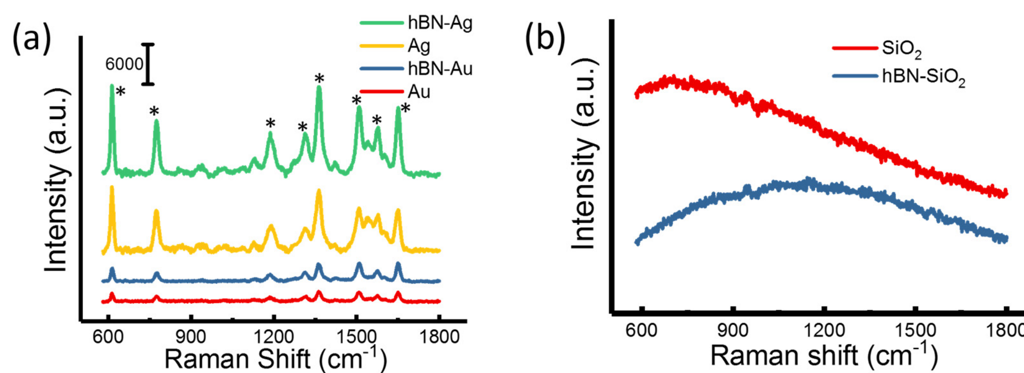

Figure 6-5 (a) Raman spectra for 10^{-3} M R6G obtained from hBN and non-hBN covered Au and Ag samples. The plots are offset vertically for clarity and (b) Raman spectra for 10^{-3} M R6G obtained from bare SiO_2/Si and hBN-SiO_2 substrates without nanoparticles. The spectra are shown without baseline correction.

conditions [315-317] and therefore, Au is commonly preferred (over Ag). In this study, we first compare the performance of hBN covered Au- and Ag-SERS substrates. Both substrates were dipped in a 10^{-3} M solution of R6G as described above. Raman spectra, collected from regions with and without hBN cover for both Au and Ag samples are summarized in Figure 6-5(a). Characteristic Raman peaks for R6G at 613, 775, 1184, 1312, 1363, 1509, 1577 and 1650 cm^{-1} are clearly visible (marked with *) [328]. As expected, the SERS spectra of R6G obtained from Ag NPs is significantly stronger than that from the Au NPs, and is consistent for hBN and non-hBN covered regions. Furthermore, for Ag and Au samples, it can be observed that the Raman signal intensity is higher from hBN covered regions than from non-hBN regions. The slightly stronger Raman signals from hBN covered regions across both samples can be attributed to superior adsorption capabilities of hBN layers over bare metal NPs and has been reported for hBN and graphene in recent studies [113, 114, 329]. For reference, Raman spectra from plain hBN-SiO_2 and bare SiO_2 after R6G immersion were also collected, however no measurable peaks corresponding to dye was observed. Raman spectra for these two samples without baseline corrections are shown in Figure 6-5(b).

Given the higher sensitivity of hBN covered Ag SERS, lower concentrations of R6G were also analysed and are shown in Figure 6-6. R6G concentration up to 10^{-8} M could be measured using the hBN-Ag SERS substrates. No measurable peaks are observed from Raman spectra corresponding to R6G concentration of 10^{-9} M, as shown in Figure 6-6(d) (without any baseline corrections). Once again, for all R6G

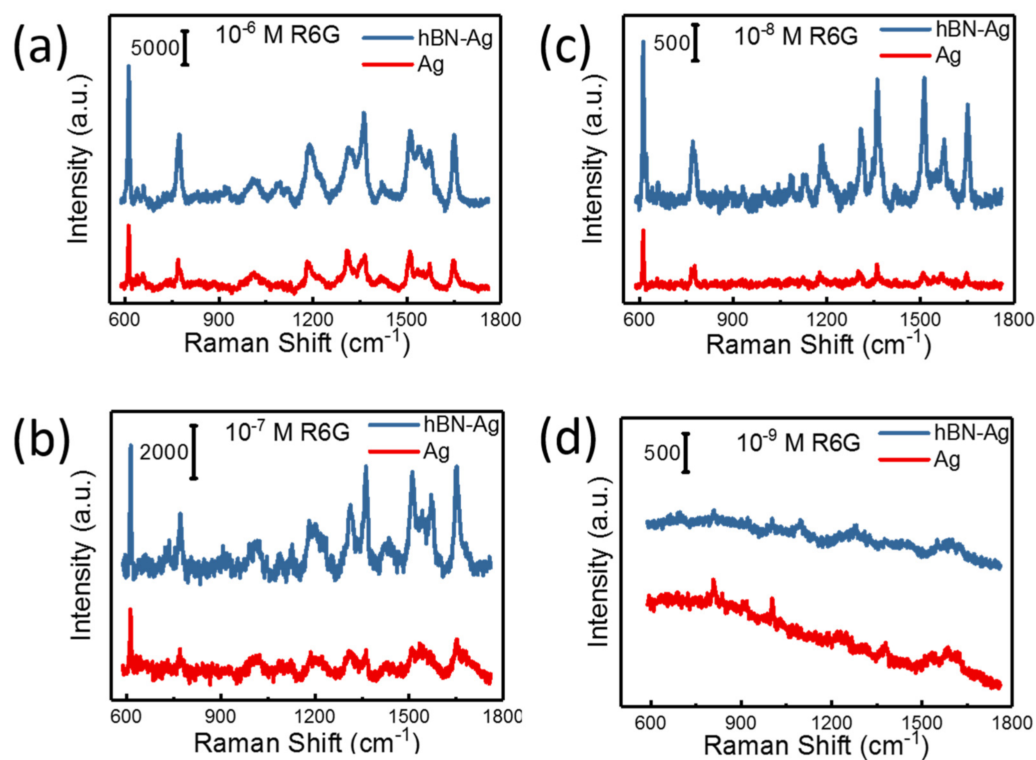

Figure 6-6 Raman spectra of varying concentrations of R6G (indicated in figure) obtained from hBN and non-hBN covered Ag SERS samples.

concentrations, the Raman signal from hBN covered Ag NPs is consistently higher than that from bare Ag NPs, in agreement with previous observations.

6.4.2 hBN for preventing oxidation of Ag NPs

Next, the role of hBN in preventing oxidation and preserving the SERS functionality of Ag NPs was tested. For this, after transferring hBN layers on to Ag-SERS substrate (also referred as hBN-AgSERS) and removing PMMA with acetone, the samples were annealed in air for 2 hours at 200, 400 and 600 ºC. It is reasonable to believe that silver oxidation will be accelerated under such annealing conditions [330, 331]. SERS activity of annealed and one non-annealed sample was once again checked using 10^{-3} M R6G solution, as described above. The effect of annealing on bare Ag NPs was also monitored and Raman spectra obtained from hBN and non-hBN covered regions, for each of the four samples are shown in Figure 6-7(a-b). The intensity of peak at 613 cm^{-1} (characteristic of R6G) is used as a measure of SERS sensitivity and plotted against annealing temperature in Figure 6-7(c) for ease of comparison. From Figure 6-7(c), it can be seen that for uncovered Ag NPs, the Raman

signal intensity decreases with increasing annealing temperature. A slight decrease in Raman intensity is also observed for hBN covered Ag NPs for annealing temperatures up to 400 °C, after which, a sharp decrease in Raman intensity is observed for annealing temperature of 600 °C. Two main factors responsible for the observed results are discussed below.

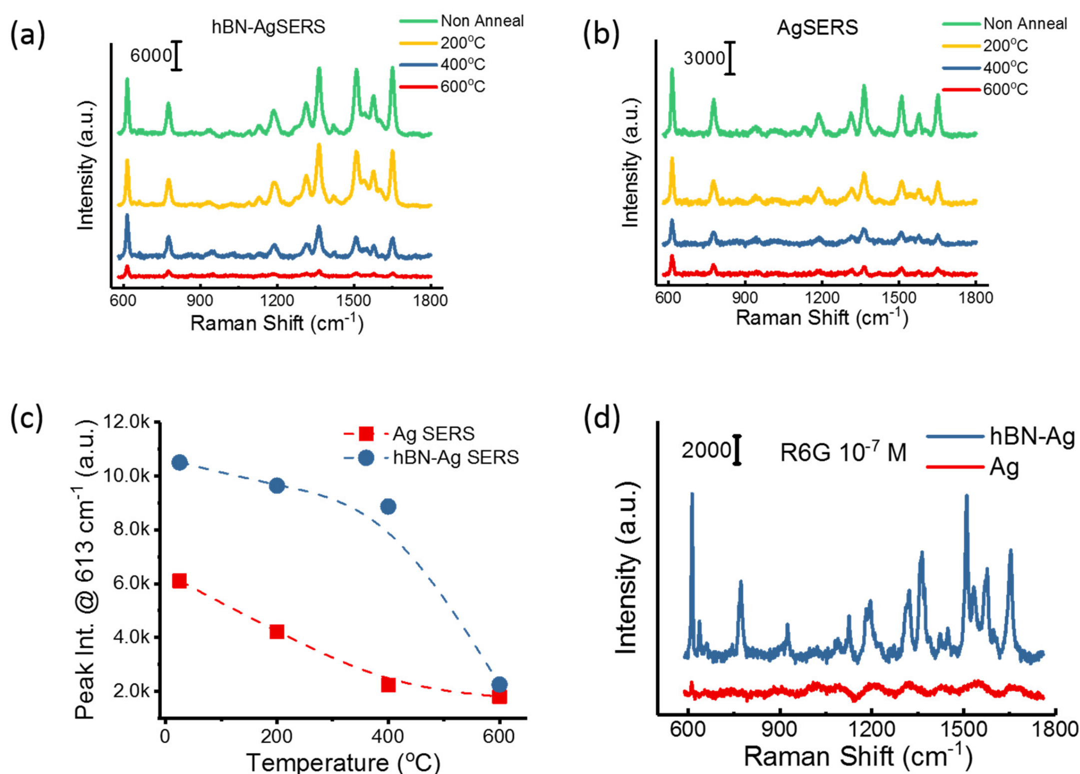

Figure 6-7 (a-b) Raman spectra for R6G obtained from hBN and non-hBN covered Ag nanoparticles for SERS samples annealed at different temperatures, (c) variation of 613 cm^{-1} peak intensity with annealing temperature and (d) Raman spectra of 10^{-7} M R6G obtained from hBN-Ag SERS sample annealed at 250 °C for 48 hours.

First, since Raman signals from hBN covered regions are consistently higher than non-hBN regions, it can be said that hBN is indeed effective in preventing oxidation of Ag NPs, at least till 400 °C. For samples annealed at 600 °C, Raman signal intensities from hBN and non-hBN covered regions are nearly same, which will be discussed separately. In the case of non-annealed sample, the lower signal for non-hBN covered Ag NPs can be attributed to oxidation of Ag NPs at room temperature (i.e. 25 °C) which can take place over few days after the transfer of hBN layers and until SERS analysis is performed. The effect of silver oxidation on SERS was further

established through prolonged annealing of samples performed in air at 250 ºC for 48 hours. The SERS functionality of the hBN covered regions on these samples was established by successfully measuring Raman signal for a much smaller R6G concentration, as shown in Figure 6-7(d). This confirms hBN's ability in preventing silver oxidation.

Secondly, during thermal annealing, silver NPs on the SiO_2 surface can diffuse and coalesce, resulting in redistribution of NPs for both hBN and non-hBN covered regions [332, 333]. SERS samples were imaged using SEM and particle distribution analysis was performed on annealed and non-annealed samples, as shown in Figure 6-8 and 6-9, respectively. Ag NP statistics presented in Figure 6-8 and 6-9 show that nanoparticle diameter and gap length between adjacent nanoparticles increased with increase in annealing temperature, for both hBN and non-hBN covered regions. This can be attributed to higher surface diffusion rates of Ag NPs with increasing annealing temperature, facilitating its coalesce to form bigger particles. Furthermore, the EM

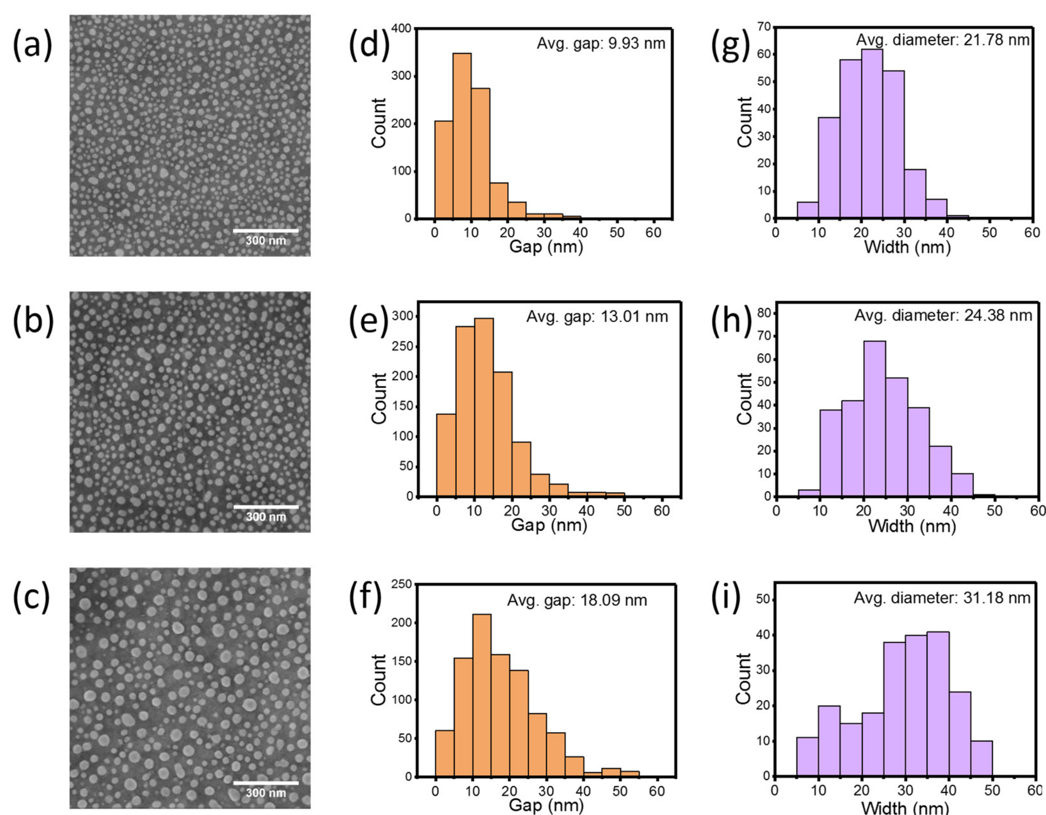

Figure 6-8 (a-c) SEM images of hBN covered Ag NPs that are as-deposited, annealed at 200 and 400ºC respectively. (d-f) gap length and Ag nanoparticle diameter distribution analysis for as-deposited and annealed samples shown in (a-c).

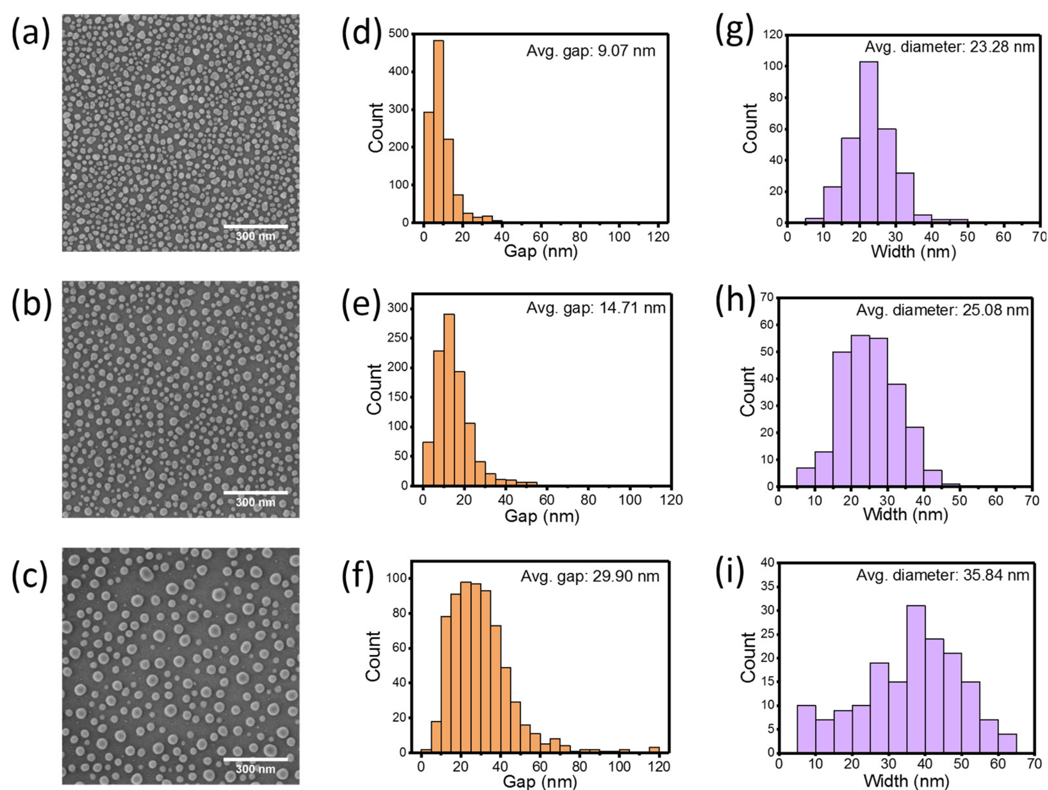

Figure 6-9 SEM images of Ag NPs that are as-deposited, annealed at 200 and 400 ºC respectively. (d-f) gap length and Ag nanoparticle diameter distribution analysis for as-deposited and annealed samples shown in (a-c).

enhancement in SERS is known to be highly sensitive to the size and separation between metal nanoparticles. The intensity of EM field drops exponentially as we move away from metal surface. Hence, the observed decrease in SERS signal from hBN covered samples, reported in Figure 6-7(c), is attributed to changes in Ag NP distribution induced by thermal annealing. Furthermore, from Figure 6-9, it can be observed that the extent of redistribution and corresponding change in particle diameter and gap length is more significant for non-hBN regions than for hBN covered regions. This is probably due to restricted surface diffusion of Ag particles imposed by the hBN coverage. Hence, by preventing oxidation and restricting re-distribution of Ag NPs during thermal annealing, hBN is able to maintain higher SERS sensitivities.

We also discuss the SERS activity and anomalous behaviour of samples annealed at 600 ºC, wherein, the R6G Raman signal intensity for hBN and non-hBN covered regions are nearly the same (Figure 6-7(c)). Figure 6-10(a) shows the SEM image of hBN-AgSERS sample annealed at 600 ºC (due to lack in contrast between Ag, hBN and SiO_2, a particle distribution analysis for this sample could not be

performed). The surface morphology of this sample is significantly different than its counterparts (Figure 6-8). From Figure 6-10(a), it appears as if the hBN layer covering Ag NPs is damaged. Mono- and few-layers of single crystal hBN (obtained via mechanical exfoliation) are known to be one of the strongest materials [14]. On the other hand, MOVPE (and CVD) grown hBN films comprise of nanometer sized grains which coalesce to form a continuous film, through the formation of grain boundaries. Point defects (and grain boundaries) in graphene have been shown to affect its mechanical properties [334, 335]. To the best of our knowledge, we have not come across a similar study on CVD/MOVPE hBN films, but given the similarity between the two materials, it is reasonable to believe that grain boundaries in MOVPE grown hBN are also more susceptible to breakage under strain (applied by Ag NPs during annealing) than single crystal hBN film. More importantly, in a recent study, Liao et al., have shown that Ag NPs can facilitate oxidative etching of hBN nanosheets, achieved by annealing Ag-NPs and hBN nanosheets in air (using a tube furnace) [336].

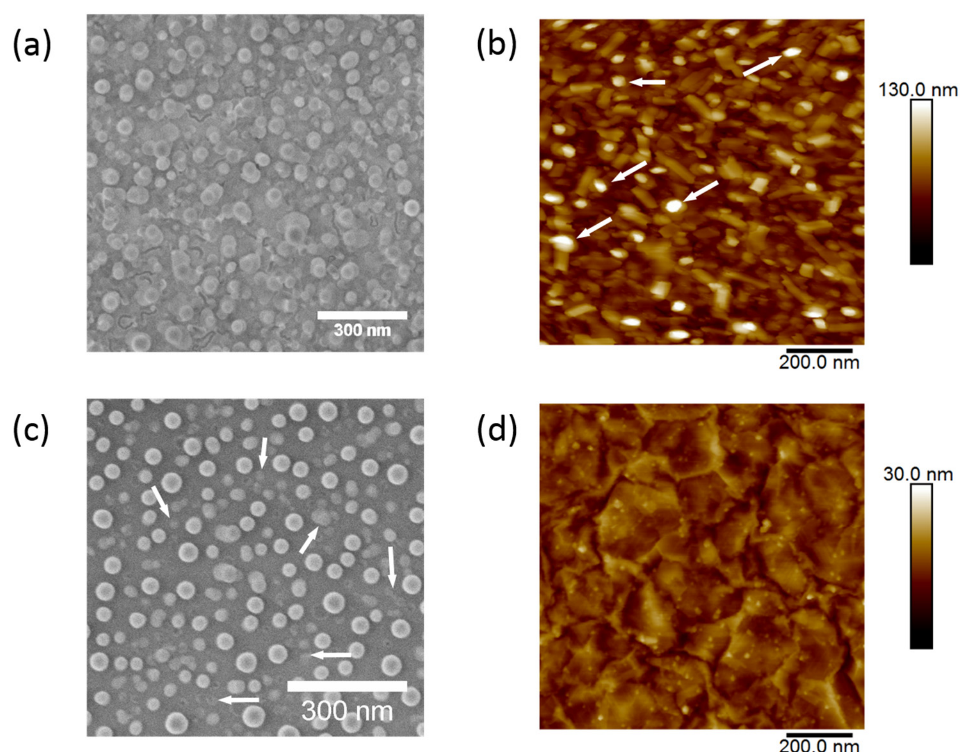

Figure 6-10 (a) SEM image of hBN covered AgSERS sample annealed at 600 ºC, (b) bare Ag NPs annealed at 600 ºC. The white arrows indicate spots on the SiO_2 surface which are reminiscent of Ag sublimation, (c-d) AFM image of hBN covered AgSERS sample annealed at 600 and 400 ºC respectively. White arrows in (c) point to Ag NPs which seem to be protruding from the hBN film.

Catalytic etching by Ag-NPs at elevated temperatures has also been utilized for synthesizing porous graphene nanosheets [337]. Unprotected Ag NPs undergo sublimation at temperatures close to 600 ºC [338, 339]. From the SEM image of uncovered Ag NPs annealed at 600 ºC shown in Figure 6-10(b), several spots (marked by white arrows) can be identified. These appear to be remnants of Ag NPs on the SiO_2 surface post sublimation. The surface topography, measured using AFM, for samples annealed at 600 and 400 ºC is shown in Figure 6-10(c) and (d), respectively. Once again, for sample annealed at 600 ºC, hBN layer appears to be ruptured and Ag NPs (marked by white arrows) can be seen to protrude through the hBN film whilst increasing the overall surface roughness of the film. In comparison, the hBN film for sample annealed at 400 ºC (and non-annealed, not shown here) appears to be wrinkled but continuous and undamaged. Hence, during annealing at 600 ºC, the catalytic etching by Ag NPs damage the hBN film. Consequently, Ag NPs are exposed to air and hBN can no longer prevent its oxidation. This can explain the loss in SERS activity after annealing the sample at 600 ºC, as observed in Figure 6-7(c).

6.5 Droplet-based SERS chip

Having successfully demonstrated the use of MOVPE grown wafer-scale hBN layers in preventing the oxidation of silver NPs, its utility can be readily extended for large area applications, showcased here through a droplet based SERS platform. In general, the development of droplet-based platforms for analytical and diagnostic techniques including SERS is being actively pursued as it combines the benefits of parallel operation, minimal reagent consumption and faster analysis [340, 341]. SERS based analysis typically involves drop casting a few microliters of an aqueous sample containing the analyte of interest on to a SERS substrate. The sample is then analysed using a spectrometer (air borne analytes can be transferred onto the substrates using additional steps). Figure 6-11(a) shows a photograph of the droplet based SERS chip. It consists of an array of circular spots, which are the SERS active regions comprising of silver NPs deposited on the SiO_2 surface using a shadow mask. hBN layer is transferred on to the substrate, using wet transfer process and PMMA was removed by annealing in air at 400 ºC for two hours. The periphery of the hBN is highlighted by a white dashed line in Figure 6-11(a). Note that hBN's refractive index imparts a colour

difference between hBN and non-hBN covered Ag NPs (green to blue, respectively) and helps in distinguishing between the two. A 2 µl droplet of 10^{-6} M R6G (equivalent to 0.958 nanograms) was carefully pipetted onto the hBN covered Ag NPs, as illustrated (where two droplets are shown to highlight that multiple droplets can be analyzed on one substrate in parallel). Raman spectrum, as shown in Figure 6-11(b) was collected after the droplet was dried is representative of R6G. Raman spectrum

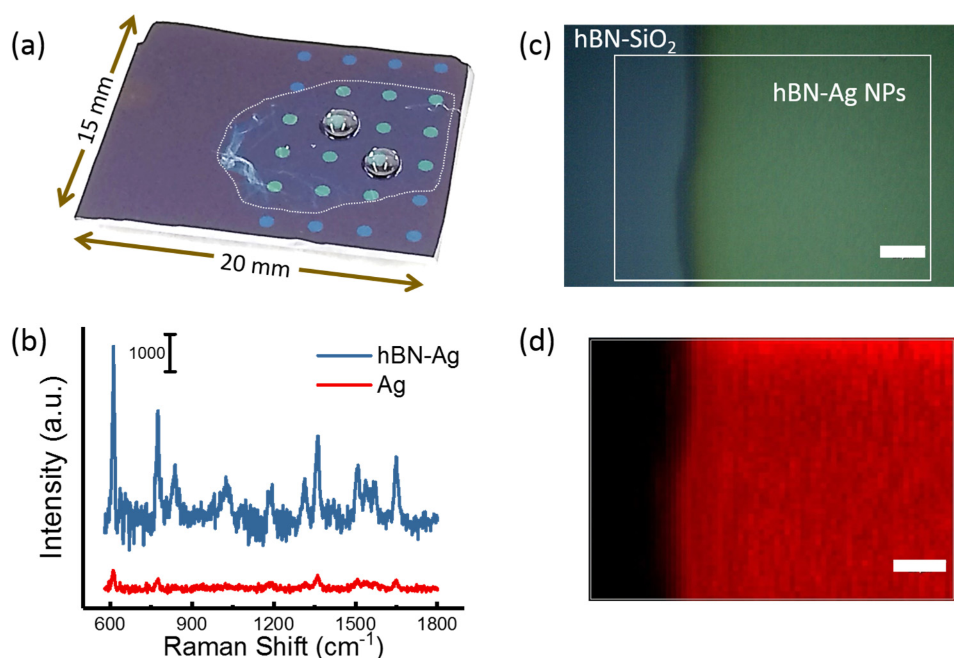

Figure 6-11 A photograph of droplet based SERS chip containing an array of Ag spots. The boundary of the hBN covered region is indicated by a dotted white line. Ag spots under hBN appear green and can be easily distinguished from the bluish uncovered Ag spots. Two 2 µL droplets of 10^{-6} M R6G are pipetted over hBN covered Ag spots, (b) Raman spectra of R6G collected after the droplets shown in (a) have dried. (c) optical microscope image of hBN covered Ag spots seen in (a) and, (d) Raman intensity map using 613 cm^{-1} peak of R6G corresponding to the white box shown in (c). Scale bars in (c-d): 20 µm.

from uncovered Ag spot is also shown in Figure 6-11(b) for comparison. Based on spectra collected at different points from the hBN covered Ag NPs regions, some non-uniformity in the Raman signal intensity was observed. The background fluorescence was also variable at different measurement points. This can be attributed to the hydrophobic nature of hBN film [183, 273], leading to unequal distribution of R6G over the hBN surface as the droplet dries gradually [342, 343]. Alternatively, the SERS

chip was immersed in a bath of 10^{-6} M R6G for 30 minutes to facilitate uniform adsorption of dye molecules over the hBN surface. Figure 6-11(c-d) shows an optical microscope image taken at the edge of the silver nanoparticle pattern. The hBN covered SiO_2 and Ag NP regions can be identified easily and are labelled for clarity. A colour coded Raman intensity map (corresponding to 613 cm^{-1} peak intensty) for area enclosed in a white box (in Figure 6-11(c)) is shown in Figure 6-11(d). The stark contrast in Raman intensity between hBN-SiO_2 and hBN-Ag NPs regions is due to the SERS. The spatial homogeneity of the 613 cm^{-1} peak intensity from the hBN-Ag NP region confirms uniform adsorption of R6G.

6.6 Summary

In summary, we demonstrated the use of large-area hBN films for SERS applications using gold and silver nanoparticles. hBN was shown to be highly effective in preventing the oxidation of silver nanoparticles, even at elevated temperatures. The SERS activity of the hBN coated Ag NPs samples was confirmed using R6G and was found to be consistently better than that of bare Ag NPs. The change in surface morphology of SERS samples was studied using AFM and SEM, which help in correlating changes in nanoparticle distribution induced by annealing to SERS enhancement. Our study specifically utilizes MOVPE grown hBN layers which can be readily scaled up for large-area applications, as demonstrated through droplet based SERS chip. In future, application of large area hBN layers can be extended for passivation of other materials as well.

Chapter 7. Epitaxial growth and characterization of AlN on hBN

7.1 Introduction

Epitaxial growth of compound semiconductor materials is at the heart of many solid-state devices, including LEDs, HEMTs, laser diodes, photodetectors and sensors. Over the years, a wide range of III-V and II-VI materials such as GaAs, InP, GaN, CdTe, ZnO and ZnSe have been deposited on suitable substrates. In recent years, there has been a paradigm shift towards the development of flexible and conformal devices [6, 344, 345]. For this, layered 2D materials, such as mica, graphene, hBN etc., are being explored as substrates for epitaxial growth of compound semiconductors [89-91, 97, 101, 346, 347]. This special class of epitaxy on 2D materials as substrates is also known as van der Waals epitaxy [348]. The unique crystal structure of 2D materials, wherein, individual layers are held together by weak van der Waals forces (as opposed to strong covalent bonds) form a shear plane. This offers a convenient method to detach hetero-structure devices from substrates post epitaxy and subsequently transfer them onto desired substrates, such as polymer sheets (for flexibility) or metallic substrates as heat sinks.

Amongst the various 2D materials, hBN is well-suited for van der Waals epitaxy as it is thermally stable and can withstand high-temperature, hydrogen-rich, epitaxial growth environments required for the deposition of III-nitrides. Wafer-scale hBN layers have been successfully deposited on sapphire substrates using MOVPE, as described in Chapter 4. In this chapter, growth of AlN on hBN is presented, which can potentially serve as templates for deep UV-LEDs.

7.2 III-nitride growth on hBN: Literature review

Solid state UV light sources are in high demand for a wide range of applications such as water purification, sterilization, disinfection and secure communications. AlGaN based materials are principal candidates for the development of energy efficient UV light sources, as they have a direct bandgap and offers the possibility of

fine tuning the emission wavelength by changing the alloy composition [197, 199, 349]. In the absence of lattice matched substrates, sapphire wafers with a few microns thick AlN buffer layer serve as templates for epitaxial growth of AlGaN based multi-quantum well (MQW) devices. AlN growth itself is challenging as several conditions need to be satisfied simultaneously. For example, the crystallinity of AlN/AlGaN layers critically depends on the growth temperature during MOVPE process. For pure AlN films, growth temperatures above 1300 °C have been shown to be beneficial in terms of reducing defects, such as screw and edge dislocations. These act as non-radiative recombination centers and reduce the internal quantum efficiency of the device [229, 350-354]. In addition to this, polarity inversion from Al- to N-polar results in the formation of epilayer with very rough surfaces and V-groves [355-358]. For MQW devices, specular surfaces are needed, which requires careful polarity control. Thick AlN layers can also undergo severe cracking, due to tensile stress in AlN film [359-361]. Currently, there is a huge interest in fabricating low-dislocation density, specular and crack-free AlN buffer layers to aid in developing high brightness deep-UV devices.

For the fabrication of flexible optoelectronic devices, epitaxial growth of III-nitride alloys on hBN has attracted attention in recent years. In 2012, Kobayashi et al. were the first to report on the growth of InGaN MQW LED structure on sapphire with a thin MOVPE-grown hBN sandwiched between the two. The device was released from sapphire and subsequently transferred onto a polymer sheet [89]. Later, Ayari et al. extended this capability to wafer-scale exfoliation of MQW InGaN LEDs grown on hBN/sapphire template [90]. The same group also reported on the growth and fabrication of a flexible AlGaN based gas sensor on hBN/sapphire template using MOVPE [94]. Other than LEDs, Hiroki et al. have used hBN layers to release AlGaN based high electron mobility devices from sapphire substrates. The devices were transferred on to copper sheets for increased heat dissipation, which resulted in an overall improvement in device performance [99]. Similarly, Glavin et al. reported on flexible GaN/AlGaN high electron mobility transistors obtained through growth on hBN/sapphire substrates for radio frequency applications [97].

III-nitride growth on hBN is an emerging field and several aspects of growth are being investigated. For example, traditionally, the growth of GaN or AlN on sapphire starts with the deposition of a thin (few tens of nanometers), low-temperature

nucleation layer, over which a thicker buffer layer is grown at higher temperature [362, 363]. hBN being a 2D material, lacks dangling bonds which makes nucleation difficult to achieve. It has been shown that GaN does not nucleate uniformly over hBN and results in the formation of randomly oriented, polycrystalline, isolated islands [89]. On the other hand, AlN serves as a better nucleation layer (on hBN), which may be attributed to the lower mobility and higher sticking coefficient of Al atoms [364]. GaN buffer layers grown on AlN nucleation layer are able to coalesce and form specular films. Alternatively, oxygen plasma treatment of hBN, has also been employed for improving nucleation [96, 365]. Plasma etching works by creating dangling bonds on the hBN surface along with pinholes, which act as step edges to facilitate the nucleation process [95]. However, samples have to be removed from the MOVPE reactor for additional plasma processing steps and risks surface contamination.

The quality of the underlying hBN layer also plays a critical role in the deposition and crystallinity of AlGaN buffer layers grown on it. In some studies, monolayer hBN on sapphire is used. The use of very thin hBN layer combined with plasma etching makes it difficult to physically detach the buffer layer from the sapphire substrate [96, 365]. On the other hand, thick hBN layers, with rough surface morphology can result in spontaneous and uncontrolled self-delamination of grown layer from substrate, as demonstrated by Snure et al. for GaN [366]. A direct correlation between defect density and surface roughness was also reported in the same study.

There are few reports on growth of pure AlN layers on hBN/sapphire substrates which can serve as templates for deep-UV devices, as described above. In the following sections, growth of AlN on sapphire and hBN/sapphire (also referred as just hBN for simplicity) substrates using MOVPE is presented. The morphology and crystallinity of the AlN films grown on hBN under different conditions was studied using a combination of different characterization methods. Structural quality of AlN epilayers was characterized using high-resolution X-ray diffraction (HR-XRD), where ω-scans of symmetric (0002) and asymmetric ($10\bar{1}2$) planes provide an estimate of dislocation density. Grazing incidence XRD (GI-XRD) was also employed to specifically investigate the polycrystallinity of the AlN layers. The overall morphology of AlN was imaged using SEM, while surface topography of hBN and AlN was measured using tapping mode AFM. Raman spectroscopy of the films provided a rapid

and non-destructive method for confirming hBN deposition on sapphire and estimating the strain in AlN films.

7.3 MOVPE deposition of AlN on hBN (and sapphire)

hBN was grown directly on sapphire substrates under continuous flow conditions[6], as detailed in Chapter 4. TEB flux and V/III ratio was 60 μmol/min and 2200, respectively. The thickness of hBN was limited to 1-2 nm, which was achieved by adjusting growth time to 1 hour (see Figures 4.3(a) and 6-3(a), for hBN films grown under same conditions). Although detailed characterization study of such hBN films has been presented in the previous chapters, for convenience, the surface topography of sapphire and hBN, obtained using AFM are shown in Figure 7-1(a) and 7-1(b), respectively. Post hydrogen anneal, the sapphire surface is atomically smooth and the vicinal step edges due to offcut are clearly visible. The as-deposited hBN film exhibits a wrinkled morphology that is characteristic of 2D material growth. Raman spectra of the two substrates are shown in Figure 7-1(c). The peak at 1371 cm^{-1} corresponds to the E_{2g} mode of sp^2 bonded hBN and along with AFM, confirms hBN deposition. The

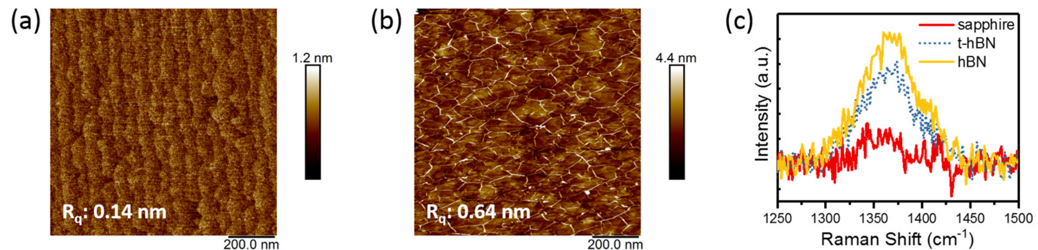

Figure 7-1 Surface topography, measured using AFM, of (a) sapphire after hydrogen annealing and (b) hBN film deposited on sapphire. Wrinkles in hBN films are clearly visible. Root mean square roughness (R_q) and scale bars are as indicated on individual figures. (c) Raman spectra of sapphire and hBN films.

---

[6] CF methodology is preferred over FME for the growth of hBN as very thin layers of hBN (< 2 nm) are required, over which AlN layers were grown subsequently. Typically, FME growth process is favoured only when thicker hBN films are required, for reasons described in Chapter 4. FME also requires periodic and multiple actuation of the mass flow controllers (MFCs) in the MOVPE reactor. Repeated actuations of MFCs can reduce their operational life. Hence, CF conditions were used instead of FME for depositing hBN.

dotted line in Figure 7-1(c) represents the Raman spectrum of another hBN film (labelled 't-hBN') which was deposited using a smaller TEB flux. Based on the intensity of E_{2g} peak, we can conclude that this hBN film is thinner and will be discussed later.

For AlN growth, trimethylaluminium (TMA) was used as Al precursor. Sapphire and hBN substrates were loaded together in the 3x2 MOVPE reactor. This provides a direct comparison of AlN growth on the two substrates under identical growth conditions. AlN itself was grown using different methods described below. The total AlN film thickness was kept between 800-900 nm in all the processes.

7.3.1 Two-step AlN growth

First, AlN growth using a conventional two-step method was studied which involves a low temperature (LT) nucleation layer grown at 900 °C, followed by a high temperature (HT) buffer layer at 1300 °C. The use of a low temperature AlN nucleation layer was first reported by Akasaki and co-workers in 1986 (later by Nakamura using low-temperature GaN). Since then, this has become the standard process for growing specular AlN and GaN films [362, 363, 367]. For the two-step process, sapphire and hBN wafers were loaded in the MOVPE chamber and baked in hydrogen, as described above. Then, AlN nucleation layer was deposited for 3 minutes at 900 °C, resulting in a 30 nm-thick layer on sapphire (determined using X-ray reflectivity measurements). Thereafter, the temperature was increased to 1300 °C, under hydrogen flow for HT-AlN buffer layer growth (800-900 nm thick). TMA flow was 70 µmol/min with a V/III ratio of 10.

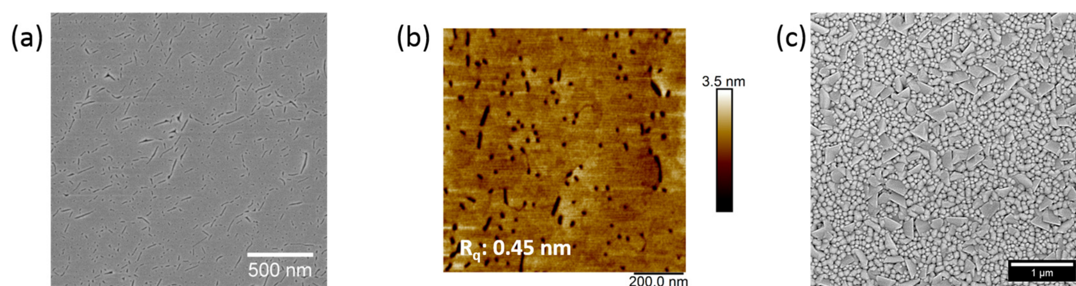

Figure 7-2 (a-b) SEM and AFM images of AlN deposited using the 2-step process on sapphire, respectively. (c) SEM image of the 2-step AlN film grown on hBN.

Figure 7-2(a) and 7-2(c) shows plan-view SEM images of AlN grown on sapphire and hBN, respectively. The surface of the AlN on sapphire looks smooth and is in agreement with the AFM results, as shown in Figure 7-2(b). Some elongated pits in the AlN film can be identified, which can be eliminated by growing thicker AlN films. On the other hand, the morphology of AlN on hBN is significantly different. It consists of nanocolumnar-like 3D features with conical tops, interspersed with randomly oriented wedge-like features, as shown in Figure 7-2(c). From the SEM images it appears as if the individual columns have not coalesced, resulting in a rough surface morphology.

7.3.2 One-step AlN growth

To understand this further, AlN was deposited on sapphire and hBN directly at 1300 °C, without a LT nucleation layer. TMA and NH_3 flow rates were same as used for the 2-step growth and no precursor pre-treatment (TMA or NH_3) was performed. From the SEM images of the two samples shown in Figure 7-3(a) and 7-3(b), it can be seen that AlN morphology is similar on both substrates and comprises of only nanocolumnar-like features that are also seen in Figure 7-2(c).

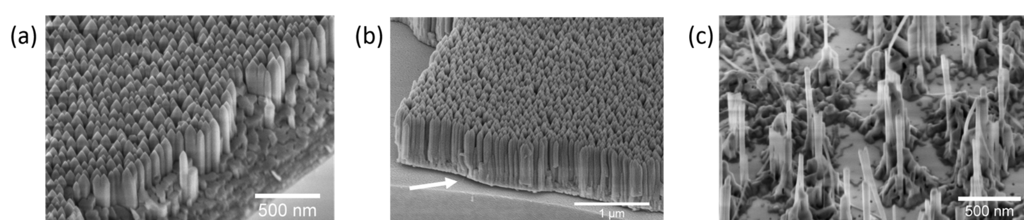

Figure 7-3(a-b) SEM image of AlN nanocolumns obtained using the 1-step growth process on sapphire and hBN, respectively. The white arrow in (b) indicates a region where AlN is delaminating from the underlying sapphire substrate due to the presence of hBN. (c) SEM image of AlN nanocolumns on sapphire after KOH etching.

The epitaxial relation between 1-step AlN and the underlying substrate, which is hBN grown on sapphire, was determined using XRD pole figure measurements. Figure 7-4(a) and 7-4(b) shows the pole figure plots of 1-step AlN grown on hBN and sapphire, respectively. Six equally spaced diffraction spots corresponding to the $(10\overline{1}2)$ plane of AlN at $\psi = 42\,^{o}$ and for $(11\overline{2}3)$ plane of sapphire at $\psi = 61\,^{o}$ can be

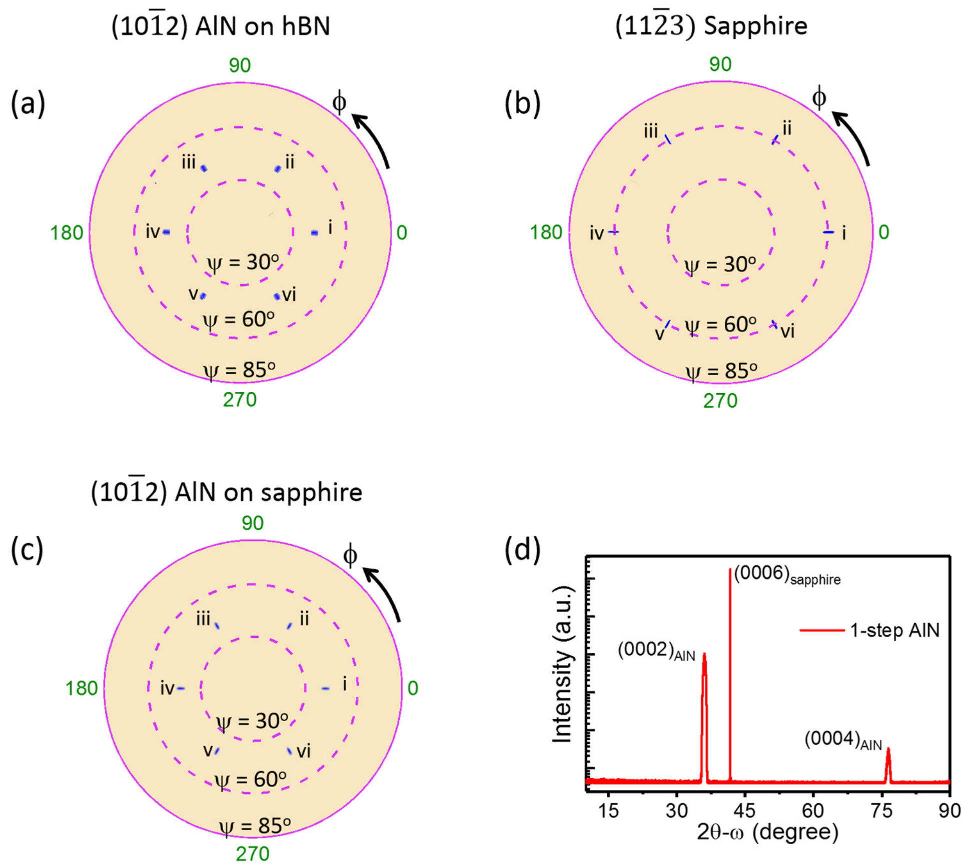

Figure 7-4 (a-c) XRD pole figures for 1-step AlN grown on hBN, sapphire and 1-step AlN grown on sapphire, respectively. The crystal planes and scan axis (ϕ and ψ) are as indicated on the figures. (d) 2θ-ω XRD for 1-step AlN grown on hBN.

identified having the same φ values, as shown in Figure 7-4(a) and 7-4(b), respectively. From this, we can establish that $[10\bar{1}2]_{AlN}||[11\bar{2}3]_{sapphire}$, which implies that the AlN lattice is rotated in-plane by 30° with respect to sapphire [89, 95]. Pole figure measurements of 1-step AlN grown on sapphire without hBN also show the same orientation of the AlN lattice with respect to sapphire, as shown in Figure 7-4(c), which is consistent with previously reported results [368, 369]. This suggests that in spite of the presence of hBN, the epitaxial relation between AlN and sapphire is the same as that without hBN. During pole figure measurements, no diffraction peak from hBN was recorded, as it is a very thin layer (< 2 nm). Figure 7-4(d) shows 2θ−ω scan for AlN on hBN sample under symmetric configuration (i.e. θ = ω). The peak at 41.69° corresponds to the (0006) planes of sapphire. With only two peaks visible for AlN at 36.02 and 76.42° pertaining to (0002) and (0004) planes, we can further infer that AlN crystal planes are predominantly oriented such that $[0001]_{AlN}||[0001]_{sapphire}$. Therefore,

the AlN nanocolumns on sapphire, as shown in Figure 7-3(a) are oriented along <0001> direction with respect to substrate.

Based on previous studies, the AlN nanocolumns have been attributed to the formation of inversion domains, resulting in AlN deposition with a mixed polarity [355, 356, 358, 370]. The nanocolumns have an Al-polar core that is surrounded by N-polar shell. A faster growth rate of the Al-polar domains causes it to outgrow the N-polar domains to form nanocolumns with conical tops. To confirm this, the AlN nanocolumns (on sapphire) were etched in hot KOH. Figure 7-3(c) shows an SEM image of 1-step AlN on sapphire after a brief dip in 1M KOH solution at 80 ^{o}C. It is well-known that N-polar AlN etches faster than Al-polar in KOH solution [355]. Due to this differential etch rate, the N-polar AlN is completely etched, leaving behind Al-polar domains, which form the core of nanocolumns. Furthermore, the apparent similarity in morphology and XRD results for AlN grown on hBN with that on sapphire, suggests that the AlN growth on hBN also has mixed polarity. KOH etching of AlN nanocolumns grown on hBN could not be performed, as the films delaminated in the chemical bath. Figure 7-3(b) indeed captures delamination of as-grown AlN nanocolumns (indicated by the white arrow) due to underlying 2D hBN. This is discussed in more detail below.

HR-XRD was used to evaluate the crystallinity of the AlN layers deposited on hBN and sapphire. Dislocations in epitaxially grown III-nitride films are generally described by means of a mosaic model, using tilt and twist of individual single-crystal grains, as illustrated in Figure 7-5(a). The degree of the tilt and twist can be estimated from the ω-scan (also known as X-ray rocking curves or XRC) of symmetric and asymmetric lattice planes [232, 371]. Figure 7-5(b) and 7-5(c) show ω-scans of (0002) and $(10\overline{1}2)$ planes for AlN layers grown under different conditions, respectively. The full-width at half- maximum (FWHM) values of XRCs are also summarized in Table 7-1 for ease of comparison. For the conventional 2-step AlN grown on sapphire, the FWHM of the (0002) and $(10\overline{1}2)$ XRC scan was measured to be 408 and 2045 arcsec, respectively, which are comparable to previously reported values [372, 373]. However, for AlN layers grown on hBN, FWHM of XRCs is considerably larger. Lower FWHM for AlN grown on sapphire is mainly due to a stronger epitaxial relation between the two, which in turn controls the orientation of individual AlN grains with respect to the basal plane of sapphire. On the other hand, the presence of hBN possibly weakens the

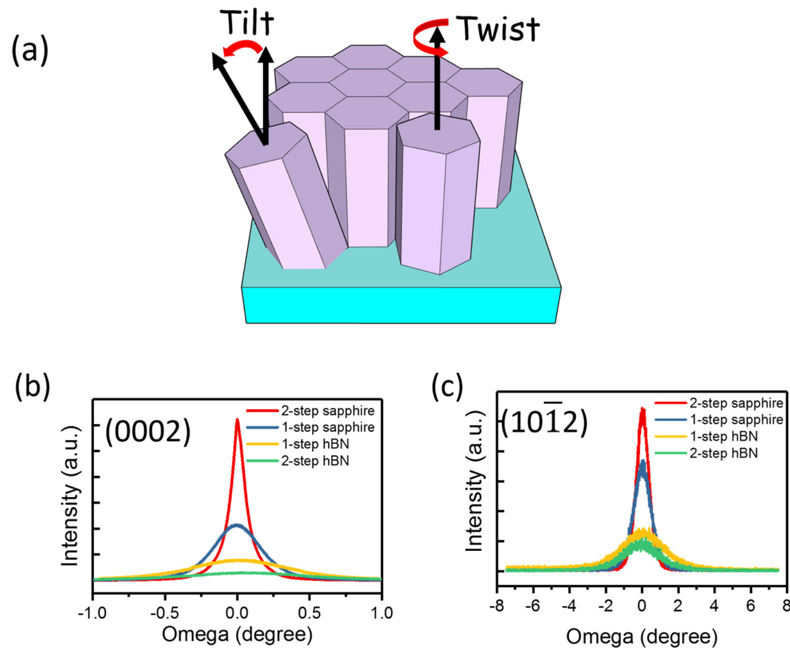

Figure 7-5 (a) Schematic illustration of tilt and twist of AlN grains on sapphire, (b) HR-XRD ω-scans for (0002) and (10$\bar{1}$2) planes of AlN grown on hBN and sapphire, using either 1-step or 2-step growth process.

Table 7-1 FWHM of XRCs obtained for AlN grown on hBN and sapphire using different growth techniques. All FWHM values are in arcsec.

FWHM (0002)

Substrate	1-step	2-step	Multi-step
Sapphire	1374	408	260
hBN	2760	3178	1940
t-hBN	-	-	956

FWHM (10$\bar{1}$2)

substrate	1-step	2-step	Multi-step
Sapphire	3860	2045	1416
hBN	6395	7892	5172
t-hBN	-	-	2239

epitaxial relation between AlN and sapphire thereby increasing both the tilt and twist of AlN grains and hence resulting in a higher defect density.

A comparison of AlN morphology on hBN using the 2- and 1-step methods suggests that while the nanocolumns can be attributed to high temperature growth, the random wedge-like features, seen only in case of 2-step AlN growth on hBN, are most likely formed during nucleation at low temperature. It is possible that the low-temperature AlN (on hBN) nucleates randomly and does not cover the entire surface of the substrate. Upon increasing the temperature, AlN nanocolumns grow directly on hBN from the uncovered regions. This explains the morphology of 2-step AlN (on hBN), as shown in Figure 7-2(c). Random nucleation of AlN on hBN may also imparts on it a polycrystalline character.

GI-XRD was employed to specifically investigate this. Compared to powder diffraction, which employs the Bragg-Brentano geometry (also known as symmetric configuration, i.e. $\omega = \theta$), the GI-XRD is distinguishable in the following aspects: (1) since the X-rays are incident at a glancing angle (ω), its pathway within the film is increased, as illustrated in Figure 7-6(a). Consequently, measurements become more

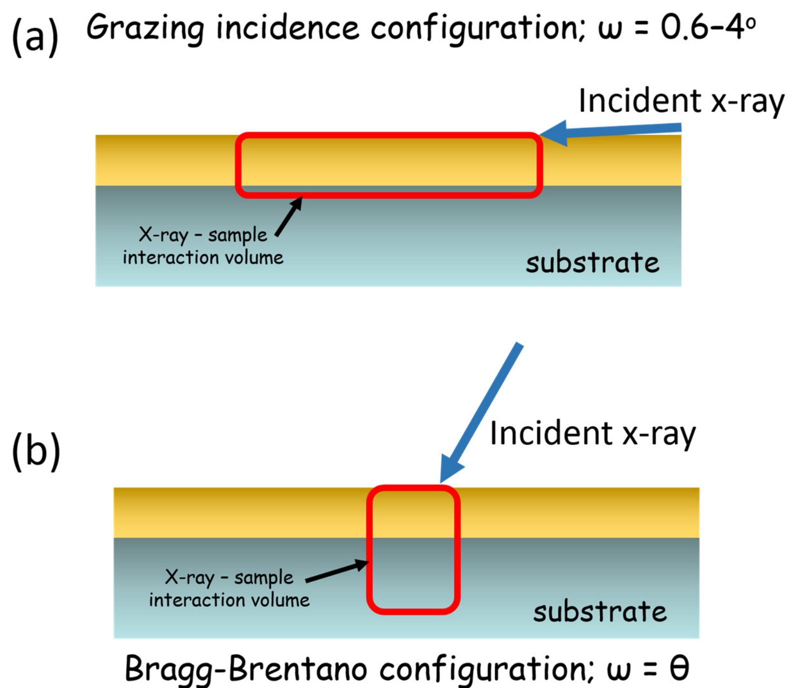

Figure 7-6 A schematic illustration of XRD measurements under (a) grazing incidence and (b) Bragg-Brentano configuration, respectively.

sensitive to the film and intense signals from the bulk substrate (if any) can be minimized or avoided completely and (2) under GI-XRD configuration, the diffraction peaks originate from tilted (and twisted) crystal planes and not from those that are parallel to the basal plane of the substrate. This scenario is illustrated schematically in Figure 7-7(a) and 7-7(b).

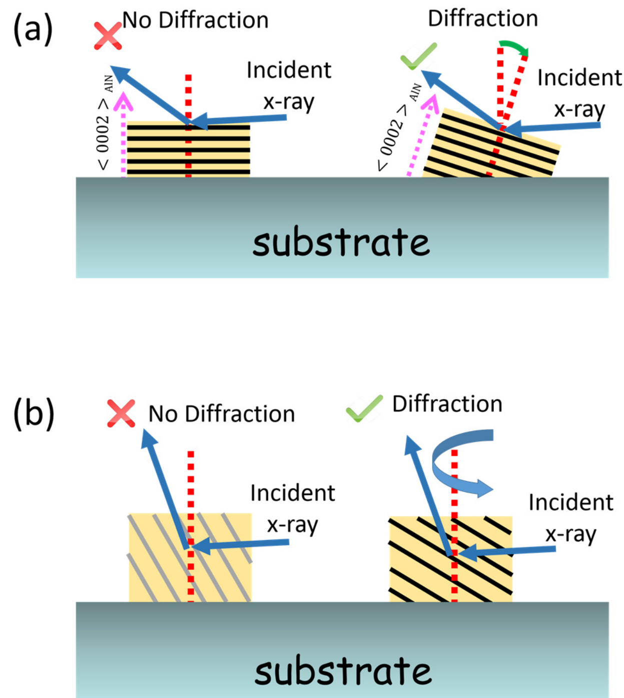

Figure 7-7 (a-b) Schematic illustration depicting how tilt and twist of crystal plains can affect diffraction under GI-XRD configuration, respectively.

For GI-XRD measurement of AlN films, the incidence angle, 'ω', was fixed at 0.6 º, while 2θ axis was scanned from 25 – 80 º. Figure 7-8 shows GI-XRD scans of different AlN films, including a blank sapphire substrate for reference. It can be observed that AlN grown directly on sapphire shows no peaks under GI-XRD configuration. This is not surprising, as it is comprised of well-oriented AlN grains with respect to the basal plane of sapphire, as governed by the strong epitaxial relation between the two. Some tilt and twist of the AlN grains is expected, which was measured using HR-XRD ω-scan, but not enough to produce a diffraction peak with an X-ray beam incident at a grazing angle. However, for AlN grown on hBN using

both 1-step and 2-step methods, more than one peak is recorded. Each of the two cases are discussed individually.

For 1-step AlN on hBN, the two distinct peaks at 36.02 and 66.03 ° are observed, corresponding to (0002) and ($10\bar{1}3$) planes and attributed to tilt and twist of the AlN grains, respectively. Furthermore, from the 2θ−ω scan under Bragg-Brentano geometry for 1-step AlN on hBN, as shown in Figure 7-4(d), no peaks other than (0002) and (0004) planes were observed. This implies that AlN layer is predominantly oriented such that most of the $(0002)_{AlN}$ crystal planes are parallel to the (0001) basal plane of the sapphire substrate. These crystal planes will not give rise to a diffraction

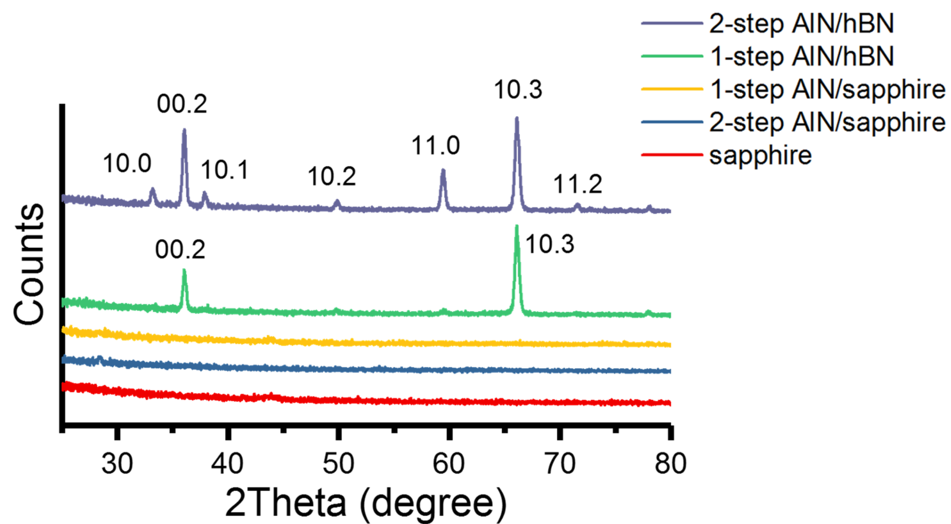

Figure 7-8 GI-XRD scans of 1-step and 2-step AlN grown on hBN and sapphire. The Miller indices of the diffractions peaks are indicated on the diffractogram.

peak under GI-XRD configuration, as described above. Only those $(0002)_{AlN}$ planes which are tilted by nearly 17.4° (for an X-ray incidence angle of 0.6°) with respect to basal plane will satisfy Bragg's diffraction condition, as illustrated in Figure 7-7(a). Such a large tilt of AlN grains is unusual in the case of AlN grown on sapphire, which explains the absence of the (0002) peak in GI-XRD scan for the same (both 1-step and 2-step growth). However, the (0002) peak is recorded for AlN grown on hBN. Therefore, it appears that a small fraction of $(0002)_{AlN}$ crystal planes are tilted by large angles, which give rise to the diffraction peak at 36.02° in Figure 7-8.

Similarly, the peak at 66.03° is attributed to in-plane twist of AlN grains. It is important to note that the $(10\overline{1}3)$ planes are already tilted, making an angle of 31.65°, with rest to the basal plane of the sapphire (or $(0001)_{AlN}$). Therefore, simply an in-plane twist of (a few of) the AlN grains is required to orient $(10\overline{1}3)$ planes such that, Bragg's diffraction condition is satisfied under GI-XRD, as illustrated in Figure 7-7(b). Furthermore, XRD pole figure measurements shown in Figure 7-4(a-c) clearly depict that AlN grains have a preferred in-plane orientation with respect to sapphire substrate, which is the same even when hBN is present between the two. The evidence for this preferential orientation is given by the appearance of six equally spaced diffraction spots for the $(10\overline{1}2)$ planes, as shown in Figure 7-4(a). If all of the AlN grains were rotated randomly in-plane, then, instead of the six diffraction spots, the data would consist of a continuous ring at ψ = 42 °. However, that is not the case. Hence, the presence of hBN sandwiched between AlN and sapphire, increases in-plane twist of some AlN grains which give rise to the $(10\overline{1}3)$ peak in GI-XRD. Such randomly oriented tilted and twisted AlN grains are likely to be present at the hBN-AlN interface.

On the other hand, multiple GI-XRD peaks are seen in Figure 7-8 for 2-step AlN grown on hBN using a low-temperature nucleation layer. In addition to the peaks associated with tilt and twist of AlN grains, it is likely, that the low mobility of Al atoms, at reduced temperature may cause random nucleation of the film. Consequently, the 2-step AlN layer has a much higher degree of disorder and a polycrystalline character. Thus, based on morphology and X-ray analyses done so far, it is clear that the standard 2-step process, involving a low-temperature nucleation layer is not suitable for AlN growth on hBN.

7.3.3 Multi-step AlN growth

In order to grow smooth AlN films on hBN, we adopted a multi-step growth process utilizing 3D and 2D growth modes, as described in [374, 375]. To prevent deposition of polycrystalline nuclei, growth was undertaken at high temperature only. Furthermore, under the growth conditions where both TMA and ammonia are introduced in the reactor simultaneously, AlN grows via a 3D mode that leads to formation of nanocolumns, as shown in Figure 7-3(a-b). To facilitate the coalescence of AlN grains, a 2D growth mode is utilized wherein, ammonia is pulsed into the reactor, whilst maintaining a continuous flow of TMA. A pulsed ammonia flow helps

overcome the low mobility of Al adatoms, increases their surface diffusion length and thus, promotes lateral growth. In the past, the flow modulation of growth precursors has been widely reported for depositing high quality AlN layers and has become central to several variations of epitaxial growth processes, namely migration-enhanced MOVPE, pulsed lateral overgrowth and flow modulation epitaxy [211, 212, 376, 377]. It is also important to note that due to ammonia pulsing, the average growth rates during 2D growth are less than achieved during 3D growth mode (for same precursor flux). Hence, 2D mode is only selectively applied for planarization of the growing film.

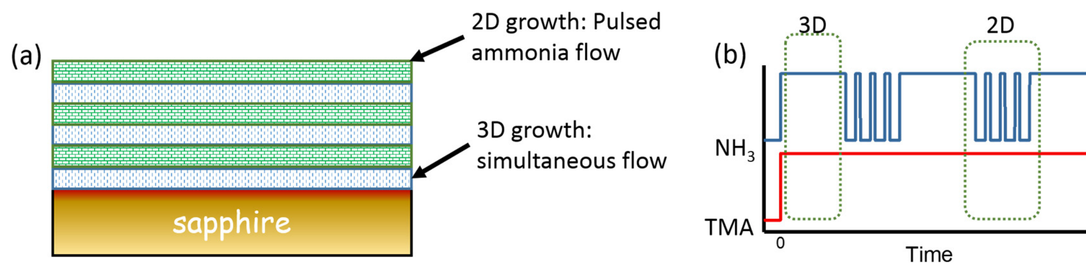

Figure 7-9 (a) Pulsed flow scheme employed in the multi-step growth process, (b) a schematic diagram representing the multi-step AlN layer grown on hBN/sapphire.

In the present study, a combination of alternating 3D and 2D growth modes is used to grow AlN on hBN and sapphire substrates, as illustrated schematically in Figure 7-9(a). The precursor flow sequence for 3D/2D growth mode is also shown schematically in Figure 7-9(b). For 3D growth, continuous flow conditions were the same as used for 1-step AlN growth (i.e. TMA flow and V/III ratio). Growth time was 5 minutes with overall growth rate of 1.6 μm/hr. For 2D growth, only ammonia was pulsed into the reactor. Each pulse cycle was 9 seconds long, of which ammonia was turned on for 3 seconds. TMA flow was also reduced to 33 μmol/min during pulsed growth. A total of 60 pulse cycles were completed, before switching again to 3D growth conditions. The 3D-2D process was alternated to deposit a total of 900 nm thick AlN.

Figure 7-10(a) and 7-10(b) show the plan-view SEM images of AlN grown on sapphire and hBN substrates using the multi-step process, respectively. A significant improvement in the surface morphology of AlN layers can be noted. Previously, 1-

step AlN growth on hBN and sapphire at high-temperatures resulted in rough surface with conical nanocolumns, due to formation of inversion domains. With the help of multi-step growth technique and improved migration of Al-atoms, the overall surface of AlN is flat on both substrates. Some hexagonal shaped AlN grains (with a flat top) can be identified in Figure 7-10(a), which have not yet coalesced. Further optimization of the 2D growth step is required. Furthermore, the multi-step growth process also improved the crystallinity of the AlN films. Switching between 3D to 2D growth modes causes the dislocations to merge or bend, resulting in an overall decrease in dislocation density. HR-XRD ω-scans of (0002) and ($10\bar{1}2$) planes for multi-step AlN layer grown on sapphire and hBN are shown in Figure 7-10(c) and 7-10(d), respectively, while the FWHM values are summarized in Table 7-1 for comparison. Based on the data in Table 1, the multi-step growth process consistently provides AlN film with reduced dislocation density. For instance, the FWHM of (0002) XRC reduced from 1374 arcsec for 1-step AlN on sapphire to 260 arcsec for multi-step AlN on sapphire. Similar improvement has been observed for AlN growth on hBN. However, the FWHM values for AlN growth on hBN are consistently larger than for AlN on sapphire and need further improvement.

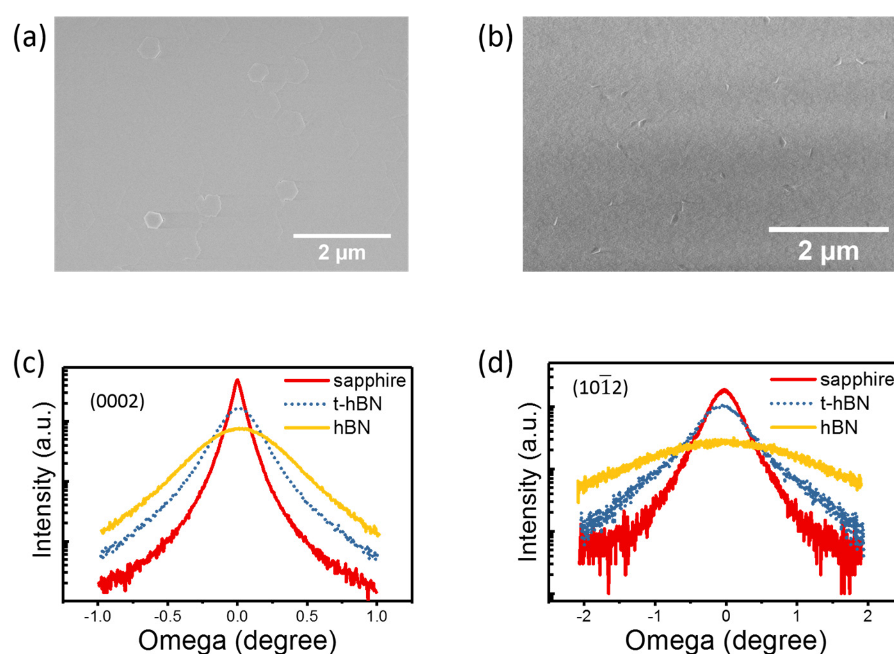

Figure 7-10 (a-b) SEM images of multi-step AlN grown on sapphire and hBN, respectively. (c-d) HR-XRD ω-scans for (0002) and ($10\bar{1}2$) planes of AlN grown on hBN and sapphire using multi-step process, respectively. t-hBN stands for sample where a thin hBN layer was grown. XRD plots are shown on logarithmic scale.

7.4 Delamination/Peeling-off AlN films

Multi-step, planar AlN films grown on hBN were easy to delaminate from the substrate using Scotch™ tape (3M, USA). In some instances, the AlN film delaminated spontaneously and is explained as follows. We observed that during wafer handling, AlN film starts to delaminate at the edge of the wafer, where the substrate was held with tweezers. Mechanical handling may result in the (unintentional) application of shear force on AlN, causing it to separate from the sapphire substrate due to the presence of hBN. Once the delamination is initiated locally, it gradually spreads freely through the whole substrate. Figure 7-11(a) shows a photograph of a 2" wafer with AlN film grown on hBN. The delaminated region can be easily identified with naked eye and only a small region can be seen to remain adhered to the substrate (indicated by arrow). The entire AlN film in Figure 7-11(a) is intact as one piece, even after delamination. In general, epitaxially grown III-nitride films on sapphire are known to be under biaxial compressive stress, due to a mismatch in the coefficient of thermal expansion between the film and substrate. A thermal compressive stress develops in the as-grown films during cool down from growth temperatures [378]. In Chapter 4, water assisted self-delamination of MOVPE-grown hBN on sapphire substrates has been described [208]. With the help of Raman spectroscopy, it was shown that hBN delamination was accompanied with a relaxation in compressive strain observed in as-grown hBN layers. The observed delamination of AlN, facilitated by hBN, may also be driven by strain relaxation.

To analyse the residual strain, Raman spectra were collected from adhered and delaminated AlN regions (for sample shown in Figure 7-11(a)), as shown in Figure 7-11(b). For the adhered region, two strong peaks at 660 and 751 cm^{-1} are seen, which correspond to the E_2 (high) mode of AlN [379, 380] and E_g mode of sapphire [381], respectively. A weak peak at 1371 cm^{-1} corresponds to the E_{2g} mode of hBN (~ 1.5 nm thick). Compared to experimentally measured E_2 (high) values for unstrained AlN (at 657.4 cm^{-1}), the corresponding Raman peak for AlN (adhered region) is shifted to higher frequencies and is consistent with presence of compressive strain in MOVPE grown AlN on sapphire.

Raman spectrum from the delaminated region is also shown in Figure 7-11(b). A few points are to be noted here. Firstly, while the E_2 (high) peak for AlN is present, the E_g sapphire peak at 751 cm^{-1} is much weaker. This is most likely due to the

substrate not being in the same focal plane as the delaminated AlN, with respect to incident laser beam. Secondly, the E_{2g} peak for hBN, shown in the inset in Figure 7-11(b), can still be observed. This indicates that some of the hBN remains attached to AlN after it separates from the substrate. Based on this, it is reasonable to assume that the entire AlN has been successfully separated from the sapphire substrate along with some underlying hBN. Thirdly, the E_2 (high) peak for delaminated AlN is red-shifted by almost 2.5 cm^{-1}. For clarity and ease of comparison, the E_2 (high) peak for adhered and delaminated AlN are plotted separately in Figure 7-11(c). The grey line in Figure 7-11(c) represents the reference value of unstrained AlN reported in literature [379, 380]. These results suggest that the compressive stress in as-grown AlN on hBN is the same as that on sapphire. Upon delamination, a relaxation in compressive stress ensues, with the E_2 (high) phonon value for the delaminated AlN becoming nearly same as that of unstrained AlN. The observed results are consistent with similar studies on GaN growth on hBN as reported by Paduano et al. and Ayari et al., wherein stress relaxation in GaN is observed upon exfoliation of the layers [94, 98].

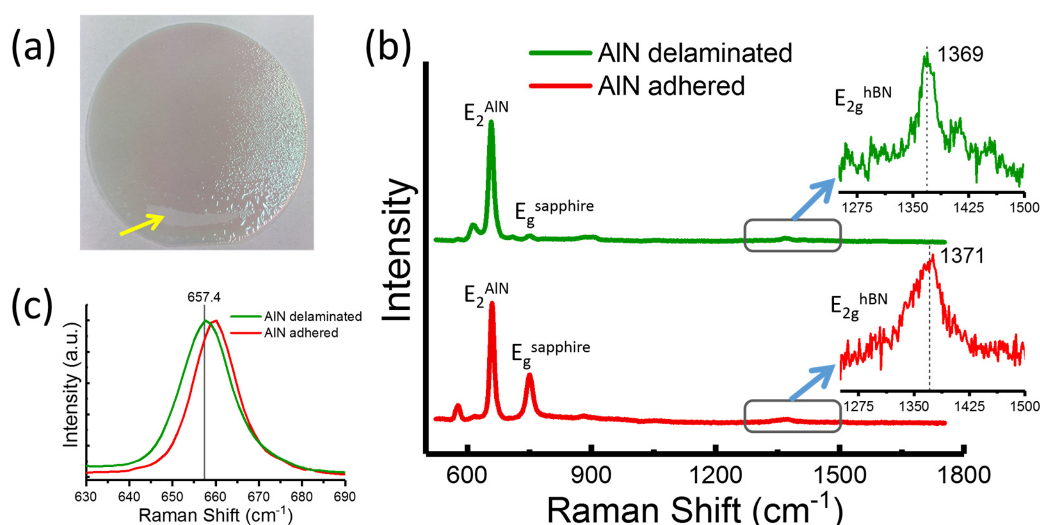

Figure 7-11 (a) A photograph of an entire 2” wafer with AlN layer deposited on hBN. The AlN film has delaminated from the underlying sapphire substrate baring a small region near the bottom, indicated by the arrow. (b) Raman spectra of the sample shown in (a), taken from adhered and delaminated regions. The two insets show the Raman peak of hBN for clarity, (c) Raman spectra of AlN in (b) are replotted to show the red-shift in E_2 (high) peak position of AlN upon delamination.

7.5 Effect of hBN thickness on AlN growth

It is apparent that hBN plays an important role in the growth of AlN. Compared to hydrogen annealed sapphire substrate, the surface roughness of hBN is nearly six-times higher, with wrinkles clearly visible in Figure 7-1(b). Furthermore, with reduced adatom mobility, AlN grown on hBN suffers from a higher dislocation density, indicated by large FWHM of XRCs. Thus, thickness and surface roughness of hBN are likely to have strong influence on the morphology and crystallinity of epitaxially grown layers on it. In a recent study, Snure et al. reported on the 'self-separation' of GaN films grown on hBN (on sapphire substrates) using MOVPE [366]. GaN films grown on rough hBN films comprise of randomly oriented 3D BN nuclei, which can easily self-separate from sapphire.

In the present study, AlN grown on thicker hBN layers resulted in outright delamination. Figure 7-12(a) shows an AFM image of a 10 nm-thick hBN layer deposited using the flow-modulation scheme, described in Chapter 4. With an increase in thickness of the hBN layer, the surface roughness of the film also increases. Due to fast delamination, structural analysis of the AlN (1-step) layers grown on it could not be performed. Furthermore, the slow hBN growth rates necessitate longer deposition times to achieve thick hBN films. More importantly, the crystallinity of AlN on thicker hBN decreases, as discussed below. Therefore, the use of thick hBN for AlN growth lacks any merit and thus, was not pursued any further.

However, by using a thinner hBN (t-hBN), the quality of AlN grown on it was improved further. Figure 7-12(b) shows the AFM image of a t-hBN layer deposited for one hour using a TEB flux of 30 μmol/min, as opposed to 60 μmol/min, used for the growth of hBN in this study. The Raman spectrum of this film is also shown in Figure 7-1(c). A lower E_{2g} band intensity suggests that the hBN layer deposited with a TEB flux of 30 μmol/min is thinner. The absence of wrinkles further reduces the surface roughness of the hBN film. Figure 7-12(c) shows SEM images of AlN grown on t-hBN using the same multi-step approach. The overall surface of the AlN layer is planar. Hexagonal grains can be identified, which are similar to the AlN grains observed when AlN is grown directly on sapphire (Figure 7-10(a)), as discussed above. With the use of a thinner and smoother hBN layer, the crystallinity of the AlN grown on top of it also improved, as indicated by the reduced FWHM of XRC. Figure 7-12(d)

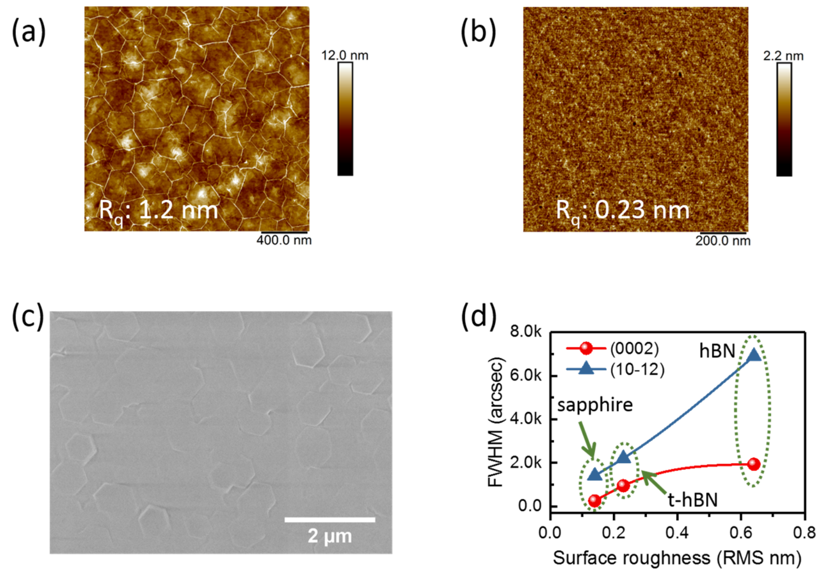

Figure 7-12 (a) AFM of a 10 nm thick hBN film deposited using FM scheme, (b) AFM of t-hBN film (~ 1nm) deposited using a lower TEB flux of 30 µmol/min, (c) SEM image of multi-step AlN grown on t-hBN and (d) FWHM of multi-step AlN grown on sapphire, hBN and t-hBN as a function of surface roughness of the three substrates.

shows the direct relation between the FWHM values from the XRCs obtained for AlN and the overall surface roughness of the substrate (hBN or sapphire). As the surface roughness of the substrate decreases, the crystallinity of AlN increases. In addition to surface roughness, a thicker hBN may weaken the epitaxial relation between AlN and sapphire and increase defect density.

7.6 Summary

The growth of AlN films using MOVPE on hBN and sapphire substrates was investigated under various conditions. AlN grown on hBN using the two-step process, involving nucleation at low temperature was polycrystalline in nature. On the other hand, direct AlN growth at high temperatures led to the formation of mixed polarity nanocolumns. A multi-step growth process involving a pulsed ammonia flow was utilized for growing smooth AlN films on hBN. Both, the surface roughness and the thickness of hBN play a critical role in the deposition of AlN films. As the thickness and surface roughness of hBN increased, the dislocation density in AlN increased, as indicated by XRD measurements. It was found that AlN layers grown on hBN could be easily separated from sapphire. AlN delamination is also accompanied by a

relaxation in the compressive strain in the AlN layer, as measured with the help of Raman spectroscopy. The present work opens new opportunities for utilizing AlN layers, grown on hBN, as templates for the development of flexible deep-UV optoelectronic devices.

Chapter 8. Conclusions and future work

8.1 Outcomes

This thesis systematically investigates wafer-scale growth of hBN on sapphire substrates using MOVPE. The effect of various MOVPE process parameters, such as, temperature, V/III ratio, precursor and carrier gas flow rates on hBN growth was carefully studied. Through this, it is apparent that hBN growth is significantly different from the growth of conventional III-nitrides, such as AlN, GaN and InN. The following are three distinguishable aspects of hBN growth:-

1. The severity of parasitic reactions between precursors – Parasitic reactions between NH_3 and organometallic precursors generally tend to increase with a reduction in the size of group-III atoms (i.e. In < Ga < Al < B) [382, 383]. However, its severity is unprecedented in the case of hBN growth. For example, under continuous flow conditions, where both TEB and ammonia are introduced in the reaction chamber simultaneously, hBN growth rates are extremely low (~ 1.5 nm/hr). These values are nearly three orders of magnitude smaller than the typical growth rates for AlN or GaN.

2. High growth temperatures – The results obtained in this study and those reported previously in literature, emphasize that high temperatures (in excess of 1500 ^{o}C) are more suitable for hBN growth, especially on non-lattice matched substrates such as sapphire (or SiC) [203, 250, 269]. Growth temperature is found to have a direct influence on hBN's crystallinity, surface morphology and impurity incorporation in the film. In this study, the growth temperatures were restricted to 1330 ^{o}C.

3. High levels of carbon incorporation – In context of III-nitride growth, the strength of covalent bonds between group-III and impurities atoms (C and O) increases with a decrease in atomic size (i.e. B-X > Al-X > Ga-X > In-X, where X is impurity atom). Consequently, the use of an organometallic compound (TEB) as boron precursor makes it much more difficult to minimize impurities from getting incorporated in hBN during growth, than in case of other III-nitrides. This has a significant impact on hBN's optical properties.

In the present study, these growth challenges were overcome to some extent by adopting the FM scheme. Parasitic reactions between ammonia and TEB were reduced significantly by pulsing the flow of the two growth precursors, leading to significant improvements in the growth rate and surface morphology of the hBN films. The layered stacking of $(0002)_{hBN}$ planes and their parallel orientation with respect to the basal plane of sapphire were confirmed with the help of cross-sectional HR-TEM. Wrinkles were a prominent feature of hBN films and they form because of thermal compressive strain arising from a mismatch of CTE between sapphire and hBN. Furthermore, in the HR-TEM images, the $(0002)_{hBN}$ lattice planes were observed to bend and conformed to the shape of wrinkles, whilst remaining parallel with respect to each other. This strongly indicates that wrinkles were most likely formed during sample cooling, post growth at 1330 °C. Along with wrinkles, nanometer-sized, debris-like features were also observed in the AFM scans of the hBN films. Using plan-view TEM, these were identified as randomly oriented 3D hBN particles, which were formed as a result of parasitic reactions between precursors.

From XPS, carbon was identified as the dominant impurity in the hBN film. Its concentration increased with an increase in TEB flux, resulting in a direct relationship between carbon doping and the growth rate of hBN. Hence, carbon incorporation could only be minimized by growing hBN at extremely low rates (< 4 nm/hr) by using the lowest configurable TEB flux (@ 10 μmol/min). Overall, under the best conditions, hBN films up to 40 nm thick could be deposited on sapphire using FME.

Water assisted self-delamination of the as-grown hBN films (thickness > 15 nm) from sapphire was also observed, as described in Chapter 4. A lack of covalent bonding between the film and the substrate, combined with differential wetting of a hydrophobic hBN and a hydrophilic sapphire, caused by DI water, facilitated the separation of the two. This provides a chemical-free method for transferring hBN films onto desired substrates. Interestingly, delamination was accompanied by flattening of wrinkles and a relaxation in compressive strain, which were observed by AFM and Raman spectroscopy, respectively, in hBN films transferred on to SiO_2/Si substrates. For the transfer of thinner hBN films, (which do not self-delaminate), a wet-chemical process was specifically designed. Both the processes are versatile, by which cm-sized hBN films could be readily transferred on to plain, textured or patterned substrates.

The optical properties of MOVPE-hBN were also studied in detail and found to be significantly affected by carbon incorporation. Due to high carbon impurity levels, no measurable NBE luminescence could be recorded from them. Instead, the emission spectrum of MOVPE-hBN was dominated by impurity related sub-bandgap UV luminescence. hBN samples also showed photoluminescence at visible wavelengths between 570-750 nm (rPL). The rPL intensity showed a strong dependence on the TEB flux. The recent discovery of quantum emitters in hBN has opened up new avenues for its application to the field of quantum computing. A number of stable SPEs were also found in MOVPE-grown hBN films that showed negligible rPL. The PL spectrum of each emitter consists of a primary well-defined peak at 590 nm (± 10 nm), which is the ZPL, followed by a phonon side band, red-shifted by 0.17 eV. The life time of emitters were of the order of few nanoseconds and is consistent with previously reported values. Such wafer-scale MOVPE- grown hBN films are ideal for monolithic integration and will prove to be well-suited for optoelectronic/photonic quantum technology based devices.

hBN is well-known for its high thermal and chemical stability. In this study, MOVPE-hBN films were utilized for the passivation of silver nanoparticles and their protection from oxidation. Being atomically thin and flexible, hBN was able to effectively wrap around Ag nanoparticles to form an impermeable barrier that prevented oxygen from attacking the Ag NPs. The plasmonic activity of hBN covered Ag NPs, remains preserved even when samples were annealed at 400°C in air, as demonstrated through SERS. Under similar conditions, the SERS sensitivity for bare Ag NPs decreased significantly because of oxidation. Large-area applications of hBN films was showcased through droplet based SERS platform, which combined the benefits of parallel processing, minimal reagent consumption and faster analysis. It also exemplified more practicable applications of hBN films. Similarly, in the foreseeable future, such large-area hBN films can be utilized for protecting metal NPs in commercially available SERS substrates, which can help increase their shelf-life.

Epitaxial growth of AlN on hBN/sapphire substrates was investigated, with the aim of developing templates for flexible deep-UV optoelectronic devices. AlN was grown on hBN under different conditions. XRD analysis of the grown samples revealed that AlN films grown on hBN using the conventional 2-step process (involving nucleation at low temperature) were polycrystalline. On the other hand,

AlN grown directly at high temperatures resulted in the formation of AlN nanocolumns with mixed polarity and a rough surface morphology. With the help of a high temperature, multi-step AlN growth process using a pulsed ammonia flow sequence, smooth AlN layers with improved crystallinity were obtained. The overall defect density of AlN grown on hBN was consistently higher than on sapphire and needs further improvement. The surface roughness and thickness of hBN were also found to have a significant impact on the defect density of AlN films. As thickness and surface roughness of underlying hBN increased, the dislocations in AlN also increased. AlN films grown on hBN could be exfoliated from bulk sapphire with relative ease using adhesive tape. Raman spectroscopy of delaminated AlN showed a relaxation in compressive strain, which could prove to be beneficial for device performance.

8.2 Recommendations for future work

In this work, wafer-scale growth and characterization of hBN using MOVPE has been investigated. Preliminary work on different applications of hBN, ranging from SPE to SERS and van der Waals epitaxial growth of AlN have also been presented. The next step would be to further explore some of the applications in greater detail. In addition to this, the present study provides opportunities for new investigations, some of which are recommended as follows:-

8.2.1 Improving the quality of hBN films

In this thesis, wafer-scale, multilayer hBN films were deposited on sapphire substrates using MOVPE. The hBN films have a partially turbostratic nature due to in-plane rotation of lattice planes, with respect to the underlying layers, as described in section 4.4. In addition to this, due to relatively high carbon incorporation (as impurity) in hBN during growth, the band edge luminescence (~ 215 nm) could not be observed. Hence, there is an enormous scope for future research work that can be undertaken to further improve the crystallinity of the hBN layers, with the ultimate aim of being able to deposit wafer-scale single-crystal hBN films. For this, several avenues may be explored. One such is undertaking hBN deposition on lattice matched substrates. Although, wafer-scale lattice matched 2D substrates are likely to be unavailable, alternatively, hBN growth on pseudo-2D substrates can be explored. An example of this is graphitized SiC. Previous studies have shown that high temperature annealing

of SiC substrate can result in the formation of epitaxial, single crystal graphene layers on the surface of the substrate (due to sublimation of Si atoms) [346, 384, 385]. Since graphene is lattice matched to hBN, it may serve as a valuable substrate and an attractive alternative to sapphire for hBN deposition. Similarly, use of a low-carbon boron precursor, such as TMB may also be explored for hBN deposition, instead of TEB used in the present study.

8.2.2 Alloying of hBN

The ability to form alloys is an important aspect of III-V semiconductors. By adjusting alloy composition, the bandgap and emission wavelengths can be tuned easily. In the context of hBN, due to its unique two-dimensional structure akin to graphene, several attempts have been made to alloy the two materials for bandgap engineering. Initial studies have revealed that although alloying of the two materials is possible, only 'dilute' alloys of $hBN_x(C_2)_{1-x}$ can be obtained [386, 387]. A 'dilute' alloy means that the concentration of either hBN or graphene in the resulting alloy is low. At higher concentrations, phase separation ensues, resulting in the formation of individual clusters of hBN and graphene. However, so far, alloying of hBN with other III-nitrides has hardly been explored. In future, dilute alloying of boron with AlN or GaN can be investigated, as a means of bandgap engineering.

8.2.3 Doping

p- and n-doping of III-V semiconductors is central to the solid-state devices such as LEDs, laser diodes, detectors or sensors. In III-nitrides, Mg is used as the dopant to create p-type material. However, p-doping of III-nitrides remains challenging due to the very large acceptor activation energy, which increases from 170 meV in GaN to 530 meV in AlN, resulting in low hole concentrations. This is a serious obstacle in the development of high efficiency deep UV LEDs using Al-rich III-nitride alloys. Recently, p-doping of hBN with magnesium has been reported [200, 221]. It was found that the acceptor ionization energies in hBN (30 meV) were an order of magnitude smaller than in AlN, and hole concentrations as high as 10^{18} cm^{-3} in p-hBN could be obtained. This makes the highly conductive p-hBN, with a large bandgap, very attractive for hetero-junction device applications. Hence, p-doping of hBN should be studied in greater detail. Due to the 2D lattice and associated structural anisotropy in hBN, it is reasonable to expect that the electrical conduction properties of the doped

samples will also be anisotropic. Therefore, the electrical conductivity in-plane and through-plane in p-hBN will have to be examined carefully. Similarly, recent attempts towards achieving n-hBN via substitutional doping of silicon atoms have been largely unsuccessful [388]. Hence, alternatives to silicon, for achieving n-doped hBN need to be investigated.

8.2.4 Flexible optoelectronic devices

In the present study, high-quality, smooth AlN films have been successfully deposited on hBN/sapphire substrates. Preliminary studies have indicated that growth temperature and thickness of hBN play a crucial role in determining the overall quality of AlN. Defect density of AlN grown on hBN is still higher than that grown on sapphire. Hence, further optimization of AlN growth conditions on hBN is needed to reduce the dislocation density. Thereafter, growth of AlGaN can be explored, including deposition of doped (p/n- type) and quantum wells layers for fabricating deep UV LEDs. In addition to this, wafer-scale hBN can also be used as templates for van der Waals epitaxial growth of thin films or nanostructures of other III-V or II-VI semiconductors.

8.2.5 Quantum emitters

The optical properties of MOVPE-hBN are significantly affected by carbon incorporation due to the use of TEB as boron precursor. Strong PL at visible wavelengths, observed from hBN grown using large TEB flux, has not been reported thus far. Results so far once again point towards the role of carbon incorporation. It is likely that carbon occupies multiple deep-level states with the bandgap, which give rise to impurity related emissions. Interestingly, the shape of PL spectra of rPL from MOVPE-hBN showed close resemblance to the PL spectrum of a typical SPE in hBN. Although the nature of defects responsible for quantized emission from hBN is not exactly known, there is growing evidence in the literature indicating towards the role of carbon atoms. It remains to be seen whether there is any commonality between defects responsible for SPE in hBN and that giving rise to rPL in MOVPE-hBN. Determining the nature of defects is crucial for deterministic creation of SPE in hBN. Compared to other deposition/bulk synthesis processes, MOVPE is uniquely positioned in this scheme of things, as it provides control over the level of carbon incorporation in hBN (to some extent), achieved through controlling TEB flux. Future

studies can be aimed towards uncovering the nature of carbon incorporation in hBN, which will help in developing a holistic understanding of impurity related optical properties of hBN.

In conclusion, it can be emphasized once again that hBN is truly a fascinating material with many remarkable properties. The detailed experimental study undertaken in this dissertation provides valuable insights into the growth, properties and applications of hBN, which along with other 2D materials is a relatively new and emerging field. With further advances, wafer-scale hBN has the potential to serve as an ideal platform for the development of new generation of flexible optoelectronic devices.

References

1. Limited, D.A.P.S. *Semiconductors - the next wave*. 2019; Available from: https://www2.deloitte.com/content/dam/Deloitte/tw/Documents/technology-media-telecommunications/tw-semiconductor-report-EN.pdf.
2. Nobelprize.org. *The Nobel Prize in Physics 2014*. Available from: https://www.nobelprize.org/nobel_prizes/physics/laureates/2014/.
3. *Solid-State Lighting Research and Development: Multi-Yera Program Plan*, U.S.D.o. Energy, Editor. 2014.
4. Moore, G.E., *Cramming more components onto integrated circuits, Reprinted from Electronics, volume 38, number 8, April 19, 1965, pp.114 ff.* IEEE Solid-State Circuits Society Newsletter, 2006. **11**(3): p. 33-35.
5. Fiori, G., F. Bonaccorso, G. Iannaccone, T. Palacios, D. Neumaier, A. Seabaugh, S.K. Banerjee, and L. Colombo, *Electronics based on two-dimensional materials.* Nature Nanotechnology, 2014. **9**(10): p. 768-779.
6. Yu, K.J., Z. Yan, M. Han, and J.A. Rogers, *Inorganic semiconducting materials for flexible and stretchable electronics.* NPJ Flexible Electronics, 2017. **1**(1): p. 4.
7. Kim, S.J., K. Choi, B. Lee, Y. Kim, and B.H. Hong, *Materials for Flexible, Stretchable Electronics: Graphene and 2D Materials.* Annual Review of Materials Research, 2015. **45**(1): p. 63-84.
8. Novoselov, K.S., A.K. Geim, S.V. Morozov, D. Jiang, Y. Zhang, S.V. Dubonos, I.V. Grigorieva, and A.A. Firsov, *Electric field effect in atomically thin carbon films.* Science, 2004. **306**(5696): p. 666-669.
9. Kalantar-zadeh, K., J.Z. Ou, T. Daeneke, M.S. Strano, M. Pumera, and S.L. Gras, *Two-Dimensional Transition Metal Dichalcogenides in Biosystems.* Advanced Functional Materials, 2015. **25**(32): p. 5086-5099.
10. Xia, F., H. Wang, D. Xiao, M. Dubey, and A. Ramasubramaniam, *Two-dimensional material nanophotonics.* Nature Photonics, 2014. **8**(12): p. 899-907.
11. Geim, A.K. and K.S. Novoselov, *The rise of graphene.* Nature Materials, 2007. **6**(3): p. 183-191.
12. Novoselov, K.S., V.I. Fal'ko, L. Colombo, P.R. Gellert, M.G. Schwab, and K. Kim, *A roadmap for graphene.* Nature, 2012. **490**(7419): p. 192-200.
13. Lee, C., X. Wei, J.W. Kysar, and J. Hone, *Measurement of the Elastic Properties and Intrinsic Strength of Monolayer Graphene.* Science, 2008. **321**(5887): p. 385-388.
14. Falin, A., Q. Cai, E.J.G. Santos, D. Scullion, D. Qian, R. Zhang, Z. Yang, S. Huang, K. Watanabe, T. Taniguchi, M.R. Barnett, Y. Chen, R.S. Ruoff, and L.H. Li, *Mechanical properties of atomically thin boron nitride and the role of interlayer interactions.* Nature Communications, 2017. **8**: p. 15815.
15. Ashton, M., J. Paul, S.B. Sinnott, and R.G. Hennig, *Topology-Scaling Identification of Layered Solids and Stable Exfoliated 2D Materials.* Physical Review Letters, 2017. **118**(10): p. 106101.
16. Geim, A.K. and I.V. Grigorieva, *Van der Waals heterostructures.* Nature, 2013. **499**(7459): p. 419-425.

17. Dean, C.R., A.F. Young, I. Meric, C. Lee, L. Wang, S. Sorgenfrei, K. Watanabe, T. Taniguchi, P. Kim, K.L. Shepard, and J. Hone, *Boron nitride substrates for high-quality graphene electronics.* Nature Nanotechnology, 2010. **5**(10): p. 722-726.
18. Du, X., I. Skachko, A. Barker, and E.Y. Andrei, *Approaching ballistic transport in suspended graphene.* Nature Nanotechnology, 2008. **3**: p. 491.
19. Balandin, A.A., *Thermal properties of graphene and nanostructured carbon materials.* Nature Materials, 2011. **10**(8): p. 569-581.
20. Sharma, A., H. Yan, L. Zhang, X. Sun, B. Liu, and Y. Lu, *Highly Enhanced Many-Body Interactions in Anisotropic 2D Semiconductors.* Accounts of Chemical Research, 2018. **51**(5): p. 1164-1173.
21. Mueller, T. and E. Malic, *Exciton physics and device application of two-dimensional transition metal dichalcogenide semiconductors.* npj 2D Materials and Applications, 2018. **2**(1): p. 29.
22. Mak, K.F. and J. Shan, *Photonics and optoelectronics of 2D semiconductor transition metal dichalcogenides.* Nature Photonics, 2016. **10**(4): p. 216-226.
23. Novoselov, K.S., D. Jiang, F. Schedin, T.J. Booth, V.V. Khotkevich, S.V. Morozov, and A.K. Geim, *Two-dimensional atomic crystals.* Proceedings of the National Academy of Sciences of the United States of America, 2005. **102**(30): p. 10451.
24. Huang, Y., E. Sutter, N.N. Shi, J. Zheng, T. Yang, D. Englund, H.-J. Gao, and P. Sutter, *Reliable Exfoliation of Large-Area High-Quality Flakes of Graphene and Other Two-Dimensional Materials.* ACS Nano, 2015. **9**(11): p. 10612-10620.
25. Jeong, H., H.M. Oh, S. Bang, H.J. Jeong, S.-J. An, G.H. Han, H. Kim, S.J. Yun, K.K. Kim, J.C. Park, Y.H. Lee, G. Lerondel, and M.S. Jeong, *Metal–Insulator–Semiconductor Diode Consisting of Two-Dimensional Nanomaterials.* Nano Letters, 2016. **16**(3): p. 1858-1862.
26. Wang, S., J. Wang, W. Zhao, F. Giustiniano, L. Chu, I. Verzhbitskiy, J. Zhou Yong, and G. Eda, *Efficient Carrier-to-Exciton Conversion in Field Emission Tunnel Diodes Based on MIS-Type van der Waals Heterostack.* Nano Letters, 2017. **17**(8): p. 5156-5162.
27. Britnell, L., R.M. Ribeiro, A. Eckmann, R. Jalil, B.D. Belle, A. Mishchenko, Y.J. Kim, R.V. Gorbachev, T. Georgiou, S.V. Morozov, A.N. Grigorenko, A.K. Geim, C. Casiraghi, A.H.C. Neto, and K.S. Novoselov, *Strong Light-Matter Interactions in Heterostructures of Atomically Thin Films.* Science, 2013. **340**(6138): p. 1311.
28. Pospischil, A., M.M. Furchi, and T. Mueller, *Solar-energy conversion and light emission in an atomic monolayer p-n diode.* Nature Nanotechnology, 2014. **9**(4): p. 257-261.
29. Das, S., R. Gulotty, A.V. Sumant, and A. Roelofs, *All Two-Dimensional, Flexible, Transparent, and Thinnest Thin Film Transistor.* Nano Letters, 2014. **14**(5): p. 2861-2866.
30. Ng, L.W.T., G. Hu, R.C.T. Howe, X. Zhu, Z. Yang, C.G. Jones, and T. Hasan, *2D Material Production Methods*, in *Printing of Graphene and Related 2D Materials: Technology, Formulation and Applications*. 2019, Springer International Publishing: Cham. p. 53-101.
31. Li, H., J. Wu, X. Huang, G. Lu, J. Yang, X. Lu, Q. Xiong, and H. Zhang, *Rapid and Reliable Thickness Identification of Two-Dimensional Nanosheets Using Optical Microscopy.* ACS Nano, 2013. **7**(11): p. 10344-10353.

32. Zheng, C.X., Z.Q. Xu, Q.H. Zhang, M.T. Edmonds, K. Watanabe, T. Taniguchi, Q.L. Bao, and M.S. Fuhrer, *Profound Effect of Substrate Hydroxylation and Hydration on Electronic and Optical Properties of Monolayer MoS2.* Nano Letters, 2015. **15**(5): p. 3096-3102.
33. Liu, Z., Y. Gong, W. Zhou, L. Ma, J. Yu, J.C. Idrobo, J. Jung, A.H. MacDonald, R. Vajtai, J. Lou, and P.M. Ajayan, *Ultrathin high-temperature oxidation-resistant coatings of hexagonal boron nitride.* Nature Communications, 2013. **4**: p. 2541.
34. Li, L.H., T. Xing, Y. Chen, and R. Jones, *Boron Nitride Nanosheets for Metal Protection.* Advanced Materials Interfaces, 2014. **1**(8): p. 1300132.
35. Cai, Q., S. Mateti, W. Yang, R. Jones, K. Watanabe, T. Taniguchi, S. Huang, Y. Chen, and L.H. Li, *Boron Nitride Nanosheets Improve Sensitivity and Reusability of Surface-Enhanced Raman Spectroscopy.* Angewandte Chemie International Edition, 2016. **55**(29): p. 8405-8409.
36. Tran, T.T., K. Bray, M.J. Ford, M. Toth, and I. Aharonovich, *Quantum emission from hexagonal boron nitride monolayers.* Nat Nano, 2016. **11**(1): p. 37-41.
37. Watanabe, K., T. Taniguchi, and H. Kanda, *Direct-bandgap properties and evidence for ultraviolet lasing of hexagonal boron nitride single crystal.* Nature Materials, 2004. **3**(6): p. 404-409.
38. Caldwell, J.D., I. Aharonovich, G. Cassabois, J.H. Edgar, B. Gil, and D.N. Basov, *Photonics with hexagonal boron nitride.* Nature Reviews Materials, 2019.
39. Calman, E.V., M.M. Fogler, L.V. Butov, S. Hu, A. Mishchenko, and A.K. Geim, *Indirect excitons in van der Waals heterostructures at room temperature.* Nature Communications, 2018. **9**(1): p. 1895.
40. Balmain, W.H., *XLVI. Observations on the formation of compounds of boron and silicon with nitrogen and certain metals.* The London, Edinburgh, and Dublin Philosophical Magazine and Journal of Science, 1842. **21**(138): p. 270-277.
41. Bundy, F.P. and J.S. Kasper, *Hexagonal Diamond—A New Form of Carbon.* The Journal of Chemical Physics, 1967. **46**(9): p. 3437-3446.
42. Pan, Z., H. Sun, Y. Zhang, and C. Chen, *Harder than Diamond: Superior Indentation Strength of Wurtzite BN and Lonsdaleite.* Physical Review Letters, 2009. **102**(5): p. 055503.
43. Qingkun, L., S. Yi, L. Zhiyuan, and Z. Yu, *Lonsdaleite – A material stronger and stiffer than diamond.* Scripta Materialia, 2011. **65**(3): p. 229-232.
44. Topsakal, M., E. Aktürk, and S. Ciraci, *First-principles study of two- and one-dimensional honeycomb structures of boron nitride.* Physical Review B, 2009. **79**(11): p. 115442.
45. Tour, A.S.a.J.M. *Graphene Electronics, Unzipped*. 2010 [cited 2019 18 September]; Available from: https://spectrum.ieee.org/semiconductors/materials/graphene-electronics-unzipped.
46. Pease, R.S., *An X-ray study of boron nitride.* Acta Crystallographica, 1952. **5**(3): p. 356-361.
47. Ooi, N., V. Rajan, J. Gottlieb, Y. Catherine, and J.B. Adams, *Structural properties of hexagonal boron nitride.* Modelling and Simulation in Materials Science and Engineering, 2006. **14**(3): p. 515-535.

48. Catellani, A., M. Posternak, A. Baldereschi, and A.J. Freeman, *Bulk and surface electronic structure of hexagonal boron nitride.* Physical Review B, 1987. **36**(11): p. 6105-6111.
49. Liu, L., Y.P. Feng, and Z.X. Shen, *Structural and electronic properties of h-BN.* Physical Review B, 2003. **68**(10): p. 104102.
50. Huang, J.Y., H. Yasuda, and H. Mori, *HRTEM and EELS Studies on the Amorphization of Hexagonal Boron Nitride Induced by Ball Milling.* Journal of the American Ceramic Society, 2000. **83**(2): p. 403-409.
51. Alkoy, S., C. Toy, T. Gönül, and A. Tekin, *Crystallization behavior and characterization of turbostratic boron nitride.* Journal of the European Ceramic Society, 1997. **17**(12): p. 1415-1422.
52. Lee, C., X. Wei, Q. Li, R. Carpick, J.W. Kysar, and J. Hone, *Elastic and frictional properties of graphene.* physica status solidi (b), 2009. **246**(11-12): p. 2562-2567.
53. Paszkowicz, W., J.B. Pelka, M. Knapp, T. Szyszko, and S. Podsiadlo, *Lattice parameters and anisotropic thermal expansion of hexagonal boron nitride in the 10–297.5 K temperature range.* Applied Physics A, 2002. **75**(3): p. 431-435.
54. Yates, B., M.J. Overy, and O. Pirgon, *The anisotropic thermal expansion of boron nitride.* The Philosophical Magazine: A Journal of Theoretical Experimental and Applied Physics, 1975. **32**(4): p. 847-857.
55. Yoon, D., Y.-W. Son, and H. Cheong, *Negative Thermal Expansion Coefficient of Graphene Measured by Raman Spectroscopy.* Nano Letters, 2011. **11**(8): p. 3227-3231.
56. Bao, W., F. Miao, Z. Chen, H. Zhang, W. Jang, C. Dames, and C.N. Lau, *Controlled ripple texturing of suspended graphene and ultrathin graphite membranes.* Nature Nanotechnology, 2009. **4**: p. 562.
57. Steward, E.G., B.P. Cook, and E.A. Kellett, *Dependence on Temperature of the Interlayer Spacing in Carbons of Different Graphitic Perfection.* Nature, 1960. **187**(4742): p. 1015-1016.
58. Steward, E.G. and B.P. Cook, *X-Ray Measurement of Thermal Expansion Perpendicular to the Layer Planes of Artificial and Natural Graphites.* Nature, 1960. **185**(4706): p. 78-80.
59. Jiang, P., X. Qian, R. Yang, and L. Lindsay, *Anisotropic thermal transport in bulk hexagonal boron nitride.* Physical Review Materials, 2018. **2**(6): p. 064005.
60. Cai, Q., D. Scullion, W. Gan, A. Falin, S. Zhang, K. Watanabe, T. Taniguchi, Y. Chen, E.J.G. Santos, and L.H. Li, *High thermal conductivity of high-quality monolayer boron nitride and its thermal expansion.* Science Advances, 2019. **5**(6): p. eaav0129.
61. Jo, I., M.T. Pettes, J. Kim, K. Watanabe, T. Taniguchi, Z. Yao, and L. Shi, *Thermal Conductivity and Phonon Transport in Suspended Few-Layer Hexagonal Boron Nitride.* Nano Letters, 2013. **13**(2): p. 550-554.
62. Castro Neto, A.H., F. Guinea, N.M.R. Peres, K.S. Novoselov, and A.K. Geim, *The electronic properties of graphene.* Reviews of Modern Physics, 2009. **81**(1): p. 109-162.
63. Hwang, E.H., S. Adam, and S.D. Sarma, *Carrier Transport in Two-Dimensional Graphene Layers.* Physical Review Letters, 2007. **98**(18): p. 186806.

64. Morozov, S.V., K.S. Novoselov, M.I. Katsnelson, F. Schedin, D.C. Elias, J.A. Jaszczak, and A.K. Geim, *Giant Intrinsic Carrier Mobilities in Graphene and Its Bilayer.* Physical Review Letters, 2008. **100**(1): p. 016602.
65. LLP, S.I. *Ceramic Products*. Available from: https://www.supervacoils.com/ceramic-products/.
66. Paine, R.T. and C.K. Narula, *Synthetic routes to boron nitride.* Chemical Reviews, 1990. **90**(1): p. 73-91.
67. Pakdel, A., C. Zhi, Y. Bando, and D. Golberg, *Low-dimensional boron nitride nanomaterials.* Materials Today, 2012. **15**(6): p. 256-265.
68. Pawlak, Z., T. Kaldonski, R. Pai, E. Bayraktar, and A. Oloyede, *A comparative study on the tribological behaviour of hexagonal boron nitride (h-BN) as lubricating micro-particles—An additive in porous sliding bearings for a car clutch.* Wear, 2009. **267**(5): p. 1198-1202.
69. Podgornik, B., T. Kosec, A. Kocijan, and Č. Donik, *Tribological behaviour and lubrication performance of hexagonal boron nitride (h-BN) as a replacement for graphite in aluminium forming.* Tribology International, 2015. **81**: p. 267-275.
70. Li, L.H., J. Cervenka, K. Watanabe, T. Taniguchi, and Y. Chen, *Strong Oxidation Resistance of Atomically Thin Boron Nitride Nanosheets.* ACS Nano, 2014. **8**(2): p. 1457-1462.
71. Li, L.H. and Y. Chen, *Atomically Thin Boron Nitride: Unique Properties and Applications.* Advanced Functional Materials, 2016. **26**(16): p. 2594-2608.
72. Eichler, J. and C. Lesniak, *Boron nitride (BN) and BN composites for high-temperature applications.* Journal of the European Ceramic Society, 2008. **28**(5): p. 1105-1109.
73. Chunyi, Z., B. Yoshio, T. Chengchun, K. Hiroaki, and G. Dimitri, *Large-Scale Fabrication of Boron Nitride Nanosheets and Their Utilization in Polymeric Composites with Improved Thermal and Mechanical Properties.* Advanced Materials, 2009. **21**(28): p. 2889-2893.
74. Ceramics, M.T. *3M™ Boron Nitride (BN)*. 2019; Available from: http://technical-ceramics.3mdeutschland.de/en/materials/3m-boron-nitride.html.
75. Abrasives, P. *Skin Care & Cosmetics*. 2019 8 July 2019]; Available from: https://www.panadyneabrasives.com/Skin-Care-Cosmetics_c2.htm.
76. Saint-Gobain. *Cosmetic Powders*. 2018; Available from: https://www.bn.saint-gobain.com/products/powders/cosmetic-powders.
77. Fiume, M.M., W.F. Bergfeld, D.V. Belsito, R.A. Hill, C.D. Klaassen, D.C. Liebler, J.G. Marks, R.C. Shank, T.J. Slaga, P.W. Snyder, and F.A. Andersen, *Safety Assessment of Boron Nitride as Used in Cosmetics.* International Journal of Toxicology, 2015. **34**(3_suppl): p. 53S-60S.
78. Lee, G.-W., M. Park, J. Kim, J.I. Lee, and H.G. Yoon, *Enhanced thermal conductivity of polymer composites filled with hybrid filler.* Composites Part A: Applied Science and Manufacturing, 2006. **37**(5): p. 727-734.
79. Zheng, J.-C., L. Zhang, A.V. Kretinin, S.V. Morozov, Y.B. Wang, T. Wang, X. Li, F. Ren, J. Zhang, C.-Y. Lu, J.-C. Chen, M. Lu, H.-Q. Wang, A.K. Geim, and K.S. Novoselov, *High thermal conductivity of hexagonal boron nitride laminates.* 2D Materials, 2016. **3**(1): p. 011004.
80. Bolotin, K.I., K.J. Sikes, J. Hone, H.L. Stormer, and P. Kim, *Temperature-Dependent Transport in Suspended Graphene.* Physical Review Letters, 2008. **101**(9): p. 096802.

81. Bolotin, K.I., K.J. Sikes, Z. Jiang, M. Klima, G. Fudenberg, J. Hone, P. Kim, and H.L. Stormer, *Ultrahigh electron mobility in suspended graphene.* Solid State Communications, 2008. **146**(9): p. 351-355.
82. Withers, F., O. Del Pozo-Zamudio, A. Mishchenko, A.P. Rooney, A. Gholinia, K. Watanabe, T. Taniguchi, S.J. Haigh, A.K. Geim, A.I. Tartakovskii, and K.S. Novoselov, *Light-emitting diodes by band-structure engineering in van der Waals heterostructures.* Nat Mater, 2015. **14**(3): p. 301-306.
83. Mayorov, A.S., R.V. Gorbachev, S.V. Morozov, L. Britnell, R. Jalil, L.A. Ponomarenko, P. Blake, K.S. Novoselov, K. Watanabe, T. Taniguchi, and A.K. Geim, *Micrometer-Scale Ballistic Transport in Encapsulated Graphene at Room Temperature.* Nano Letters, 2011. **11**(6): p. 2396-2399.
84. Bresnehan, M.S., M.J. Hollander, M. Wetherington, M. LaBella, K.A. Trumbull, R. Cavalero, D.W. Snyder, and J.A. Robinson, *Integration of Hexagonal Boron Nitride with Quasi-freestanding Epitaxial Graphene: Toward Wafer-Scale, High-Performance Devices.* Acs Nano, 2012. **6**(6): p. 5234-5241.
85. Bhimanapati, G.R., Z. Lin, V. Meunier, Y. Jung, J. Cha, S. Das, D. Xiao, Y. Son, M.S. Strano, V.R. Cooper, L.B. Liang, S.G. Louie, E. Ringe, W. Zhou, S.S. Kim, R.R. Naik, B.G. Sumpter, H. Terrones, F.N. Xia, Y.L. Wang, J. Zhu, D. Akinwande, N. Alem, J.A. Schuller, R.E. Schaak, M. Terrones, and J.A. Robinson, *Recent Advances in Two-Dimensional Materials beyond Graphene.* Acs Nano, 2015. **9**(12): p. 11509-11539.
86. Kim, K.K., A. Hsu, X. Jia, S.M. Kim, Y. Shi, M. Dresselhaus, T. Palacios, and J. Kong, *Synthesis and Characterization of Hexagonal Boron Nitride Film as a Dielectric Layer for Graphene Devices.* ACS Nano, 2012. **6**(10): p. 8583-8590.
87. Chan, M.Y., K. Komatsu, S.-L. Li, Y. Xu, P. Darmawan, H. Kuramochi, S. Nakaharai, A. Aparecido-Ferreira, K. Watanabe, T. Taniguchi, and K. Tsukagoshi, *Suppression of thermally activated carrier transport in atomically thin MoS2 on crystalline hexagonal boron nitride substrates.* Nanoscale, 2013. **5**(20): p. 9572-9576.
88. Dean, C., A.F. Young, L. Wang, I. Meric, G.H. Lee, K. Watanabe, T. Taniguchi, K. Shepard, P. Kim, and J. Hone, *Graphene based heterostructures.* Solid State Communications, 2012. **152**(15): p. 1275-1282.
89. Kobayashi, Y., K. Kumakura, T. Akasaka, and T. Makimoto, *Layered boron nitride as a release layer for mechanical transfer of GaN-based devices.* Nature, 2012. **484**(7393): p. 223-227.
90. Ayari, T., S. Sundaram, X. Li, Y.E. Gmili, P.L. Voss, J.P. Salvestrini, and A. Ougazzaden, *Wafer-scale controlled exfoliation of metal organic vapor phase epitaxy grown InGaN/GaN multi quantum well structures using low-tack two-dimensional layered h-BN.* Applied Physics Letters, 2016. **108**(17): p. 171106.
91. Makimoto, T., K. Kumakura, Y. Kobayashi, T. Akasaka, and H. Yamamoto, *A Vertical InGaN/GaN Light-Emitting Diode Fabricated on a Flexible Substrate by a Mechanical Transfer Method Using BN.* Applied Physics Express, 2012. **5**(7): p. 072102.
92. Chung, K., H. Oh, J. Jo, K. Lee, M. Kim, and G.-C. Yi, *Transferable single-crystal GaN thin films grown on chemical vapor-deposited hexagonal BN sheets.* Npg Asia Materials, 2017. **9**: p. e410.
93. Li, X., M.B. Jordan, T. Ayari, S. Sundaram, Y. El Gmili, S. Alam, M. Alam, G. Patriarche, P.L. Voss, J. Paul Salvestrini, and A. Ougazzaden, *Flexible*

metal-semiconductor-metal device prototype on wafer-scale thick boron nitride layers grown by MOVPE. Scientific Reports, 2017. **7**(1): p. 786.

94. Ayari, T., C. Bishop, M.B. Jordan, S. Sundaram, X. Li, S. Alam, Y. ElGmili, G. Patriarche, P.L. Voss, J.P. Salvestrini, and A. Ougazzaden, *Gas sensors boosted by two-dimensional h-BN enabled transfer on thin substrate foils: towards wearable and portable applications.* Scientific Reports, 2017. **7**(1): p. 15212.
95. Wu, Q., Y. Guo, S. Sundaram, J. Yan, L. Zhang, T. Wei, X. Wei, J. Wang, A. Ougazzaden, and J. Li, *Exfoliation of AlN film using two-dimensional multilayer hexagonal BN for deep-ultraviolet light-emitting diodes.* Applied Physics Express, 2018. **12**(1): p. 015505.
96. Li, Q., Q. Wu, J. Gao, T. Wei, J. Sun, H. Hong, Z. Dou, Z. Zhang, M.H. Rümmeli, P. Gao, J. Yan, J. Wang, J. Li, Y. Zhang, and Z. Liu, *Direct Growth of 5 in. Uniform Hexagonal Boron Nitride on Glass for High-Performance Deep-Ultraviolet Light-Emitting Diodes.* Advanced Materials Interfaces, 2018. **5**(18): p. 1800662.
97. Glavin, N.R., K.D. Chabak, E.R. Heller, E.A. Moore, T.A. Prusnick, B. Maruyama, D.E. Walker Jr., D.L. Dorsey, Q. Paduano, and M. Snure, *Flexible Gallium Nitride for High-Performance, Strainable Radio-Frequency Devices.* Advanced Materials, 2017. **29**(47): p. 1701838.
98. Paduano, Q., M. Snure, G. Siegel, D. Thomson, and D. Look, *Growth and characteristics of AlGaN/GaN heterostructures on sp2-bonded BN by metal–organic chemical vapor deposition.* Journal of Materials Research, 2016. **31**(15): p. 2204-2213.
99. Hiroki, M., K. Kumakura, Y. Kobayashi, T. Akasaka, T. Makimoto, and H. Yamamoto, *Suppression of self-heating effect in AlGaN/GaN high electron mobility transistors by substrate-transfer technology using h-BN.* Applied Physics Letters, 2014. **105**(19): p. 193509.
100. Wu, C., A.M. Soomro, F. Sun, H. Wang, Y. Huang, J. Wu, C. Liu, X. Yang, N. Gao, X. Chen, J. Kang, and D. Cai, *Large-roll growth of 25-inch hexagonal BN monolayer film for self-release buffer layer of free-standing GaN wafer.* Scientific Reports, 2016. **6**: p. 34766.
101. Alaskar, Y., S. Arafin, D. Wickramaratne, M.A. Zurbuchen, L. He, J. McKay, Q. Lin, M.S. Goorsky, R.K. Lake, and K.L. Wang, *Towards van der Waals Epitaxial Growth of GaAs on Si using a Graphene Buffer Layer.* Advanced Functional Materials, 2014. **24**(42): p. 6629-6638.
102. Berry, V., *Impermeability of graphene and its applications.* Carbon, 2013. **62**: p. 1-10.
103. Hu, S., M. Lozada-Hidalgo, F.C. Wang, A. Mishchenko, F. Schedin, R.R. Nair, E.W. Hill, D.W. Boukhvalov, M.I. Katsnelson, R.A.W. Dryfe, I.V. Grigorieva, H.A. Wu, and A.K. Geim, *Proton transport through one-atom-thick crystals.* Nature, 2014. **516**: p. 227.
104. Gupta, V., A. Kumar, and N. Ray, *Permeability of two-dimensional graphene and hexagonal-boron nitride to hydrogen atom.* AIP Conference Proceedings, 2018. **1953**(1): p. 140013.
105. Leenaerts, O., B. Partoens, and F.M. Peeters, *Graphene: A perfect nanoballoon.* Applied Physics Letters, 2008. **93**(19): p. 193107.
106. Zhang, Y., Q. Shi, Y. Liu, Y. Wang, Z. Meng, C. Xiao, K. Deng, D. Rao, and R. Lu, *Hexagonal Boron Nitride with Designed Nanopores as a High-*

Efficiency Membrane for Separating Gaseous Hydrogen from Methane. The Journal of Physical Chemistry C, 2015. **119**(34): p. 19826-19831.

107. Lei, W., D. Portehault, D. Liu, S. Qin, and Y. Chen, *Porous boron nitride nanosheets for effective water cleaning.* Nature Communications, 2013. **4**: p. 1777.
108. Homaeigohar, S. and M. Elbahri, *Graphene membranes for water desalination.* Npg Asia Materials, 2017. **9**: p. e427.
109. Husain, E., T.N. Narayanan, J.J. Taha-Tijerina, S. Vinod, R. Vajtai, and P.M. Ajayan, *Marine Corrosion Protective Coatings of Hexagonal Boron Nitride Thin Films on Stainless Steel.* ACS Applied Materials & Interfaces, 2013. **5**(10): p. 4129-4135.
110. Shen, L., Y. Zhao, Y. Wang, R. Song, Q. Yao, S. Chen, and Y. Chai, *A long-term corrosion barrier with an insulating boron nitride monolayer.* Journal of Materials Chemistry A, 2016. **4**(14): p. 5044-5050.
111. Jing, Z., Y. Yingchao, and L. Jun, *Investigation of hexagonal boron nitride as an atomically thin corrosion passivation coating in aqueous solution.* Nanotechnology, 2016. **27**(36): p. 364004.
112. Zihlmann, S., P. Makk, C.A.F. Vaz, and C. Schönenberger, *Role of hexagonal boron nitride in protecting ferromagnetic nanostructures from oxidation.* 2D Materials, 2016. **3**(1): p. 011008.
113. Cai, Q., L.H. Li, Y. Yu, Y. Liu, S. Huang, Y. Chen, K. Watanabe, and T. Taniguchi, *Boron nitride nanosheets as improved and reusable substrates for gold nanoparticles enabled surface enhanced Raman spectroscopy.* Physical Chemistry Chemical Physics, 2015. **17**(12): p. 7761-7766.
114. Cai, Q., S. Mateti, K. Watanabe, T. Taniguchi, S. Huang, Y. Chen, and L.H. Li, *Boron Nitride Nanosheet-Veiled Gold Nanoparticles for Surface-Enhanced Raman Scattering.* ACS Applied Materials & Interfaces, 2016. **8**(24): p. 15630-15636.
115. Kim, G., M. Kim, C. Hyun, S. Hong, K.Y. Ma, H.S. Shin, and H. Lim, *Hexagonal Boron Nitride/Au Substrate for Manipulating Surface Plasmon and Enhancing Capability of Surface-Enhanced Raman Spectroscopy.* ACS Nano, 2016. **10**(12): p. 11156-11162.
116. Dai, P., Y. Xue, X. Wang, Q. Weng, C. Zhang, X. Jiang, D. Tang, X. Wang, N. Kawamoto, Y. Ide, M. Mitome, D. Golberg, and Y. Bando, *Pollutant capturing SERS substrate: porous boron nitride microfibers with uniform silver nanoparticle decoration.* Nanoscale, 2015. **7**(45): p. 18992-18997.
117. Chugh, D., C. Jagadish, and H. Tan, *Large-Area Hexagonal Boron Nitride for Surface Enhanced Raman Spectroscopy.* Advanced Materials Technologies. **0**(0): p. 1900220.
118. Zunger, A., A. Katzir, and A. Halperin, *Optical properties of hexagonal boron nitride.* Physical Review B, 1976. **13**(12): p. 5560-5573.
119. Hoffman, D.M., G.L. Doll, and P.C. Eklund, *Optical properties of pyrolytic boron nitride in the energy range 0.05-10 eV.* Physical Review B, 1984. **30**(10): p. 6051-6056.
120. Tarrio, C. and S.E. Schnatterly, *Interband transitions, plasmons, and dispersion in hexagonal boron nitride.* Physical Review B, 1989. **40**(11): p. 7852-7859.
121. Taylor, C.A., S.W. Brown, V. Subramaniam, S. Kidner, S.C. Rand, and R. Clarke, *Observation of near-band-gap luminescence from boron nitride films.* Applied Physics Letters, 1994. **65**(10): p. 1251-1253.

122. Solozhenko, V.L., A.G. Lazarenko, J.P. Petitet, and A.V. Kanaev, *Bandgap energy of graphite-like hexagonal boron nitride.* Journal of Physics and Chemistry of Solids, 2001. **62**(7): p. 1331-1334.
123. Evans, D.A., A.G. McGlynn, B.M. Towlson, M. Gunn, D. Jones, T.E. Jenkins, R. Winter, and N.R.J. Poolton, *Determination of the optical band-gap energy of cubic and hexagonal boron nitride using luminescence excitation spectroscopy.* Journal of Physics: Condensed Matter, 2008. **20**(7): p. 075233.
124. Watanabe, K., T. Taniguchi, K. Miya, Y. Sato, K. Nakamura, T. Niiyama, and M. Taniguchi, *Hexagonal boron nitride as a new ultraviolet luminescent material and its application—Fluorescence properties of hBN single-crystal powder.* Diamond and Related Materials, 2011. **20**(5): p. 849-852.
125. Watanabe, K., T. Taniguchi, T. Niiyama, K. Miya, and M. Taniguchi, *Far-ultraviolet plane-emission handheld device based on hexagonal boron nitride.* Nature Photonics, 2009. **3**(10): p. 591-594.
126. Furthmüller, J., J. Hafner, and G. Kresse, *Ab initio calculation of the structural and electronic properties of carbon and boron nitride using ultrasoft pseudopotentials.* Physical Review B, 1994. **50**(21): p. 15606-15622.
127. Blase, X., A. Rubio, S.G. Louie, and M.L. Cohen, *Quasiparticle band structure of bulk hexagonal boron nitride and related systems.* Physical Review B, 1995. **51**(11): p. 6868-6875.
128. Xu, Y.-N. and W.Y. Ching, *Calculation of ground-state and optical properties of boron nitrides in the hexagonal, cubic, and wurtzite structures.* Physical Review B, 1991. **44**(15): p. 7787-7798.
129. Vuong, T.Q.P., G. Cassabois, P. Valvin, V. Jacques, R. Cuscó, L. Artús, and B. Gil, *Overtones of interlayer shear modes in the phonon-assisted emission spectrum of hexagonal boron nitride.* Physical Review B, 2017. **95**(4): p. 045207.
130. Cassabois, G., P. Valvin, and B. Gil, *Intervalley scattering in hexagonal boron nitride.* Physical Review B, 2016. **93**(3): p. 035207.
131. Schué, L., L. Sponza, A. Plaud, H. Bensalah, K. Watanabe, T. Taniguchi, F. Ducastelle, A. Loiseau, and J. Barjon, *Bright Luminescence from Indirect and Strongly Bound Excitons in h-BN.* Physical Review Letters, 2019. **122**(6): p. 067401.
132. Cassabois, G., P. Valvin, and B. Gil, *Hexagonal boron nitride is an indirect bandgap semiconductor.* Nature Photonics, 2016. **10**(4): p. 262.
133. Vuong, T.Q.P., G. Cassabois, P. Valvin, S. Liu, J.H. Edgar, and B. Gil, *Exciton-phonon interaction in the strong-coupling regime in hexagonal boron nitride.* Physical Review B, 2017. **95**(20): p. 201202.
134. Pierret, A., J. Loayza, B. Berini, A. Betz, B. Plaçais, F. Ducastelle, J. Barjon, and A. Loiseau, *Excitonic recombinations in h-BN: From bulk to exfoliated layers.* Physical Review B, 2014. **89**(3): p. 035414.
135. Choi, S., T.T. Tran, C. Elbadawi, C. Lobo, X. Wang, S. Juodkazis, G. Seniutinas, M. Toth, and I. Aharonovich, *Engineering and Localization of Quantum Emitters in Large Hexagonal Boron Nitride Layers.* ACS Applied Materials & Interfaces, 2016. **8**(43): p. 29642-29648.
136. Tran, T.T., C. Elbadawi, D. Totonjian, C.J. Lobo, G. Grosso, H. Moon, D.R. Englund, M.J. Ford, I. Aharonovich, and M. Toth, *Robust Multicolor Single Photon Emission from Point Defects in Hexagonal Boron Nitride.* ACS Nano, 2016. **10**(8): p. 7331-7338.

137. Xu, Z.-Q., C. Elbadawi, T.T. Tran, M. Kianinia, X. Li, D. Liu, T.B. Hoffman, M. Nguyen, S. Kim, J.H. Edgar, X. Wu, L. Song, S. Ali, M. Ford, M. Toth, and I. Aharonovich, *Single photon emission from plasma treated 2D hexagonal boron nitride.* Nanoscale, 2018. **10**(17): p. 7957-7965.
138. Vogl, T., G. Campbell, B.C. Buchler, Y. Lu, and P.K. Lam, *Fabrication and Deterministic Transfer of High-Quality Quantum Emitters in Hexagonal Boron Nitride.* ACS Photonics, 2018. **5**(6): p. 2305-2312.
139. Bourrellier, R., S. Meuret, A. Tararan, O. Stéphan, M. Kociak, L.H.G. Tizei, and A. Zobelli, *Bright UV Single Photon Emission at Point Defects in h-BN.* Nano Letters, 2016. **16**(7): p. 4317-4321.
140. Klein, J., M. Lorke, M. Florian, F. Sigger, L. Sigl, S. Rey, J. Wierzbowski, J. Cerne, K. Müller, E. Mitterreiter, P. Zimmermann, T. Taniguchi, K. Watanabe, U. Wurstbauer, M. Kaniber, M. Knap, R. Schmidt, J.J. Finley, and A.W. Holleitner, *Site-selectively generated photon emitters in monolayer MoS2 via local helium ion irradiation.* Nature Communications, 2019. **10**(1): p. 2755.
141. Chakraborty, C., L. Kinnischtzke, K.M. Goodfellow, R. Beams, and A.N. Vamivakas, *Voltage-controlled quantum light from an atomically thin semiconductor.* Nature Nanotechnology, 2015. **10**: p. 507.
142. Srivastava, A., M. Sidler, A.V. Allain, D.S. Lembke, A. Kis, and A. Imamoğlu, *Optically active quantum dots in monolayer WSe2.* Nature Nanotechnology, 2015. **10**: p. 491.
143. Tonndorf, P., R. Schmidt, R. Schneider, J. Kern, M. Buscema, G.A. Steele, A. Castellanos-Gomez, H.S.J. van der Zant, S. Michaelis de Vasconcellos, and R. Bratschitsch, *Single-photon emission from localized excitons in an atomically thin semiconductor.* Optica, 2015. **2**(4): p. 347-352.
144. Toth, M. and I. Aharonovich, *Single Photon Sources in Atomically Thin Materials.* Annual Review of Physical Chemistry, 2019. **70**(1): p. 123-142.
145. Kianinia, M., B. Regan, S.A. Tawfik, T.T. Tran, M.J. Ford, I. Aharonovich, and M. Toth, *Robust Solid-State Quantum System Operating at 800 K.* ACS Photonics, 2017. **4**(4): p. 768-773.
146. Müller, G. and P. Rudolph, *Crystal Growth from the Melt*, in *Encyclopedia of Materials: Science and Technology*, K.H.J. Buschow, et al., Editors. 2001, Elsevier: Oxford. p. 1866-1872.
147. Friedrich, J., *Methods for Bulk Growth of Inorganic Crystals: Crystal Growth*, in *Reference Module in Materials Science and Materials Engineering*. 2016, Elsevier.
148. Kubota, Y., K. Watanabe, O. Tsuda, and T. Taniguchi, *Deep ultraviolet light-emitting hexagonal boron nitride synthesized at atmospheric pressure.* Science, 2007. **317**(5840): p. 932-934.
149. Taniguchi, T. and K. Watanabe, *Synthesis of high-purity boron nitride single crystals under high pressure by using Ba–BN solvent.* Journal of Crystal Growth, 2007. **303**(2): p. 525-529.
150. Kubota, Y., K. Watanabe, O. Tsuda, and T. Taniguchi, *Hexagonal Boron Nitride Single Crystal Growth at Atmospheric Pressure Using Ni−Cr Solvent.* Chemistry of Materials, 2008. **20**(5): p. 1661-1663.
151. Zhigadlo, N.D., *Crystal growth of hexagonal boron nitride (hBN) from Mg–B–N solvent system under high pressure.* Journal of Crystal Growth, 2014. **402**: p. 308-311.

152. Hoffman, T.B., B. Clubine, Y. Zhang, K. Snow, and J.H. Edgar, *Optimization of Ni–Cr flux growth for hexagonal boron nitride single crystals.* Journal of Crystal Growth, 2014. **393**: p. 114-118.
153. Liu, S., R. He, Z. Ye, X. Du, J. Lin, H. Jiang, B. Liu, and J.H. Edgar, *Large-Scale Growth of High-Quality Hexagonal Boron Nitride Crystals at Atmospheric Pressure from an Fe–Cr Flux.* Crystal Growth & Design, 2017. **17**(9): p. 4932-4935.
154. Liu, S., R. He, L. Xue, J. Li, B. Liu, and J.H. Edgar, *Single Crystal Growth of Millimeter-Sized Monoisotopic Hexagonal Boron Nitride.* Chemistry of Materials, 2018. **30**(18): p. 6222-6225.
155. Edgar, J.H., T.B. Hoffman, B. Clubine, M. Currie, X.Z. Du, J.Y. Lin, and H.X. Jiang, *Characterization of bulk hexagonal boron nitride single crystals grown by the metal flux technique.* Journal of Crystal Growth, 2014. **403**: p. 110-113.
156. Watanabe, K. and T. Taniguchi, *Hexagonal Boron Nitride as a New Ultraviolet Luminescent Material and Its Application.* International Journal of Applied Ceramic Technology, 2011. **8**(5): p. 977-989.
157. Léonard, S., S. Ingrid, F. Frédéric, L. Annick, and B. Julien, *Characterization methods dedicated to nanometer-thick hBN layers.* 2D Materials, 2017. **4**(1): p. 015028.
158. Yu, Q., J. Lian, S. Siriponglert, H. Li, Y.P. Chen, and S.-S. Pei, *Graphene segregated on Ni surfaces and transferred to insulators.* Applied Physics Letters, 2008. **93**(11): p. 113103.
159. Obraztsov, A.N., E.A. Obraztsova, A.V. Tyurnina, and A.A. Zolotukhin, *Chemical vapor deposition of thin graphite films of nanometer thickness.* Carbon, 2007. **45**(10): p. 2017-2021.
160. Reina, A., X. Jia, J. Ho, D. Nezich, H. Son, V. Bulovic, M.S. Dresselhaus, and J. Kong, *Large Area, Few-Layer Graphene Films on Arbitrary Substrates by Chemical Vapor Deposition.* Nano Letters, 2009. **9**(1): p. 30-35.
161. Li, X., W. Cai, J. An, S. Kim, J. Nah, D. Yang, R. Piner, A. Velamakanni, I. Jung, E. Tutuc, S.K. Banerjee, L. Colombo, and R.S. Ruoff, *Large-Area Synthesis of High-Quality and Uniform Graphene Films on Copper Foils.* Science, 2009. **324**(5932): p. 1312-1314.
162. Kim, K.S., Y. Zhao, H. Jang, S.Y. Lee, J.M. Kim, K.S. Kim, J.-H. Ahn, P. Kim, J.-Y. Choi, and B.H. Hong, *Large-scale pattern growth of graphene films for stretchable transparent electrodes.* Nature, 2009. **457**: p. 706.
163. Lee, Y.-H., L. Yu, H. Wang, W. Fang, X. Ling, Y. Shi, C.-T. Lin, J.-K. Huang, M.-T. Chang, C.-S. Chang, M. Dresselhaus, T. Palacios, L.-J. Li, and J. Kong, *Synthesis and Transfer of Single-Layer Transition Metal Disulfides on Diverse Surfaces.* Nano Letters, 2013. **13**(4): p. 1852-1857.
164. Lee, Y.-H., X.-Q. Zhang, W. Zhang, M.-T. Chang, C.-T. Lin, K.-D. Chang, Y.-C. Yu, J.T.-W. Wang, C.-S. Chang, L.-J. Li, and T.-W. Lin, *Synthesis of Large-Area MoS2 Atomic Layers with Chemical Vapor Deposition.* Advanced Materials, 2012. **24**(17): p. 2320-2325.
165. Kang, K., S. Xie, L. Huang, Y. Han, P.Y. Huang, K.F. Mak, C.-J. Kim, D. Muller, and J. Park, *High-mobility three-atom-thick semiconducting films with wafer-scale homogeneity.* Nature, 2015. **520**: p. 656.
166. Cai, Z., B. Liu, X. Zou, and H.-M. Cheng, *Chemical Vapor Deposition Growth and Applications of Two-Dimensional Materials and Their Heterostructures.* Chemical Reviews, 2018. **118**(13): p. 6091-6133.

167. Okada, M., T. Sawazaki, K. Watanabe, T. Taniguch, H. Hibino, H. Shinohara, and R. Kitaura, *Direct Chemical Vapor Deposition Growth of WS2 Atomic Layers on Hexagonal Boron Nitride.* ACS Nano, 2014. **8**(8): p. 8273-8277.
168. Nagashima, A., N. Tejima, Y. Gamou, T. Kawai, and C. Oshima, *Electronic dispersion relations of monolayer hexagonal boron nitride formed on the Ni(111) surface.* Physical Review B, 1995. **51**(7): p. 4606-4613.
169. Nagashima, A., N. Tejima, Y. Gamou, T. Kawai, and C. Oshima, *Electronic Structure of Monolayer Hexagonal Boron Nitride Physisorbed on Metal Surfaces.* Physical Review Letters, 1995. **75**(21): p. 3918-3921.
170. Auwärter, W., H.U. Suter, H. Sachdev, and T. Greber, *Synthesis of One Monolayer of Hexagonal Boron Nitride on Ni(111) from B-Trichloroborazine (ClBNH)3.* Chemistry of Materials, 2004. **16**(2): p. 343-345.
171. Shi, Y., C. Hamsen, X. Jia, K.K. Kim, A. Reina, M. Hofmann, A.L. Hsu, K. Zhang, H. Li, Z.-Y. Juang, M.S. Dresselhaus, L.-J. Li, and J. Kong, *Synthesis of Few-Layer Hexagonal Boron Nitride Thin Film by Chemical Vapor Deposition.* Nano Letters, 2010. **10**(10): p. 4134-4139.
172. Lee, K.H., H.-J. Shin, J. Lee, I.-y. Lee, G.-H. Kim, J.-Y. Choi, and S.-W. Kim, *Large-Scale Synthesis of High-Quality Hexagonal Boron Nitride Nanosheets for Large-Area Graphene Electronics.* Nano Letters, 2012. **12**(2): p. 714-718.
173. Kim, K.K., A. Hsu, X.T. Jia, S.M. Kim, Y.S. Shi, M. Hofmann, D. Nezich, J.F. Rodriguez-Nieva, M. Dresselhaus, T. Palacios, and J. Kong, *Synthesis of Monolayer Hexagonal Boron Nitride on Cu Foil Using Chemical Vapor Deposition.* Nano Letters, 2012. **12**(1): p. 161-166.
174. Song, L., L.J. Ci, H. Lu, P.B. Sorokin, C.H. Jin, J. Ni, A.G. Kvashnin, D.G. Kvashnin, J. Lou, B.I. Yakobson, and P.M. Ajayan, *Large Scale Growth and Characterization of Atomic Hexagonal Boron Nitride Layers.* Nano Letters, 2010. **10**(8): p. 3209-3215.
175. Paffett, M.T., R.J. Simonson, P. Papin, and R.T. Paine, *Borazine adsorption and decomposition at Pt(111) and Ru(001) surfaces.* Surface Science, 1990. **232**(3): p. 286-296.
176. Kim, G., A.R. Jang, H.Y. Jeong, Z. Lee, D.J. Kang, and H.S. Shin, *Growth of High-Crystalline, Single-Layer Hexagonal Boron Nitride on Recyclable Platinum Foil.* Nano Letters, 2013. **13**(4): p. 1834-1839.
177. Morscher, M., M. Corso, T. Greber, and J. Osterwalder, *Formation of single layer h-BN on Pd(111).* Surface Science, 2006. **600**(16): p. 3280-3284.
178. Corso, M., T. Greber, and J. Osterwalder, *h-BN on Pd(110): a tunable system for self-assembled nanostructures?* Surface Science, 2005. **577**(2): p. L78-L84.
179. Müller, F. and S. Grandthyll, *Monolayer formation of hexagonal boron nitride on Ag(001).* Surface Science, 2013. **617**: p. 207-210.
180. Lee, J.S., S.H. Choi, S.J. Yun, Y.I. Kim, S. Boandoh, J.-H. Park, B.G. Shin, H. Ko, S.H. Lee, Y.-M. Kim, Y.H. Lee, K.K. Kim, and S.M. Kim, *Wafer-scale single-crystal hexagonal boron nitride film via self-collimated grain formation.* Science, 2018. **362**(6416): p. 817-821.
181. Caneva, S., R.S. Weatherup, B.C. Bayer, R. Blume, A. Cabrero-Vilatela, P. Braeuninger-Weimer, M.-B. Martin, R. Wang, C. Baehtz, R. Schloegl, J.C. Meyer, and S. Hofmann, *Controlling Catalyst Bulk Reservoir Effects for Monolayer Hexagonal Boron Nitride CVD.* Nano Letters, 2016. **16**(2): p. 1250-1261.
182. Caneva, S., R.S. Weatherup, B.C. Bayer, B. Brennan, S.J. Spencer, K. Mingard, A. Cabrero-Vilatela, C. Baehtz, A.J. Pollard, and S. Hofmann,

Nucleation Control for Large, Single Crystalline Domains of Monolayer Hexagonal Boron Nitride via Si-Doped Fe Catalysts. Nano Letters, 2015. **15**(3): p. 1867-1875.
183. Kim, S.M., A. Hsu, M.H. Park, S.H. Chae, S.J. Yun, J.S. Lee, D.-H. Cho, W. Fang, C. Lee, T. Palacios, M. Dresselhaus, K.K. Kim, Y.H. Lee, and J. Kong, *Synthesis of large-area multilayer hexagonal boron nitride for high material performance.* Nature Communications, 2015. **6**: p. 8662.
184. Corso, M., W. Auwärter, M. Muntwiler, A. Tamai, T. Greber, and J. Osterwalder, *Boron Nitride Nanomesh.* Science, 2004. **303**(5655): p. 217-220.
185. Goriachko, A., He, M. Knapp, H. Over, M. Corso, T. Brugger, S. Berner, J. Osterwalder, and T. Greber, *Self-Assembly of a Hexagonal Boron Nitride Nanomesh on Ru(0001).* Langmuir, 2007. **23**(6): p. 2928-2931.
186. Auwärter, W., *Hexagonal boron nitride monolayers on metal supports: Versatile templates for atoms, molecules and nanostructures.* Surface Science Reports, 2019. **74**(1): p. 1-95.
187. Kidambi, P.R., R. Blume, J. Kling, J.B. Wagner, C. Baehtz, R.S. Weatherup, R. Schloegl, B.C. Bayer, and S. Hofmann, *In Situ Observations during Chemical Vapor Deposition of Hexagonal Boron Nitride on Polycrystalline Copper.* Chemistry of Materials, 2014. **26**(22): p. 6380-6392.
188. Ismach, A., H. Chou, D.A. Ferrer, Y. Wu, S. McDonnell, H.C. Floresca, A. Covacevich, C. Pope, R. Piner, M.J. Kim, R.M. Wallace, L. Colombo, and R.S. Ruoff, *Toward the Controlled Synthesis of Hexagonal Boron Nitride Films.* ACS Nano, 2012. **6**(7): p. 6378-6385.
189. Ji, Y., B. Calderon, Y. Han, P. Cueva, N.R. Jungwirth, H.A. Alsalman, J. Hwang, G.D. Fuchs, D.A. Muller, and M.G. Spencer, *Chemical Vapor Deposition Growth of Large Single-Crystal Mono-, Bi-, Tri-Layer Hexagonal Boron Nitride and Their Interlayer Stacking.* ACS Nano, 2017. **11**(12): p. 12057-12066.
190. Meng, J., X. Zhang, Y. Wang, Z. Yin, H. Liu, J. Xia, H. Wang, J. You, P. Jin, D. Wang, and X.-M. Meng, *Aligned Growth of Millimeter-Size Hexagonal Boron Nitride Single-Crystal Domains on Epitaxial Nickel Thin Film.* Small, 2017. **13**(18): p. 1604179.
191. Lu, G., T. Wu, Q. Yuan, H. Wang, H. Wang, F. Ding, X. Xie, and M. Jiang, *Synthesis of large single-crystal hexagonal boron nitride grains on Cu–Ni alloy.* Nat Commun, 2015. **6**.
192. Laskowski, R., P. Blaha, and K. Schwarz, *Bonding of hexagonal BN to transition metal surfaces: An ab initio density-functional theory study.* Physical Review B, 2008. **78**(4): p. 045409.
193. Jang, S.K., J. Youn, Y.J. Song, and S. Lee, *Synthesis and Characterization of Hexagonal Boron Nitride as a Gate Dielectric.* Scientific Reports, 2016. **6**: p. 30449.
194. Koepke, J.C., J.D. Wood, Y. Chen, S.W. Schmucker, X. Liu, N.N. Chang, L. Nienhaus, J.W. Do, E.A. Carrion, J. Hewaparakrama, A. Rangarajan, I. Datye, R. Mehta, R.T. Haasch, M. Gruebele, G.S. Girolami, E. Pop, and J.W. Lyding, *Role of Pressure in the Growth of Hexagonal Boron Nitride Thin Films from Ammonia-Borane.* Chemistry of Materials, 2016. **28**(12): p. 4169-4179.
195. Lin, W.-H., V.W. Brar, D. Jariwala, M.C. Sherrott, W.-S. Tseng, C.-I. Wu, N.-C. Yeh, and H.A. Atwater, *Atomic-Scale Structural and Chemical Characterization of Hexagonal Boron Nitride Layers Synthesized at the Wafer-*

Scale with Monolayer Thickness Control. Chemistry of Materials, 2017. **29**(11): p. 4700-4707.
196. Uchida, Y., S. Nakandakari, K. Kawahara, S. Yamasaki, M. Mitsuhara, and H. Ago, *Controlled Growth of Large-Area Uniform Multilayer Hexagonal Boron Nitride as an Effective 2D Substrate.* ACS Nano, 2018. **12**(6): p. 6236-6244.
197. Hirayama, H., *Growth Techniques of AlN/AlGaN and Development of High-Efficiency Deep-Ultraviolet Light-Emitting Diodes*, in *III-Nitride Ultraviolet Emitters: Technology and Applications*, M. Kneissl and J. Rass, Editors. 2016, Springer International Publishing: Cham. p. 75-113.
198. Zhu, D., D.J. Wallis, and C.J. Humphreys, *Prospects of III-nitride optoelectronics grown on Si.* Reports on Progress in Physics, 2013. **76**(10).
199. Khan, A., K. Balakrishnan, and T. Katona, *Ultraviolet light-emitting diodes based on group three nitrides.* Nature Photonics, 2008. **2**(2): p. 77-84.
200. Dahal, R., J. Li, S. Majety, B.N. Pantha, X.K. Cao, J.Y. Lin, and H.X. Jiang, *Epitaxially grown semiconducting hexagonal boron nitride as a deep ultraviolet photonic material.* Applied Physics Letters, 2011. **98**(21): p. 211110.
201. Kobayashi, Y. and T. Akasaka, *Hexagonal BN epitaxial growth on (0001) sapphire substrate by MOVPE.* Journal of Crystal Growth, 2008. **310**(23): p. 5044-5047.
202. Majety, S., J. Li, W.P. Zhao, B. Huang, S.H. Wei, J.Y. Lin, and H.X. Jiang, *Hexagonal boron nitride and 6H-SiC heterostructures.* Applied Physics Letters, 2013. **102**(21): p. 213505.
203. Chubarov, M., H. Pedersen, H. Högberg, Z. Czigany, and A. Henry, *Chemical vapour deposition of epitaxial rhombohedral BN thin films on SiC substrates.* CrystEngComm, 2014. **16**(24): p. 5430-5436.
204. Ahmed, K., R. Dahal, A. Weltz, J.-Q. Lu, Y. Danon, and I.B. Bhat, *Growth of hexagonal boron nitride on (111) Si for deep UV photonics and thermal neutron detection.* Applied Physics Letters, 2016. **109**(11): p. 113501.
205. Umehara, N., A. Masuda, T. Shimizu, I. Kuwahara, T. Kouno, H. Kominami, and K. Hara, *Influences of growth parameters on the film formation of hexagonal boron nitride thin films grown on sapphire substrates by low-pressure chemical vapor deposition.* Japanese Journal of Applied Physics, 2016. **55**(5S): p. 05FD09.
206. Nakamura, K., *Preparation and Properties of Boron Nitride Films by Metal Organic Chemical Vapor Deposition.* Journal of The Electrochemical Society, 1986. **133**(6): p. 1120-1123.
207. Paduano, Q., M. Snure, D. Weyburne, A. Kiefer, G. Siegel, and J. Hu, *Metalorganic chemical vapor deposition of few-layer sp2 bonded boron nitride films.* Journal of Crystal Growth, 2016. **449**: p. 148-155.
208. Chugh, D., J. Wong-Leung, L. Li, M. Lysevych, H.H. Tan, and C. Jagadish, *Flow modulation epitaxy of hexagonal boron nitride.* 2D Materials, 2018. **5**(4): p. 045018.
209. Li, X., S. Sundaram, Y. El Gmili, T. Ayari, R. Puybaret, G. Patriarche, P.L. Voss, J.P. Salvestrini, and A. Ougazzaden, *Large-Area Two-Dimensional Layered Hexagonal Boron Nitride Grown on Sapphire by Metalorganic Vapor Phase Epitaxy.* Crystal Growth & Design, 2016. **16**(6): p. 3409-3415.
210. Kobayashi, Y. and T. Makimoto, *Growth of Boron Nitride on 6H–SiC Substrate by Flow-Rate Modulation Epitaxy.* Japanese Journal of Applied Physics, 2006. **45**(4B): p. 3519-3521.

211. Fareed, R.S.Q., R. Jain, R. Gaska, M.S. Shur, J. Wu, W. Walukiewicz, and M.A. Khan, *High quality InN/GaN heterostructures grown by migration enhanced metalorganic chemical vapor deposition.* Applied Physics Letters, 2004. **84**(11): p. 1892-1894.
212. Chen, Z., R.S.Q. Fareed, M. Gaevski, V. Adivarahan, J.W. Yang, A. Khan, J. Mei, and F.A. Ponce, *Pulsed lateral epitaxial overgrowth of aluminum nitride on sapphire substrates.* Applied Physics Letters, 2006. **89**(8): p. 081905.
213. Fareed, R.S.Q., J.W. Yang, J. Zhang, V. Adivarahan, V. Chaturvedi, and M.A. Khan, *Vertically faceted lateral overgrowth of GaN on SiC with conducting buffer layers using pulsed metalorganic chemical vapor deposition.* Applied Physics Letters, 2000. **77**(15): p. 2343-2345.
214. Ramesh, S., N. Kobayashi, and Y. Horikoshi, *Migration-enhanced epitaxy growth and characterization of high quality ZnSe/GaAs superlattices.* Applied Physics Letters, 1990. **57**(11): p. 1102-1104.
215. Horikoshi, Y., M. Kawashima, and H. Yamaguchi, *Migration-Enhanced Epitaxy of GaAs and AlGaAs.* Japanese Journal of Applied Physics, 1988. **27**(Part 1, No. 2): p. 169-179.
216. Yamaguchi, H., M. Kawashima, and Y. Horikoshi, *Migration-enhanced epitaxy.* Applied Surface Science, 1988. **33-34**: p. 406-412.
217. Hajime, A. and H. Yoshiji, *Migration-Enhanced Epitaxy and its Application*, in *Molecular Beam Epitaxy: Materials and Applications for Electronics and Optoelectronics*. 2019, Wiley. p. 41-56.
218. Horikoshi, Y., *Flow Rate Modulated Vapor Epitaxy*, in *Encyclopedia of Materials: Science and Technology*, K.H.J. Buschow, et al., Editors. 2001, Elsevier: Oxford. p. 3187-3194.
219. Yang, X., S. Nitta, K. Nagamatsu, S.-Y. Bae, H.-J. Lee, Y. Liu, M. Pristovsek, Y. Honda, and H. Amano, *Growth of hexagonal boron nitride on sapphire substrate by pulsed-mode metalorganic vapor phase epitaxy.* Journal of Crystal Growth, 2018. **482**: p. 1-8.
220. Jiang, H.X. and J.Y. Lin, *Hexagonal boron nitride for deep ultraviolet photonic devices.* Semiconductor Science and Technology, 2014. **29**(8).
221. Majety, S., J. Li, X.K. Cao, R. Dahal, B.N. Pantha, J.Y. Lin, and H.X. Jiang, *Epitaxial growth and demonstration of hexagonal BN/AlGaN p-n junctions for deep ultraviolet photonics.* Applied Physics Letters, 2012. **100**(6): p. 061121.
222. Chubarov, M., H. Pedersen, H. Högberg, J. Jensen, and A. Henry, *Growth of High Quality Epitaxial Rhombohedral Boron Nitride.* Crystal Growth & Design, 2012. **12**(6): p. 3215-3220.
223. Rice, A., A. Allerman, M. Crawford, T. Beechem, T. Ohta, C. Spataru, J. Figiel, and M. Smith, *Effects of deposition temperature and ammonia flow on metal-organic chemical vapor deposition of hexagonal boron nitride.* Journal of Crystal Growth, 2018. **485**: p. 90-95.
224. Paduano, Q.S., M. Snure, J. Bondy, and T.W.C. Zens, *Self-terminating growth in hexagonal boron nitride by metal organic chemical vapor deposition.* Applied Physics Express, 2014. **7**(7).
225. Kim, D.Y., N. Han, H. Jeong, J. Kim, S. Hwang, K. Song, S.-Y. Choi, and J.K. Kim, *Pressure-Dependent Growth of Wafer-Scale Few-layer h-BN by Metal–Organic Chemical Vapor Deposition.* Crystal Growth & Design, 2017. **17**(5): p. 2569-2575.
226. Chubarov, M., H. Pedersen, H. Högberg, V. Darakchieva, J. Jensen, P.O.Å. Persson, and A. Henry, *Epitaxial CVD growth of sp2-hybridized boron nitride*

using aluminum nitride as buffer layer. physica status solidi (RRL) – Rapid Research Letters, 2011. **5**(10-11): p. 397-399.
227. Akiyama, K., T. Araki, H. Murakami, Y. Kumagai, and A. Koukitu, *In situ gravimetric monitoring of decomposition rate on the surface of 0001 c-plane sapphire for the high temperature growth of AlN.* physica status solidi c, 2007. **4**(7): p. 2297-2300.
228. Stringfellow, G.B., *Organometallic Vapor-Phase Epitaxy: Theory and Practice*. 2nd ed. 1999: Academic Press.
229. Ponce, F.A., *Defects and Interfaces in GaN Epitaxy.* MRS Bulletin, 2013. **22**(2): p. 51-57.
230. Cullity, B.D., *Elements of x-ray diffraction.* 2014.
231. Fewster, P.F., *X-Ray Scattering from Semiconductors*. X-Ray Scattering from Semiconductors.
232. Moram, M.A. and M.E. Vickers, *X-ray diffraction of III-nitrides.* Reports on Progress in Physics, 2009. **72**(3): p. 036502.
233. Bruker. *Atomic Force Microscopes*. 2019; Available from: https://www.bruker.com/products/surface-and-dimensional-analysis/atomic-force-microscopes/campaigns/afm-microscopes.html.
234. Horiba. *What is Raman Spectroscopy?* [cited 2020; Available from: https://www.horiba.com/en_en/raman-imaging-and-spectroscopy/.
235. Mohiuddin, T.M.G., A. Lombardo, R.R. Nair, A. Bonetti, G. Savini, R. Jalil, N. Bonini, D.M. Basko, C. Galiotis, N. Marzari, K.S. Novoselov, A.K. Geim, and A.C. Ferrari, *Uniaxial strain in graphene by Raman spectroscopy: G peak splitting, Gruneisen parameters, and sample orientation.* Physical Review B, 2009. **79**(20): p. 205433.
236. Yu, T., Z. Ni, C. Du, Y. You, Y. Wang, and Z. Shen, *Raman Mapping Investigation of Graphene on Transparent Flexible Substrate: The Strain Effect.* The Journal of Physical Chemistry C, 2008. **112**(33): p. 12602-12605.
237. Rice, C., R.J. Young, R. Zan, U. Bangert, D. Wolverson, T. Georgiou, R. Jalil, and K.S. Novoselov, *Raman-scattering measurements and first-principles calculations of strain-induced phonon shifts in monolayer* MoS_2*.* Physical Review B, 2013. **87**(8): p. 081307.
238. Ng, S.M.S.K.K., *Physics and Properties of Semiconductors—A Review*, in *Physics of Semiconductor Devices*. p. 5-75.
239. Ghobadi, N., *Band gap determination using absorption spectrum fitting procedure.* International Nano Letters, 2013. **3**(1): p. 2.
240. Fox, M., *Optical Properties of Solids*. 2001: Oxford University Press.
241. Saini, S., *Methods for Obtaining the Optical Response after CW Excitation*, in *Optical Techniques for Solid-State Materials Characterization*, A.J.T. Rohit P. Prasankumar, Editor. 2011, CRC Press.
242. Jure Demsar, T.D., *Carrier Dynamics in Bulk Semiconductors and Metals after Ultrashort Pulse* in *Optical Techniques for Solid-State Materials Characterization*, A.J.T. Rohit P. Prasankumar, Editor. 2011, CRC Press
243. *Scanning Electron Microscope*. 30/08/2019]; Available from: http://www.ammrf.org.au/myscope/pdfs/sem.pdf.
244. Yacobi, B.G. and D.B. Holt, *Cathodoluminescence*, in *Cathodoluminescence Microscopy of Inorganic Solids*. 1990, Springer US: Boston, MA. p. 55-88.
245. Vennéguès, P. and B. Beaumont, *Transmission electron microscopy study of the nitridation of the (0001) sapphire surface.* Applied Physics Letters, 1999. **75**(26): p. 4115-4117.

246. Hashimoto, T., Y. Terakoshi, M. Ishida, M. Yuri, O. Imafuji, T. Sugino, A. Yoshikawa, and K. Itoh, *Structural investigation of sapphire surface after nitridation.* Journal of Crystal Growth, 1998. **189-190**: p. 254-258.
247. Uchida, K., A. Watanabe, F. Yano, M. Kouguchi, T. Tanaka, and S. Minagawa, *Nitridation process of sapphire substrate surface and its effect on the growth of GaN.* Journal of Applied Physics, 1996. **79**(7): p. 3487-3491.
248. Kawser, A., D. Rajendra, W. Adam, J.Q.L. James, D. Yaron, and B.B. Ishwara, *Effects of sapphire nitridation and growth temperature on the epitaxial growth of hexagonal boron nitride on sapphire.* Materials Research Express, 2017. **4**(1): p. 015007.
249. Snure, M., Q. Paduano, and A. Kiefer, *Effect of surface nitridation on the epitaxial growth of few-layer sp(2) BN.* Journal of Crystal Growth, 2016. **436**: p. 16-22.
250. Chubarov, M., H. Pedersen, H. Högberg, S. Filippov, J.A.A. Engelbrecht, J. O'Connel, and A. Henry, *Boron nitride: A new photonic material.* Physica B: Condensed Matter, 2014. **439**: p. 29-34.
251. Reich, S., A.C. Ferrari, R. Arenal, A. Loiseau, I. Bello, and J. Robertson, *Resonant Raman scattering in cubic and hexagonal boron nitride.* Physical Review B, 2005. **71**(20): p. 205201.
252. Gorbachev, R.V., I. Riaz, R.R. Nair, R. Jalil, L. Britnell, B.D. Belle, E.W. Hill, K.S. Novoselov, K. Watanabe, T. Taniguchi, A.K. Geim, and P. Blake, *Hunting for Monolayer Boron Nitride: Optical and Raman Signatures.* Small, 2011. **7**(4): p. 465-468.
253. Nemanich, R.J., S.A. Solin, and R.M. Martin, *Light scattering study of boron nitride microcrystals.* Physical Review B, 1981. **23**(12): p. 6348-6356.
254. Serrano, J., A. Bosak, R. Arenal, M. Krisch, K. Watanabe, T. Taniguchi, H. Kanda, A. Rubio, and L. Wirtz, *Vibrational Properties of Hexagonal Boron Nitride: Inelastic X-Ray Scattering and Ab Initio Calculations.* Physical Review Letters, 2007. **98**(9): p. 095503.
255. Kadleíková, M., J. Breza, and M. Veselý, *Raman spectra of synthetic sapphire.* Microelectronics Journal, 2001. **32**(12): p. 955-958.
256. Androulidakis, C., E.N. Koukaras, M. Poss, K. Papagelis, C. Galiotis, and S. Tawfick, *Strained hexagonal boron nitride: Phonon shift and Gruneisen parameter.* Physical Review B, 2018. **97**(24): p. 241414.
257. Jang, A.R., S. Hong, C. Hyun, S.I. Yoon, G. Kim, H.Y. Jeong, T.J. Shin, S.O. Park, K. Wong, S.K. Kwak, N. Park, K. Yu, E. Choi, A. Mishchenko, F. Withers, K.S. Novoselov, H. Lim, and H.S. Shin, *Wafer-Scale and Wrinkle-Free Epitaxial Growth of Single-Orientated Multilayer Hexagonal Boron Nitride on Sapphire.* Nano Letters, 2016. **16**(5): p. 3360-3366.
258. Page, R., J. Casamento, Y. Cho, S. Rouvimov, H.G. Xing, and D. Jena, *Rotationally aligned hexagonal boron nitride on sapphire by high-temperature molecular beam epitaxy.* Physical Review Materials, 2019. **3**(6): p. 064001.
259. Shi, Y.M., C. Hamsen, X.T. Jia, K.K. Kim, A. Reina, M. Hofmann, A.L. Hsu, K. Zhang, H.N. Li, Z.Y. Juang, M.S. Dresselhaus, L.J. Li, and J. Kong, *Synthesis of Few-Layer Hexagonal Boron Nitride Thin Film by Chemical Vapor Deposition.* Nano Letters, 2010. **10**(10): p. 4134-4139.
260. Deng, S. and V. Berry, *Wrinkled, rippled and crumpled graphene: an overview of formation mechanism, electronic properties, and applications.* Materials Today, 2016. **19**(4): p. 197-212.

261. Zhang, Y., T. Gao, Y. Gao, S. Xie, Q. Ji, K. Yan, H. Peng, and Z. Liu, *Defect-like Structures of Graphene on Copper Foils for Strain Relief Investigated by High-Resolution Scanning Tunneling Microscopy.* ACS Nano, 2011. **5**(5): p. 4014-4022.
262. Jin, C.S., G. Fethullah, K.K. Kang, K.E. Sung, H.G. Hee, K.S. Min, S. Hyeon-Jin, Y. Seon-Mi, C. Jae-Young, P.M. Ho, Y.C. Woong, P. Didier, and L.Y. Hee, *Synthesis of Large-Area Graphene Layers on Poly-Nickel Substrate by Chemical Vapor Deposition: Wrinkle Formation.* Advanced Materials, 2009. **21**(22): p. 2328-2333.
263. Jeong, H., D.Y. Kim, J. Kim, S. Moon, N. Han, S.H. Lee, O.F.N. Okello, K. Song, S.-Y. Choi, and J.K. Kim, *Wafer-scale and selective-area growth of high-quality hexagonal boron nitride on Ni(111) by metal-organic chemical vapor deposition.* Scientific Reports, 2019. **9**(1): p. 5736.
264. Conley, H.J., B. Wang, J.I. Ziegler, R.F. Haglund, S.T. Pantelides, and K.I. Bolotin, *Bandgap Engineering of Strained Monolayer and Bilayer MoS2.* Nano Letters, 2013. **13**(8): p. 3626-3630.
265. Cassabois, G., P. Valvin, and B. Gil, *Hexagonal boron nitride is an indirect bandgap semiconductor.* Nature Photonics, 2016. **10**: p. 262.
266. Imam, M., L. Souqui, J. Herritsch, A. Stegmüller, C. Höglund, S. Schmidt, R. Hall-Wilton, H. Högberg, J. Birch, R. Tonner, and H. Pedersen, *Gas Phase Chemistry of Trimethylboron in Thermal Chemical Vapor Deposition.* The Journal of Physical Chemistry C, 2017. **121**(47): p. 26465-26471.
267. Imam, M., C. Höglund, S. Schmidt, R. Hall-Wilton, J. Birch, and H. Pedersen, *Plasma CVD of hydrogenated boron-carbon thin films from triethylboron.* The Journal of Chemical Physics, 2018. **148**(3): p. 034701.
268. Jacobsohn, L.G., R.K. Schulze, M.E.H. Maia da Costa, and M. Nastasi, *X-ray photoelectron spectroscopy investigation of boron carbide films deposited by sputtering.* Surface Science, 2004. **572**(2): p. 418-424.
269. Vuong, T.Q.P., G. Cassabois, P. Valvin, E. Rousseau, A. Summerfield, C.J. Mellor, Y. Cho, T.S. Cheng, J.D. Albar, L. Eaves, C.T. Foxon, P.H. Beton, S.V. Novikov, and B. Gil, *Deep ultraviolet emission in hexagonal boron nitride grown by high-temperature molecular beam epitaxy.* 2D Materials, 2017. **4**(2): p. 021023.
270. Leon, J.A., N.C. Mamani, A. Rahim, L.E. Gomez, M.A.P.d. Silva, and G.M. Gusev, *Transferring Few-Layer Graphene Sheets on Hexagonal Boron Nitride Substrates for Fabrication of Graphene Devices.* Graphene, 2014. **Vol.03No.03**: p. 11.
271. Ho, K.H., L.S. Kyu, L.S. Goo, L. Eunho, and C. Kilwon, *Wetting-Assisted Crack- and Wrinkle-Free Transfer of Wafer-Scale Graphene onto Arbitrary Substrates over a Wide Range of Surface Energies.* Advanced Functional Materials, 2016. **26**(13): p. 2070-2077.
272. Suk, J.W., A. Kitt, C.W. Magnuson, Y. Hao, S. Ahmed, J. An, A.K. Swan, B.B. Goldberg, and R.S. Ruoff, *Transfer of CVD-Grown Monolayer Graphene onto Arbitrary Substrates.* ACS Nano, 2011. **5**(9): p. 6916-6924.
273. Pakdel, A., Y. Bando, and D. Golberg, *Plasma-Assisted Interface Engineering of Boron Nitride Nanostructure Films.* ACS Nano, 2014. **8**(10): p. 10631-10639.
274. Silly, M.G., P. Jaffrennou, J. Barjon, J.S. Lauret, F. Ducastelle, A. Loiseau, E. Obraztsova, B. Attal-Tretout, and E. Rosencher, *Luminescence properties of*

hexagonal boron nitride: Cathodoluminescence and photoluminescence spectroscopy measurements. Physical Review B, 2007. **75**(8): p. 085205.
275. Museur, L., G. Brasse, A. Pierret, S. Maine, B. Attal-Tretout, F. Ducastelle, A. Loiseau, J. Barjon, K. Watanabe, T. Taniguchi, and A. Kanaev, *Exciton optical transitions in a hexagonal boron nitride single crystal.* physica status solidi (RRL) – Rapid Research Letters, 2011. **5**(5-6): p. 214-216.
276. Galvani, T., F. Paleari, H.P.C. Miranda, A. Molina-Sánchez, L. Wirtz, S. Latil, H. Amara, and F. Ducastelle, *Excitons in boron nitride single layer.* Physical Review B, 2016. **94**(12): p. 125303.
277. Watanabe, K. and T. Taniguchi, *Jahn-Teller effect on exciton states in hexagonal boron nitride single crystal.* Physical Review B, 2009. **79**(19): p. 193104.
278. Arnaud, B., S. Lebègue, P. Rabiller, and M. Alouani, *Huge Excitonic Effects in Layered Hexagonal Boron Nitride.* Physical Review Letters, 2006. **96**(2): p. 026402.
279. Marini, A., *Ab Initio Finite-Temperature Excitons.* Physical Review Letters, 2008. **101**(10): p. 106405.
280. Watanabe, K., T. Taniguchi, T. Kuroda, O. Tsuda, and H. Kanda, *Time-resolved photoluminescence in band-edge region of hexagonal boron nitride single crystals.* Diamond and Related Materials, 2008. **17**(4): p. 830-832.
281. Museur, L. and A. Kanaev, *Near band-gap photoluminescence properties of hexagonal boron nitride.* Journal of Applied Physics, 2008. **103**(10): p. 103520.
282. Jaffrennou, P., J. Barjon, J.-S. Lauret, B. Attal-Trétout, F. Ducastelle, and A. Loiseau, *Origin of the excitonic recombinations in hexagonal boron nitride by spatially resolved cathodoluminescence spectroscopy.* Journal of Applied Physics, 2007. **102**(11): p. 116102.
283. Watanabe, K., T. Taniguchi, T. Kuroda, and H. Kanda, *Effects of deformation on band-edge luminescence of hexagonal boron nitride single crystals.* Applied Physics Letters, 2006. **89**(14): p. 141902.
284. Schué, L., B. Berini, A.C. Betz, B. Plaçais, F. Ducastelle, J. Barjon, and A. Loiseau, *Dimensionality effects on the luminescence properties of hBN.* Nanoscale, 2016. **8**(13): p. 6986-6993.
285. Huafeng, Y., W. Freddie, G. Elias, L. Edward, B. Liam, F. Alexandre, P. Vincenzo, H. Sarah, B. David, and C. Cinzia, *Dielectric nanosheets made by liquid-phase exfoliation in water and their use in graphene-based electronics.* 2D Materials, 2014. **1**(1): p. 011012.
286. Zhao, W., Z. Ghorannevis, L. Chu, M. Toh, C. Kloc, P.-H. Tan, and G. Eda, *Evolution of Electronic Structure in Atomically Thin Sheets of WS2 and WSe2.* ACS Nano, 2013. **7**(1): p. 791-797.
287. Splendiani, A., L. Sun, Y. Zhang, T. Li, J. Kim, C.-Y. Chim, G. Galli, and F. Wang, *Emerging Photoluminescence in Monolayer MoS2.* Nano Letters, 2010. **10**(4): p. 1271-1275.
288. Mak, K.F., C. Lee, J. Hone, J. Shan, and T.F. Heinz, *Atomically Thin MoS_2: A New Direct-Gap Semiconductor.* Physical Review Letters, 2010. **105**(13): p. 136805.
289. Kuc, A., N. Zibouche, and T. Heine, *Influence of quantum confinement on the electronic structure of the transition metal sulfide* $\boldsymbol{TS_2}$. Physical Review B, 2011. **83**(24): p. 245213.

290. Bourrellier, R., *Luminescence at Defects in h-BN : Excitons at Stacking Faults and Single Photon Emitters*. 2014, Université Paris Sud - Paris XI.
291. Bourrellier, R., M. Amato, L.H. Galvão Tizei, C. Giorgetti, A. Gloter, M.I. Heggie, K. March, O. Stéphan, L. Reining, M. Kociak, and A. Zobelli, *Nanometric Resolved Luminescence in h-BN Flakes: Excitons and Stacking Order.* ACS Photonics, 2014. **1**(9): p. 857-862.
292. Museur, L., E. Feldbach, and A. Kanaev, *Defect-related photoluminescence of hexagonal boron nitride.* Physical Review B, 2008. **78**(15): p. 155204.
293. Vogl, T., Y. Lu, and P. Koy Lam, *Room temperature single photon source using fiber-integrated hexagonal boron nitride.* Journal of Physics D: Applied Physics, 2017. **50**(29): p. 295101.
294. Martínez, L.J., T. Pelini, V. Waselowski, J.R. Maze, B. Gil, G. Cassabois, and V. Jacques, *Efficient single photon emission from a high-purity hexagonal boron nitride crystal.* Physical Review B, 2016. **94**(12): p. 121405.
295. Tran, T.T., C. Zachreson, A.M. Berhane, K. Bray, R.G. Sandstrom, L.H. Li, T. Taniguchi, K. Watanabe, I. Aharonovich, and M. Toth, *Quantum Emission from Defects in Single-Crystalline Hexagonal Boron Nitride.* Physical Review Applied, 2016. **5**(3): p. 034005.
296. Mendelson, N., Z.-Q. Xu, T.T. Tran, M. Kianinia, J. Scott, C. Bradac, I. Aharonovich, and M. Toth, *Engineering and Tuning of Quantum Emitters in Few-Layer Hexagonal Boron Nitride.* ACS Nano, 2019. **13**(3): p. 3132-3140.
297. Ziegler, J., A. Blaikie, A. Fathalizadeh, D. Miller, F.S. Yasin, K. Williams, J. Mohrhardt, B.J. McMorran, A. Zettl, and B. Alemán, *Single-Photon Emitters in Boron Nitride Nanococoons.* Nano Letters, 2018. **18**(4): p. 2683-2688.
298. Chejanovsky, N., M. Rezai, F. Paolucci, Y. Kim, T. Rendler, W. Rouabeh, F. Fávaro de Oliveira, P. Herlinger, A. Denisenko, S. Yang, I. Gerhardt, A. Finkler, J.H. Smet, and J. Wrachtrup, *Structural Attributes and Photodynamics of Visible Spectrum Quantum Emitters in Hexagonal Boron Nitride.* Nano Letters, 2016. **16**(11): p. 7037-7045.
299. Tawfik, S.A., S. Ali, M. Fronzi, M. Kianinia, T.T. Tran, C. Stampfl, I. Aharonovich, M. Toth, and M.J. Ford, *First-principles investigation of quantum emission from hBN defects.* Nanoscale, 2017. **9**(36): p. 13575-13582.
300. Lee, K.H. and J.H. Crawford, *Luminescence of the F center in sapphire.* Physical Review B, 1979. **19**(6): p. 3217-3221.
301. Ghamnia, M., C. Jardin, and M. Bouslama, *Luminescent centres F and F+ in α-alumina detected by cathodoluminescence technique.* Journal of Electron Spectroscopy and Related Phenomena, 2003. **133**(1): p. 55-63.
302. Reshchikov, M.A. and H. Morkoç, *Luminescence properties of defects in GaN.* Journal of Applied Physics, 2005. **97**(6): p. 061301.
303. Schmechel, R., H. Werheit, T.U. Kampen, and W. Mönch, *Photoluminescence of boron carbide.* Journal of Solid State Chemistry, 2004. **177**(2): p. 566-568.
304. Iwano, Y., T. Kittaka, H. Tabuchi, M. Soukawa, S. Kunitsugu, K. Takarabe, and K. Itoh, *Study of Amorphous Carbon Nitride Films Aiming at White Light Emitting Devices.* Japanese Journal of Applied Physics, 2008. **47**(10): p. 7842-7844.
305. Wang, B., K. Ostrikov, T. van der Laan, R. Shao, and L. Li, *Structure and photoluminescence of boron-doped carbon nanoflakes grown by hot filament chemical vapour deposition.* Journal of Materials Chemistry C, 2015. **3**(5): p. 1106-1112.

306. Xu, J., M. Shalom, F. Piersimoni, M. Antonietti, D. Neher, and T.J.K. Brenner, *Color-Tunable Photoluminescence and NIR Electroluminescence in Carbon Nitride Thin Films and Light-Emitting Diodes.* Advanced Optical Materials, 2015. **3**(7): p. 913-917.
307. Grosso, G., H. Moon, B. Lienhard, S. Ali, D.K. Efetov, M.M. Furchi, P. Jarillo-Herrero, M.J. Ford, I. Aharonovich, and D. Englund, *Tunable and high-purity room temperature single-photon emission from atomic defects in hexagonal boron nitride.* Nature Communications, 2017. **8**(1): p. 705.
308. Li, Q., Q. Zhou, L. Shi, Q. Chen, and J. Wang, *Recent advances in oxidation and degradation mechanisms of ultrathin 2D materials under ambient conditions and their passivation strategies.* Journal of Materials Chemistry A, 2019. **7**(9): p. 4291-4312.
309. Le Ru, E.C. and P.G. Etchegoin, *Chapter 1 - A quick overview of surface-enhanced Raman spectroscopy*, in *Principles of Surface-Enhanced Raman Spectroscopy*, E.C. Le Ru and P.G. Etchegoin, Editors. 2009, Elsevier: Amsterdam. p. 1-27.
310. Le Ru, E.C., E. Blackie, M. Meyer, and P.G. Etchegoin, *Surface Enhanced Raman Scattering Enhancement Factors: A Comprehensive Study.* The Journal of Physical Chemistry C, 2007. **111**(37): p. 13794-13803.
311. Le Ru, E.C. and P.G. Etchegoin, *Chapter 4 - SERS enhancement factors and related topics*, in *Principles of Surface-Enhanced Raman Spectroscopy*, E.C. Le Ru and P.G. Etchegoin, Editors. 2009, Elsevier: Amsterdam. p. 185-264.
312. Nie, S. and S.R. Emory, *Probing Single Molecules and Single Nanoparticles by Surface-Enhanced Raman Scattering.* Science, 1997. **275**(5303): p. 1102-1106.
313. Jia, M., S. Li, L. Zang, X. Lu, and H. Zhang, *Analysis of Biomolecules Based on the Surface Enhanced Raman Spectroscopy.* Nanomaterials (Basel, Switzerland), 2018. **8**(9): p. 730.
314. Lee, K.-S. and M.A. El-Sayed, *Gold and Silver Nanoparticles in Sensing and Imaging: Sensitivity of Plasmon Response to Size, Shape, and Metal Composition.* The Journal of Physical Chemistry B, 2006. **110**(39): p. 19220-19225.
315. Han, Y., R. Lupitskyy, T.-M. Chou, C.M. Stafford, H. Du, and S. Sukhishvili, *Effect of Oxidation on Surface-Enhanced Raman Scattering Activity of Silver Nanoparticles: A Quantitative Correlation.* Analytical Chemistry, 2011. **83**(15): p. 5873-5880.
316. Erol, M., Y. Han, S.K. Stanley, C.M. Stafford, H. Du, and S. Sukhishvili, *SERS Not To Be Taken for Granted in the Presence of Oxygen.* Journal of the American Chemical Society, 2009. **131**(22): p. 7480-7481.
317. Pinkhasova, P., H. Chen, M.W.G.M. Verhoeven, S. Sukhishvili, and H. Du, *Thermally annealed Ag nanoparticles on anodized aluminium oxide for SERS sensing.* RSC Advances, 2013. **3**(39): p. 17954-17961.
318. Bao, L., S.M. Mahurin, and S. Dai, *Controlled Layer-By-Layer Formation of Ultrathin TiO2 on Silver Island Films via a Surface Sol−Gel Method for Surface-Enhanced Raman Scattering Measurement.* Analytical Chemistry, 2004. **76**(15): p. 4531-4536.
319. Formo, E.V., S.M. Mahurin, and S. Dai, *Robust SERS Substrates Generated by Coupling a Bottom-Up Approach and Atomic Layer Deposition.* ACS Applied Materials & Interfaces, 2010. **2**(7): p. 1987-1991.

320. Amendola, V., R. Pilot, M. Frasconi, O.M. Maragò, and M.A. Iatì, *Surface plasmon resonance in gold nanoparticles: a review.* Journal of Physics: Condensed Matter, 2017. **29**(20): p. 203002.
321. Li, J.F., Y.F. Huang, Y. Ding, Z.L. Yang, S.B. Li, X.S. Zhou, F.R. Fan, W. Zhang, Z.Y. Zhou, D.Y. Wu, B. Ren, Z.L. Wang, and Z.Q. Tian, *Shell-isolated nanoparticle-enhanced Raman spectroscopy.* Nature, 2010. **464**: p. 392.
322. Xu, W., J. Xiao, Y. Chen, Y. Chen, X. Ling, and J. Zhang, *Graphene-Veiled Gold Substrate for Surface-Enhanced Raman Spectroscopy.* Advanced Materials, 2013. **25**(6): p. 928-933.
323. Xu, W., X. Ling, J. Xiao, M.S. Dresselhaus, J. Kong, H. Xu, Z. Liu, and J. Zhang, *Surface enhanced Raman spectroscopy on a flat graphene surface.* Proceedings of the National Academy of Sciences, 2012. **109**(24): p. 9281-9286.
324. Chilkoor, G., S.P. Karanam, S. Star, N. Shrestha, R.K. Sani, V.K.K. Upadhyayula, D. Ghoshal, N.A. Koratkar, M. Meyyappan, and V. Gadhamshetty, *Hexagonal Boron Nitride: The Thinnest Insulating Barrier to Microbial Corrosion.* ACS Nano, 2018. **12**(3): p. 2242-2252.
325. Zhou, F., Z. Li, G.J. Shenoy, L. Li, and H. Liu, *Enhanced Room-Temperature Corrosion of Copper in the Presence of Graphene.* ACS Nano, 2013. **7**(8): p. 6939-6947.
326. Schriver, M., W. Regan, W.J. Gannett, A.M. Zaniewski, M.F. Crommie, and A. Zettl, *Graphene as a Long-Term Metal Oxidation Barrier: Worse Than Nothing.* ACS Nano, 2013. **7**(7): p. 5763-5768.
327. Garcia, A.G.F., M. Neumann, F. Amet, J.R. Williams, K. Watanabe, T. Taniguchi, and D. Goldhaber-Gordon, *Effective Cleaning of Hexagonal Boron Nitride for Graphene Devices.* Nano Letters, 2012. **12**(9): p. 4449-4454.
328. Hildebrandt, P. and M. Stockburger, *Surface-enhanced resonance Raman spectroscopy of Rhodamine 6G adsorbed on colloidal silver.* The Journal of Physical Chemistry, 1984. **88**(24): p. 5935-5944.
329. Cai, Q., A. Du, G. Gao, S. Mateti, B.C.C. Cowie, D. Qian, S. Zhang, Y. Lu, L. Fu, T. Taniguchi, S. Huang, Y. Chen, R.S. Ruoff, and L.H. Li, *Molecule-Induced Conformational Change in Boron Nitride Nanosheets with Enhanced Surface Adsorption.* Advanced Functional Materials, 2016. **26**(45): p. 8202-8210.
330. Lv, J., F. Lai, L. Lin, Y. Lin, Z. Huang, and R. Chen, *Thermal stability of Ag films in air prepared by thermal evaporation.* Applied Surface Science, 2007. **253**(17): p. 7036-7040.
331. McMahon, M.D., R. Lopez, H.M. Meyer, L.C. Feldman, and R.F. Haglund, *Rapid tarnishing of silver nanoparticles in ambient laboratory air.* Applied Physics B, 2005. **80**(7): p. 915-921.
332. Thompson, C.V., *Solid-State Dewetting of Thin Films.* Annual Review of Materials Research, 2012. **42**(1): p. 399-434.
333. Sui, M., P. Pandey, S. Kunwar, M.Y. Li, Q. Zhang, and J. Lee, *Evolution of self-assembled Ag nanostructures on c-plane sapphire by the systematic control of annealing temperature.* Superlattices and Microstructures, 2016. **100**: p. 1128-1142.
334. Huang, P.Y., C.S. Ruiz-Vargas, A.M. van der Zande, W.S. Whitney, M.P. Levendorf, J.W. Kevek, S. Garg, J.S. Alden, C.J. Hustedt, Y. Zhu, J. Park, P.L. McEuen, and D.A. Muller, *Grains and grain boundaries in single-layer graphene atomic patchwork quilts.* Nature, 2011. **469**: p. 389.

335. Ruiz-Vargas, C.S., H.L. Zhuang, P.Y. Huang, A.M. van der Zande, S. Garg, P.L. McEuen, D.A. Muller, R.G. Hennig, and J. Park, *Softened Elastic Response and Unzipping in Chemical Vapor Deposition Graphene Membranes.* Nano Letters, 2011. **11**(6): p. 2259-2263.
336. Liao, Y., K. Tu, X. Han, L. Hu, J.W. Connell, Z. Chen, and Y. Lin, *Oxidative Etching of Hexagonal Boron Nitride Toward Nanosheets with Defined Edges and Holes.* Scientific Reports, 2015. **5**: p. 14510.
337. Lin, Y., K.A. Watson, J.-W. Kim, D.W. Baggett, D.C. Working, and J.W. Connell, *Bulk preparation of holey graphene via controlled catalytic oxidation.* Nanoscale, 2013. **5**(17): p. 7814-7824.
338. Asoro, M.A., D. Kovar, and P.J. Ferreira, *In situ Transmission Electron Microscopy Observations of Sublimation in Silver Nanoparticles.* ACS Nano, 2013. **7**(9): p. 7844-7852.
339. Sui, M., S. Kunwar, P. Pandey, Q. Zhang, M.-Y. Li, and J. Lee, *Investigation on the morphology and optical properties of self-assembled Ag Nanostructures on c-plane GaN by the control of annealing temperature and duration.* Nano-Structures & Nano-Objects, 2018. **15**: p. 28-39.
340. Feng, W., E. Ueda, and P.A. Levkin, *Droplet Microarrays: From Surface Patterning to High-Throughput Applications.* Advanced Materials, 2018. **30**(20): p. 1706111.
341. Garcia-Cordero, J.L. and Z.H. Fan, *Sessile droplets for chemical and biological assays.* Lab on a Chip, 2017. **17**(13): p. 2150-2166.
342. Deegan, R.D., O. Bakajin, T.F. Dupont, G. Huber, S.R. Nagel, and T.A. Witten, *Capillary flow as the cause of ring stains from dried liquid drops.* Nature, 1997. **389**: p. 827.
343. Hu, H. and R.G. Larson, *Evaporation of a Sessile Droplet on a Substrate.* The Journal of Physical Chemistry B, 2002. **106**(6): p. 1334-1344.
344. Bitla, Y. and Y.-H. Chu, *MICAtronics: A new platform for flexible X-tronics.* FlatChem, 2017. **3**: p. 26-42.
345. Yu, J., L. Wang, Z. Hao, Y. Luo, C. Sun, J. Wang, Y. Han, B. Xiong, and H. Li, *Van der Waals Epitaxy of III-Nitride Semiconductors Based on 2D Materials for Flexible Applications.* Advanced Materials: p. 1903407.
346. Kim, J., C. Bayram, H. Park, C.-W. Cheng, C. Dimitrakopoulos, J.A. Ott, K.B. Reuter, S.W. Bedell, and D.K. Sadana, *Principle of direct van der Waals epitaxy of single-crystalline films on epitaxial graphene.* Nature Communications, 2014. **5**: p. 4836.
347. Yoo, H., K. Chung, Y.S. Choi, C.S. Kang, K.H. Oh, M. Kim, and G.-C. Yi, *Microstructures of GaN Thin Films Grown on Graphene Layers.* Advanced Materials, 2012. **24**(4): p. 515-518.
348. Koma, A., *Van der Waals epitaxy for highly lattice-mismatched systems.* Journal of Crystal Growth, 1999. **201-202**: p. 236-241.
349. Hirayama, H., N. Maeda, S. Fujikawa, S. Toyoda, and N. Kamata, *Recent progress and future prospects of AlGaN-based high-efficiency deep-ultraviolet light-emitting diodes.* Japanese Journal of Applied Physics, 2014. **53**(10): p. 100209.
350. Imura, M., K. Nakano, N. Fujimoto, N. Okada, K. Balakrishnan, M. Iwaya, S. Kamiyama, H. Amano, I. Akasaki, T. Noro, T. Takagi, and A. Bandoh, *Dislocations in AlN Epilayers Grown on Sapphire Substrate by High-Temperature Metal-Organic Vapor Phase Epitaxy.* Japanese Journal of Applied Physics, 2007. **46**(4A): p. 1458-1462.

351. Imura, M., K. Nakano, N. Fujimoto, N. Okada, K. Balakrishnan, M. Iwaya, S. Kamiyama, H. Amano, I. Akasaki, T. Noro, T. Takagi, and A. Bandoh, *High-Temperature Metal-Organic Vapor Phase Epitaxial Growth of AlN on Sapphire by Multi Transition Growth Mode Method Varying V/III Ratio.* Japanese Journal of Applied Physics, 2006. **45**(11): p. 8639-8643.
352. Ohba, Y. and A. Hatano, *Growth of high-quality AlN and AlN/GaN/AlN heterostructure on sapphire substrate.* Japanese Journal of Applied Physics Part 2-Letters, 1996. **35**(8b): p. L1013-L1015.
353. Yamamoto, N., H. Itoh, V. Grillo, S.F. Chichibu, S. Keller, J.S. Speck, S.P. DenBaars, U.K. Mishra, S. Nakamura, and G. Salviati, *Cathodoluminescence characterization of dislocations in gallium nitride using a transmission electron microscope.* Journal of Applied Physics, 2003. **94**(7): p. 4315-4319.
354. Rosner, S.J., E.C. Carr, M.J. Ludowise, G. Girolami, and H.I. Erikson, *Correlation of cathodoluminescence inhomogeneity with microstructural defects in epitaxial GaN grown by metalorganic chemical-vapor deposition.* Applied Physics Letters, 1997. **70**(4): p. 420-422.
355. Eom, D., J. Kim, K. Lee, M. Jeon, C. Heo, J. Pyeon, and O. Nam, *AlN Nanostructures Fabricated on a Vicinal Sapphire (0001) Substrate.* Crystal Growth & Design, 2015. **15**(3): p. 1242-1248.
356. Stolyarchuk, N., T. Markurt, A. Courville, K. March, O. Tottereau, P. Vennéguès, and M. Albrecht, *Impact of sapphire nitridation on formation of Al-polar inversion domains in N-polar AlN epitaxial layers.* Journal of Applied Physics, 2017. **122**(15): p. 155303.
357. Hussey, L., R.M. White, R. Kirste, S. Mita, I. Bryan, W. Guo, K. Osterman, B. Haidet, Z. Bryan, M. Bobea, R. Collazo, and Z. Sitar, *Sapphire decomposition and inversion domains in N-polar aluminum nitride.* Applied Physics Letters, 2014. **104**(3): p. 032104.
358. Paduano, Q.S., D.W. Weyburne, J. Jasinski, and Z. Liliental-Weber, *Effect of initial process conditions on the structural properties of AlN films.* Journal of Crystal Growth, 2004. **261**(2): p. 259-265.
359. Raghavan, S. and J.M. Redwing, *Intrinsic stresses in AlN layers grown by metal organic chemical vapor deposition on (0001) sapphire and (111) Si substrates.* Journal of Applied Physics, 2004. **96**(5): p. 2995-3003.
360. Brunner, F., A. Mogilatenko, V. Kueller, A. Knauer, and M. Weyers, *Stress evolution during AlxGa1−xN/AlN growth on sapphire.* Journal of Crystal Growth, 2013. **376**: p. 54-58.
361. Hearne, S., E. Chason, J. Han, J.A. Floro, J. Figiel, J. Hunter, H. Amano, and I.S.T. Tsong, *Stress evolution during metalorganic chemical vapor deposition of GaN.* Applied Physics Letters, 1999. **74**(3): p. 356-358.
362. Nakamura, S., *Gan Growth Using Gan Buffer Layer.* Japanese Journal of Applied Physics 1991. **30**(10a): p. L1705-L1707.
363. Amano, H., N. Sawaki, I. Akasaki, and Y. Toyoda, *Metalorganic vapor phase epitaxial growth of a high quality GaN film using an AlN buffer layer.* Applied Physics Letters, 1986. **48**(5): p. 353-355.
364. Katona, T.M., P. Cantu, S. Keller, Y. Wu, J.S. Speck, and S.P. DenBaars, *Maskless lateral epitaxial overgrowth of high-aluminum-content AlxGa1−xN.* Applied Physics Letters, 2004. **84**(24): p. 5025-5027.
365. Wu, Q., J. Yan, L. Zhang, X. Chen, T. Wei, Y. Li, Z. Liu, X. Wei, Y. Zhang, J. Wang, and J. Li, *Growth mechanism of AlN on hexagonal BN/sapphire*

substrate by metal–organic chemical vapor deposition. CrystEngComm, 2017. **19**(39): p. 5849-5856.

366. Snure, M., G. Siegel, D.C. Look, and Q. Paduano, *GaN and AlGaN/GaN heterostructures grown on two dimensional BN templates.* Journal of Crystal Growth, 2017. **464**: p. 168-174.
367. Amano, H., I. Akasaki, K. Hiramatsu, N. Koide, and N. Sawaki, *Effects of the Buffer Layer in Metalorganic Vapor-Phase Epitaxy of GaN on Sapphire Substrate.* Thin Solid Films, 1988. **163**: p. 415-420.
368. Sun, C.J., P. Kung, A. Saxler, H. Ohsato, K. Haritos, and M. Razeghi, *A crystallographic model of (00·1) aluminum nitride epitaxial thin film growth on (00·1) sapphire substrate.* Journal of Applied Physics, 1994. **75**(8): p. 3964-3967.
369. Morita, M., N. Uesugi, S. Isogai, K. Tsubouchi, and N. Mikoshiba, *Epitaxial Growth of Aluminum Nitride on Sapphire Using Metalorganic Chemical Vapor Deposition.* Japanese Journal of Applied Physics, 1981. **20**(1): p. 17-23.
370. Mohn, S., N. Stolyarchuk, T. Markurt, R. Kirste, M.P. Hoffmann, R. Collazo, A. Courville, R. Di Felice, Z. Sitar, P. Vennéguès, and M. Albrecht, *Polarity Control in Group-III Nitrides beyond Pragmatism.* Physical Review Applied, 2016. **5**(5): p. 054004.
371. Kobayashi, K., A.A. Yamaguchi, S. Kimura, H. Sunakawa, A. Kimura, and A. Usui, *X-Ray Rocking Curve Determination of Twist and Tilt Angles in GaN Films Grown by an Epitaxial-Lateral-Overgrowth Technique.* Japanese Journal of Applied Physics, 1999. **38**(Part 2, No. 6A/B): p. L611-L613.
372. Li, H., T.C. Sadler, and P.J. Parbrook, *AlN heteroepitaxy on sapphire by metalorganic vapour phase epitaxy using low temperature nucleation layers.* Journal of Crystal Growth, 2013. **383**: p. 72-78.
373. Li, X.-H., S. Wang, H. Xie, Y.O. Wei, T.-T. Kao, M.M. Satter, S.-C. Shen, P. Douglas Yoder, T. Detchprohm, R.D. Dupuis, A.M. Fischer, and F.A. Ponce, *Growth of high-quality AlN layers on sapphire substrates at relatively low temperatures by metalorganic chemical vapor deposition.* physica status solidi (b), 2015. **252**(5): p. 1089-1095.
374. Chen, Z., S. Newman, D. Brown, R. Chung, S. Keller, U.K. Mishra, S.P. Denbaars, and S. Nakamura, *High quality AlN grown on SiC by metal organic chemical vapor deposition.* Applied Physics Letters, 2008. **93**(19): p. 191906.
375. Guo, Y., Y. Fang, J. Yin, Z. Zhang, B. Wang, J. Li, W. Lu, and Z. Feng, *Improved structural quality of AlN grown on sapphire by 3D/2D alternation growth.* Journal of Crystal Growth, 2017. **464**: p. 119-122.
376. Fareed, Q., R. Gaska, and M.S. Shur. *Migration enhanced metal organic chemical vapor deposition of AlN/GaN/InN-based heterostructures*. in *International Semiconductor Device Research Symposium*. 2003.
377. Kobayashi, N., T. Makimoto, Y. Yamauchi, and Y. Horikoshi, *Flow-rate modulation epitaxy of GaAs and AlGaAs.* Journal of Applied Physics, 1989. **66**(2): p. 640-651.
378. Yang, S., R. Miyagawa, H. Miyake, K. Hiramatsu, and H. Harima, *Raman Scattering Spectroscopy of Residual Stresses in Epitaxial AlN Films.* Applied Physics Express, 2011. **4**(3): p. 031001.
379. Hayes, J.M., M. Kuball, Y. Shi, and J.H. Edgar, *Temperature Dependence of the Phonons of Bulk AlN.* Japanese Journal of Applied Physics, 2000. **39**(Part 2, No. 7B): p. L710-L712.

380. Davydov, V.Y., Y.E. Kitaev, I.N. Goncharuk, A.N. Smirnov, J. Graul, O. Semchinova, D. Uffmann, M.B. Smirnov, A.P. Mirgorodsky, and R.A. Evarestov, *Phonon dispersion and Raman scattering in hexagonal GaN and AlN.* Physical Review B, 1998. **58**(19): p. 12899-12907.
381. Porto, S.P.S. and R.S. Krishnan, *Raman Effect of Corundum.* The Journal of Chemical Physics, 1967. **47**(3): p. 1009-1012.
382. Chen, C.H., H. Liu, D. Steigerwald, W. Imler, C.P. Kuo, M.G. Craford, M. Ludowise, S. Lester, and J. Amano, *A study of parasitic reactions between NH3 and TMGa or TMAl.* Journal of Electronic Materials, 1996. **25**(6): p. 1004-1008.
383. Nakamura, K., O. Makino, A. Tachibana, and K. Matsumoto, *Quantum chemical study of parasitic reaction in III–V nitride semiconductor crystal growth.* Journal of Organometallic Chemistry, 2000. **611**(1): p. 514-524.
384. Kobayashi, Y., H. Hibino, T. Nakamura, T. Akasaka, T. Makimoto, and N. Matsumoto, *Boron Nitride Thin Films Grown on Graphitized 6H–SiC Substrates by Metalorganic Vapor Phase Epitaxy.* Japanese Journal of Applied Physics, 2007. **46**(4B): p. 2554-2557.
385. Emtsev, K.V., A. Bostwick, K. Horn, J. Jobst, G.L. Kellogg, L. Ley, J.L. McChesney, T. Ohta, S.A. Reshanov, J. Röhrl, E. Rotenberg, A.K. Schmid, D. Waldmann, H.B. Weber, and T. Seyller, *Towards wafer-size graphene layers by atmospheric pressure graphitization of silicon carbide.* Nature Materials, 2009. **8**(3): p. 203-207.
386. Uddin, M.R., J. Li, J.Y. Lin, and H.X. Jiang, *Carbon-rich hexagonal (BN)C alloys.* Journal of Applied Physics, 2015. **117**(21).
387. Uddin, M.R., T.C. Doan, J. Li, K.S. Ziemer, J.Y. Lin, and H.X. Jiang, *Electrical transport properties of (BN)-rich hexagonal (BN)C semiconductor alloys.* AIP Advances, 2014. **4**(8).
388. Majety, S., T.C. Doan, J. Li, J.Y. Lin, and H.X. Jiang, *Electrical transport properties of Si-doped hexagonal boron nitride epilayers.* AIP Advances, 2013. **3**(12).